Search for the Decay $K_L \to \pi^0 \nu\overline{\nu}$ with a Neutron-Insensitive GeV-Energy Photon Detector

Department of Physics, Graduate School of Science, Kyoto University
Yosuke Maeda

January 5, 2016

Abstract

A search for the CP-violating rare decay of a neutral kaon, $K_L \to \pi^0\nu\overline{\nu}$, was performed with the data taken in the first physics run of a new experiment, named KOTO, which was launched at the Japan Proton Accelerator Research Complex.

The decay $K_L \to \pi^0\nu\overline{\nu}$ is called as the "golden mode" due to its high potential to probe the physics beyond the Standard Model of elementary particle physics. Hence measurement of its branching ratio can lead to understanding of the matter-dominated universe.

Experiments with high sensitivity require use of an intense K_L beam and complete background rejection. In other words, the key for such experiments is a detector with high performance in a high-rate environment. This requirement is especially tight for in-beam detectors, which needs to own high photon detection efficiency for enough background suppression under a large flux of neutrons and low energy photons.

In order to meet these requirements, a novel GeV-energy photon detector with aerogel as a Čerenkov radiator was designed and constructed for the KOTO experiment. Both blindness to neutrons and high detection efficiency to photons are achieved since protons and charged pions produced by neutrons have small velocity and emit no or less Čerenkov light than electrons and positrons from photons. Performance of the installed detector, especially responses to high energy photons, was evaluated by tagging photons from the $K_L \to 3\pi^0$ decay. A ratio of efficiency for > 1 GeV photons to simulation expectation was evaluated as 1.025 ± 0.050(stat.)±0.068(syst.), which indicates the measured efficiency is consistent with simulation expectation within an uncertainty of 8.2%. An over veto probability due to beam particles was found to be as small as 4.1% despite their large flux of ~ 300 MHz. These studies showed that the detector was successfully working as expected in the real beam condition.

A search for the $K_L \to \pi^0\nu\overline{\nu}$ decay was then performed with the whole KOTO detector system including the above new detector. The high-rate environment affected particle detection efficiency for various veto detectors through pile-ups of accidental hits, which can cause serious background from K_L decays. A new method of waveform analysis as well as various possibilities of K_L decays to background contribution was studied for cut optimization. As a result, one event was observed in the signal region with background expectation of 0.34 ± 0.16. Finally, a 90%-confidence-level upper limit for $\mathrm{Br}(K_L \to \pi^0\nu\overline{\nu})$ was obtained as

$$\mathrm{Br}(K_L \to \pi^0\nu\overline{\nu}) < 5.1 \times 10^{-8}$$

which is comparable with the current world record (2.6×10^{-8}), regardless of the short data taking period. This work proved strong potential of this experiment to search for the $K_L \to \pi^0\nu\overline{\nu}$ decay with 10^{-11} sensitivity in future.

Acknowledgement

This work would never be accomplished without supports from many people. I would like to acknowledge everyone on this occasion.

First of all, I would like to express my appreciation to Prof. Noboru Sasao, who introduced me to the world of elementary particle physics. I am always impressed by his enthusiasm for physics, deep insight and rich ideas on experiments. Thanks to him, I now know joy of experimental physics. I am also deeply grateful to Prof. Tadashi Nomura and Prof. Hajime Nanjo. They have taught me basis of particle physics and various experimental technique since my undergraduate days. It is no exaggeration to say all my research activities are based on discussion with them. I have learnt how I should promote my research.

I would like to thank the staff members of the KOTO experiment, Prof. T. Yamanaka, Prof. T. K. Komatsubara, Prof. G. Y. Lim, Prof. T. Inagaki, Prof. S. Suzuki, Prof. T. Shinkawa, Prof. Y. Tajima, Prof. H. Watanabe, Prof. C. Myron, Prof. T. Monica, Prof. Y. W. Wah, Prof. J. Comfort, Prof. Y. B. Hsiung, Prof. A. S. Kurilin, Prof. M. Togawa, Prof. T. Matsumura, and Prof. K. Shiomi. Their invaluable advice and lots of encouragement in various occasions were always necessary for my studies. Furthermore, I really appreciated countless hardware supports in the detector construction. Prof. K. Shiomi is also a colleague in the Kyoto University Cycling Club. I have learned a lot from his strong leadership in both situation. I would like to appreciate discussions and cooperation from members of the Kyoto kaon group, Dr. H. Morii, Mr. N. Kawasaki, Mr. D. Naito, Mr. T. Usuki, Mr. G. Takahashi, Mr. T. Hineno, Prof. T. Masuda Mr. S. Seki, Mr. K. Nakagiri, Mr. I. Kamiji and Mr. S. Shinohara. I was able to enjoy research works in the early days of my laboratory life thanks to Dr. H. Morii's kind supports. Mr. D. Naito has been my colleague since our undergraduate days, and I would like to thank him for working with me for long time. My life in Tokai village at the beam line survey phase was very fruitful thanks to Ms. M. Sasaki and Prof. T. Shimogawa. Prof. T. Shimogawa provided us car driving as well as many discussions on experiments. I need to send them Hitachi beef in return. I am also grateful to KOTO colleagues who worked together in J-PARC and KEK, Dr. R. Ogata, Dr. E. Iwai, Dr. Y. D. Ri, Dr. J. W. Lee, Dr. K. Sato, Ms. R. Murayama, Mr. Y. Sugiyama, Ms. Y. Yanagida, Mr. Y. Nakaya, Mr. H. Yokota, Mr. S. Banno, Mr. Y. Odani, Mr. T. Ota, Mr. Y. Takashima, Mr. T. Toyoda, Ms. M. Isoe, Mr. K. Miyazaki, Mr. G. H. Lee, Mr. J. W. Ko, Dr. K. Y. Baek, Dr. Y. C. Tung, Dr. J. Ma, Dr. J. Xu and Dr. D. McFarland. Special thanks go to Ms. C. Erba, Ms. C. Carruth, Ms. J. Miller, Ms. J. Micallef and Mr. N. Wahllon, who helped detector assembly, data taking and analysis as summer students from U.S. I also thank Mr. K. Sekine, Mr. M. Sakaba and other people from Futaba Kogyo for their helps in detector installation and construction at J-PARC.

I have been received lots of support from people in the laboratory of high energy physics in Kyoto University: Prof. T. Nakaya, Prof. M. Yokoyama, Prof. A. Minamino, Prof. A. K. Ichikawa, Prof M. Ishino, Prof. T. Sumida, Prof. N. Taniguchi, Prof. K. Hiraide, Mr. N. Nagai, Dr. K. Nitta,

Prof. Y. Kurimoto, Mr. O. Daniel, Dr. Y. Nakajima, Prof. K. Matsuoka, Dr. M. Otani, Mr. T. Yamauchi, Dr. A. Murakami, Mr. K. Goda, Dr. P. Litchfield, Prof. M. Ikeda, Dr. K. Ieki, Mr. S. Akiyama, Mr. T. Nagasaki, Dr. C. Bronner, Mr. S. Takahashi, Dr. T. Kikawa, Mr. N. Kamo, Mr. K. Yoshida, Dr. K. Suzuki, Mr. H. Kubo, Mr. K. Huang, Mr. T. Hiraki, Ms. S. Hirota, Mr. T. Tashiro, Mr. T. Hayashino, Mr. T. Kunigo, Mr. K. Nakamura, Mr. M. Jiang, Mr. Y. Ishiyama, Ms. S. Yanagita, Ms. M. Yamamoto, Mr. S. Ban, Mr. K. Kondo, Mr. K. Haneda, Mr. R. Monden, Mr. S. Tanaka, Mr. S. Akatsuka, Mr. Y. Noguchi, Mr. Y. Ashida, Ms. A. Hiramoto, Ms. Y. Nakanishi, Dr. K. Nakamura, Dr. P. Nikhul, Dr. S. V. Cao, Dr. B. Quilain, Ms. A. Nakao, Ms. M. Mori, Ms. M. Iwaki, Ms. S. Yamashita, and Ms. E. Hayashi. All the seminars, colloquiums, discussions and conversations, as well as coffee breaks, Nabe parties and Karaoke parties, were my pleasures. I learned and enjoyed a lot. I am really happy that I have spent a long time with members in this laboratory.

My heartfelt appreciation goes to my parents, who have raised and kept supporting me for many year. Finally, I would like to express my greatest gratitude to my little sparrow who has been always just besides me, and made me be here.

January, 2016
Yosuke Maeda

Contents

Chapter 1

Introduction

In this chapter, motivations to study the rare decay of neutral kaon, $K_L \to \pi^0\nu\overline{\nu}$, in the KOTO experiment are summarized as well as the status of experimental searches. Finally, the outline of this thesis is described.

1.1 Physics of kaons

1.1.1 History of Kaons

Since the discovery of the Higgs boson in 2013 [1, 2], existence of all particles that is predicted in the Standard Model (SM) of elementary particle physics were experimentally confirmed. In the SM, four kinds of fermions, the up-type and down-type quarks, charged leptons and neutrinos, are predicted as elementary particles constituting materials. Each type contains three kinds of particles, which is called "generations." These are summarized in Table 1.1. The SM also accommodates three kinds of forces, namely, strong, electromagnetic and weak interactions, with corresponding gauge bosons. Among particles in Table 1.1, all are involved in the weak interaction, which is meditated by $W^{\pm}$ and Z^0 bosons, whereas only quarks are also involved in the strong interaction, which is mediated by gluons. Those with electric charge, or all except neutrinos, feel the electromagnetic interaction by photons. Each particle listed in Table 1.1 has its partner called an "anti-particle," which owns the same mass and opposite charges. Quarks are basically observed in the form of composite particles called "mesons" or "baryons," where the former consists of a pair of a quark and an anti-quark and the latter consists of three quarks or anti-quarks.

Kaons are kinds of mesons including an s or $\bar{s}$ quark. These were first discovered as "V particles" in the cloud chamber experiment in 1947 by G. D. Rochester and C. C. Butler [3]. At that time, they observed decays of neutral kaons into two charged pions, where these kaons were generated through strong interaction by cosmic ray particles. This was the first discovery of particles with a second-generation quark. Although they were mainly generated through the strong interaction, their decay was governed by the weak interaction. This feature of kaons as well as existence of an s quark, they have been played various critical roles for understanding of basic symmetries in physics and a structure among generations so far: $\theta - \tau$ puzzle in the parity violation [4], Cabibbo mixing [5], GIM mechanism [6], discovery of CP-violation in K_L decay [7], and establishment of direct CP-violation [8, 9]. The most critical role kaons have ever played would be those related to CP symmetry, or symmetry between particles and anti-particles, whose understanding is necessary in order to know how the today's matter-dominated universe was created [10]. The importance of

Table 1.1: Ferimions predicted in the SM.

	the first generation	the second generation	the third generation
quark	up (u)	charm (c)	top (t)
	down (d)	strange (s)	bottom (b)
lepton	electron (e)	muon (μ)	tau (τ)
	electron neutrino (ν_e)	muon neutrino (ν_μ)	tau neutrino (ν_τ)

this issue is still unchanged even today and further experimental studies with kaons are necessary. The following sections describe the CP-violation in the neutral kaon system.

1.1.2 CP-violation in neutral kaon system

$K^0 - \bar{K^0}$ mixing

Neutral kaon is a meson including s quark with electric charge of 0. The following two states are possible:

$$K^0 = (\bar{s}, d), \tag{1.1}$$
$$\bar{K^0} = (s, \bar{d}). \tag{1.2}$$

These are in relation of a particle and an anti-particle. In observing these particle decays, which are mediated with the weak interaction, both particles have common decay mode such as $\pi\pi$ or $\pi\pi\pi$ final states, and it is essentially impossible to distinguish from which state these pions are derived. Actually, weak interaction with box diagrams as in Fig. 1.1 gives transition probability between K^0 and $\bar{K^0}$. From the above discussion, a kaon state at decay should be considered as a mixed state of K^0 and $\bar{K^0}$. Assuming an equal mixing of K^0 and $\bar{K^0}$, the following two states, named K_1 and K_2, are possible:

$$K_1 = \frac{1}{\sqrt{2}}(K^0 + \bar{K^0}), \tag{1.3}$$
$$K_2 = \frac{1}{\sqrt{2}}(K^0 - \bar{K^0}). \tag{1.4}$$

These states are CP eigenstates as shown below:

$$CP\,|K_1\rangle = \frac{1}{\sqrt{2}}(|\bar{K^0}\rangle + |K^0\rangle) = |K_1\rangle\,, \tag{1.5}$$
$$CP\,|K_2\rangle = \frac{1}{\sqrt{2}}(|\bar{K^0}\rangle - |K^0\rangle) = -\,|K_2\rangle\,, \tag{1.6}$$

although K^0 and $\bar{K^0}$ themselves are not CP eigenstates. Even after the discovery of parity violation in 1957 [12], CP symmetry was believed to hold. Under this assumption, the K_1 state, with CP even eigenvalue, would mainly decay into two pions, and the K_2 state, with CP odd eigenvalue, would mainly decay into three pions, where each final state is CP even and odd, respectively. Considering three-pion system to have smaller Q-value or available energy in its decay, K_2 is expected to have longer lifetime. These states were predicted by M. Gell-Mann and A. Pais in 1954 [13]

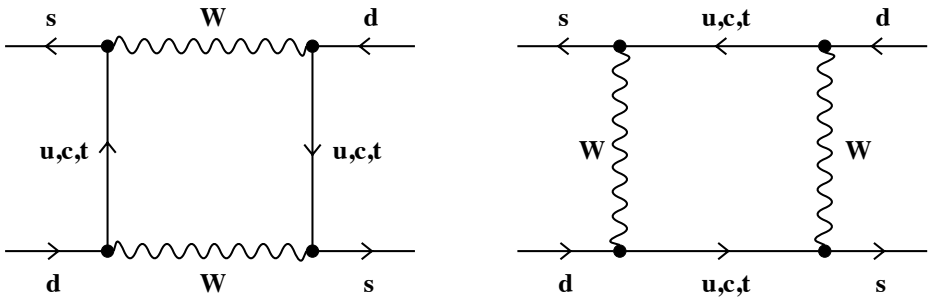

Figure 1.1: Feynman diagrams for $K^0 - \bar{K^0}$ mixing. Quoted from Ref. [11].

and corresponding long-lived neutral kaons actually were observed in 1956 [14] in addition to so-far known neutral kaons with shorter lifetime and existence of both states was confirmed. The observed these two states were then named K_S (K short) and K_L (K long) according to their lifetime.

Discovery of CP violation

Although observed K_S and K_L states were thought to be CP even and odd states, respectively, it was proved that this was not exactly correct in 1964 by the team lead by J. W. Cronin and V. L. Fitch [7]. They observed so-far-believed CP odd neutral kaon states, K_L, had decayed into two charged pions system, which was in CP even states. This phenomenon is now interpreted as an unequal mixing of K_0 and $\bar{K^0}$ in K_S and K_L states, which resulted in a small contamination of CP even component K_1 in the K_L state:

$$\begin{aligned} |K_L\rangle &= \frac{1}{\sqrt{1+\epsilon^2}}(|K_2\rangle + \epsilon\,|K_1\rangle) \\ &= \frac{1}{\sqrt{2(1+\epsilon^2)}}((1+\epsilon)\,|K^0\rangle - (1-\epsilon)\,|\bar{K^0}\rangle), \end{aligned} \tag{1.7}$$

and similarly for K_S,

$$\begin{aligned} |K_S\rangle &= \frac{1}{\sqrt{1+\epsilon^2}}(|K_1\rangle + \epsilon\,|K_2\rangle) \\ &= \frac{1}{\sqrt{2(1+\epsilon^2)}}((1+\epsilon)\,|K^0\rangle + (1-\epsilon)\,|\bar{K^0}\rangle). \end{aligned} \tag{1.8}$$

The parameter ϵ indicates a degree of contamination and hence a size of CP-violation. As the world average, it is obtained as [16]

$$|\epsilon| = (2.282 \pm 0.011) \times 10^{-3}. \tag{1.9}$$

This type of CP-violation is called "indirect CP-violation."

The indirect CP-violation is also observed in semi-leptonic decays of K_L, which allows determination of from which of K^0 or $\bar{K^0}$ decayed with the charge of an emitted lepton. If the mixing of K^0 and $\bar{K^0}$ in K_L is equal, the same number of such decays with l^- and l^+ must be observed,

where $l^{\pm}$ denotes $e^{\pm}$ or $\mu^{\pm}$. Actually, such a charge asymmetry has been observed [15] and the world average value is given as [16]

$$\begin{aligned} A_L &= \frac{\Gamma(K_L \to \pi^- l^+ \nu_l) - \Gamma(K_L \to \pi^+ l^- \bar{\nu}_l)}{\Gamma(K_L \to \pi^- l^+ \nu_l) + \Gamma(K_L \to \pi^+ l^- \bar{\nu}_l)} \\ &= (3.32 \pm 0.06) \times 10^{-3}, \end{aligned} \tag{1.10}$$

where a weighted average for the electron mode and the muon mode is shown.

Direct CP-violation

Another source of CP-violation is possible, where the CP-odd component K_2 *directly* decays into CP-even two pion systems due to CP-violation in the decay process:

$$\langle \pi\pi | \mathscr{H} | K_L \rangle \sim \langle \pi\pi | \mathscr{H} | K_2 \rangle + \epsilon \langle \pi\pi | \mathscr{H} | K_1 \rangle , \tag{1.11}$$

where $\mathscr{H}$ denotes Hamiltonian of weak interaction. This "direct CP-violation," as given by the first term in the right hand side of Eq. (1.11), was formalized by T. T. Wu and C. N. Yang [17] soon after the discovery of the *indirect* CP-violation. Contribution of the direct CP-violation in decay into $\pi^+\pi^-$ final states is usually denoted as ϵ' and this gives

$$\frac{\langle \pi^+\pi^- | \mathscr{H} | K_L \rangle}{\langle \pi^+\pi^- | \mathscr{H} | K_S \rangle} = \eta_{+-} \sim \epsilon + \epsilon'. \tag{1.12}$$

Due to isospin difference in the $\pi^0\pi^0$ modes, different contribution of the direct CP-violation is expected as

$$\frac{\langle \pi^0\pi^0 | \mathscr{H} | K_L \rangle}{\langle \pi^0\pi^0 | \mathscr{H} | K_S \rangle} = \eta_{00} \sim \epsilon - 2\epsilon'. \tag{1.13}$$

Although it is difficult to measure the small effect of the direct CP-violation only by observing the $K_L \to \pi^+\pi^-$ decay, Equations (1.12) and (1.13) allow to extract its effects by simultaneous measurements of the four decays, $K_L \to \pi^+\pi^-$, $K_L \to \pi^0\pi^0$, $K_S \to \pi^+\pi^-$ and $K_L \to \pi^0\pi^0$ as

$$\frac{\Gamma(K_L \to \pi^+\pi^-)/\Gamma(K_S \to \pi^+\pi^-)}{\Gamma(K_L \to \pi^0\pi^0)/\Gamma(K_S \to \pi^0\pi^0)} \sim \left| \frac{\eta_{+-}}{\eta_{00}} \right|^2 \sim 1 + 6\mathrm{Re}(\epsilon'/\epsilon). \tag{1.14}$$

Continuous efforts to measure this ratio had been made [18] and today non-zero value is obtained as the world average [16]

$$\mathrm{Re}(\epsilon'/\epsilon) = (1.65 \pm 0.26) \times 10^{-3}. \tag{1.15}$$

The existence of this direct CP-violation was critical to discriminate various models to explain CP-violation and was important evidence to support the Kobayashi-Maskawa model described in the next section.

1.1.3 Kobayashi-Maskawa mechanism

Today, CP violation is measured and established in not only kaons as discussed in Sec. 1.1.2, but also B mesons by B-factory experiments such as Belle and *BABAR* [19]. These CP violation as well as quark mixing among three generations are explained by the Kobayashi-Maskawa(KM) mechanism [20], which originated from an idea of quark mixing by Cabibbo [5] and obtained as its extension

to the six types of quarks with three generations so as to accommodate CP violation naturally by M. Kobayashi and T. Maskawa.

In this model, quark mixing among the three generations is governed with a 3×3 complex matrix $V_{\rm CKM}$ as follows:

$$\begin{pmatrix} d' \\ s' \\ b' \end{pmatrix} = V_{\rm CKM} \begin{pmatrix} d \\ s \\ b \end{pmatrix}, \tag{1.16}$$

where d, s and b indicate mass eigenstates and those with a prime($'$) are weak eigenstates for corresponding generations. The matrix $V_{\rm CKM}$ is called "CKM matrix" and written as

$$V_{\rm CKM} = \begin{pmatrix} V_{ud} & V_{us} & V_{ub} \\ V_{cd} & V_{cs} & V_{cb} \\ V_{td} & V_{ts} & V_{tb} \end{pmatrix}. \tag{1.17}$$

Using this CKM matrix, the Lagrangian of the charged current in the weak interaction is given by

$$\mathscr{L}_{\rm CC} = \frac{g}{\sqrt{2}}[\bar{u_i} V_{ij} d_j W^- + \bar{d_j} V_{ij}^* u_i W^+], \tag{1.18}$$

where $u_i = (u, c, t)$ is the left-handed up-type quarks, $d_i = (d, s, b)$ is the left-handed down type quarks, and $W^\pm$ are the weak bosons. The CP conjugation of Eq. (1.18) will be then

$$\mathscr{L}_{\rm CC}^{CP} = \frac{g}{\sqrt{2}}[\bar{d_i} V_{ij} u_j W^+ + \bar{u_j} V_{ij}^* d_j W^-], \tag{1.19}$$

which would be different from $\mathscr{L}_{\rm CC}$ hence CP is violated when $V_{ij} \neq V_{ij}^*$. Existence of complex components then is essential in considering CP violation in the SM.

The CKM matrix has four free parameters of three rotation angles and one complex phase and the effect of CP violation can be concentrated in this phase. Following the Wolfenstein parameterization [21], $V_{\rm CKM}$ is written as

$$V_{\rm CKM} = \begin{pmatrix} 1 - \lambda^2/2 & \lambda & A\lambda^3(\rho - i\eta) \\ -\lambda & 1 - \lambda^2/2 & A\lambda^2 \\ A\lambda^3(1 - \rho - i\eta) & -A\lambda^2 & 1 \end{pmatrix} + O(\lambda^4), \tag{1.20}$$

where

$$\lambda = \frac{|V_{us}|}{\sqrt{|V_{ud}|^2 + |V_{us}|^2}}, \tag{1.21}$$

$$A\lambda^2 = \lambda \left| \frac{V_{cb}}{V_{us}} \right|, \tag{1.22}$$

$$A\lambda^3(\rho + i\eta) = V_{ub}^*. \tag{1.23}$$

Here, η is the only parameter causing CP-violation and the size of this value is a measure of CP-violation in the SM. It is convenient to define $\bar{\rho}$ and $\bar{\eta}$ as

$$\bar{\rho} \sim \rho(1 - \lambda^2/2) \tag{1.24}$$

$$\bar{\eta} \sim \eta(1 - \lambda^2/2) \tag{1.25}$$

and illustrate allowed region obtained as a result of measurement in $\bar{\rho}$-$\bar{\eta}$ plane. A unitarity condition in the CKM matrix is written as

$$V_{ud}V_{ub}^* + V_{cd}V_{cb}^* + V_{td}V_{tb}^* = 0, \tag{1.26}$$

$$-\left(\frac{V_{ud}V_{ub}^*}{V_{cd}V_{cb}^*}\right) - \left(\frac{V_{td}V_{tb}^*}{V_{cd}V_{cb}^*}\right) = 1, \tag{1.27}$$

here, the first term in Eq. (1.27) indicates

$$-\left(\frac{V_{ud}V_{ub}^*}{V_{cd}V_{cb}^*}\right) = \bar{\rho} + i\bar{\eta}, \tag{1.28}$$

hence the triangle formed by $(0,0)$, $(\bar{\rho},\bar{\eta})$ and $(1,0)$ in $\bar{\rho}$-$\bar{\eta}$ plane is called "unitarity triangle." Generally, measurements on CP-violating parameters correspond to measuring a part of this triangle such as angles, length of sides or its height. Examination of whether these measurement results really for the unitarity triangle is then a critical validation of the KM mechanism. Figure 1.2 shows a summary of various measurement in $\bar{\rho}$-$\bar{\eta}$ plane. All measurement gives consistent results and the global fit gives parameters in Eq. (1.20) as [22]

$$A = 0.810^{+0.018}_{-0.024}, \tag{1.29}$$

$$\lambda = 0.22548^{+0.00068}_{-0.00034}, \tag{1.30}$$

$$\bar{\rho} = 0.1453^{+0.0133}_{-0.0073}, \tag{1.31}$$

$$\bar{\eta} = 0.343^{+0.011}_{-0.012}. \tag{1.32}$$

The unitarity of the CKM matrix is evaluated as a sum of three angles in the unitarity triangle in Fig. 1.2, for example, and yields [16]

$$\phi_1 + \phi_2 + \phi_3 = (175 \pm 9)^\circ, \tag{1.33}$$

which is well consistent with the SM prediction. These facts indicate the KM mechanism successfully describes weak interactions in the quark sector including CP-violation.

1.2 $K_L \to \pi^0\nu\overline{\nu}$

1.2.1 $K_L \to \pi^0\nu\overline{\nu}$ in the Standard Model

Among various K_L decay modes, the rare decay $K_L \to \pi^0\nu\overline{\nu}$ [23] should be given a special position due to its unique features. Decay diagrams for the $K_L \to \pi^0\nu\overline{\nu}$ mode are shown in Fig. 1.3. This decay proceed through what is called Flavor Changing Neutral Current (FCNC), where $s \to d$ transition occurs with a loop of heavy particles like $W^\pm$ boson and t quark. Since a tree level FCNC process is prohibited in the standard model, this decay process is allowed only as a second order effect of electroweak interaction and hence is strongly suppressed. Although this suppression makes observation of the $K_L \to \pi^0\nu\overline{\nu}$ process difficult, possible effects from new physics would be given as clearer signals thanks to this small branching fraction, which will be discussed in the next section.

The most critical point on this decay mode is sensitivity to the CP-violation. t quark mainly contributes the loop in the diagrams of Fig. 1.3 thanks to the GIM mechanism [6], although all

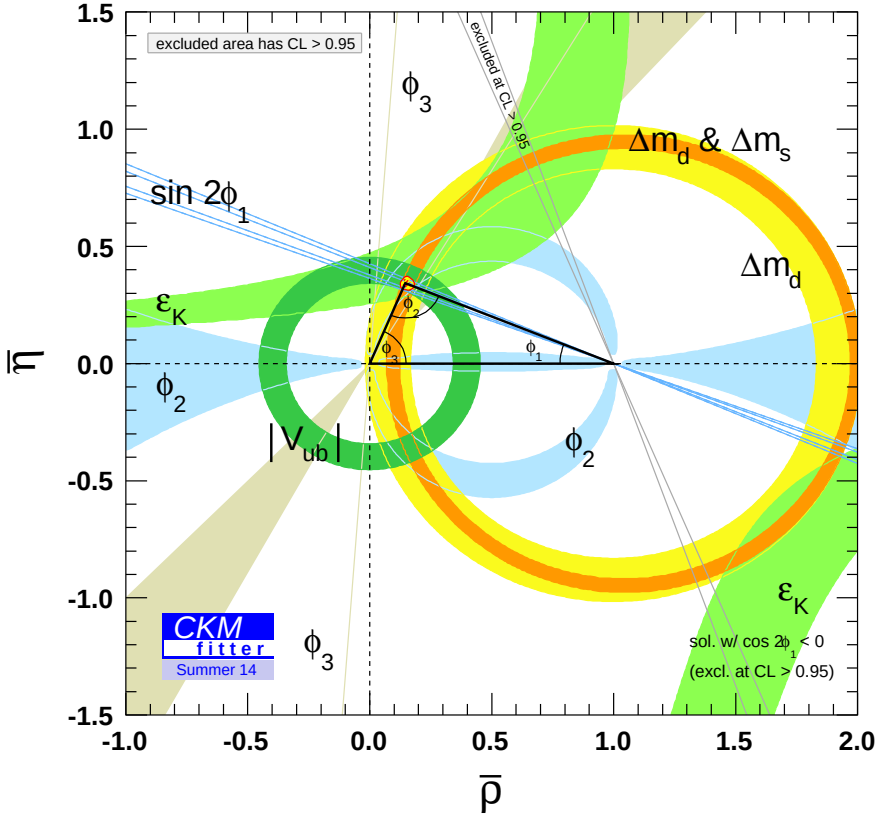

Figure 1.2: The unitarity triangle and the result of a global fit for $\bar{\rho}$ and $\bar{\eta}$. Taken from Ref. [22].

the three kinds of the up-type quarks, u, c and t are basically possible. In addition, as shown in the following equations, the mixing of K^0 and $\bar{K^0}$ makes t quark contribution dominant, which can have an imaginary component in coupling constants :

$$\begin{aligned} A(K_L \to \pi^0 \nu\bar{\nu}) &\sim A(K_2 \to \pi^0 \nu\bar{\nu}) \\ &= \frac{1}{\sqrt{2}}(A(K^0 \to \pi^0 \nu\bar{\nu}) - A(\bar{K^0} \to \pi^0 \nu\bar{\nu})) \\ &\propto V_{td}^* V_{ts} - V_{ts}^* V_{td} \\ &\propto 2i\eta, \end{aligned} \tag{1.34}$$

where A denotes decay amplitude and effect of the indirect CP violation is neglected since $|\epsilon| \ll 1$. Contribution of u and c quarks are neglected since their couplings only have real components and finally disappear considering the K^0 and $\bar{K^0}$ mixing. Equation (1.34) shows the fact that the decay $K_L \to \pi^0 \nu\bar{\nu}$ is purely derived from the direct CP violation and the branching ratio of this decay itself represents the size of the CP violation. In the unitarity triangle, measurement of the $K_L \to \pi^0 \nu\bar{\nu}$ branching fraction correspond to that of its height. Hence precise measurement of the $K_L \to \pi^0 \nu\bar{\nu}$ branching fraction will give a determination of the η value with corresponding precision. Now that most of CP-violating parameters are derived from measurements in B meson systems, information

from the kaon sector is critical for further confirmation of the validity of the CKM mechanism. It is also useful for discrimination of various new physics models to compare measurements from kaons and B mesons.

Another important key of this mode is small theoretical uncertainty in branching ratio prediction. The branching ratio of the $K_L \to \pi^0\nu\bar{\nu}$ decay is expressed as follows [24]:

$$\mathrm{Br}(K_L \to \pi^0\nu\bar{\nu}) = \kappa_L \left(\frac{\mathrm{Im}\lambda_t}{\lambda^5} X(x_t) \right)^2, \tag{1.35}$$

where $\lambda_t = V_{ts}^* V_{td}$ in the CKM matrix, x_t is the square of the mass ratio of the top quark to the W boson and $x_t = m_t^2/M_W^2$, $X(x_t)$ is the Inami-Lim loop function [25] with QCD higher order corrections, and the factor κ_L includes other effects which is given as

$$\kappa_L = (2.231 \pm 0.013) \times 10^{-10} \left(\frac{\lambda}{0.225} \right)^8. \tag{1.36}$$

The loop effect, as given in the function $X(x_t)$, is reliably calculated. This is because the internal states of this decay process involves only heavy particles such as top quark, W and Z bosons as shown in Fig. 1.3 hence effects from long-distance interactions from light quarks are negligible. Although there could be an uncertainty in calculation of hadron matrix element, which is included in κ_L, it is canceled by using the well-measured branching ratio of the $K^+ \to \pi^0 e^+ \nu_e$ decay, whose matrix element is identical to that of the $K_L \to \pi^0\nu\bar{\nu}$ decay due to isospin symmetry [26].

Taking the above discussion into account, the SM prediction of the $K_L \to \pi^0\nu\bar{\nu}$ branching fraction with two-loop electroweak corrections is given as [27]

$$\mathrm{Br}(K_L \to \pi^0\nu\bar{\nu}) = (3.00 \pm 0.30) \times 10^{-11}, \tag{1.37}$$

where the first error indicates parametric one and the last one comes from theoretical uncertainty. Here, the total error is dominated by uncertainty of CKM parameters and the theoretical uncertainty is dominated by QCD calculation in the loop function $X(x_t)$ [27]. The size of the theoretical error is as small as 1.2%, which is hardly seen in other CP-violating processes.

As shown in Eq. (1.32) the η value is obtained with an error level of a few percent which mainly comes from measurements in B system. Hence 5% measurement of η from the $K_L \to \pi^0\nu\bar{\nu}$ decay, corresponding to 10% precision in branching ratio, would be comparable with results from B decays and would give a critical test of the CP-violation in the KM mechanism from the kaon system.

1.2.2 $K_L \to \pi^0\nu\bar{\nu}$ in Beyond-SM physics

The $K_L \to \pi^0\nu\bar{\nu}$ decay is a powerful tool for not only precise check of the SM, but also searches for physics beyond the SM. In order to account for the matter-dominated universe, the amount of CP-violation given by the SM or the KM-mechanism is know to be insufficient [29]. Therefore, a new source of CP-violation should exist, which can be probed by a search for this CP-violating $K_L \to \pi^0\nu\bar{\nu}$ decay. Although $O(10^{-11})$ sensitivity is required for examination of the SM as in the previous section, experiments with lower sensitivity also has an importance because possible new physics effect gives the larger branching ratio than the SM expectation by a factor of 10 or more.

Before discussing new physics scenarios, an indirect upper limit given by Y. Grossman and Y. Nir [30] must be mentioned. They pointed out the following relation between branching fractions

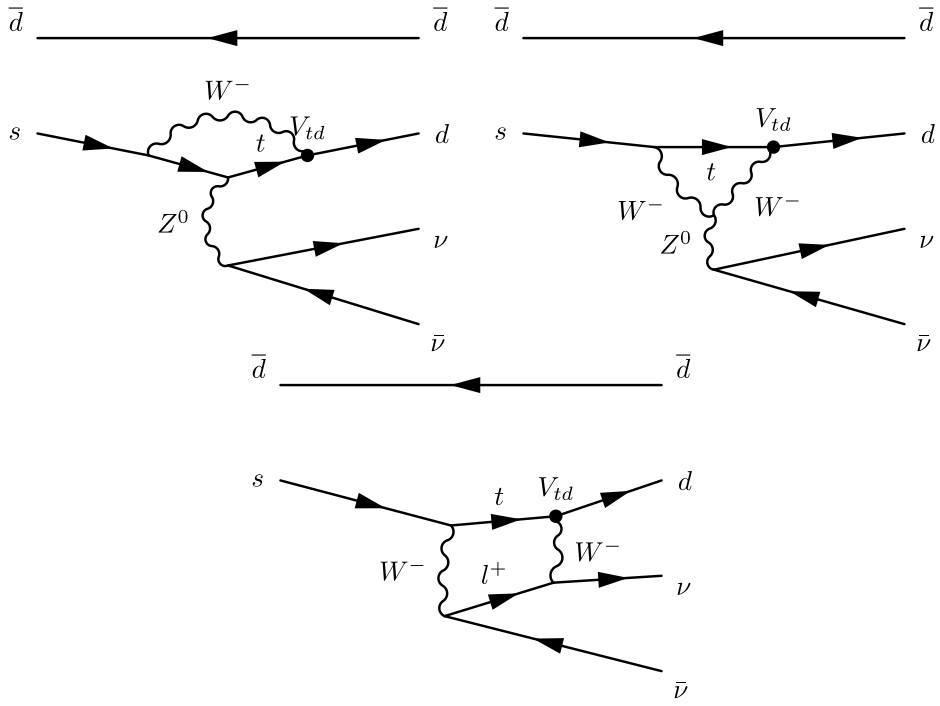

Figure 1.3: Feynman diagrams for the $K_L \to \pi^0\nu\bar{\nu}$ decay. Quoted from Ref. [28].

of the $K^+ \to \pi^+\nu\bar{\nu}$ decay and the $K_L \to \pi^0\nu\bar{\nu}$ decay,

$$\mathrm{Br}(K_L \to \pi^0\nu\bar{\nu}) \lesssim \frac{1}{r_{\mathrm{is}}}\frac{\tau_{K_L}}{\tau_{K^+}} \times \mathrm{Br}(K^+ \to \pi^+\nu\bar{\nu}) \tag{1.38}$$

$$\sim 4.3 \times \mathrm{Br}(K^+ \to \pi^+\nu\bar{\nu}), \tag{1.39}$$

where τ_{K_L} and τ_{K^+} indicate the lifetimes of K_L and K^+, respectively, and $r_{\mathrm{is}} = 0.954$ is the isospin breaking factor [31]. This equation assumes only isospin symmetry and hence independent of new physics models. This limit, called "Grossman-Nir bound," is obtained from measurements of the $K^+ \to \pi^+\nu\bar{\nu}$ decay and new physics effects are allowed to give as large branching fraction as this bound at maximum. The branching fraction of the $K^+ \to \pi^+\nu\bar{\nu}$ decay was obtained by the E787/E949 experiment in the Brookhaven National Laboratory (BNL) [32] as

$$\mathrm{Br}(K^+ \to \pi^+\nu\bar{\nu}) = (1.73^{+1.15}_{-1.05}) \times 10^{-11}. \tag{1.40}$$

From this result, Grossman-Nir bound for the $K_L \to \pi^0\nu\bar{\nu}$ decay is given as

$$\mathrm{Br}(K_L \to \pi^0\nu\bar{\nu}) < 1.4 \times 10^{-9} \text{ (90\% Confidence Level (C.L.))}. \tag{1.41}$$

$K_L \to \pi^0\nu\bar{\nu}$ searches with better sensitivity than this value are at least necessary to probe new physics effects.

In various new physics models, the $K_L \to \pi^0\nu\bar{\nu}$ branching fraction would be modified drastically through contributions of unknown heavy particles in the loop of its diagram in Fig. 1.3. Below, predictions of the $K_L \to \pi^0\nu\bar{\nu}$ branching fraction in several specific new physics models are described,

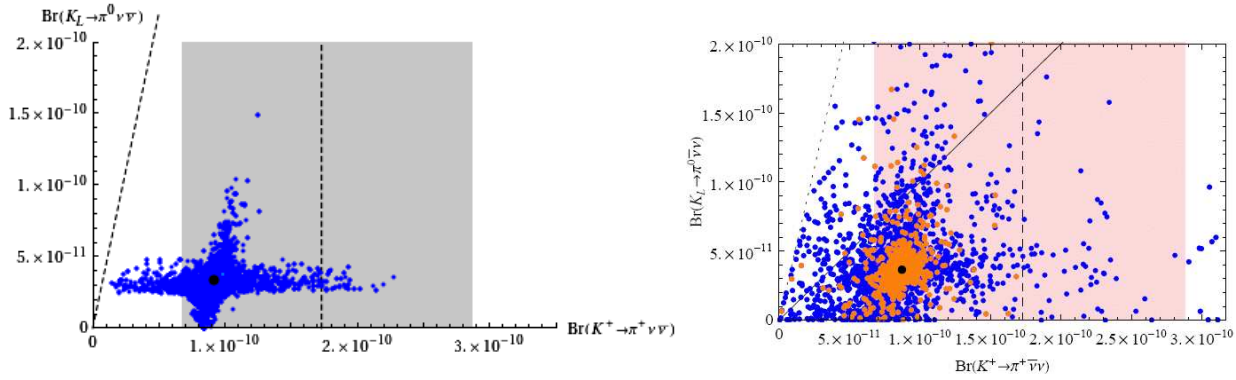

Figure 1.4: Possible branching fractions for the $K_L \to \pi^0\nu\overline{\nu}$ and $K^+ \to \pi^+\nu\overline{\nu}$ decays in the Littlest Higgs model with T-Parity (left, [34]) and the Randall-Sundrum custodial symmetry (right, [35]).

following Ref. [33], in relation with that for the $K^+ \to \pi^+\nu\overline{\nu}$ decay. The Littlest Higgs model with T-Parity (LHT) [34] and the Randall-Sundrum model with custodial symmetry (RSc) [35] can give the branching fraction larger than the SM prediction, while their new physics effect to B mesons, particularly the $B_{s,d} \to \mu^+\mu^-$ decays, is expected to be small, hence limits from searches by LHC experiments [36] are not yet stringent. Possible branching fraction in these models are shown in Fig. 1.4. The Z' model, where a new boson Z' directly causes a flavor changing interaction [37], can also give observable effects. As for supersymmetric (SUSY) models, the minimal supersymmetric SM (MSSM) with wino loop [38] is still available even with results of direct searches in LHC.

In any cases, precision measurement of $K_L \to \pi^0\nu\overline{\nu}$ as well as $K^+ \to \pi^+\nu\overline{\nu}$ is necessary in order to distinguish various new physics scenarios. A special attention should also be paid for measurements of rare B decays or direct searches of new particles such as SUSY particles and the Z' boson. The unique feature of the $K_L \to \pi^0\nu\overline{\nu}$ decay, the much-suppressed and well-understood standard model contribution, is an outstanding advantage in searches for physics beyond the SM.

1.2.3 Experiments to search for $K_L \to \pi^0\nu\overline{\nu}$

Various experiments to search for the $K_L \to \pi^0\nu\overline{\nu}$ decay have been conducted so far. The history of upper limit of its branching ratio is shown in Fig. 1.5 [23, 39, 40, 41, 42, 43, 44, 45]. Here, overviews of recent experiments as well as the KOTO experiment, the subject of this thesis, are described.

KTeV experiment

This experiment was conducted in 1996-1997 and 1999 at Fermi National Accelerator Laboratory in the U.S. Its main purposes were the precise measurements of the direct CP-violation parameter $\mathrm{Re}(\epsilon'/\epsilon)$ [9] and various rare decays of K_L. The high energy proton beam of 800 GeV from the Tevatron accelerator was used for production of the K_L beam. The layout of the detector system is shown in Fig. 1.6. Charged particle tracks were detected and their momentum was analyzed by the spectrometer consisting of the drift chambers and the analysis magnet. In addition, energy of electromagnetic particles was measured by the calorimeter made of undoped cesium iodide (CsI) crystals. Two kinds of search for $K_L \to \pi^0\nu\overline{\nu}$ decay were performed; One used $\pi^0 \to \gamma\gamma$ decay to identify π^0 in the final state [41] and the other used $\pi^0 \to e^+e^-\gamma$ decay [42].

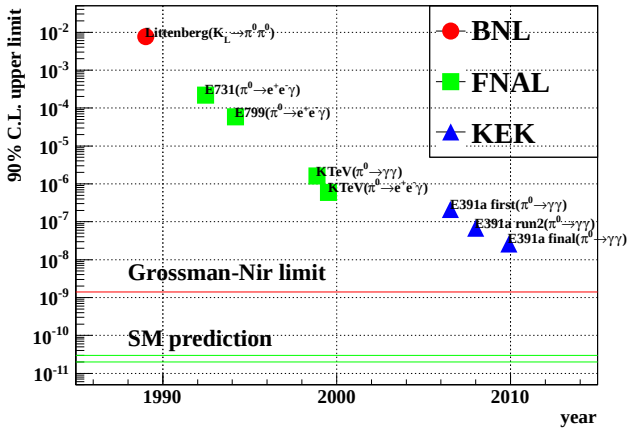

Figure 1.5: History of measured upper limit of $\mathrm{Br}(K_L \to \pi^0\nu\overline{\nu})$. The kinds of markers indicates the sites of each experiment.

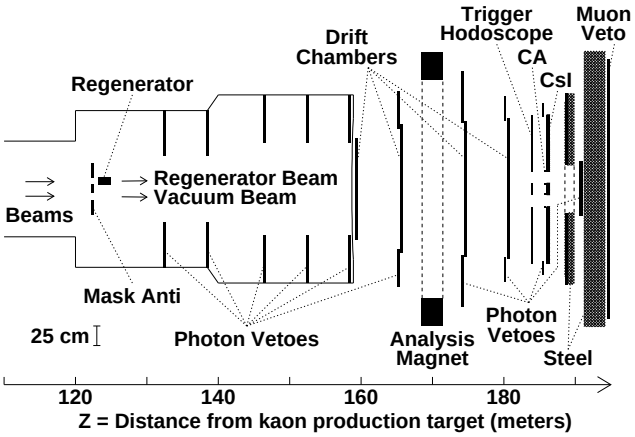

Figure 1.6: Outline of KTeV detector. Quoted from Ref. [9].

The KOTO experiment reuses the CsI crystals used as the electromagnetic calorimeter in this experiment, which were shipped to Japan in 2007-2008 [46].

E391a experiment

This was the first dedicated experiment to search for $K_L \to \pi^0\nu\overline{\nu}$ decay, which used the 12 GeV proton synchrotron of the High Energy Accelerator Research Organization (KEK) in Japan. The outlook of the E391a detector is like Fig. 1.7. It was designed so that extra particles which were emitted concurrently with two photons in general K_L decays were completely detected. Data taking was performed in 2004 and 2005 and the final result was obtained as [45]

$$\mathrm{Br}(K_L \to \pi^0\nu\bar{\nu}) < 2.6 \times 10^{-8} \ (90\% \ \mathrm{C.L.}). \tag{1.42}$$

This result is the most stringent limit for the branching fraction of $K_L \to \pi^0\nu\overline{\nu}$ among the direct search.

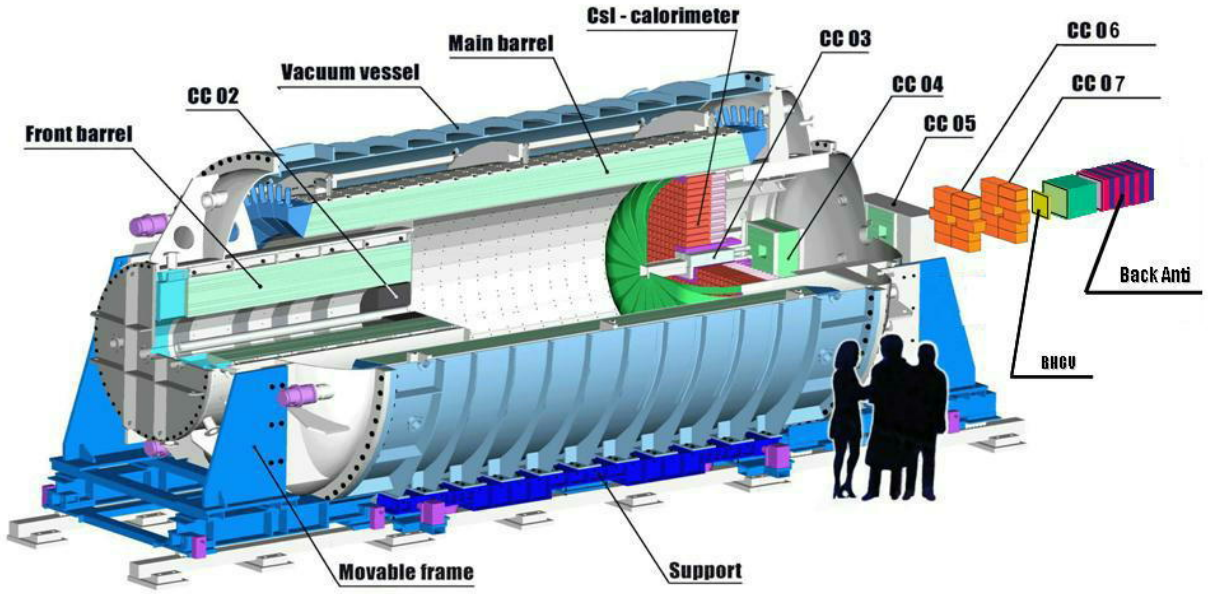

Figure 1.7: Outlook of E391a detector. Quoted from Ref. [18].

KOTO experiment

The KOTO, standing for "K^0 at TOkai," experiment is the successor of the KEK E391a experiment, which was launched at the Japan Proton Accelerator Research Complex (J-PARC) [47] in Tokai Village, Ibaraki Prefecture. Intense K_L beam which was obtained from the 30-GeV proton beam from the Main Ring (MR) [48] of the facility was used. The goal of this experiment is to achieve sensitivity of the branching ratio predicted in the SM. Although the same experimental technique with the E391a experiment is adopted and its barrel structure is reused, the other parts are newly constructed in order to reduce background further and to cope with the high-rate environment: the higher-granularity electromagnetic calorimeter with CsI crystals used in the KTeV experiment, the new beam line and the other detectors.

1.3 Purpose and outline of this thesis

As described so far, measurement of $K_L \to \pi^0\nu\overline{\nu}$ is an excellent probe to understand the CP-violation in the SM and the matter-antimatter asymmetry in the universe with beyond-SM physics. However, much more efforts are required to improve sensitivity of experiments and search for new physics. Although the ultimate goal is to achieve sensitivity of 10^{-13} level, corresponding $\sim$100 SM events, experiments should proceed step-by-step in understanding detector performance and background properties one by one. In this thesis, launch of the KOTO experiment and analysis of the first data are described, as a step toward the ultimate measurement of the $K_L \to \pi^0\nu\overline{\nu}$ decay. The key point is high efficiency even under high-rate environment. This requirement is the most severe in the in-beam photon detector, since it is exposed to a large flux of neutrons but needs high detection efficiency for GeV-energy photons from K_L decays. This thesis focuses on the design and

in-situ performance evaluation of such a detector, named as Beam Hole Photon Veto or BHPV. Understanding of background property in the analysis of $K_L \to \pi^0\nu\overline{\nu}$ search is another essential point in order to achieve high sensitivity. Hence background, particularly K_L-induce events, is studied for the first search of $K_L \to \pi^0\nu\overline{\nu}$ events in this experiment.

The outline of this thesis is as follows. Chapter 2 describes detail of the KOTO experiment, which includes its conceptual design and basic principle. Design of detectors and data acquisition system are also explained. Data taking condition is described in Chap. 3. Before going to the performance study of the BHPV detector, event reconstruction procedures and the scheme of Monte Carlo (MC) simulation are summarized in Chap. 4 and chap. 5, respectively. Performance studies of BHPV in the first physics run is discussed in Chap. 6 and analysis of the $K_L \to \pi^0\nu\overline{\nu}$ search with the data is described in Chap. 7. Finally, Chap. 8 concludes this thesis.

Chapter 2

The KOTO Experiment

The overview of the KOTO experiment is described in this chapter.

2.1 Principle of the experiment

In this section, the concept of this experiment is described. Details of the actual apparatus will be explained in the next section.

2.1.1 Signal identification

In the KOTO experiment, $K_L \to \pi^0\nu\overline{\nu}$ events are identified by observing events with "π^0 and nothing" from a neutral K_L beam. Since an incident K_L is neutral, it is not possible to measure its incident position and timing or to select its momentum by magnets like charged particles. As for the final state, the visible particle is only one π^0 as neutrinos are not easily detected. The π^0 is detected possibly through its two following decay modes: $\pi^0 \to \gamma\gamma$ and $\pi^0 \to e^+e^-\gamma$. In the latter decay, which is called "Dalitz decay," precise vertex position is available by tracking an electron and a positron. However, its branching fraction is only 1.174% [16], and further decrease of acceptance is expected due to a requirement of enough spatial separation of an electron and a position in detection. The former decay with two photons in the final state is then suitable to obtain higher statistics.

From the discussion above, the signal condition is recast as "two photons and nothing." The verification of "nothing," which means there are no other visible particles at the same time, is realized by surrounding the decay volume completely with veto detectors and requiring anti-coincidence for all of them. As shown in Tab. 2.1, only the $K_L \to 2\gamma$ and the $K_L \to \pi^0\nu\overline{\nu}$ decays satisfy this condition among K_L decay modes and contribution by other decay modes is removed.

In summary, the detector design is like Fig. 2.1, where detail of each component is described later. Finally, kinematics of π^0 is reconstructed from the two photons and various event selection cuts are applied in order to distinguish signals from background. Important cut variables are vertex position Z_{vtx} and transverse momentum of reconstructed π^0, where each is defined with respect to the beam axis. Figure 2.2 shows simulated Z_{vtx}-P_{T} distribution for $K_L \to \pi^0\nu\overline{\nu}$ events with all the other kinematic and veto cuts applied, where those inside the box indicated with solid black line are regarded as $K_L \to \pi^0\nu\overline{\nu}$ signals. Detail of reconstruction and background is described in Secs. 2.1.2 and 2.1.4, respectively.

Table 2.1: Main K_L decay modes and their branching ratios together with the SM prediction value for $K_L \to \pi^0\nu\overline{\nu}$ decay. Maximum momentum of π^0 in the final states are also added if exists. The value for $K_L \to \pi^0\nu\overline{\nu}$ is the SM prediction [27] and others are taken form Ref. [16].

Decay mode	Branching ratio	Maximum momentum of π^0
$K_L \to \pi^\pm e^\mp \nu_e$ ($Ke3$)	$40.55 \pm 0.11\%$	-
$K_L \to \pi^\pm \mu^\mp \nu_\mu$ ($K\mu 3$)	$27.04 \pm 0.07\%$	-
$K_L \to 3\pi^0$	$19.52 \pm 0.12\%$	139 MeV/c
$K_L \to \pi^+\pi^-\pi^0$	$12.54 \pm 0.05\%$	133 MeV/c
$K_L \to \pi^+\pi^-$	$(1.967 \pm 0.010) \times 10^{-3}$	-
$K_L \to \pi^\pm e^\mp \nu_e \gamma$	$(3.79 \pm 0.06) \times 10^{-3}$	-
$K_L \to 2\pi^0$	$(8.64 \pm 0.06) \times 10^{-4}$	209 MeV/c
$K_L \to \pi^\pm \mu^\mp \nu_\mu \gamma$	$(5.65 \pm 0.23) \times 10^{-4}$	-
$K_L \to 2\gamma$	$(5.47 \pm 0.04) \times 10^{-4}$	-
$K_L \to \pi^0\nu\overline{\nu}$	$(3.00 \pm 0.30) \times 10^{-11}$	231 MeV/c

2.1.2 π^0 reconstruction

In order to ensure a decay occurs inside fiducial region and discriminate background contribution such as the $K_L \to 2\gamma$ decay, π^0 needs to be reconstructed. Observable variables are only two photons' energies and hit positions on the calorimeter, which are not enough to reconstruct fully kinematics of the decay π^0. However, if observed two photons are assumed to come from π^0 decay, the following simple relation between an opening angle of the two photons and their energies is obtained:

$$\begin{aligned} M_{\pi^0}^2 &= (e_1 + e_2)^2 - (\vec{p_1} + \vec{p_2})^2 \\ &= 2e_1e_2(1 - \cos\theta), \end{aligned} \tag{2.1}$$

where e_i and $\vec{p_i}$ $(i = 1, 2)$ are energy and momentum of each decay photon. Further assumption is introduced in order to reconstruct full kinematics of decay π^0, where it is supposed to decay on the beam axis. Various cut variables are then calculated based on the reconstructed kinematics and used for event selection. The detail of the reconstruction process is explained in Sec. 4.3.3.

2.1.3 Neutral beam

First of all, an intense source of K_L is necessary to search for rare signals. Such a K_L source is available as a secondary neutral beam from an intense proton beam provided by the J-PARC accelerators [47]. Concepts of the neutral beam are explained in Fig. 2.3. A production target is bombarded with the primary proton and secondary particles generated in the target are guided to the detector with a collimator system into 16° direction with respect to the primary beam and a solid angle of 7.8 μstr. Charged particles are removed by a dipole magnet and neutral beam is obtained.

Quality of the K_L beam was critical for the experiment as well as intensity. Important features are summarized below.

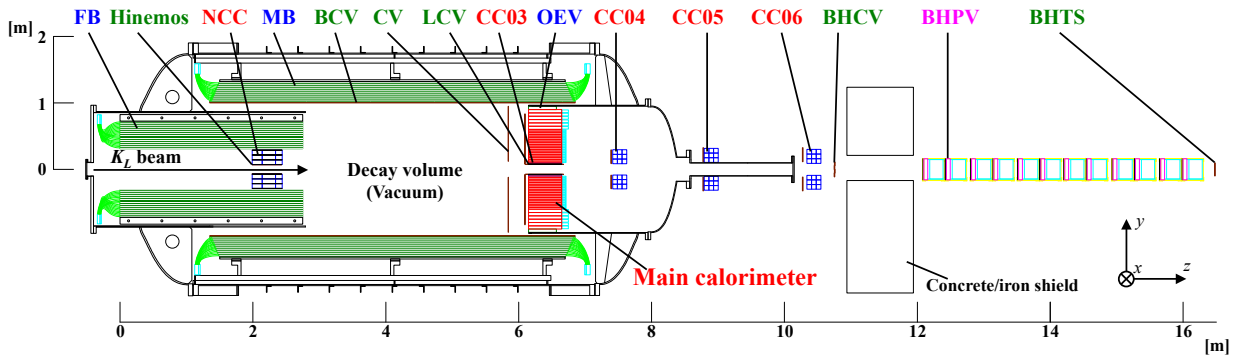

Figure 2.1: Cut-out-view of the KOTO detector assembly in the physics run in May, 2013. Detectors with their names written in blue, green and red letter consists of mainly lead-scintillator sampling calorimeter, plastic scintillator and undoped CsI crystal, respectively. The downstream detector named as BHPV is lead-aerogel sandwich detector. Detail of each detector appears in Section 2.2.5 and 2.2.6.

Narrowly-collimated beam

In the π^0 reconstruction process, assumption of decay on the beam axis is necessary as described in Sec. 2.1.2. This requires K_L beam with a small cross section, which is called "pencil beam," so that deviation of decay vertex from the beam axis is neglected. This pencil beam method also plays an important role to give a kinematical limit on transverse momentum of beam K_L. Thanks to this feature, transverse momentum of incident K_L is considered to be zero and that of a decay π^0 is clearly resolved. Since π^0 from the $K_L \to \pi^0\nu\overline{\nu}$ decay tends to have large transverse momentum due to emission of two neutrinos, this is one of the most critical kinematic variable for signal identification and the narrow beam is indispensable for this experiment.

Long beam line

At the production target, neutral short-lived particles which can mimic the $K_L \to \pi^0\nu\overline{\nu}$ signal are also generated. For example, it is possible that a Λ particle gives the same state of "two photons and nothing" with $K_L \to \pi^0\nu\overline{\nu}$ through its decay of $\Lambda \to \pi^0 n$. In order to suppress contaminations from such short-lived particles, the beam line is designed to be long so that they completely decay out before reaching the detector. In this experiment, distance between the production target and the detector is 21.5 m. As a result of a Geant4 [49] simulation with the hadron package of QGSP_BERT [50], where a gold target was bombarded with 30 GeV protons, the relative Λ yield to that of K_L at the detector position was estimated to be 3×10^{-15}. This number[*1] is small enough compared to expected sensitivity of this experiment. As a result, only stable or long-lived neutral particles,

[*1] In this simulation, Λ particles generated in the target were collected at its surface and the number of those within the direction of $16 \pm 1^\circ$ with respect to incident protons was counted considering survival probability after the 21.5-m-long beam line for each Λ.

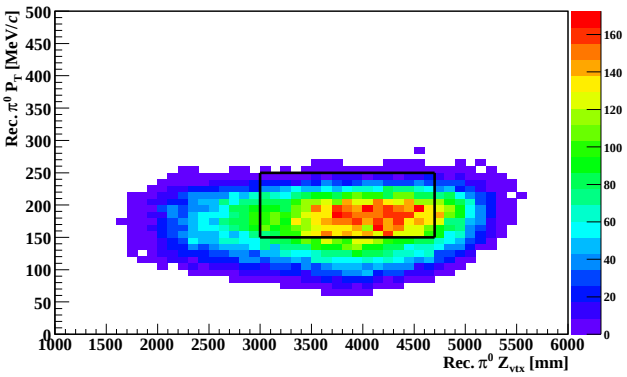

Figure 2.2: Z_{vtx}-P_{T} distribution for $K_L \to \pi^0\nu\overline{\nu}$ decay in MC after applying all veto and kinematic cuts. The black box indicates the signal region.

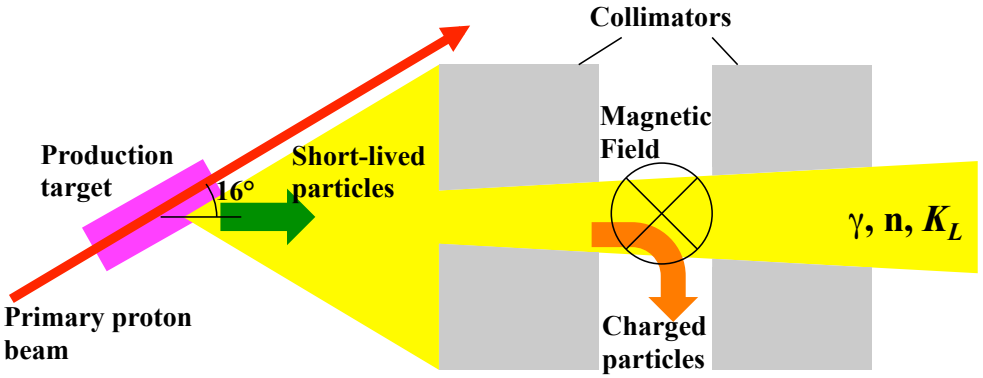

Figure 2.3: Conceptual design of the K_L beam.

namely photons, neutrons and K_Ls, survive in the beam. Since photons do not decay and neutron decay is negligibly small, hits in detectors outside the beam region are mainly derived from decay particles from K_L.

Well-collimated beam

This requirement is the most critical for background reduction. The beam contains unavoidable "halo" components, which means a portion of beam particles exists outside the beam core. Neutrons or K_Ls in such region can make background through interaction of detector materials or the $K_L \to 2\gamma$ decay, for example. The edge of the beam hence needs to be sharply collimated so as to minimize such particles.

2.1.4 Backgrounds

Since the required "positive" signals are only two photons in the calorimeter, understanding and reducing background events is crucial. In the KOTO experiment, background is expected to come from the following two sources.

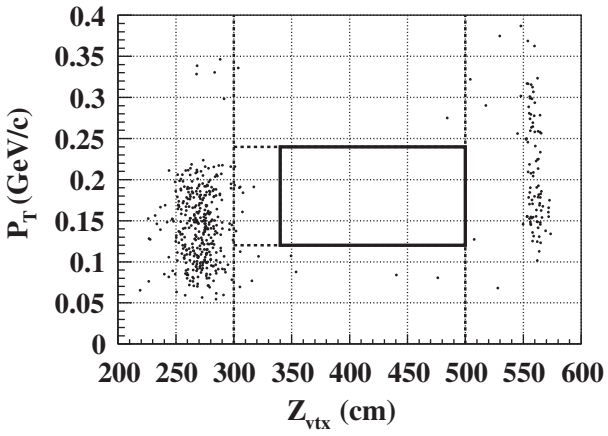

Figure 2.4: $Z_{\rm vtx}$-$P_{\rm T}$ distribution in the final analysis of the KEK E391a experiment [45].

K_L-induced background
As described in Sec. 2.1.1, discrimination of signal events from other K_L decays is done by detection of charged particles or extra photons emitted at the same time with two photons by the hermetic veto detector system. In the real situation, however, finite inefficiency of detectors, which causes background if such particles are not detected. K_L had various decay modes hence background contribution needs to be evaluated for each mode. The largest contribution is expected to come from the $K_L \to 2\pi^0$ decay, where two among four photons in the final states hit the calorimeter and the remaining two are not detected due to inefficiency of detectors. To reduce and estimate the number of background events, understanding of response for each detector is necessary.

Neutron-induced background
Neutrons in the beam halo region, referred to as "halo neutrons" below, can hit the detector materials and mimic the $K_L \to \pi^0\nu\overline{\nu}$ decay by the following mechanisms. One is π^0 or η production in detectors located upstream or downstream of the decay region. Figure 2.4 shows the $Z_{\rm vtx}$-$P_{\rm T}$ distribution in the final analysis of the E391a experiment [45], where the vertical bands at $\rm Z_{vtx}$ = 270 cm and $\rm Z_{vtx}$ = 560 cm came from neutron interactions with veto detectors placed around corresponding positions. Events in tails of these bands would be in the signal region. This type of event was considered to be the major background in the E391a experiment. In order to reduce this background, optimization of detector design such as positions and materials is critical. Another mechanism is neutron interaction in the calorimeter. When a neutron directly hit the calorimeter, it would make two photon-like hits and such events could mimic a $K_L \to \pi^0\nu\overline{\nu}$ event. Here, another neutron is generated in hadronic interaction by the incident neutron, the secondary neutron travels inside the calorimeter and it makes another hit. Detail of this background will be discussed in Sec. 7.4.8.

2.1.5 Normalization

To convert the number of observed events into the branching fraction of the $K_L \to \pi^0\nu\overline{\nu}$ decay, the number of K_L decays in the fiducial region needs to be counted. The $K_L \to 3\pi^0$, $K_L \to 2\pi^0$ and

$K_L \to 2\gamma$ decay modes are suitable for this purpose because they contain only photons in the final states and K_L mass is fully reconstructed except $K_L \to 2\gamma$ decay. Hence, detectors and triggers needs to be designed so that such events are collected in parallel with physics data. Difference of acceptance between these decays and the $K_L \to \pi^0\nu\overline{\nu}$ decay is corrected with a help of Monte Carlo (MC) simulations. The detailed way of normalization is described in Sec. 7.3.1.

2.2 Experimental apparatus

This section gives detailed description of the actual experimental setup in May, 2013.

2.2.1 Proton accelerator

The intense proton beam with the energy of 30 GeV was provided by the J-PARC accelerator complex in Fig. 2.5, which consisted of the linac [51], the 3 GeV Rapid Cycling Synchrotron (RCS) [52] and the Main Ring (MR) [48]. Negative hydrogen ions (H^-) were accelerated up to 181 MeV[*2] in the linac and injected to the RCS accelerator with the charge-exchange injection scheme [54]. Converted protons were accelerated up to 3 GeV in the RCS and some portion of these protons were transported to the MR accelerator[*3]. The MR accelerated protons up to 30 GeV and provided them to experimental facilities. For the KOTO experiment, protons were "slowly" extracted from the accelerator so that beam intensity during extraction time of 2 seconds would be constant. This way of extraction was necessary for experiment where secondary particles need to be identified one by one, avoiding pileups of events. A shot of extracted protons in a single acceleration cycle was called a "spill" and how constantly the protons are extracted in a spill is one of the most important performances in this extraction scheme. This was evaluated with a "spill duty factor" defined as below,

$$\frac{\left[\int_0^T I(t)\mathrm{d}t\right]^2}{\int_0^T \mathrm{d}t \int_0^T I^2(t)\mathrm{d}t}, \tag{2.2}$$

where T is the extraction time or the spill length, and $I(t)$ is the beam current of extracted protons. When this value is close to 1, the beam is extracted constantly and the time structure of the extracted beam is completely flat. In the beam time in May, 2013, the duty factor was approximately 50%.

Intensity of the beam is also an important factor. "Beam power," which is given in units of W, is defined as the total energy of accelerated protons per unit time, and a measure of the beam intensity. In the beam time of May, 2013, 3×10^{13} protons were accelerated to 30 GeV every 6 s and the corresponding power was 24 kW, while the design value was 291 kW, which corresponds to 2×10^{14} protons every 3.3 s. The proposal of the KOTO experiment [56] assumes data taking for 3 snowmass years[*4] with the design beam power.

2.2.2 Experimental facility

The KOTO experiment site is located in the Hadron Experimental Facility (HEF) of J-PARC, which is written as "Hadron Beam Facility" in Fig. 2.5. Extracted protons are transported to

[*2] The design energy of 400 MeV was achieved in 2014 [53].
[*3] The main part of protons were provided to the Material and Life Science Experimental Facility shown in Fig. 2.5.
[*4] One snow mass year corresponds to 10^7 s.

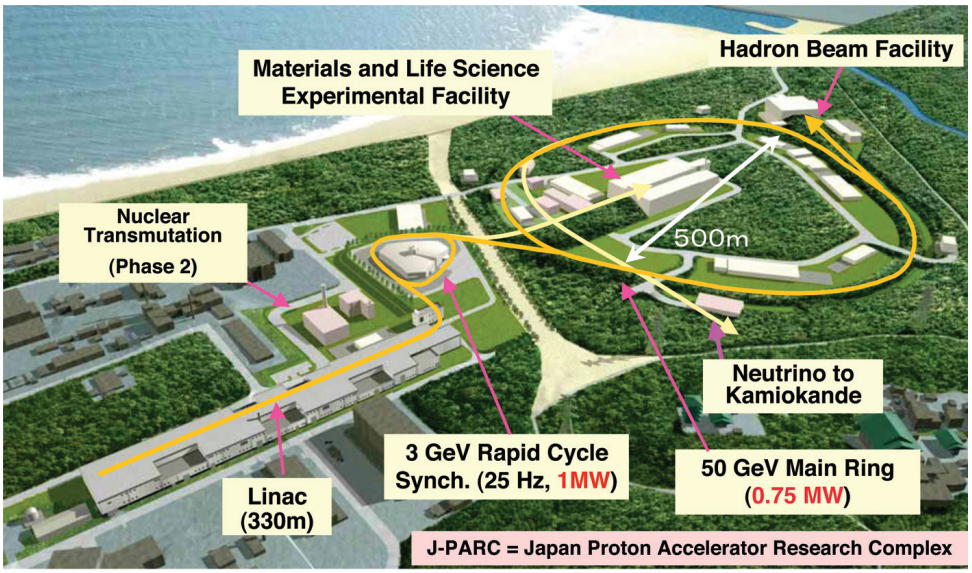

Figure 2.5: Overview of J-PARC. Quoted from Ref. [47].

HEF through the area named "Switch Yard" (SY), as shown in Fig. 2.6. The layout inside HEF is shown in Fig. 2.7. The "T1 target," located in the center of the figure, is bombarded with the transported protons to create secondary particles. This target is shared among all experiments carried out in HEF; secondary particles are extracted into various beam lines, where apparatus of each experiment is placed. Secondary neutral beam is extracted into 16° direction with respect to the primary proton line as shown in Fig. 2.7 for the KOTO experiment. Its beam line and detectors have been constructed along the line.

2.2.3 Target

A series of nickel disks, which was directly soaked in water for cooling as shown in Fig. 2.8, was originally planned to be used as the T1 target. However, when the beam intensity was not high, heavier martial with a larger atomic number was used instead of the nickel target to compensate for low beam intensity and obtain a larger number of secondary particles. A gold square-bar with dimensions of 6×6 mm^2 in cross section and 66 mm in length, as shown in Fig. 2.9, was used in the beam time in 2013 [59]. It was mounted on a copper base and cooled indirectly by water through the copper base. Before the installation of this gold target, several different types of targets were used. A platinum rod was used as the target before the summer shut down in 2012. Beam line simulations are based on the platinum target, which has been prepared for prediction of fluxes and energy spectra of beam particles other than K_L, and its results are also used in case of the gold target since these materials have similar physical properties[*5].

[*5] Simulated fluxes of beam photons, neutrons and K_Ls with Geant3 agreed between the platinum and the gold target within 22%. Here, material definition except for the target was not completely the same between these simulations.

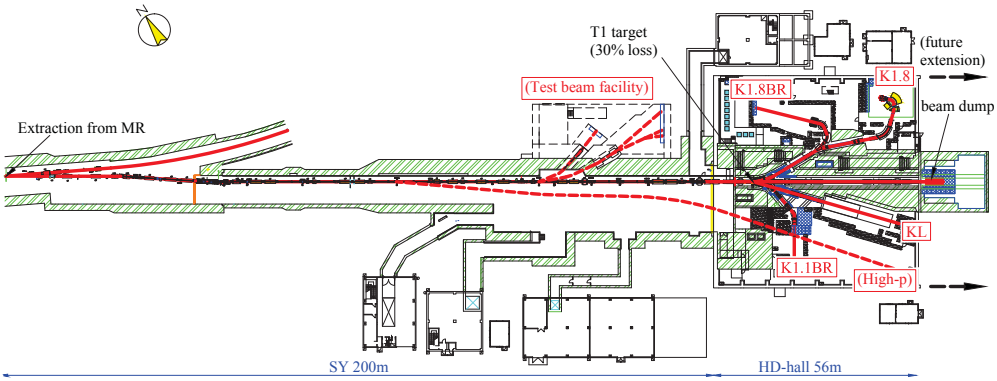

Figure 2.6: The proton transport line after extraction from the MR accelerator to the experimental hall. Quoted from Ref. [58].

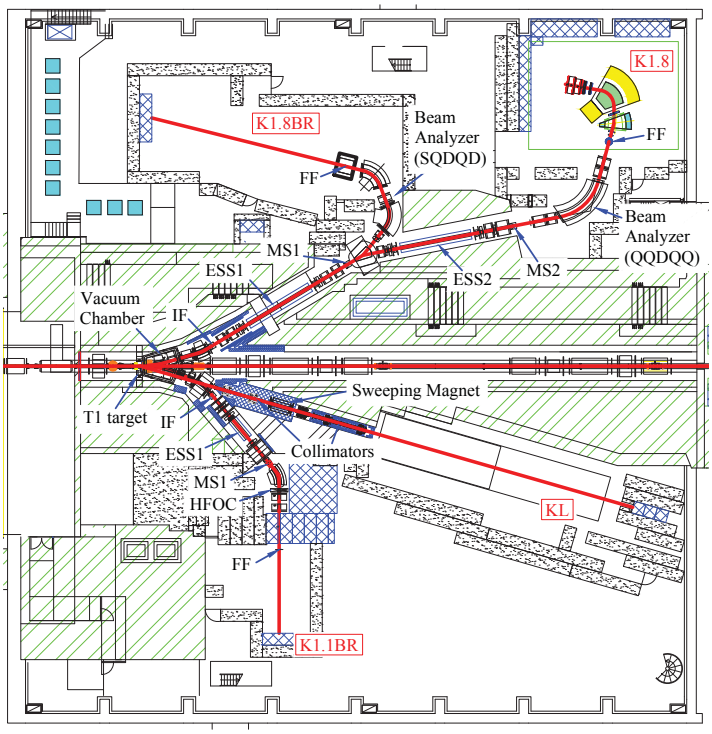

Figure 2.7: Layout inside HEF. Quoted from Ref. [58].

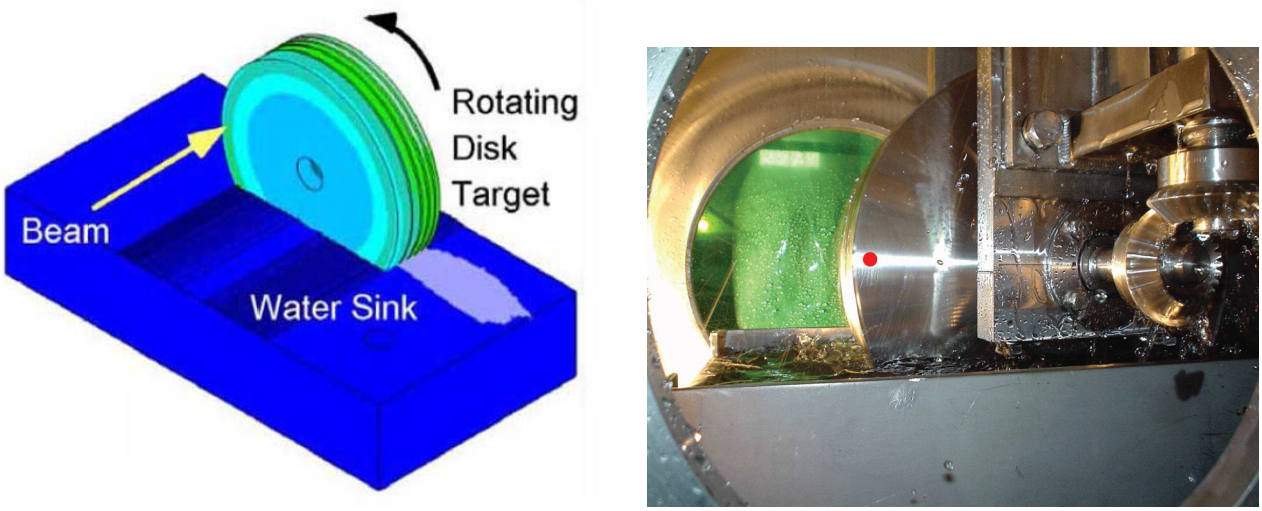

Figure 2.8: The nickel T1 target. The left figure (quoted from Ref. [56]) shows conceptual design. The right one (quoted from Ref. [57]) is its photograph, where the red point indicates the beam hit position.

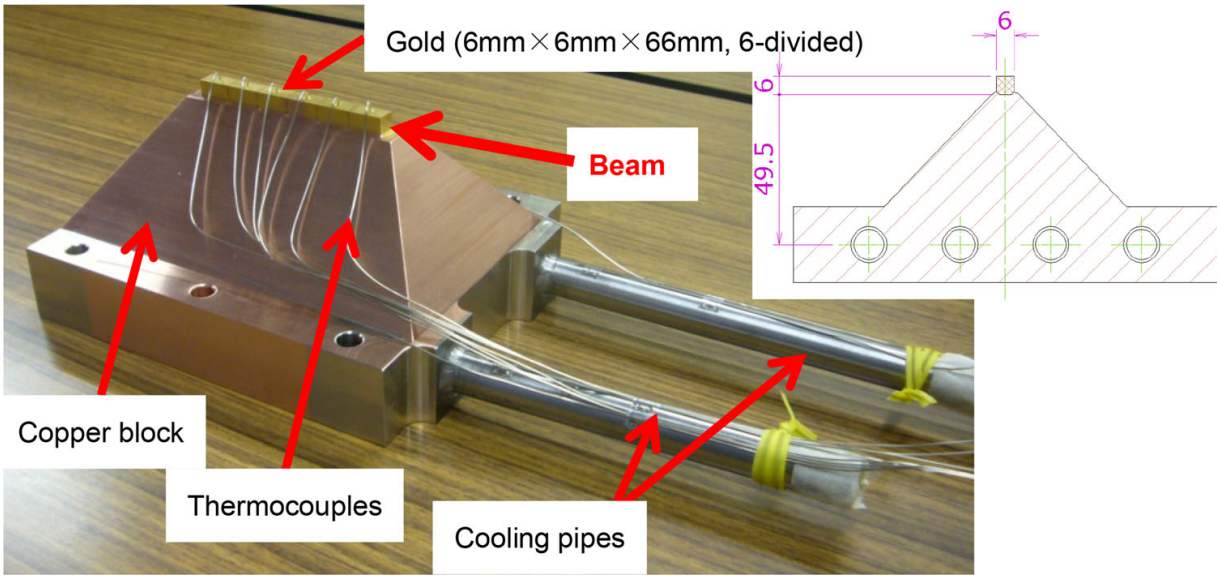

Figure 2.9: The gold T1 target used in the physics run in May, 2013. Quoted from Ref. [59].

2.2.4 Beam Line

Secondary particles from the target are extracted to the KOTO detector system through the "KL beam line" placed along 16° line with respect to the primary proton beam line. Components of the beam line are shown in Fig. 2.10. It consists of a photon absorber, two stages of collimators, a sweeping magnet, and a beam plug. The photon absorber is cuboid lead with dimensions of 34×36 mm^2 in cross section and 70 mm in length as the photograph of Fig. 2.11. Thanks to its short radiation length compared with hadronic interaction length, the photon flux is drastically reduced while the yield of K_L is maintained. As seen in Fig. 2.11, longer absorber with length of 90 mm is also prepared in order to study beam properties with a different condition. These are exchangeable remotely. The collimators are mainly made of iron and tungsten is partially used. The purpose of the collimator system is to provide neutral beam with well-defined edges and small halo component. As discussed in Sec. 2.1.4, neutrons in the beam halo could interact with detector materials and make serious background. The collimation lines are designed so as to minimize such neutrons by reducing their scattering at the inner surface of the collimators. Resultant particle spectra and fluxes are shown in Fig. 2.13 and Table 2.2. Detail of the design is found in Ref. [60]. Relative-position alignment of the two collimators is critical to obtain the designed beam shape. This was achieved by using a dedicated beam profile monitor [61] in advance of detector construction. The sweeping magnet and the beam plug are located between the two collimators. In the magnet, 1.2 T magnetic field[*6] is applied in order to eliminate unnecessary charged particles. Figure 2.12 shows a photograph of the beam plug. This is made of brass and used to stop most of the beam when access inside the experimental area is needed during accelerator operation. This is also used for detector calibration; penetrating charged particles are tagged more easily with the plug closed thanks to low-rate environment, which are useful for calibration of some detectors

2.2.5 Calorimeter

An electromagnetic calorimeter used in the KOTO experiment consists of undoped cesium iodide (CsI) cuboid crystals. Two kinds of shapes with different cross sections exist, 25×25 mm^2 and 50×50 mm^2, referred to as "small" and "large" crystals, respectively. Both are 500-mm long, which is equivalent to 27 radiation length (X_0). Each crystal is wrapped with 13-μm-thick aluminized mylar. The number of small (large) crystals is 2,240 (476). These crystals are stacked in the stainless-steel cylinder which had been used in KEK E391a experiment and whose inner radius is 953 mm as shown in Fig. 2.14. As mentioned in Sec. 1.2.3, these crystals were previously used in the KTeV experiment [46]. The readout and monitor system for each crystal is illustrated in Fig. 2.15. Scintillation light of each small (large) crystal is read by a Hamamatsu [65] photomultiplier tube (PMT) R5364 (R5330). Silicon transparent rubber called "silicon cookie" [66] and a UV filter are inserted between the crystal and the PMT, where the former is for their optical contact and the latter is for reduction of slow component in scintillation light. Although PMTs of the KTeV experiment are reused, the high voltage (HV) system is newly developed [67] for the KOTO experimental conditions: low-power-consumption HV supplier with Cockcroft-Walton (CW) base [68] to reduce heat in vacuum, preamplifier for higher gain and differential signal output for reduction of noise. In order to monitor gain of the PMTs, the calorimeter is equipped with the laser system [69], where pulse laser is injected to liquid dye and scintillation light from the dye is distributed to each PMTs via quartz fibers. This system was also used in the KTeV experiment.

[*6] Although the design field is 2 T as described in Fig. 2.10, this was weakened for safety reasons in May, 2013.

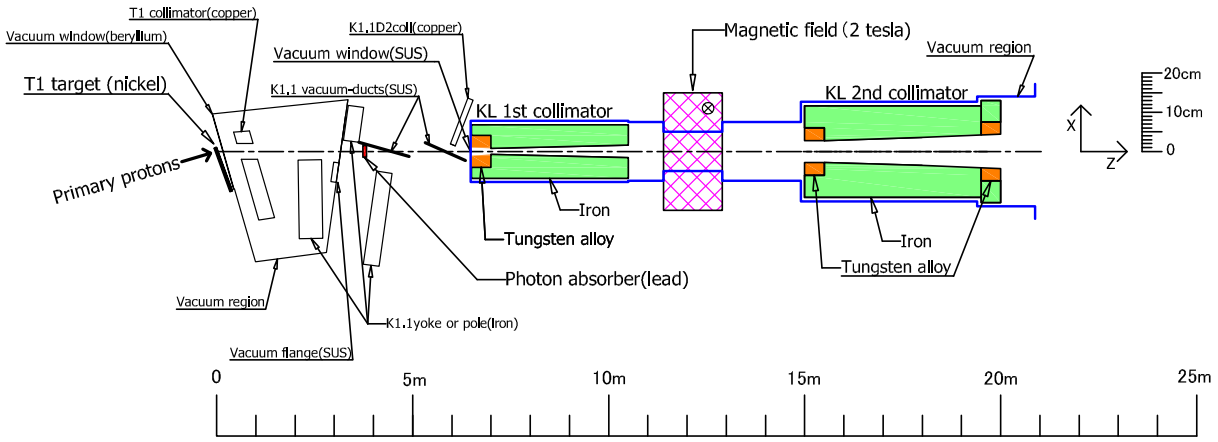

Figure 2.10: Schematic view of the KL beam line. [60]

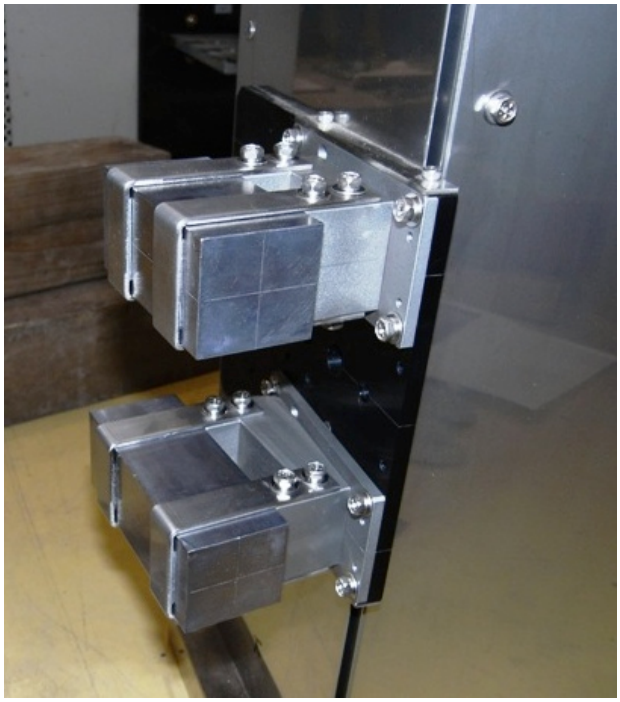

Figure 2.11: Photograph of the photon absorbers. Those with two kinds of thicknesses are installed and remotely exchangeable for each other during beam operation. This photograph was taken and provided by H. Watanabe.

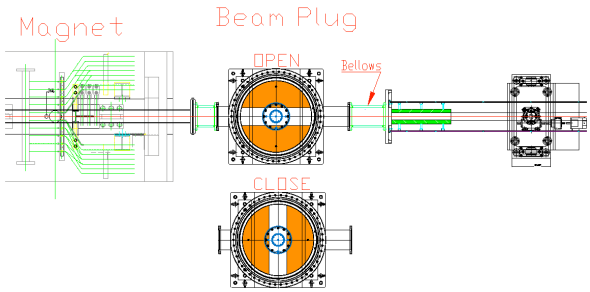

Figure 2.12: Outline(top) and photograph(bottom) of the beam plug. Quoted from Ref. [62].

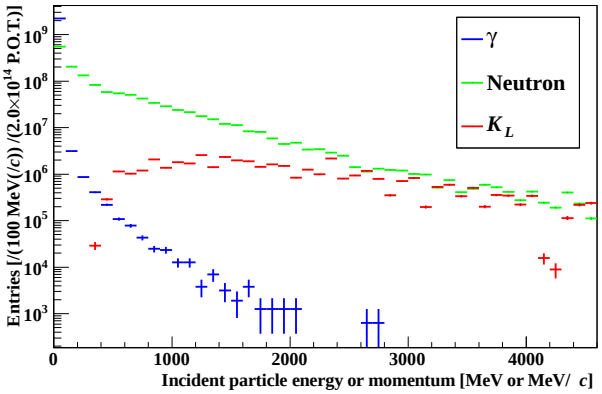

Figure 2.13: Simulated energy or momentum distribution of beam particles. The K_L component was scaled by a factor of 1.76 to fit the yield with measurements [28, 63, 64].

Table 2.2: Particle fluxes from the beam line simulation. The platinum target and the 70-mm-thick lead absorber are assumed.

Particles	Flux for 2.0×10^{14} P.O.T.
γ (> 1 MeV)	2.23×10^9
γ (> 50 MeV)	1.38×10^7
neutron (> 1 MeV)	1.40×10^9
neutron (> 1 GeV)	1.61×10^8
K_L	4.19×10^7

2.2.6 Veto detectors

Veto detectors are categorized into photon veto and charged veto detectors according to the kinds of particles to detect. The photon veto detectors are mainly lead-scintillator sandwich or undoped CsI calorimeter and the charged veto detectors consist of plastic scintillator. Most of the detectors except for ones named CC05, CC06, BHCV and BHPV, are placed inside the vacuum.

Front Barrel (FB) and Main Barrel (MB)
These detector are the largest detectors and placed to detect photons emitted into the traverse direction from K_L decays as shown in Fig. 2.1. Both are lead-plastic scintillator sandwich detectors and scintillation light is read by PMTs of Hamamatsu R329-EGPX [71] via wavelength shifting fibers embedded in grooves of scintillator plates. The FB (MB) detector consists of 16 (32) modules, each of which has the inner and outer sub-modules, as shown in Fig. 2.16. Detailed parameters are summarized in Tab. 2.3. These modules are arranged to form a barrel shape with its inner radius of 0.3 m and 1 m in FB and MB, respectively and cover the transverse region of the neutral beam. This is shown in Fig. 2.17. These detectors are originally constructed for KEK E391a experiment and reused in the KOTO experiment. More information will be found in Ref. [72].

Barrel Photon Veto (BCV)
A plastic scintillator layer with thickness of 10 mm is equipped in the inner surface of the MB detector. As same with MB, the BCV detector consists of 32 modules and signals of each module are read from both sides via wavelength shifting fibers.

Neutron Collar Counter (NCC) and Hinemos
The NCC detector is located inside FB. The role of this detector is to detect photons generated from the $K_L \to 3\pi^0$ or the $K_L \to 2\pi^0$ decays, especially those coming from upstream of this detector. This detector is also assigned another critical role related to neutron background; in the previous KEK E391a experiment, the largest background was caused by halo neutrons through π^0 production in this kind of detector. Therefore, the NCC detector is designed so that this type of

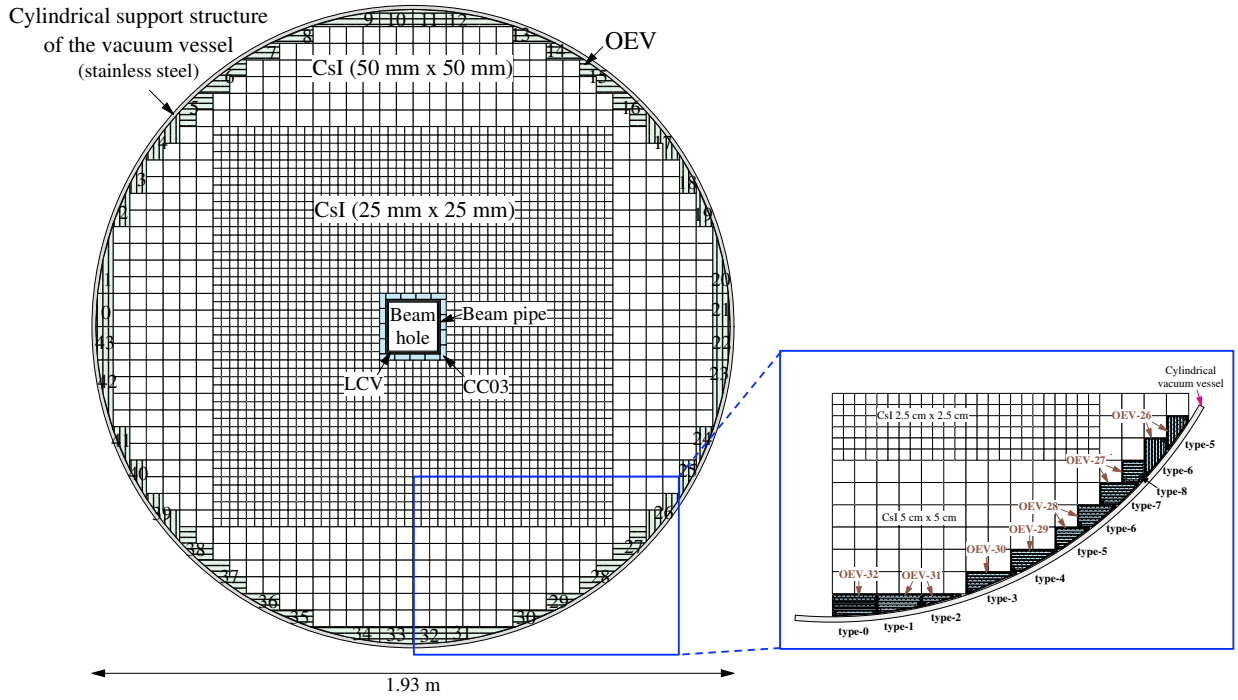

Figure 2.14: Configuration of the CsI calorimeter and related detectors. Quoted from Ref. [70] and partially modified.

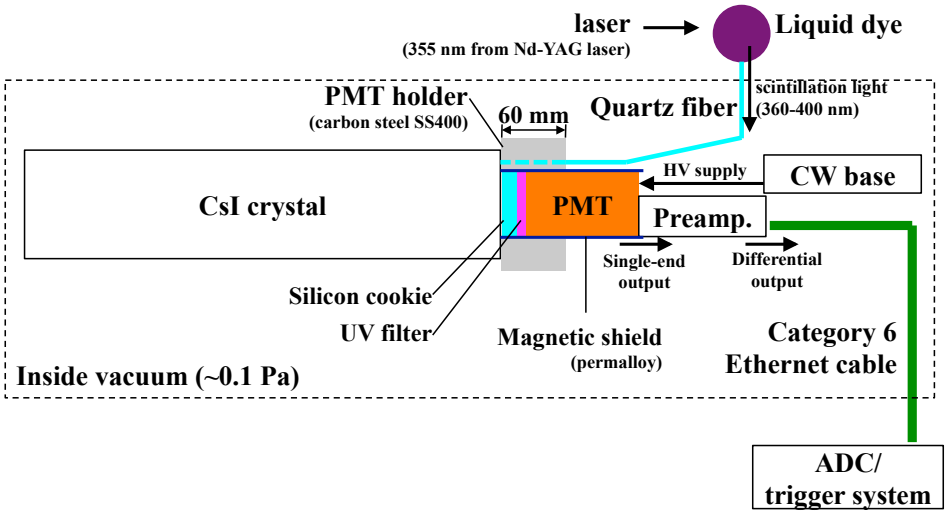

Figure 2.15: Outline of the calorimeter system.

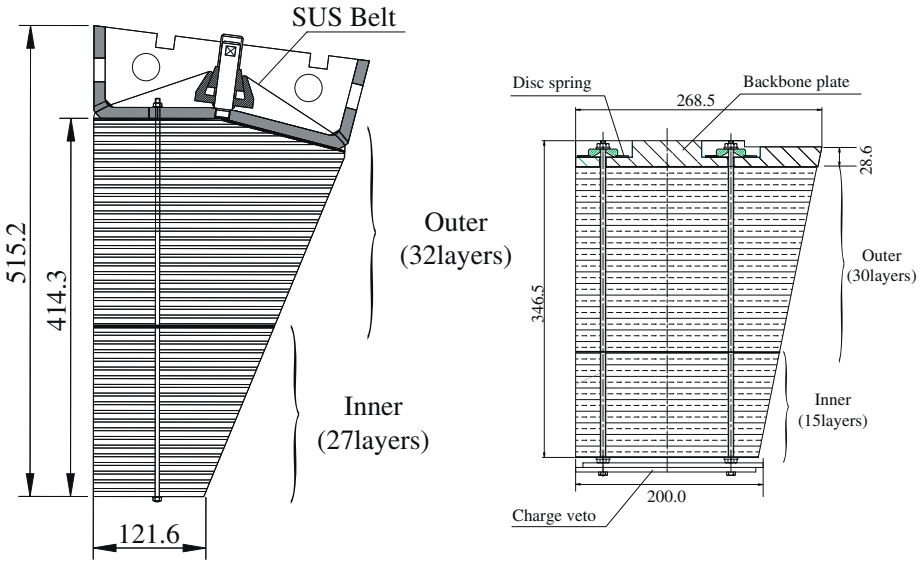

Figure 2.16: Module structure of FB (left) and MB (right). Quoted from Ref. [72].

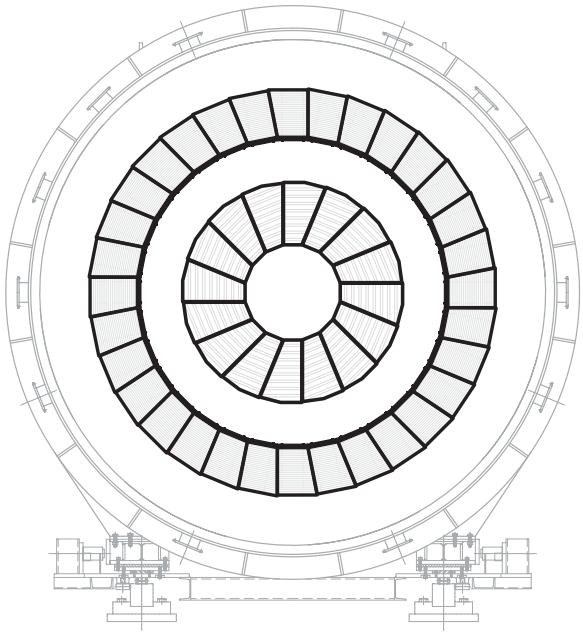

Figure 2.17: Arrangement of the FB and MB modules. The inner (outer) ring indicates FB (MB). Quoted from Ref. [45].

Table 2.3: Detailed configuration of the FB and MB detectors.

	FB	MB
Length in z-direction	2.75 m	5.5 m
Scintillator type	MS resin [73]	
Wavelength shifting fibers	BCF-91A (Bicron)	Y11-M (Kuraray)
Thickness of scintillator	5 mm	5 mm
Thickness of lead	1.5 mm	1 mm for the inner layer 2 mm for the outer layer
The number of inner layers	27	15
The number of outer layers	32	30
The number of modules	16	32
Readout	single end	both ends
The number of channels	32	128

background is reduced as well as the flux of halo neutrons is measured. For these purposes, undoped CsI crystals are adopted as fully-active material and they are segmented along the beam direction in order to measure longitudinal shower development for separation of neutrons and photons. The overall structure is shown in Fig. 2.18. Main parts are CsI crystals with dimensions of 66×66 mm^2 in cross section and 446 mm in length. Each crystal is divided into the three regions named front, middle and rear regions, and scintillation light in the crystals is read by PMTs via 40 wavelength shifting fibers. Among the 40 fibers, four fibers are optically connected to only one segment of the above three regions and the other 28 fibers are commonly attached to all the regions. The former and latter readout is called "individual" readout and "common" readout and used for halo neutron measurement and veto of extra photons from K_L decay, respectively. The beam hole is maintained by a CFRP pipe and its inner surface is equipped with plastic scintillator detector named Hinemos (Horizontal Inner NCC Edge Mounted Scintillator) [74]. Gaps between the structure and regular modules are filled with outer modules, which had pentagonal shape and directly read by PMTs. In this thesis, information of only "common" readout is used. More information on this detector is described in Refs. [75, 76].

Charged Veto (CV)

The CV detector is covering the front surface of the CsI calorimeter with two layers of 3-mm-thick plastic scintillator in order to detect charged particle events with high efficiency. The upstream (downstream) layer is called the "front" ("rear") plane. Each plane consists of modules with a 7-cm-wide plastic scintillator strip and seven wavelength shifting fibers viewed from the both ends with Hamamatsu Multi Pixel Photon Counters (MPPCs). Figure 2.19 shows the overall structure of one plane of the detector and a schematic view of each module. Readout with shorter (longer) fibers out of a scintillator strip is named a "short-fiber-side" ("long-fiber-side") channel. The specifications are summarized in Table. 2.4. Thanks to long attenuation length of wavelength shifting fibers and high photon detection efficiency of MPPCs, large photoelectron yields are obtained over the wide region of the detector and this feature is critical in order to keep high efficiency for charged particles in the whole region. The front (rear) plane is filled with 96 (88) scintillator strip modules with various

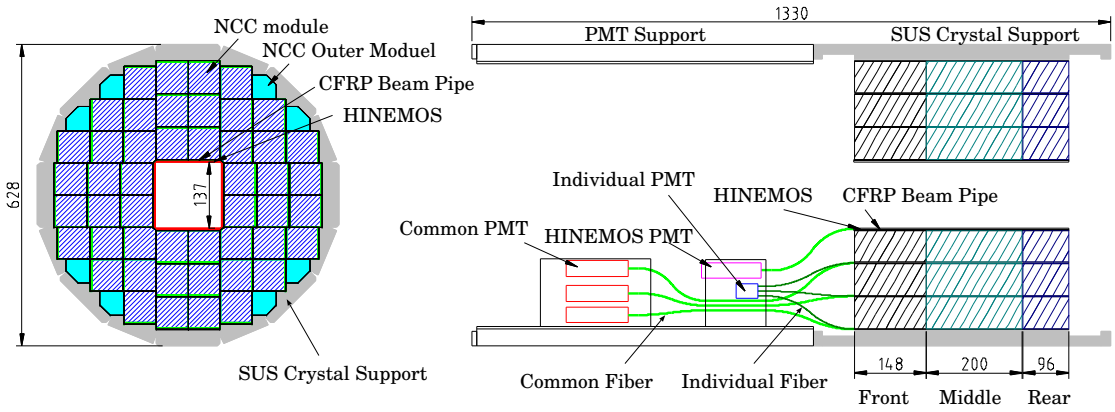

Figure 2.18: Structure of the NCC detector. The left figure is a front view and the right one is a side view. Quoted from Ref. [77].

Table 2.4: Specifications of the CV detector.

Scintillator	BC404 (Saint-Gobain [78])
Wavelength shifting fibers	Y-11(350)MSJ (Kuraray [79])
	1 mm in diameter
Glue	EJ500 (Eljen [80])
Photosensor	MPPC S10943-0928(X) (Hamamatsu)
	3×3 mm^2 photosensitive area
	60×60 pixels (50-μm pitch)
Reflector	Tetolight (Oike [81])
	12-μm-thick polyester film
	one side aluminized

length so as to form a hexadecagon without gaps between neighboring modules as shown in Fig. 2.19. Fibers are laid on grooves of scintillator strip and these are glued with optical cement using the automatic glueing system, which was developed for this detector and its photograph is shown in Fig. 2.20. Detail of the production procedures is described in App A. After the gluing process, modules are wrapped with thin film as reflector and equipped with connectors to attach MPPCs at the both ends of fibers. Finally, they are fixed on the carbon fiber reinforced plastic (CFRP) plate with thickness of 0.8 mm with fluorocarbon wires. The CFRP plate is supported with aluminum structure which consisted of U-channels welded one another to form a hexadecagon. The readout and control system including photosensor, voltage controller and preamplifier, were custom-built for this detector. The MPPCs are equipped with peltier cooler so as to keep their temperature within (10$\pm$0.1) °C with feedback system. Preamplifier with a gain of 50 is connected to compensate for small gain of a MPPC. These MPPCs and preamplifiers are mounted on the aluminum support structure. Control of these components as well as voltage supply for the MPPCs and monitoring of detector operation is managed remotely. More information is found in Refs. [82, 83, 84].

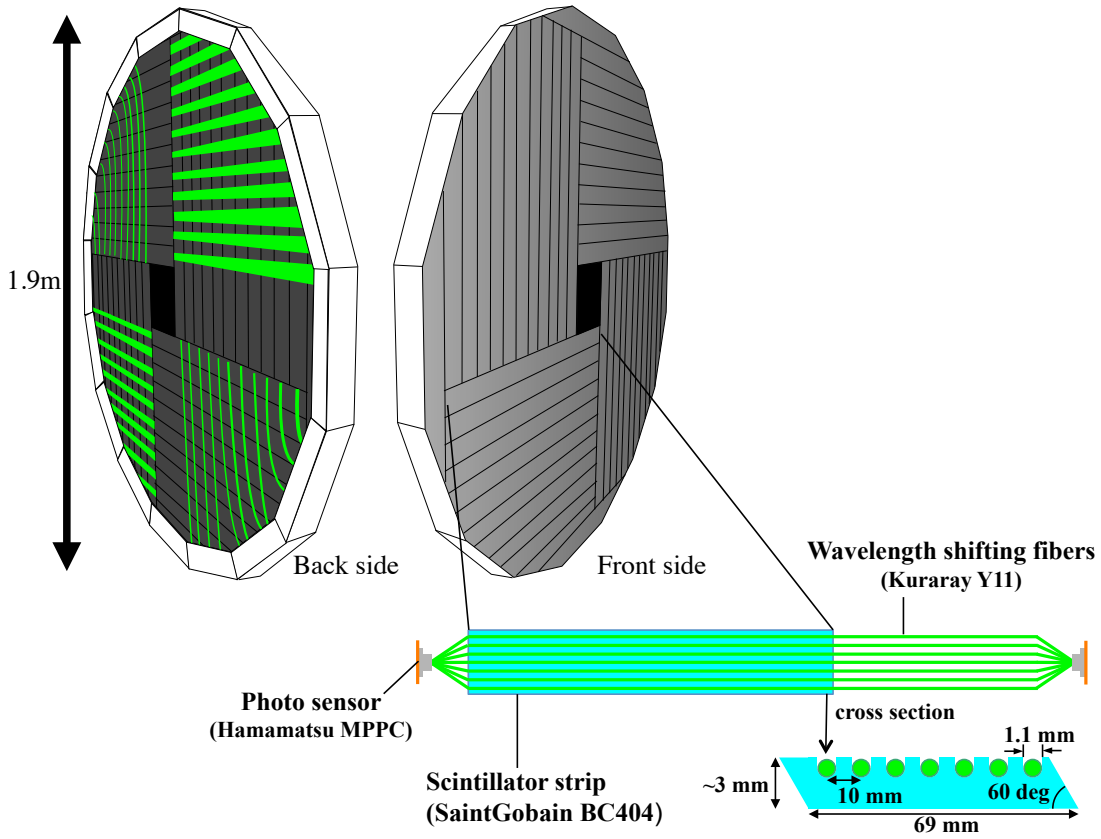

Figure 2.19: Overview of the CV detector. The top part of the figure was drawn by D. Naito.

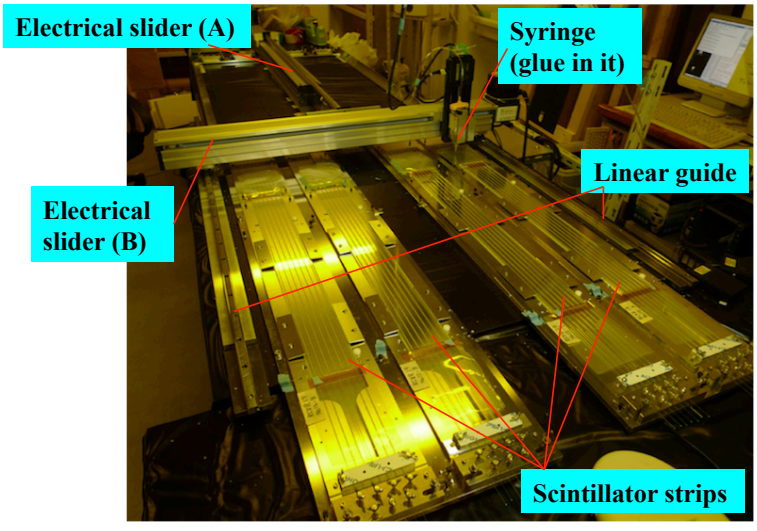

Figure 2.20: Photograph of scintillator-fiber gluing system for CV module production. Glueing of four modules in total were processed at a time. The slider A pushed or pulled the slider B which was equipped with a syringe with glue inside. Speed of the slider A was controlled so that the constant amount of glue was applied.

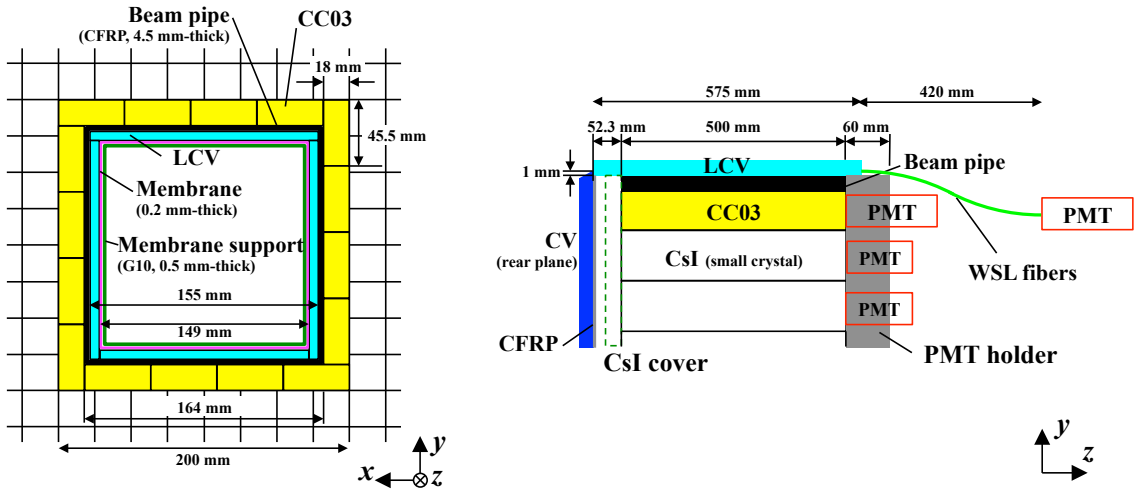

Figure 2.21: Detectors around the beam hole of the calorimeter. The left figure in a front view and the right one is a side view.

Outer Edge Veto (OEV)

Since the CsI crystals of the calorimeter is stored inside the cylinder-shaped structure, the outer gaps are filled with lead-plastic scintillator modules with various kinds of shapes as shown in Fig. 2.14. Scintillator is based on MS-resin [73] and 5 mm in thickness. Wavelength shifting fibers of Kuraray [79] Y11(200)M are embedded in each layer and they are viewed by Hamamatsu 1-inch PMT (R1924A) from the downstream side. The total number of readout is 44. Each lead layer is 1.5 mm in thickness and alternate layers of scintillator and lead are accommodated with a structure of 2-mm-thick stainless steel to avoid deformation against load of the CsI crystals. More information is found in Ref. [70].

CC03 and Liner Charged Veto (LCV)

Structure around the calorimeter beam hole is shown in Fig. 2.21. Square shape is maintained by the beam pipe made of 4.5-mm-thick CFRP. Space between the beam pipe and the regular small CsI crystals are filled with the CC03[*7] detector, which consists of 16 cuboid CsI crystals with cross section of 45.5×18 mm^2 and length of 500 mm, the same with crystals of the calorimeter. Two 1/2-inch PMTs of Hamamatsu H3165-10MOD, which is modified for use in vacuum environment, are equipped with each crystal. The inner surface of the beam pipe is covered with plastic scintillator detector, named LCV, in order to increase detection efficiency for charged particles hitting from inside of the beam hole. The LCV detector consists of four 3-mm-thick plastic scintillator modules, each of which has 15 wavelength shifting fibers. The same kinds of scintillator and fibers with CV are adopted. Scintillation light in each module is viewed only from the downstream with a PMT of the same type with CC03. More detail of CC03 and LCV is described in Refs. [85] and [86], respectively.

[*7] "CC" stands for Collar Counter.

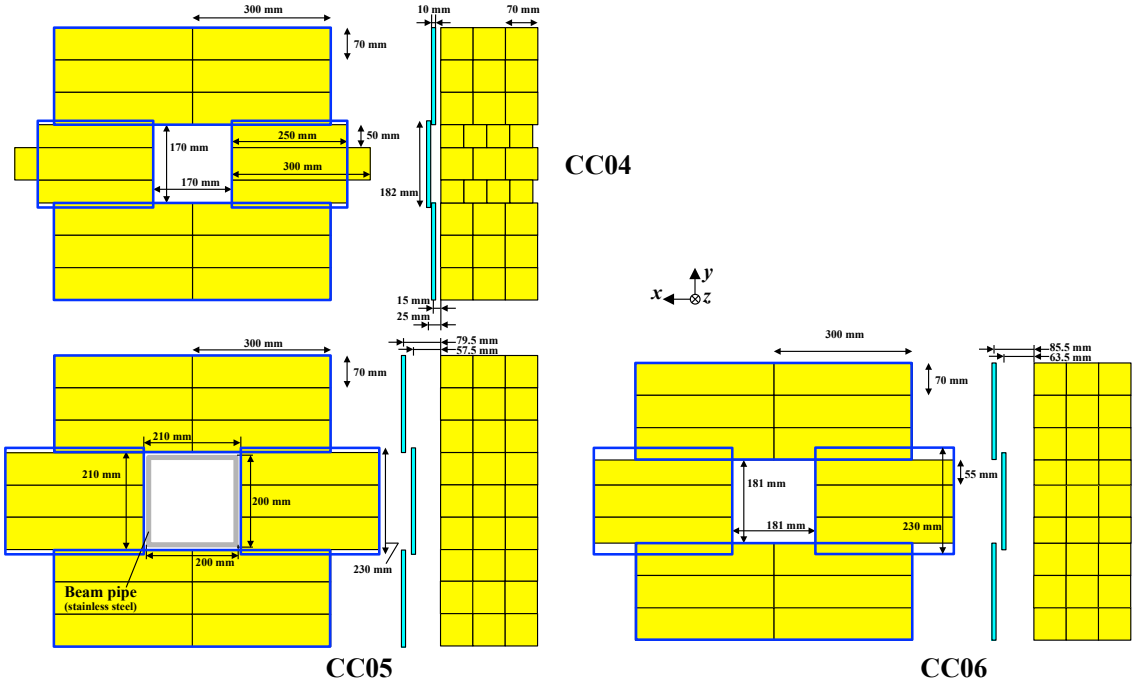

Figure 2.22: Configuration of the downstream collar counters. Front view (left) and side view (right) for each of CC04, CC05 and CC06 are shown. Yellow blocks indicate CsI crystals and blue lines or cyan box indicate plastic scintillator modules.

Downstream collar counters

In the downstream of the CsI calorimeter, a series of collar counters name CC04, CC05 and CC06 are installed for detection of photons and charged particles which escape into the downstream direction through the calorimeter beam hole. Each detector is a stack of undoped CsI crystals around the beam and equipped with a plastic scintillator layer in the upstream, as shown in Fig. 2.22. CC04 is located inside the vacuum tank. Detail for these detectors is in Refs. [87, 88].

Beam Hole Charged Veto (BHCV)

The BHCV detector consists of eight 3 mm-thick plastic scintillator of EJ204 (Eljen [80]) with dimensions of 60 $\times$ 115 mm^2 covering 225 $\times$ 225 mm^2 region in the neutral beam, as shown in Fig. 2.23. It detects charged particles escaping into the beam direction from K_L decays, particularly $\pi^{\pm}$ from the $K_L \to \pi^+\pi^-\pi^0$ decay. The modules are arranged to have overlapping regions to eliminate gaps between modules. Scintillation light in each modules is read from one side with a 2-inch PMT assembly of Hamamatsu [65] H7195MOD. This PMT is equipped with external HV supply for each of the last three dynodes in order to reduce gain deviation in high-rate environment.

Beam Hole Photon Veto (BHPV)

The BHPV detector is located in the most downstream of the KOTO detector system and is placed inside the neutral beam in order to detect K_L decay photons escaping in the beam direction. As mentioned in Sec. 2.2.4, the neutral beam contains a large number of neutrons as well as K_Ls and

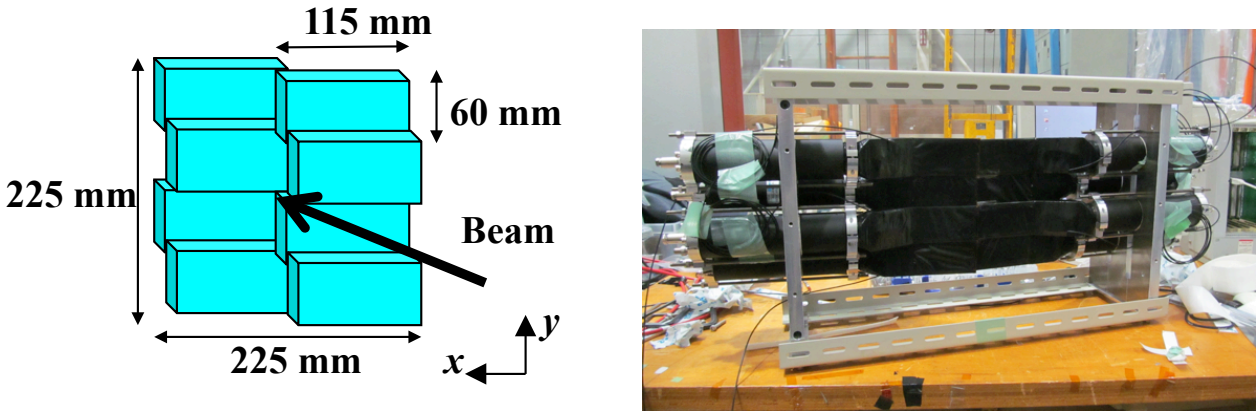

Figure 2.23: Outlook of the BHCV detector. The left figure shows a schematic view of module arrangement and the right one is a photograph of the real detector before installation.

the neutron flux is expected to reach up to 100 MHz. Even in such a sever condition, this detector needs to have high efficiency for photons from K_L decays, better than 99.5% for high energy photons with >1 GeV in order to suppress background from the $K_L \to 2\pi^0$ decay for a search of signal events with the SM sensitivity. Therefore, blindness for neutrons is critical for this detector from the view point of performance deterioration due to high counting rates and reduction of unnecessary veto signals from these neutrons.

In order to meet these requirements, a lead-aerogel sampling detector is newly developed for the KOTO experiment [94]. Structure of a single module is shown in Fig. 2.24. A series of these modules arrayed along the beam constitutes the detector system. Aerogel with refractive index of $n = 1.03$ is used. Its dimensions in a module are 320×320 mm^2 in cross section and 58 mm in thickness, where two layers of tiles are arranged in a 2×2 grid. These tiles had been originally made for the KEK E248 (AIDA) experiment [91] and are reused for this detector. Thickness of lead sheets is 1.5 mm or 3.0 mm, which varies depending on modules, and the cross section was 398 mm and 318 mm in horizontal and vertical direction, respectively.

In a module, an incident photon is converted into an electromagnetic shower in the lead layer, aerogel Čerenkov light generated by electrons and positrons in the shower is collected by light collection system, which consists of two flat mirrors and Winston cone funnels [92], and finally detected by 5-inch PMTs of Hamamatsu R1250 [93]. Since neutrons basically produced protons or pions by scattering or hadronic interaction and no or less Čerenkov light is generated due to their slow velocity, the detector is blind to neutron incidence. Further neutron separation is achieved using difference in shower development in electromagnetic interaction and hadronic interaction. The former develops into the forward direction and the latter tends to have more isotropic angular distribution. Hence by requiring coincidence of consecutive three or more modules in photon detection, more rejection of neutron hit events is expected while keeping efficiency for high energy photons.

In the physics run, twelve modules are installed with lead and aerogel sampling as shown in Fig. 2.25. Plastic scintillator counter with dimensions of 20×20 cm^2 in cross section and 5 mm in thickness followed for the purpose of calibration.

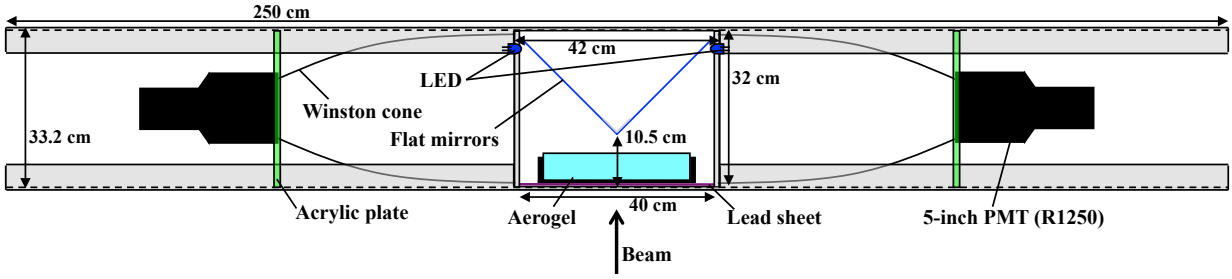

Figure 2.24: Diagram of a single module of the BHPV detector (top view).

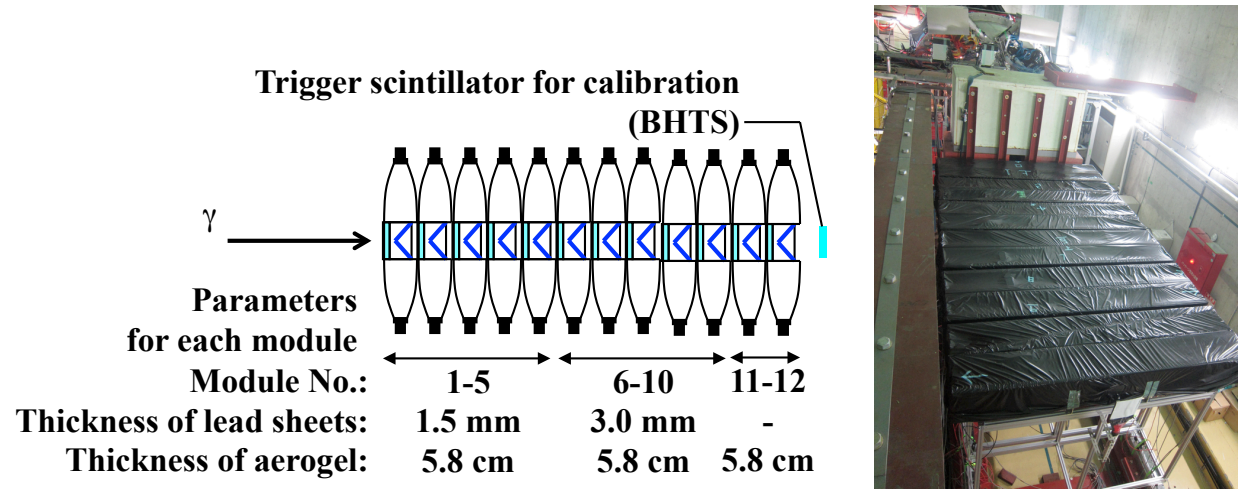

Figure 2.25: Configuration of the BHPV detector in the physics run of May, 2013. (Left) Sampling of lead and aerogel for each module. No lead sheets were inserted in the last two modules since showers started in these modules did not satisfy "coincidence of three or more consecutive modules" and lead sheets in these modules did not effectively work as converter. (Right) Photograph of overview of the detector. The beam came from the upper direction. This photograph was taken and provided by H. Watanabe.

2.2.7 Vacuum and cooling system

The decay region must be kept in vacuum because neutrons can interact with residual gas in the beam region, and π^0 can be generated, which mimics a signal event. In order to suppress this type of background enough small, the decay volume needs to be evacuated down to $O(10^{-5})$ Pa. The overall vacuum system is shown in Fig. 2.26. The whole KOTO detector system except downstream detectors including CC05, CC06 and beam hole detectors is placed inside the large vacuum tank. Vacuum of the decay region, called the high-vacuum region, is kept around 5×10^{-5} Pa, which is separated with the detector region, called the low-vacuum region. Pressure of the low-vacuum region is kept less than 1 Pa as a buffer region. This structure, with no detectors inside the high-vacuum region, is necessary to avoid deterioration of vacuum due to outgassing and obtain vacuum level of $O(10^{-5})$ Pa. Separation of these vacuum regions is achieved by thin files called membrane. Its structure is shown in Fig. 2.27. It consists of four layers and total amount of material was as

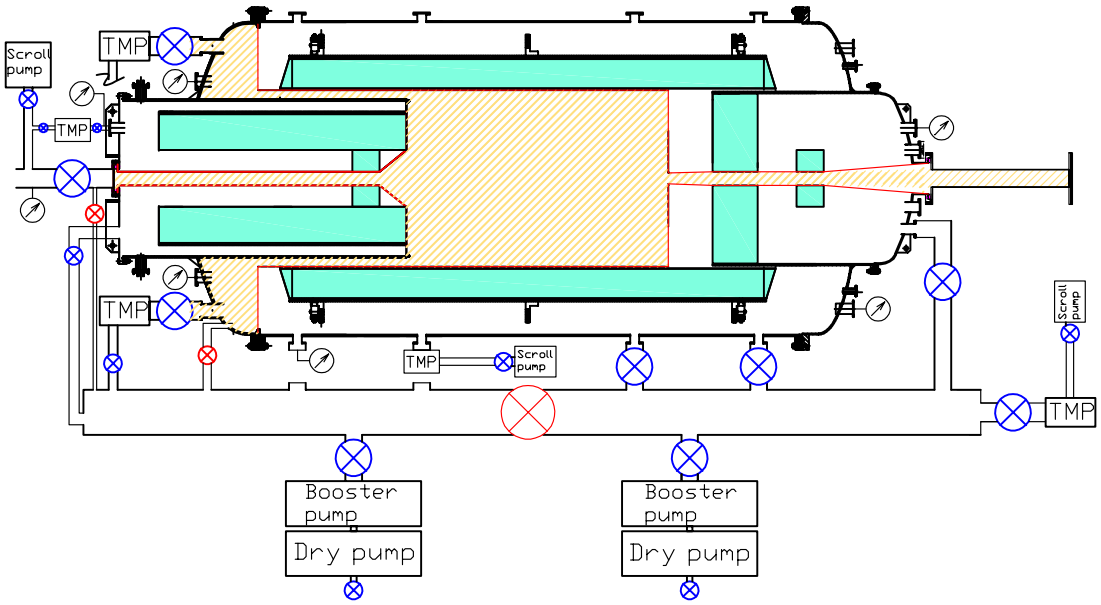

Figure 2.26: Outline of the vacuum system. The hatched region indicates the high vacuum region with a level of 10^{-5} Pa and the surrounding hollow region, including detectors shown with green color, indicates the low vacuum region. The red (blue) circled cross marks with represents closed (open) bulbs. Boxes with letters such as "TMP" and "Booster pump" corresponds to vacuum pumps. "TMP" stands for Turbo Molecule Pump. Circled arrow marks show places where vacuum monitors are installed. This figure was prepared by H. Watanabe.

small as 202 μg/cm^2. The thickness is critical and must be kept as less as possible for reduction of background since any inactive material on the inner surface of detectors can increase inefficiency for K_L decay particles generated inside the decay region.

Since most of the KOTO detectors are located inside the vacuum of 1 Pa as mentioned above, various attentions need to be paid for their operation. Outgassing from detector material is one of the serious issues, which affects transparency of silicon cookies used for optical contact in the main calorimeter. In order to prevent such affect from the upstream detectors, the low-vacuum region is separated into the upstream section and the downstream section.

A cooling system is also necessary for detector operation in the vacuum environment. Cooling water with temperature of 10°C is flowing through copper cooling pipes for heat dissipation of PMTs and front-end electronics (FEE). Cooling pipes are introduced close to PMTs or FEE and thermal contact was achieved through copper tapes or coper bars so that heat is easily transferred to outside of the vacuum through cooling water. In case of CV, heat from FEE, including the preamplifiers and the peltier coolers, is dissipated through the aluminum structure. Cooling pipes make thermal contact at four points in each plane and FEE is also thermally coupled to the structure via silicon heat dissipation sheets. Thermocouples are attached in order to monitor temperature of PMTs for each detector, upstream and downstream of the calorimeter crystal, cooling pipes, the CV aluminum frame and vacuum chamber wall.

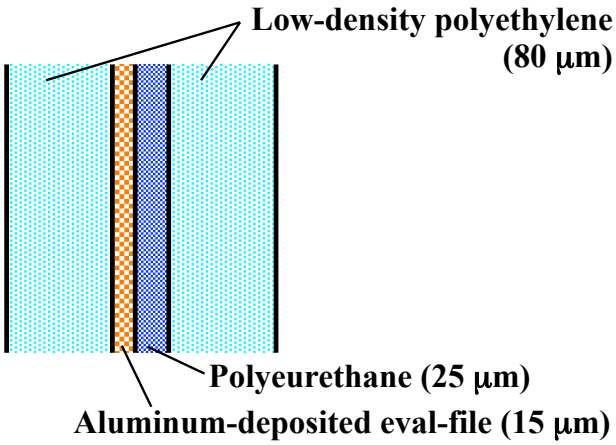

Figure 2.27: Structure of the membrane used to separate the two vacuum regions.

2.2.8 Data acquisition system

In the KOTO experiment, signals from all the detectors are recorded as digitized waveform with 125-MHz or 500-MHz sampling analog-to-digital converter (ADC) modules. For each event and each channel, waveform of 512-ns range, which corresponds to 64 (256) samples in case of 125-MHz (500-MHz) sampling, is stored. The diagram of the KOTO data acquisition system is shown in Fig. 2.28. Triggers are issued based on these waveform information. Pipeline processing is adapted in order to eliminate dead time, where waveform data is stored in a pipeline buffer to wait for trigger decision. Data is once placed on the temporary local storage in J-PARC and then transferred to KEK for long-time storage. Detailed description is in Ref. [95] and overview of the system is presented below.

Readout scheme

The ADC modules are custom-built for the KOTO experiment. The 125-MHz-sampling ADC [96] is used for all the detectors except BHCV and BHPV. The system is optimized mainly for readout of the calorimeter, which occupies approximately 70% of total readout channels. The dynamic range of the ADC is 14 bits in order to measure photon energy from 1 MeV up to 1 GeV in each channel of the calorimeter [67]. Each module has 16 channels of analog inputs as shown in Fig 2.29. Signals from undoped CsI crystals in the calorimeter or plastic scintillator in veto detectors have narrow pulse shapes with a few tens ns, which is too sharp to record waveform with 125 MHz sampling. Therefore, a ten-pole Bessel filter is used to widen an input pulse into a Gaussian shape with $\sigma = 27$ ns [90] as shown in Fig. 2.30. More sampling points are then available with relatively slow sampling of 125 MHz, which results in excellent timing resolution. In the prototype calorimeter, timing resolution better than 1 ns was obtained for energy deposit larger than 20 MeV [89, 90]. Thanks to this feature, use of expensive 500-MHz ADC with a large dynamic range is avoided and cost for readout is reduced.

The ADC requires differential signals as an input with respect to noise reduction. Therefore, shielded-twisted-pair cables are used for signal transmission. Ethernet cables of category 6 are adopted, where only outside two among four pairs are used in order to avoid cross talks and thus one cable is assigned for two channels. Availability of commercial products is helpful to reduce

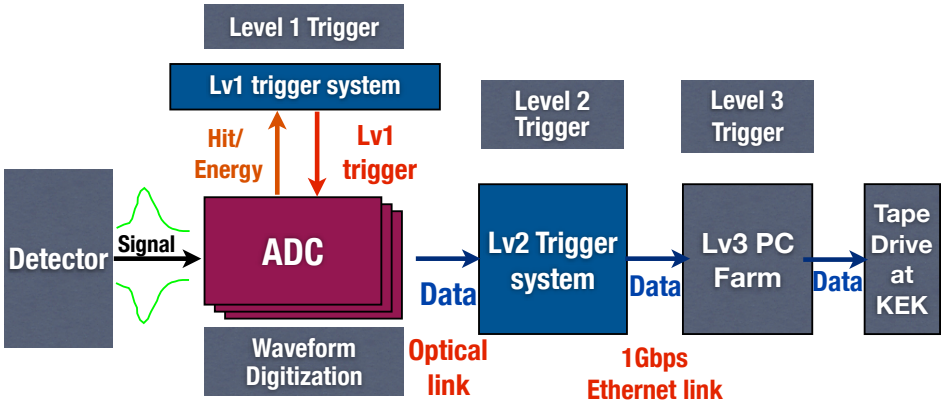

Figure 2.28: Diagram of the KOTO data acquisition system. In the physics run, no event selection was applied in the Level 3 trigger and the "Lv3 PC Farm" worked just as the local storage. Quoted from Ref. [95].

cost. The calorimeter and CV are designed to output differential signals from their preamplifiers, whereas other detectors give single-end signals. Converters modules are used to change these single-end signals to differential ones.

For detectors located inside the beam, namely BHCV and BHPV, ADC modules with 500-MHz sampling and 12-bits dynamic range [97] are used. They record signal waveforms from these detectors without shaping because single counting rates are too high and wide pulses as in the 125 MHz ADCs cause event pileups.

Trigger and data storage

Events are triggered with two stages using digitized waveform information. The first stage trigger decision, which is called "Level 1 trigger", is judged every clock of 125 MHz, based on information of total energy deposit in a detector system. Waveform sum in all channels of ADC modules for a detector system of interest is used as total energy information. When a peak is found in the summed waveform and its height exceeded a given threshold, Level 1 trigger is issued and an "event" was defined, or timing of 64 or 256 samples to be recorded is determined from the trigger timing. This trigger scheme is called "Et trigger." Et trigger decision is able to be made detector by detector and the final Level 1 trigger decision is made as a combination of Et trigger signals from several detectors. In the physics data taking, Et trigger signal by the calorimeter is basically used in triggering physics events with "online-veto," or anti-coicidence of Et trigger signals by veto detectors. Information of events with the Level 1 accept is sent to the "Level 2 trigger" system via optical links. Here, event information is once stored in its temporary memory and further trigger decision is made using waveform of 64 or 256 samples. In the physics run, Center Of Energy (COE) of the calorimeter is calculated with energy information of each crystal and used for the Level 2 trigger decision. Since COE positions of $K_L \to \pi^0\nu\bar{\nu}$ events are expected to deviated from the center of the calorimeter due to large transverse momentum of the decay π^0 this value is useful to discriminate the $K_L \to 3\pi^0$, $K_L \to 2\pi^0$ or $K_L \to 2\gamma$ decays which give COE positions close to the center. Detail of the COE trigger is described in Sec. 3.3.1. Events which pass the Level 2 trigger are transferred and stored

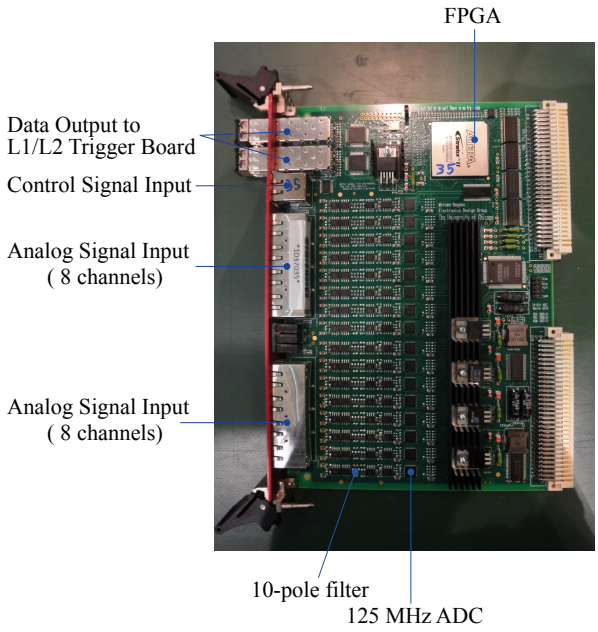

Figure 2.29: Photograph of a 125-MHz-sampling ADC module. Quoted from Ref. [64].

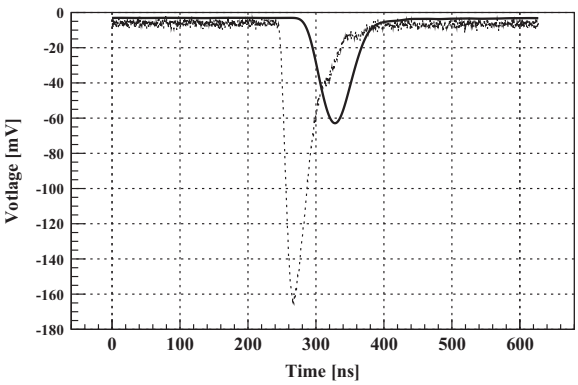

Figure 2.30: Waveform shaping in 125-MHz ADCs in a simulation. Points show an input pulse and the solid line is a waveform after shaping with the 10-pole filter, obtained by circuit simulation. Quoted from Ref. [64].

in the buffer memory of the Level 2 trigger system. They are sent to the storage of the PC farm every spill via 1 Gbps Ethernet and stored after compression. The maximum number of events to be stored in the Level 2 buffer memory is 8192 events per spill in the May 2013 run. The stored data in the PC farm are transferred to the storage in KEK Central Computing System (KEKCC) for offline analysis.

Chapter 3

Data Taking

This chapter describes the condition of data taking in the KOTO first physics run in May, 2013.

3.1 Overview

Construction of all the KOTO detector system, including the downstream detectors located outside the vacuum tank, was finished in the middle of April, 2013 and the KOTO experiment conducted the first physics run. The data set used in this thesis was collected during 19 May - 23 May, 2013, which corresponds to a period of 100 hours. Unfortunately, the data taking was terminated due to the radiation leakage accident in the Hadron Experimental Facility [98], although the run was originally planned to continue by the end of the next month. In the following sections, detail of various experimental conditions in the May run is described.

3.1.1 Accelerator Condition

The beam power in the MR accelerator was 23.8kW, which corresponds to 3×10^{13} P. O. T. for every beam extraction with repetition rate of 6 s. The intensity of the extracted beam from MR is monitored with the two kinds of devices. The Switch Yard Intensity Monitor (SYIM) monitors intensity of the extracted beam itself by counting the number of scattered particles at vacuum windows. The yields of secondary particles from the target are monitored by the Target Monitor (TMon), which consists of a series of plastic scintillators and is located in 50° direction with respect to the primary beam line as shown in Fig. 3.1. Figure 3.2 shows measured SYIM and TMon counts per spill as a function of time during the data taking period. Blank regions correspond to the accelerator maintenance period. The beam power slightly increased after this beam break.

3.1.2 Environment

Vacuum level is separately monitored for the detector region and the decay region. The vacuum level in the detector region is critical for stable operation of PMTs since insufficient evacuation can cause discharge in PMTs. In the physics run, it was maintained to be less than 0.1 Pa. The vacuum in the decay region directly affected background of this experiment as described in Sec. 2.2.7 and was kept at around 5×10^{-5} Pa.

Temperature of various detector components was monitored with thermocouples in order to confirm stable operation of detector systems. An example of temperature monitor for the calorimeter

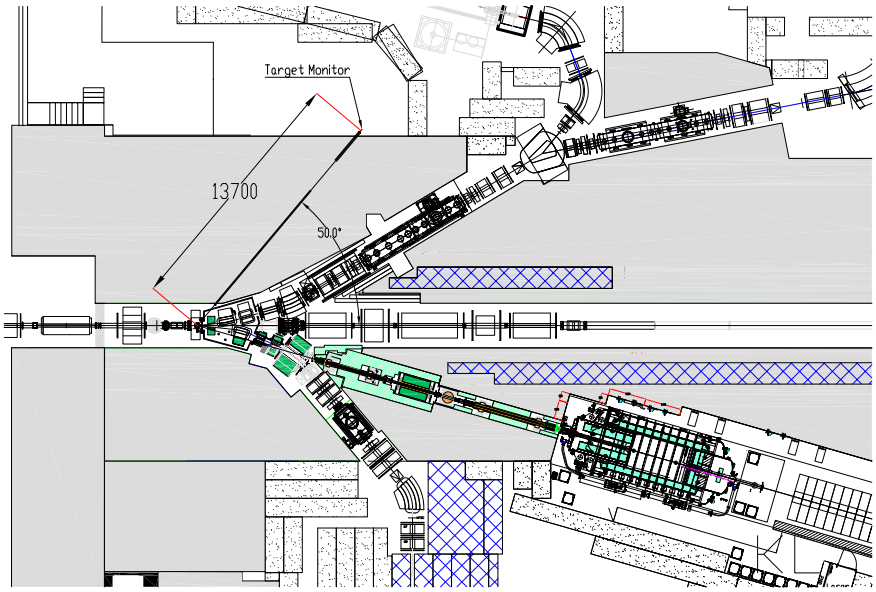

Figure 3.1: Position of the Target Monitor. Prepared by H. Watanabe.

is shown in Fig. 3.3. Temperature stability is critical especially for performance of the calorimeter since outputs from a CsI crystal were known to have a slight temperature dependence of -1.4%/°C [16]. As shown in Fig. 3.3, temperature for all measurement positions was found to be stable within 0.1 C° level.

3.2 Detector Condition

3.2.1 Dead channels

There existed several dead channels where any signals were not observed, although they were not critical in the analysis of the $K_L \to \pi^0\nu\overline{\nu}$ search. Two channels were in the calorimeter, two in CV and one in CC03. These are summarized in Fig. 3.4. Positions of modules with the dead channels are shown with colored lines for each detector. Although information of these two dead channels in the calorimeter was completely unavailable, simulation studies showed decrease of signal acceptance and increase of $K_L \to 2\pi^0$ background was not large, as described in App. B. Energy deposit of these two channels were treated to be zero in the Monte Carlo simulation described in Chap. 5 so that effects of dead channels were properly considered in estimation of both signal acceptance and background.

Both the two channels in CV were located in the rear plane. They shared the same signal cable and it was guessed that there were some troubles in the cable such as disconnection or break inside the vacuum tank. In these modules, particles were detected with single-end readout. Increase of inefficiency due to lack of information was found to be smaller than requirement even with single side readout from a study based on data taken prior to the physics run [82, 83, 84]. More on this study and effects of these dead channels are in App. B.

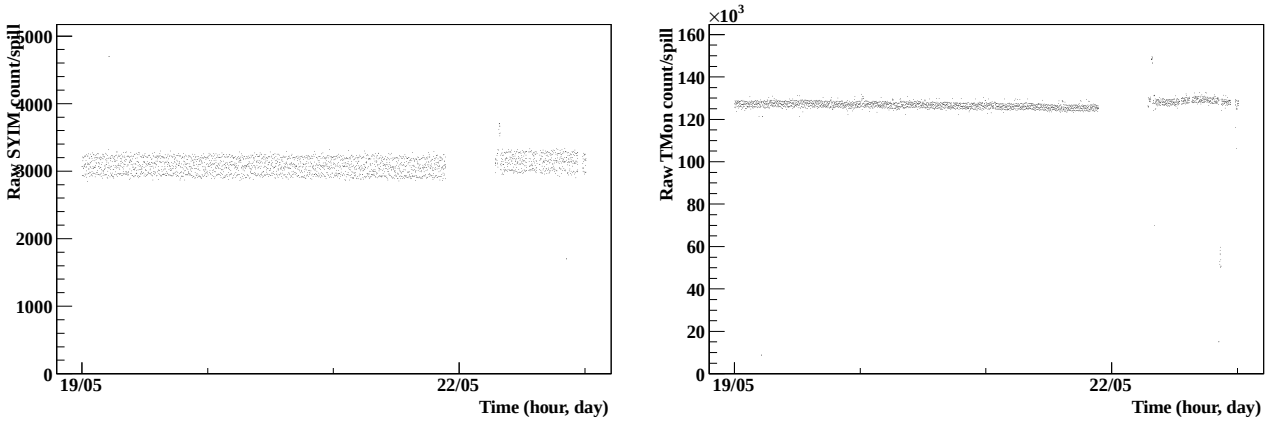

Figure 3.2: Beam stability monitored with SYIM (left) and TMon (right).

The one dead channel in CC03 was due to a broken PMT. Since each CC03 CsI crystal is read by two PMTs and the partner PMT was alive, information of the corresponding crystal was not completely lost hence no dead crystals exists.

3.3 Trigger Condition

Data taking was performed with various trigger conditions,

for corresponding purposes Events with various trigger conditions were collected simultaneously in order to obtain data for normalization, calibration or other purposes as well as the main analysis of the $K_L \to \pi^0\nu\overline{\nu}$ search. The maximum number of events to be taken in a spill, around 8 k events, was shared among these triggers by adjusting energy threshold and prescale factors. Below, detailed condition for each trigger is described.

3.3.1 Physics Trigger

This was the main trigger to collect $K_L \to \pi^0\nu\overline{\nu}$ events and designed to take as many events as possible with the minimum losses of signal acceptance. As the Level 1 trigger, an Et trigger signal from the calorimeter and online-veto by MB, CV, NCC and CC03 were required. Event were rejected by this trigger when Et signals from at least one of these four veto detectors were issued at the same time as Et trigger timing of the calorimeter. The veto energy thresholds for each trigger are summarized in Table 3.1. The event rate with the calorimeter Et information was ∼258 k per spill and this was reduced to ∼27 k per spill with the online-veto. Trigger selection with an "online-Center-Of-Energy (COE)" value was then applied as the Level 2 trigger decision. An online-COE value is given as

$$\frac{\sqrt{\left(\sum E_i x_i\right)^2 + \left(\sum E_i y_i\right)^2}}{\sum E_i}, \tag{3.1}$$

where E_i, x_i and y_i are energy, x and y positions for the i-th crystal. Here, an energy value for a channel was obtained from ADC counts of 64 samples and the crystal positions were given for each channel in advance. Since the majority of neutral K_L decay events, such as $K_L \to 3\pi^0$, gives a

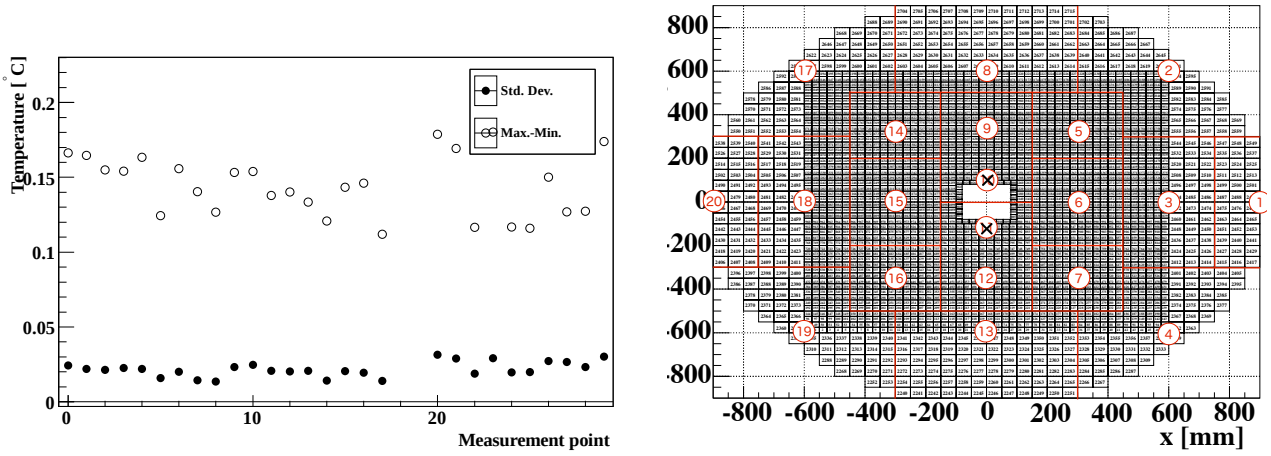

Figure 3.3: Monitored temperature of the calorimeter. In the left figure, the open circles indicate difference of the maximum and the minimum measured temperature over the measurement period and the closed circles indicate standard deviation. Measurement position numbers are illustrated in the right figure. The right figure was quoted from Ref. [64].

Table 3.1: Online veto threshold.

Detector	Energy threshold
calorimeter	550 MeV
MB	50 MeV
CV	1 MeV
NCC	60 MeV
CC03	60 MeV
COE	165 mm

small COE value or balanced energy deposition on the calorimeter in the xy plane while large energy imbalance is required for signal events as a result of the P_{T} requirement, this cut can effectively reduce the trigger rate without losing signal efficiency. As shown in Table 3.1, the online-COE value was required to be larger than 165 mm and finally the event rate was reduced to ∼8 k events per spill.

3.3.2 Normalization Trigger

In this trigger, the online-COE cut was removed from the physics trigger described above. By this trigger, $K_L \to 3\pi^0$, $K_L \to 2\pi^0$ and $K_L \to 2\gamma$ events are collected, which is used for normalization as described in Sec. 7.3. Prescale of 30 was applied and approximately 700 events were collected every spill.

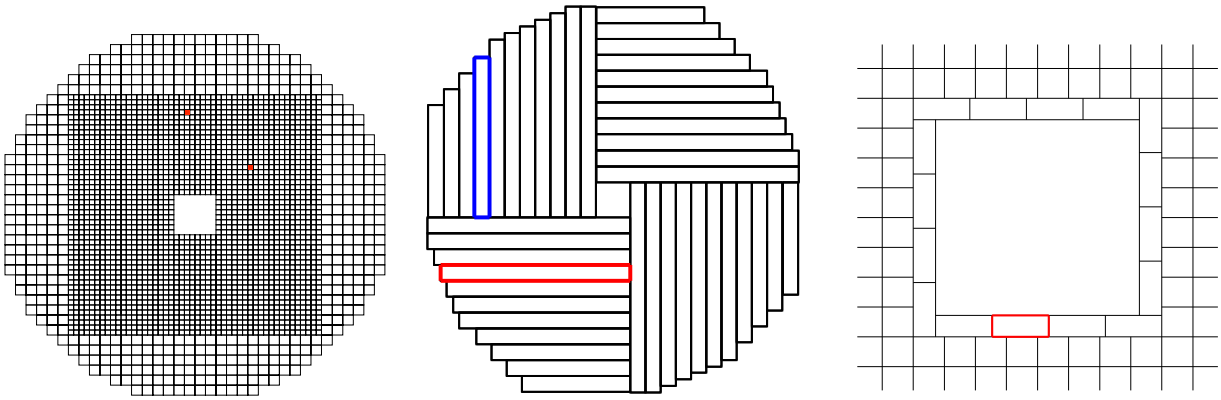

Figure 3.4: Positions of modules with the dead channel. The left, middle and right figures are for the calorimeter, CV and CC03, respectively. Each detector was seen from the upstream direction and modules with dead channels are shown with red or blue. As for CV, the red (blue) color shows readout of short-fiber (long-fiber) side was not available.

3.3.3 Minimum Bias Trigger

In this trigger, the decision was made only by Et trigger of the calorimeter without any online veto. Prescale of 300 was applied and approximately 700 events were collected every spill.

3.3.4 $3\pi^0$ Calibration Trigger

This trigger was used to collect $K_L \to 3\pi^0$ data for calibration of the calorimeter, which is described in App. C. Six photons are emitted in the $K_L \to 3\pi^0$ decay and six hit clusters are detected when all six photons hit the calorimeter. Since no other K_L decays generate as many as six photons, $K_L \to 3\pi^0$ events are effectively collected by counting the number of clusters For this purpose, the "region counting method" was used in addition to the conditions of the normalization trigger. In the region counting, the calorimeter was segmented into twelve regions as shown in Fig. 3.5 and trigger decision was made when hits in four or more regions were recorded. An Et signal was calculated for all the channels in each region and a hit in a region was identified with the Et signal larger than 120 MeV. Prescale of 10 was applied and approximately 300 events were collected for every spill.

3.3.5 External Triggers

The following five kinds of additional triggers were implemented as external triggers:

Clock trigger Events were triggered by 10 Hz periodic clock signal to take random trigger data for evaluation of noise and counting rates in beam periods.

LASER trigger The laser for the calorimeter calibration was flashed with frequency of 5 Hz and events were triggered synchronized with this timing.

LED trigger Another 10 Hz clock was used for a trigger, which flashed all the LEDs installed in veto detectors. Data taken with this trigger were used for evaluation of timing and gain stability for the detectors. This trigger as well as the clock trigger is essential for ADC calibration and stability evaluation of the BHPV detector as described in Secs. 6.2 and 6.3.1.

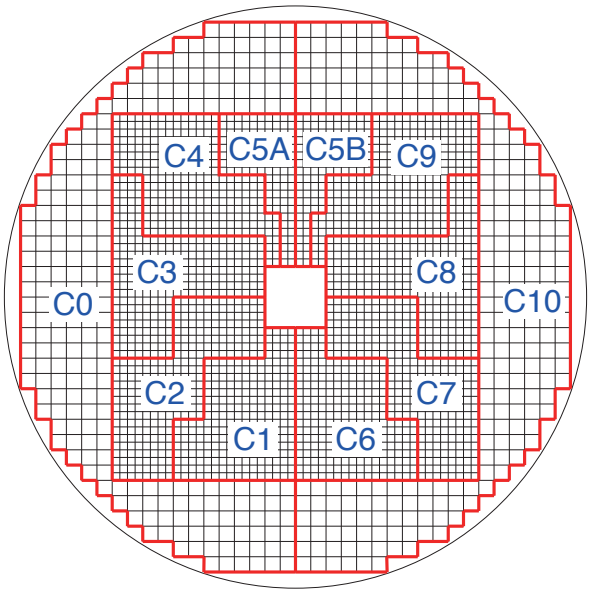

Figure 3.5: Segmentation used in the region counting trigger. Quoted from Ref [64].

TMon trigger Signals from the target monitor (TMon) were inputted with proper prescaling. Approximately 100 events were triggered every spill. Data taken with this trigger were used to evaluate accidental hits.

Cosmic ray trigger Dedicated trigger counters for cosmic rays events were placed at the top and bottom of the vacuum tank around the calorimeter and the upstream part of FB. The trigger signal was formed by coincidence of hits in both top and bottom counters for each region.

3.3.6 Cosmic Ray Trigger during Off-Spill Timing

For continuous monitoring of detector stability, cosmic ray data were collected in the off-spill timing in addition to that by "cosmic ray trigger" in the above. NCC, OEV and the calorimeter were used as sources of this trigger. The same trigger scheme with the Et trigger as the physics trigger was used for the calorimeter. In case of NCC, Et trigger with the same threshold for the online-veto was used as a trigger[*1]. As for OEV, the number of hit modules was required to be two or more. The numbers of collected events per spill were approximately 50, 50 and 150 for NCC, OEV and the calorimeter, respectively.

3.3.7 Dead time in the physics run

There existed 17% dead time due to data management of the Level 2 trigger system, which mainly came from the data transfer speed inside the Level 2 trigger system, from the temporary memory to the buffer memory. Since all events of any trigger types were processed through the Level 2

[*1] Unable to set different threshold due to specification of the trigger system.

trigger system, this loss was common for events from all the trigger types regardless of whether any selections were applied or not.

3.4 Special Runs for Calibration

In addition to the physics run, some special runs were performed mainly for calibration of detectors.

3.4.1 Beam Muon Run

In this run, the "beam plug" described in Sec. 2.2.4 was closed. Most of beam particles were stopped by the beam plug and detector counting rates decreased. In this condition, penetrating charged particles were triggered with coincidence of two detectors. These data were used mainly for calibration of beam hole detectors, where cosmic ray data were not available for in-situ calibration due to their geometry. Timing calibration and evaluation of aerogel light yields for BHPV were performed using data taken with this trigger as described in Secs. 6.2.3 in 6.2.2. Events were triggered by an Et signal of BHCV and a hit in plastic scintillator detector located behind BHPV, were required in offline analysis. The threshold of the BHCV Et trigger corresponded to approximately 40 keV or 80 keV, depending on runs.

This run was also useful to collect events of charged particle penetration for detectors around the beam, namely collar counters and channels close to the beam in the calorimeter and CV. For this purpose, events were triggered by coincidence of NCC and downstream collar counters.

In order to monitor stability of these detectors regularly, this run was performed every two days.

3.4.2 Aluminum Target Run

In this run, an aluminum plate with 5 mm in thickness and 100 mm in diameter was inserted into the beam core at the downstream of FB as shown in Fig. 3.6. This run had two purposes. One was calibration of the absolute energy scale of the calorimeter, where two photon clusters from π^0s generated in the target due to interactions of beam neutrons were detected and reconstructed. Since the z position of the target and thus the π^0 generation position was known, π^0 mass was reconstructed using Eq. (2.1). Conversely, with the nominal π^0 mass given, it was possible to correct measured energies of these photons. In the physics run, this data was used to correct the absolute energy scale of the calorimeter energy calibration and detail is described in App. C.

The other purpose was the estimation of background due to "hadron cluster events," which is described in Sec. 7.4.8.

3.4.3 Cosmic Muon Run

During the accelerator maintenance period before and after the beam time, cosmic muon data was collected. Events were triggered by Et signals of MB and the calorimeter as well as those of NCC and downstream collar counters. External triggers, mainly clock, laser and LED triggers were also implemented. These events were used for detector calibration and evaluation of their stability.

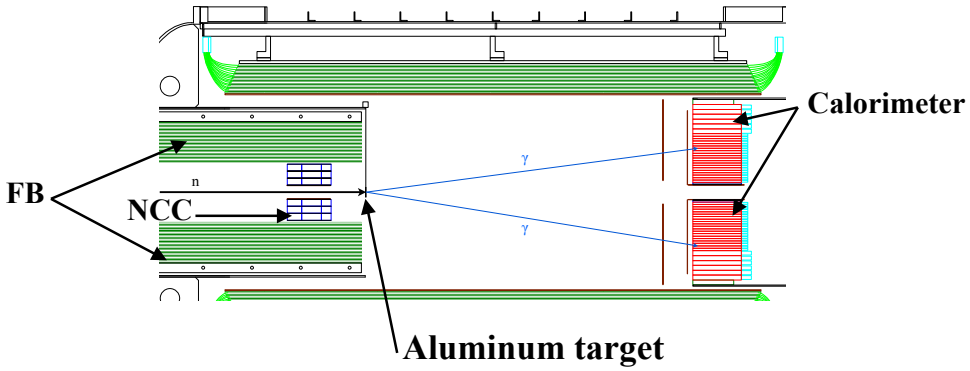

Figure 3.6: Position of the aluminum target. Quoted from Ref. [64].

Chapter 4

Event Reconstruction

The methods to extract physical quantities from the obtained data are explained in this chapter.

4.1 Overview

As described in Chaps. 2 and 3, data for each channel was recorded as waveforms of 125-MHz or 500-MHz sampling. Digitized values of the voltage information, which was called "ADC count," were recorded every 8 or 2 ns. Event reconstruction processes began from energy and timing extraction from waveform information. π^0 was then reconstructed from these information of the calorimeter. Veto decision was made based on waveform of all the veto detectors together with reconstructed π^0 vertex position and timing. In calculating energy and timing of veto detectors, methods of timing reconstruction were critical for background rejection. When multi hits exists in a single waveform, a hit can be missed due to wrong timing calculation, which gives additional inefficiency of the detector. For this reason, a method of timing calculation, which was robust for pulse pileups, was introduced.

In the following sections, energy and timing calculation methods are first explained for each case of detectors whose signals are read with the 125-MHz and 500-MHz ADC in Sec. 4.2 and event reconstruction procedures based on these energies and timings follows.

4.2 Energy and timing extraction from waveform

4.2.1 Detectors with 125-MHz ADCs

The waveform data for each channel taken with the 125-MHz ADC consists of 64 sampling points for each event. Single energy and timing values were extracted from the waveform data for each channel with the following procedures.

Pedestal definition
Baseline of waveform, called pedestal below, was first defined. Averaged values and standard deviations of the first and the last five samples were calculated and the averaged value with the smaller standard deviation was used. The pedestal value was subtracted from each of 64 samples.

Energy

Energy was defined as an integral of all 64 samples after subtracting pedestal, multiplied with a calibration constant in order to convert it into energy. Calibration constants were obtained for channel by channel using cosmic or beam muon data. Overview of the analysis for major detectors is described in App. C.

Timing

As mentioned in Sec. 4.1, timing information is critical particularly in veto decision. Two kinds of timing calculation methods were used. One is the "constant fraction method," where timing is calculated based on a rising edge of a pulse. Timing fluctuation due to different pulse heights is small and a good timing resolution is obtained. Hence this method was used as a primary way to define timing in the KOTO experiment. The other is the "parabola fitting method," which was newly introduced in order to handle pulse pileups in the physics run. Timing is determined based on points around the peak of a pulse and this method is robust for pileups of multiple pulses.

An example of timing calculation by the constant fraction method is illustrated in the left of Fig. 4.1. The largest ADC count in a 64-sample event window is regarded as the peak of the pulse and the timing is defined as interpolation of the sample numbers into the half-peak-height in the rising edge.

The calculation procedure for timing with the parabola fitting method is shown in the right of Fig. 4.1. In this process, 64-sample waveform information is smoothed by taking the moving average in order to avoid regarding local fluctuation due to noise as a peak. Peaks in a 64-sample event window are then searched as local maximum points above the threshold and one whose timing was closest to the "nominal timing" is chosen. The threshold and the nominal timing are given detector by detector. These values are described in App. D. Three samples of the selected peak, the maximum point and its neighboring ones in both sides, are fitted with a parabola function

$$A(t - B)^2 + C, \tag{4.1}$$

where parameters A, B and C are calculated analytically. The peak timing, represented by the parameter B is used as timing of the channel. Detailed procedures of calculation of parabola fit timing in App. D.

For timing obtained with both methods, difference of timing offsets among channels was finally corrected by adding what was called a timing calibration constant. Procedures to obtain timing calibration constants for several detectors are given in App. C.

The constant fraction timing gave better timing resolution, but the timing with this definition was easily affected by pulse overlapping. Wrong timing calculation as shown in Fig. 4.2 would give inefficiency. On the other hand, proper timing is obtained when the parabola fitting method is used[*1]. The veto detectors require information of both energy and timing in veto decision and such wrong timing is critical in reducing background events. The constant fraction method was used for timing calculation of the calorimeter, since the calorimeter is less affected by event pileups thanks to the high granularity and better timing resolution is desirable in π^0 reconstruction. On the other hand, pulse pileups are more serious in veto detectors with lower granularity. Hence the parabola fit time was used in all the other detectors with 125-MHz ADC readout.

[*1] More sophisticated methods are available to distinguish overlapping pulses such as the template fitting methods studied in Refs. [89, 90] or Ref. [99]. Although these methods needs longer CPU time, the parabola fitting method has an advantage to save time of calculation thanks to availability of analytic calculation.

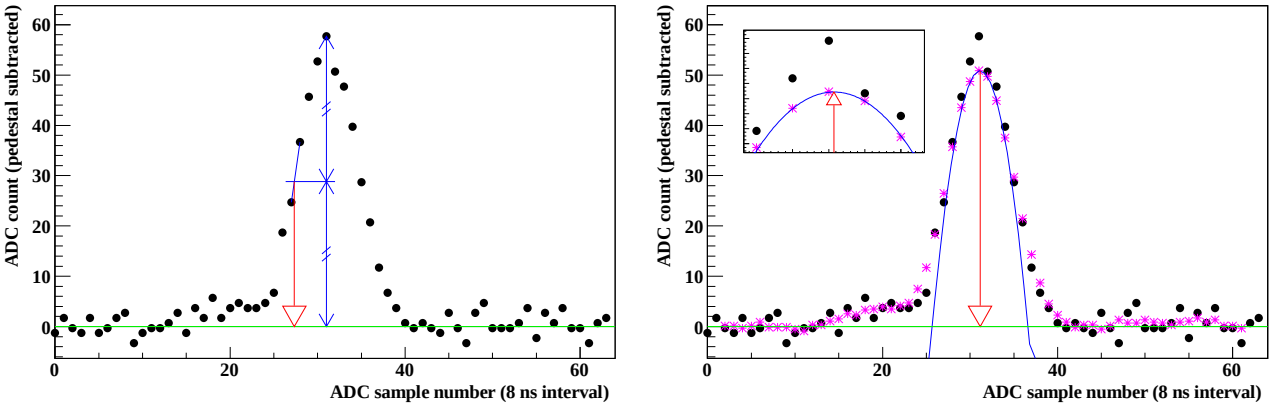

Figure 4.1: Definition of the constant fraction timing (left) and parabola fit timing (right). Black points are waveform data. Green lines and red arrows represent the pedestal and the defined timing, respectively. In the right figure, purple points shows the waveform after taking moving average. and the blue curve is the parabola function obtained by fitting the three points around the peak. A zoomed view around the peak is also drawn in the left top corner. The data points were taken from a certain channel of the CsI calorimeter in the physics data and common in both figures. An integral of the waveform corresponds to ∼6 MeV energy deposit.

4.2.2 Detectors with 500-MHz ADCs

As described in Sec. 2.2.8, data from the BHCV and BHPV detectors is recorded as 256-sample waveform with 500-MHz ADC in order to handle high counting rates. Since probability to have two or more pulses in an event window is not negligible, multiple hits are distinguished one by one and energy and timing values for each hit are recorded. This scheme is also important in order to avoid regarding off-timing hits caused due to high counting rates as a true hit reduce to issue unnecessary veto signals.

Pedestal definition
Pedestal is defined as the most probable ADC count among 256 samples in each event and each channel by fitting a histogram of ADC values of 256 samples with a Gaussian.

Pulse identification
As in the timing calculation for data taken with 125-MHz ADCs, peaks were searched for from 256 samples data with the pedestal subtracted in order to identify multiple hits in a single event window. Local maxima exceeding the given threshold, 10 (30) ADC counts for BHPV (BHCV), were regarded as peaks. Detail of this process is in App. D.

Energy and timing
For each peak found in the process above, energy and timing values are assigned and recorded as well as the number of peaks in the event window. Energy is calculated as an integral of 15 (25) samples around the sample identified as a peak for BHPV (BHCV). The integral value is then multiplied

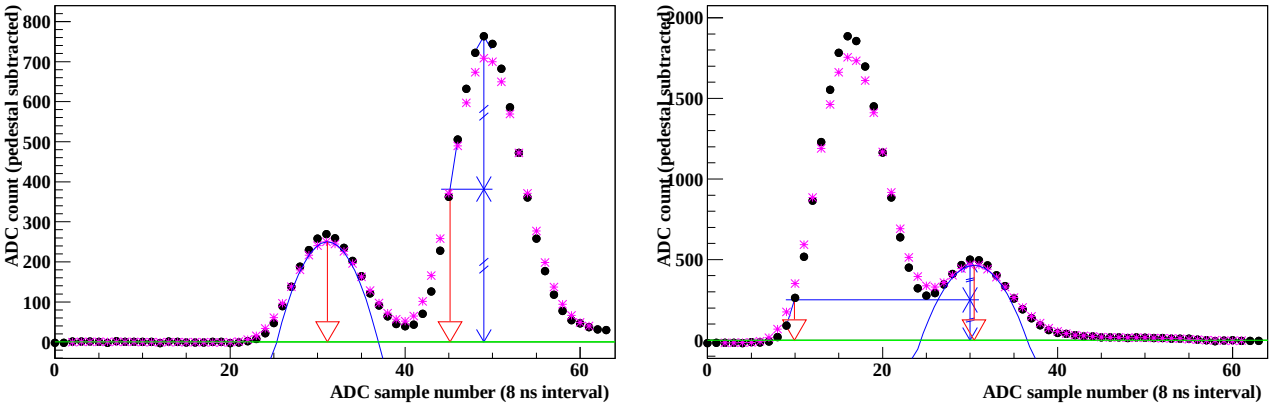

Figure 4.2: Examples of wrong timing calculation with the constant fraction method. The red arrows with (without) a parabola curve indicate timing obtained by the parabola fitting (constant fraction) method. The pulse to be detected is located around the ∼30th sample. In the left panel, an accidental hit with larger pulse height exists. In this case, the constant fraction timing is obtained as indicated by the right red arrow since timing is calculated based on the largest peak in 64 samples. This kind of mistake is reduced by limiting a peak search range. In the right panel, such a hit exists in more closer timing to the nominal hit. Although limitation of peak search timing is applied, the constant fraction timing is calculated based on the earlier pulse. Even in this case, timing with the parabola fitting is still stable.

with an energy calibration constant to have the number of photoelectrons or energy deposit in units of MeV. Timing of each peak is calculated with the constant fraction method and corrected with a timing calibration constant, as is described in the previous section.

Examples of multiple-hits identification for BHCV and BHPV are shown in Fig. 4.3.

4.3 Event reconstruction with the calorimeter

When a high energy photon hit a dense material, an electromagnetic shower is created and the shower particles spread out with respect to the incident point of the photon. The typical transverse size of the shower is called Molière radius, and 3.57 cm[16] in case of CsI crystal. This is larger than the size of each crystal hence there should be hits in several crystals. This group of hit crystals is called a "cluster." Clusters with large total energy are regarded as signals of photon incidence and used for π^0 or K_L reconstruction. Below, overview of the clustering procedures and incident photon reconstruction are explained. Detailed description is found in Ref. [64].

4.3.1 Clustering

First, hit crystals are identified by requiring at least 3 MeV energy deposit for each channel and they are called "cluster seed crystals." In the following processes, crystals with energy deposit smaller than 3 MeV are not used at all. Then, one seed crystal is arbitrarily chosen and other seed crystals are searched for around the first crystal. When such a crystal is found, the new crystal is made

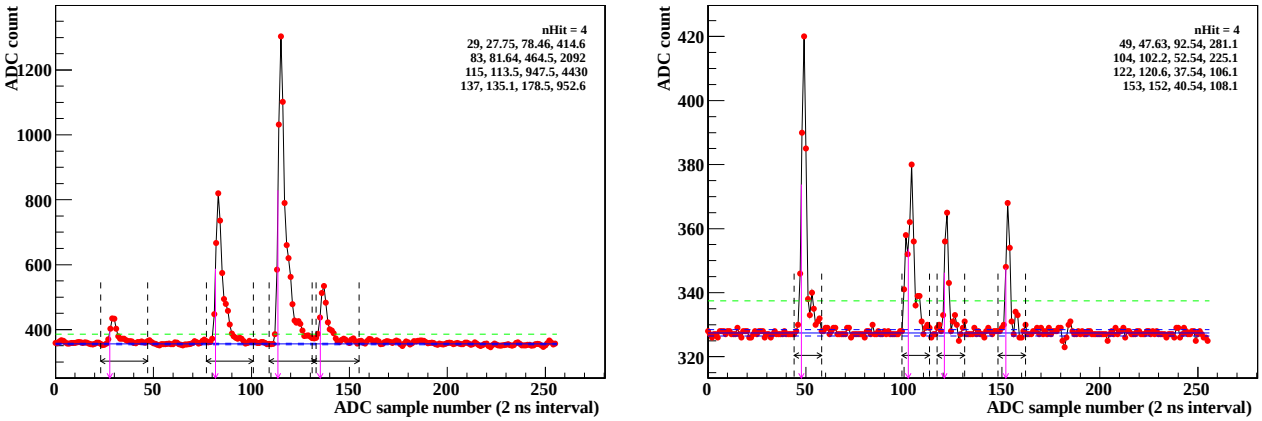

Figure 4.3: Examples of energy and timing extraction from waveforms with 500-MHz sampling. The left (right) figure is for BHCV (BHPV). The solid and dashed blue lines indicate pedestal and its 1σ region, respectively. The green dashed lines show the threshold required in search of pulses. The purple and black arrows show timing and integration range to get energy for each identified pulse, respectively. Difference between BHCV and BHPV is the pulse height threshold and the length of integration.

to join the same group, or cluster, with the first crystal. This process is repeated until no other seed crystals around each one in the cluster are found. Energy, position and timing of the cluster is then calculated as the total energy deposit of all the crystals in the cluster, the center of energy and weighted average time, respectively.

When there remain seed crystals which do not join the first cluster, one seed crystal is chosen among such crystals and the same processes are repeated so that all the seed crystals belong to any clusters. If a cluster consists of a single crystal after the whole processes above, it is called an "isolated hit crystal" and not used in event reconstruction but only for veto as described in Sec. 4.3.5. Below, in referring to a cluster, it is regarded to contain two or more crystals.

4.3.2 Photon cluster selection

In reconstructing a π^0 by assuming $\pi \to 2\gamma$ decay or K_L with the $K_L \to 2\gamma$, $K_L \to 2\pi \to 4\gamma$ and $K_L \to 3\pi \to 6\gamma$ decays, clusters in the calorimeter were considered to be formed by photons' incidence from the features of simultaneous multiple hits in the calorimeter and veto of charged particles by the CV detector, which was applied in the following analysis for many cases. Among identified clusters, one with its total energy larger than 20 MeV was called a "photon cluster" and only these photon clusters were used in the following reconstruction processes. When N photons are required in reconstructing events, only events with $N' \geq N$ are selected and analyzed, where N' is the number of photon clusters for an event. In case that $N' > N$, the combination of N photon clusters whose timing difference is the minimum is used in the reconstruction process. In analysis of the $K_L \to \pi^0\nu\overline{\nu}$ decay or $K_L \to 2\gamma$, $N = 2$ and $N = 4$ or $N = 6$ for reconstruction of $K_L \to 2\pi^0$ or $K_L \to 3\pi^0$ decays, respectively. $N = 5$ was for analysis of the BHPV performance evaluation

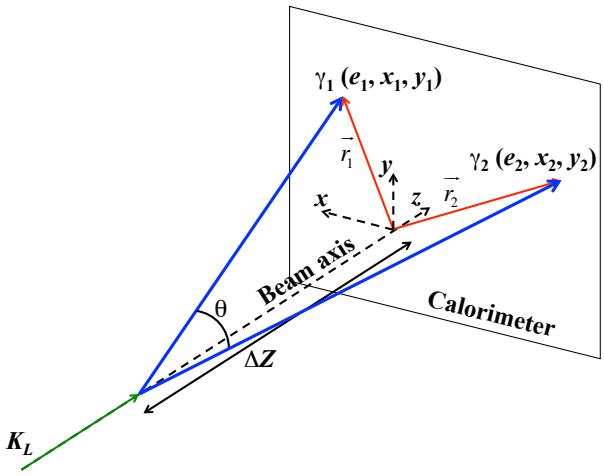

Figure 4.4: Illustration of the π^0 reconstruction.

described in Chap. 6. Photon clusters which are not used in reconstruction and clusters which are not regarded as photon clusters are treated as "extra clusters" and used for veto as described in Sec. 4.3.5.

4.3.3 π^0 reconstruction with energy and position correction

As already described in Sec. 2.1.2, π^0 is reconstructed from any pair of photon clusters on the calorimeter assuming their invariant mass is equal to the nominal π^0 mass (M_{π^0}) and x, y vertex position of the parent π^0 to be zero. Below, energy and photon hit xy position on the calorimeter surface are denoted as e_i, x_i and y_i, respectively as show in Fig. 4.4. An opening angle of the two photons, θ, is calculated as

$$\cos\theta = 1 - \frac{M_{\pi^0}^2}{2e_1e_2}. \tag{4.2}$$

Using this angle and with the assumption of zero xy vertex position, the z vertex position, written as $Z_{\rm vtx}$, is calculated from the following equations:

$$(1-\cos^2\theta)(\Delta Z)^4 + (2\vec{r_1}\cdot\vec{r_2} - (r_1^2+r_2^2)\cos^2\theta)(\Delta Z)^2 + (\vec{r_1}\cdot\vec{r_2})^2 - r_1^2r_2^2\cos^2\theta = 0, \tag{4.3}$$

$$Z_{\rm vtx} = Z_{\rm CsI} - \Delta Z, \tag{4.4}$$

where Eq. (4.3) is derived from the Law of Cosine on the triangle made of two photon tracks. $\vec{r_i}(i=1,2)$ are two-dimensional vectors for the i-th photon hit position on the calorimeter surface and given as $\vec{r_i} = (x_i, y_i)$, and $r_i = |\vec{r_i}|$. Notation of other variables follows Fig. 4.4. This equation is a quadratic equation of $(\Delta Z)^2$, and two solution for $Z_{\rm vtx}$ are possible when both of two solutions of $(\Delta Z)^2$ were real numbers and positive. In case of two photon analysis, events with such two solutions in Eq. (4.3) are discarded.

Once the z vertex position is obtained, incident angle of each photon is calculated. Correction is then applied for energy and position of each photon cluster using this angle. The z vertex position is again calculated with the same procedures for the updated photon cluster information. Other variables to be used in the following event selection are calculated using this value; Transverse

momentum of the reconstructed π^0, written as $P_{\rm T}$, is calculated from the vector sum of transverse momentum for each photons as follows:

$$P_{\rm T} = \left| \sum_{i=1,2} e_i \frac{\vec{r_i}}{\sqrt{r_i^2 + (\Delta Z)^2}} \right|. \tag{4.5}$$

Vertex time for i-th photon cluster, $t^i_{\rm vtx}$, is calculated by using distance between the vertex position and the photon hit position at the calorimeter surface as

$$t^i_{\rm vtx} = t_i - \frac{\sqrt{r_i^2 + (\Delta Z)^2}}{c}, \tag{4.6}$$

where t_i is timing of the i-th photon cluster and c is the speed of light. The event vertex time $T_{\rm vtx}$ is given as a weighted average of the above vertex time and for N photon case, it is calculated as

$$T_{\rm vtx} = \sum_{i=1}^{N} \frac{t^i_{\rm vtx}/\sigma_{\rm t}(e_i)^2}{\sum_{j=1}^{N} 1/\sigma_{\rm t}(e_j)^2}, \tag{4.7}$$

where $\sigma_{\rm t}(e_i)$ is resolution for each vertex time and given as a function of energy for the photon cluster and given as

$$\sigma_{\rm t}(e) = \frac{3.8}{\sqrt{e}} \oplus 0.19, \tag{4.8}$$

where e is given in units of MeV and that of the resultant value is ns.

The $K_L \to 2\gamma$ decay is also reconstructed with the same way above. In this case, the mass of K_L is assumed instead of M_{π^0} and other processes are identical.

4.3.4 K_L reconstruction

In the analysis of normalization modes, the $K_L \to 3\pi^0$ and $K_L \to 2\pi^0$ decay, K_L is reconstructed from six or four clusters on the calorimeter, assuming these clusters came from photons from the $K_L \to 3\pi^0$ or $K_L \to 2\pi^0$ decay, respectively. For N photon clusters ($N = 4, 6$), $(\Pi_{i=0}^{N/2-1} \binom{N-2i}{2})/(N/2)! = 3(15)$ possible combinations to form two (three) π^0s in $K_L \to 2\pi^0$ ($K_L \to 3\pi^0$) reconstruction. z vertex position for each pair of photons is calculated with Eq. (4.3) and the event z vertex $Z_{\rm vtx}$ is obtained as a weighted average in each combination:

$$Z_{\rm vtx} = \sum_{i=1}^{N/2} \frac{Z_i/\sigma_i^2}{\sum_j^{N/2} 1/\sigma_j^2}, \tag{4.9}$$

where Z_i is reconstructed π^0 z vertex for the i-th pair of photons and σ_i is its resolution given as a function of energies of the two photons clusters. To evaluate agreement of these $N/2$ z vertices, the following the z-vertex χ^2_z is defined for each combination:

$$\chi^2_z = \sum_{i=1}^{N/2} \frac{(Z_i - \bar{Z})^2}{\sigma_i^2}. \tag{4.10}$$

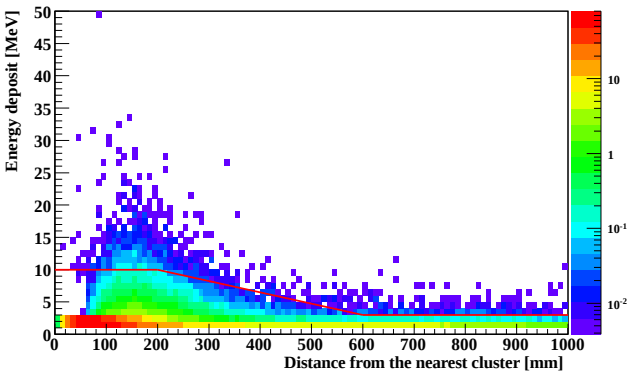

Figure 4.5: Distribution of energy and distance from the nearest cluster of isolated hit crystals in $K_L \to \pi^0\nu\overline{\nu}$ simulation. The red line indicates distance-dependent energy threshold and an event would be rejected when any isolated crystal was above this line.

Among the possible combinations, one with the minimum χ^2_z is selected as the correct pairing of N photons. Zero xy vertex positions are then modified to have finite values by interpolating center of energy x or y positions on the calorimeter to z position given by $Z_{\rm vtx}$ assuming the target to be a point source. Energy and position corrections described in Sec. 4.3.3 with the updated vertex for this combination are then applied, and again K_L is reconstructed using modified photon cluster information. The final photon pairing, χ^2_z and xyz vertex position are determined as a result of the second reconstruction. The following timing calculation for each photon and the vertex is the same with Sec. 4.3.3.

4.3.5 Veto cuts based on the calorimeter information

As already mentioned, extra clusters and isolated hit crystals are used for veto. The extra cluster veto means to reject events with extra clusters whose vertex time corresponding is within 10 ns from the event vertex time. In the veto by isolated hit crystals, events with such a crystal with energy deposit larger than a given threshold, which depends on distance to the nearest cluster, denoted as l, are rejected when its hit time was within 10 ns from that of the nearest cluster. The threshold is set to be looser for smaller l since isolated hit crystals with small energy deposit were often produced close to the main cluster for a single photon incidence and events are overkilled with tight threshold in such a region. The actual threshold values are then given as follows and also illustrated in Fig. 4.5:

$$10 \text{ MeV}, \qquad l \leq 200 \text{ mm} \tag{4.11}$$

$$(13.5 - 0.0175l) \text{ MeV}, \quad 200 < l \leq 600 \text{ mm} \tag{4.12}$$

$$3 \text{ MeV}, \qquad l > 600 \text{ mm}. \tag{4.13}$$

4.4 Reconstruction of veto information

Decision of anti-coincidence by each veto detector was basically made with the maximum energy deposit among "modules" of the detector system whose hit timing was inside the veto window

given detector by detector. Here, information of a "module" for detectors with single-side readout corresponds to energy deposit and timing of each channel. As for detectors with dual readouts, information from outputs of both channels was combined for each unit of these detectors. Such methods for each detector are explained in Sec. 4.4.1. General procedures to obtain "veto energy" and "veto timing" are then described in Sec. 4.4.2. Different methods are employed for the BHPV detector, which are separately presented in the last of this section.

4.4.1 Module information for dual readout detectors

MB and BCV

Scintillation light is read from two side via wavelength shifting fibers in the MB and BCV detectors and finite time of light propagation should be considered. Suppose the z positions of the two readouts are z_0 and z_1, and the effective light propagation speed is v, which is described in Sec. 5.4.1, detection timing of light generated at the position of z ($z_0 < z < z_1$) at timing of $t = 0$ is given as $t_0 = (z - z_0)/v$ and $t_1 = (z_1 - z)/v$ for each readout, respectively. Hence the average timing of both channels in a module is used as the module timing since this gives a constant timing of

$$\frac{t_0 + t_1}{2} = \frac{z_1 - z_0}{v}, \tag{4.14}$$

which is independent of the hit position. The module energy is given as a sum of energies in both sides with correction of the z position dependence. The hit z position z_{rec} is obtained by taking timing difference in the two channels,

$$t_0 - t_1 = \left(\frac{z - z_0}{v}\right) - \left(\frac{z_1 - z}{v}\right) = 2\frac{z}{v} - \frac{z_0 + z_1}{v}, \tag{4.15}$$

and defined as

$$z_{\mathrm{rec}} = \frac{v}{2}(t_0 - t_1), \tag{4.16}$$

where $\Delta z_{\mathrm{rec}} = 0$ corresponds to the center of the module in the z direction. The position dependence of outputs as a function of the reconstructed hit z position is fitted with the following function and these examples are shown in Fig. 4.6:

$$\exp\left(\frac{-z_{\mathrm{rec}}}{\Lambda + \alpha z_{\mathrm{rec}}}\right), \quad \text{for the upstream readout} \tag{4.17}$$

$$\exp\left(\frac{z_{\mathrm{rec}}}{\Lambda - \alpha z_{\mathrm{rec}}}\right), \quad \text{for the downstream readout,} \tag{4.18}$$

where Λ and α are fit parameters, which are shown in Table 4.1. Detail of these parameters can be found in Ref. [64]. Using Eqs. (4.17), the module energy is given as

$$\frac{e_{\mathrm{u}}}{\exp\left(\frac{-z_{\mathrm{rec}}}{\Lambda+\alpha z_{\mathrm{rec}}}\right)} + \frac{e_{\mathrm{d}}}{\exp\left(\frac{z_{\mathrm{rec}}}{\Lambda-\alpha z_{\mathrm{rec}}}\right)}, \tag{4.19}$$

where e_{u} (e_{d}) is energy deposit for the upstream (downstream) readout.

CV, CC03 and the scintillator parts of the downstream collar counters

For other detectors with dual readout, the module timing and energy were defined simply as an average (or sum[*2]) of those for two channels. In modules with a dead channel in CV and CC03, energy and timing of the live channel without any processes were used as outputs of the module.

[*2] Energy of CV was given as a sum of two channels.

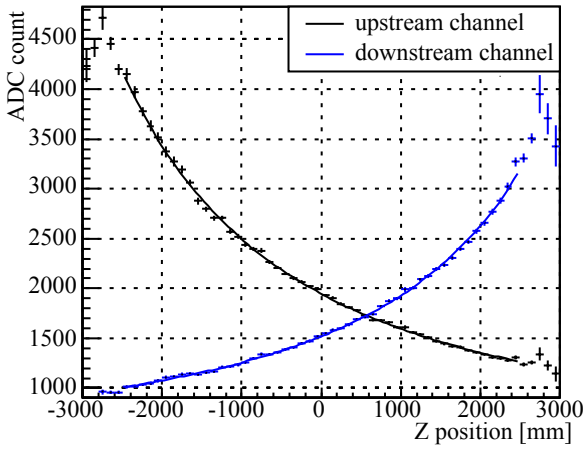

Figure 4.6: Position dependence of outputs for each channel of the MB detector.

Table 4.1: Parameters used in extraction of veto information in MB and BCV detector. Values presented here were used commonly for MB and BCV.

Parameters	Values
v	168.1 mm/ns
Λ	4920.5 mm
α	0.495

4.4.2 Calculation of veto energy and timing

Module timing values were first corrected using reconstructed $Z_{\rm vtx}$ and $T_{\rm vtx}$ values, where time of flight (TOF) was calculated is subtracted in order to reduce hit time difference due to each module position. This process is given in the following equation:

$$t_{\rm veto} = t_{\rm mod} - (T_{\rm vtx} + L/c), \tag{4.20}$$

where $t_{\rm veto}$ is timing used in veto decision, $t_{\rm mod}$ is timing of the module, L is the reconstructed photon track length from the vertex position to the detector module, and c is the speed of light. For MB and BCV, L was calculated with reconstructed hit z position from the timing difference as

$$L = \sqrt{r^2 + (Z_{\rm vtx} - z_{\rm center} - z_{\rm rec})^2}, \tag{4.21}$$

where r is the inner radius of the corresponding module of MB or BCV and $z_{\rm center}$ is the z position at the module center. $z_{\rm rec}$ is defined in the previous section (Sec. 4.4.1). For CV, L was calculated using the xy position at a center of each module x_0 and y_0 as

$$L = \sqrt{x_0^2 + y_0^2 + (z_{\rm CV} - Z_{\rm vtx})^2}, \tag{4.22}$$

where $z_{\rm CV}$ is the z position at the front or the rear plain of CV. For the downstream detectors, L was given as difference between the upstream z position of the corresponding detector $z_{\rm get}$ and the event z vertex as

$$L = z_{\rm det} - Z_{\rm vtx}. \tag{4.23}$$

For other detectors, particularly FB and NCC, L was given as difference between the upstream of the calorimeter and the event z vertex, denoted as ΔZ, instead of the actual detector position. This is because a resultant $t_{\rm veto}$ value is strongly affected by a wrong z vertex position derived from an incorrect photon pairing. This effect is reduced by using the calorimeter z position as follows:

$$\begin{aligned} t_{\rm veto} &= t_{\rm mod} - (T_{\rm vtx} + \Delta Z/c) \\ &\sim t_{\rm mod} - (t_{\rm cluster} - \Delta Z/c + \Delta Z/c) \\ &= t_{\rm mod} - t_{\rm cluster}, \end{aligned} \tag{4.24}$$

where t_{cluster} denotes photon hit timing in the calorimeter and the radial component in Eq. (4.6) is neglected. Dependence on Z_{vtx} is removed from Eq. (4.20) by giving $L = \Delta Z$ and miscalculation of veto timing is reduced.

As the next step, modules whose t_{veto} value obtained in the above process was within the "veto window" were selected in each detector. This veto window is defined detector by detector. Here, the scintillator parts of CC04, CC05, and CC06 were treated as separate detectors. Finally, the detector veto energy and timing was defined as those of the module with maximum module energy among the selected ones. When any modules with their t_{veto} values within the veto window are not found in a detector system, the veto energy of the detector was set to be 0. The event was rejected if the veto energy of any veto detector systems exceeded their threshold.

4.4.3 BHPV

Veto decision by the BHPV detector is based on coincidence of modules and is different from the other detectors. Hence a separate reconstruction method of veto information was developed. Hit timing for each pulse was corrected by subtracting TOF. Defining t_i^j as a hit timing of the i-th pulse identified in 256-sample waveform data in a channel of the j-th module ($j = 0, 1, \cdots, 11$), the TOF correction is expressed as

$$t_i'^j = t_i^j - \frac{jL_{\mathrm{mod}} + \sum_{k=0}^{j-1} \delta l_{k,k+1}}{c}. \tag{4.25}$$

Here, timing after the TOF correction is denoted with a prime($'$), the module with $j = 0$ represents the most upstream one, $L_{\mathrm{mod}} = 332$ mm is the width of a single BHPV module in the z-direction, $\delta l_{m,n}$ is the gap width between the m-th and n-th module which was measured in alignment of the detector and ranging from 3 mm to 57 mm, and c is the speed of light.

Using this corrected timing, hits due to electromagnetic showers developing into the downstream direction were in identified as coincidence among consecutive modules. Detail of the algorithm is as follows. Here, a hit in a channel was defined with an identified pulse with a photoelectron yield larger than 2.5 photoelectrons. For the earliest hit in the most upstream module, existence of hits in the two readouts of the following module was checked. Coincidence of these two modules was identified when such a hit was found within ± 10 ns from that of the first module. This process was repeated until such a hit is not found in the next module. The number of module with successive hits was defined as the number of coincidence modules and used for veto decision. The coincidence timing, denoted as $t_{\mathrm{coincidence}}$ was then calculated as an average hit timing with the TOF correction. The same process was applied for the remaining hits to search for another coincidence hits. An example of these procedure and waveform sample in the corresponding event are shown in Fig. 4.7 and Fig. 4.8, respectively.

The final veto decision was made in a similar way for other detectors, described in Sec. 4.4.2. BHPV veto timing was defined as

$$t_{\mathrm{veto}} = t_{\mathrm{coincidence}} - (T_{\mathrm{vtx}} + (z_{\mathrm{BHPV}} - Z_{\mathrm{vtx}})/c). \tag{4.26}$$

the event would be vetoed when the maximum number of coincidence modules was three or more among coincidences whose veto timing was within a given veto window.

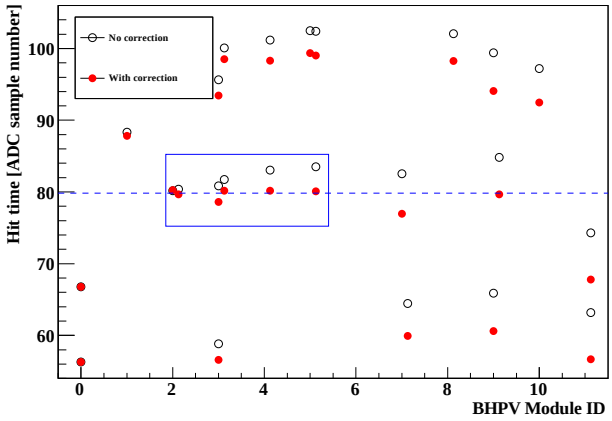

Figure 4.7: Example of hit timing map in BHPV. The black points show timing of identified pulse with the procedure described in Sec. 4.2.2 before the TOF correction. The red points are the same but the timing calibration and the TOF correction were applied. The blue box is an identified coincidence and the dashed line indicates its timing.

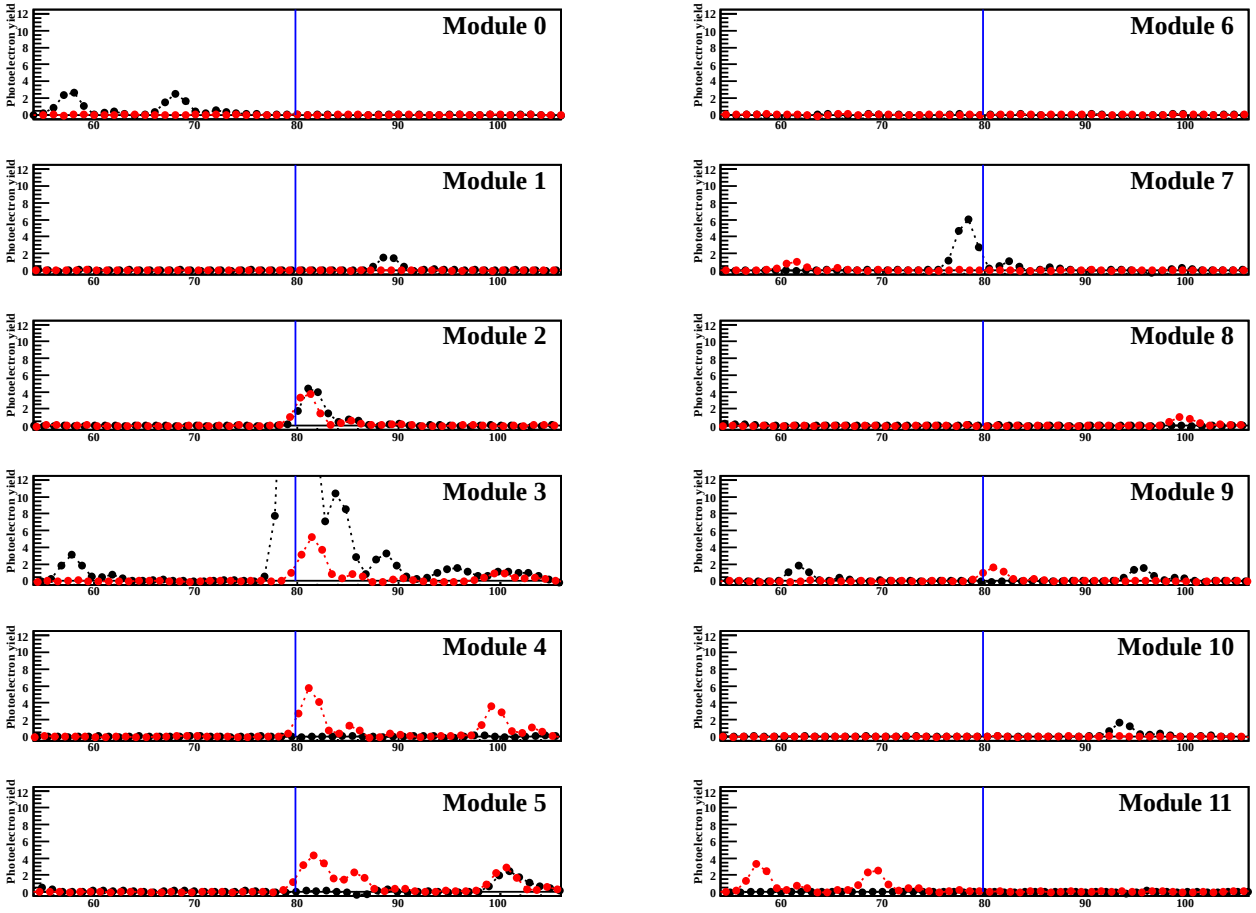

Figure 4.8: Waveform in the event of Fig. 4.7. The horizontal axis indicates the ADC sample number with shift due to timing calibration and TOF correction. The vertical axis shows the number of photoelectrons in pulse height. The blue line in each panel indicates the coincidence timing. The black and red waveforms correspond to two readouts of each module.

Chapter 5

Monte Carlo Simulation

In this chapter, the detail of the Monte Carlo (MC) simulation used in the analysis of this thesis will be described.

5.1 Overview of the Monte Carlo simulation

A principal purpose of the MC simulation is to evaluate acceptance of signal and normalization modes and to estimate background contribution in the analysis of these modes. The simulation consists of following three steps: (i) generation of incident K_Ls, (ii) simulation of K_L decay and interaction of daughter particles inside the detectors, and (iii) conversion of simulated information considering detector responses.

Below, detail of each step is described. In Sec. 5.2, a model with which the incident K_Ls are generated in the step (i) is explained. The step (ii) is processed by Geant4 [49] package with version 4.9.5p02. It is a toolkit to simulate the passage of particles through matter and widely used in high energy physics and various other fields such as space physics and medical application. All the KOTO detectors shown in Figure 2.1 are constructed in the simulation, and decays of incident K_Ls, tracking of daughter particles and their interaction inside the detectors are simulated by Geant4. In Sec. 5.4, a method to convert outputs with the above process to measurement data format in the step (iii) is described as well as response of each detector implemented in this analysis.

5.2 K_L generation

At the first step of the simulation, a K_L is generated at the beam line exit, which is located at the distance of 21.5 m from the primary target. Its 3-momentum and incident xy position are given with a model which is described the following sections.

5.2.1 Momentum distribution

A K_L was generated with a measured distribution with the real K_L beam because it is difficult to make reliable prediction with MC simulations, which involve hadronic interactions of protons in the metal target. The measurements were performed with a spectrometer and the KOTO calorimeter in February and June, 2012, before installation of the other detectors [100]. $K_L \to \pi^+\pi^-\pi^0$ and $K_L \to \pi^+\pi^-$ events were reconstructed and the obtained momentum distribution was converted

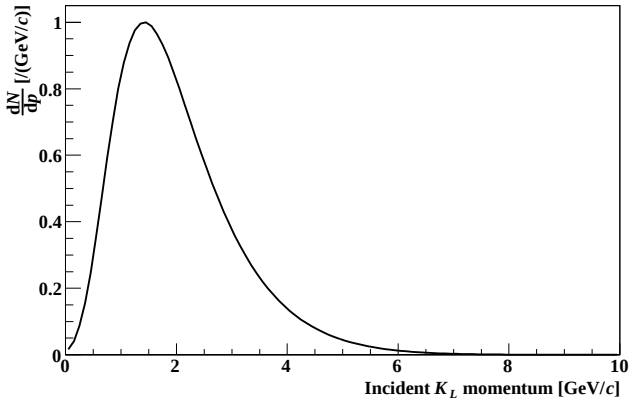

Figure 5.1: The K_L momentum spectrum used in the MC simulations.

into that at the exit of the second collimator with a help of MC simulations. The result was fitted with the following asymmetric Gaussian:

$$\exp(-\frac{(p-\mu)^2}{2(\sigma_0(1-(A+Sp)(p-\mu))^2}), \tag{5.1}$$

where p is the momentum of an incident K_L, μ corresponds to the peak momentum, and σ_0 the width of the distribution, which is modified by a quadratic of p with parameters A and S. The momentum p and parameters μ and σ_0 were given in the unit of GeV/c. The best fit parameters used in the MC simulation were

$$\mu = 1.41991, \tag{5.2}$$
$$\sigma_0 = 0.810237, \tag{5.3}$$
$$A = -0.301413, \tag{5.4}$$
$$S = 0.017092, \tag{5.5}$$

with which the K_L spectrum is shown as in Fig. 5.1.

5.2.2 Incident position and direction

Position and direction of incident K_Ls were given by a simplified optical simulation. The K_L vertex inside the target and its direction were randomly generated and the track was extrapolated toward the downstream direction. If the track passed the collimator, the generated vertex and direction information was used and if it did not, the above process was repeated.

In the decision of the vertex position inside the target, the "target image" as illustrated in Fig. 5.2 was used instead of the real target position. Here, the z and the z' axes are taken along the direction of the K_L beam and the primary proton beam, respectively, and the x axis to be perpendicular to the z axis inside the plane made by the z and the z' axis. The y axis is defined to be perpendicular to the plane. The target image in the x direction is then projection of the real target length along the z' axis to the x axis. The K_L generation position was assumed to distribute uniformly along the x axis within $\pm$9.1 mm. Similarly, y position is given as a random number $\pm$1.0 mm, considering the spread of the primary proton beam.

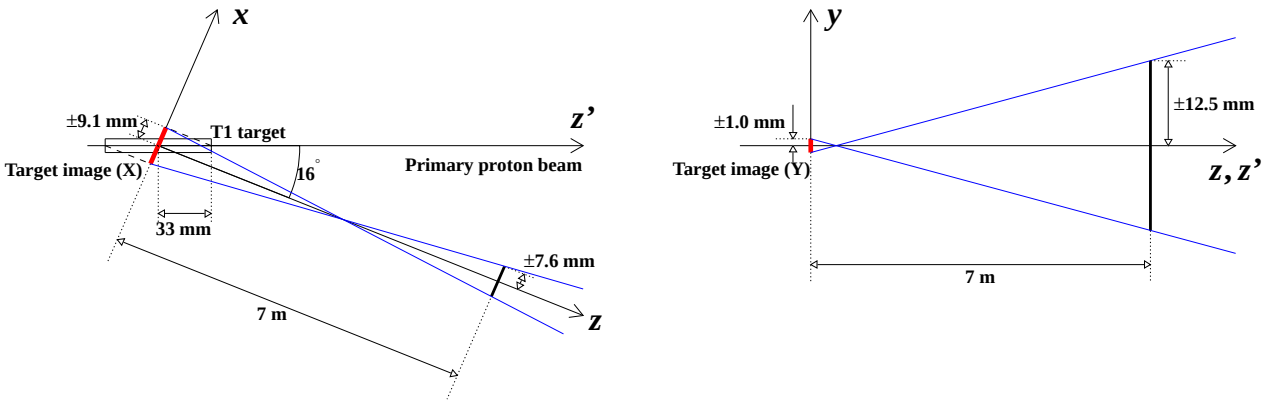

Figure 5.2: Illustration of the target images in x direction (left) and y direction (right). The red line in each figure represents the target image for the direction. The black bold lines are the apertures of the collimator for x and y directions and the blue lines indicates the edge beam.

The judgement of collimator passage was based on the xy position at $z = 7$ m from the center of the target, where the hole size of the collimator is the narrowest. The extrapolated x position was required to be within ± 7.7 mm and y position ± 12.5 mm.

5.3 Simulation of K_L decay and detectors

5.3.1 K_L Decay simulation

The K_L decay process, including generation of daughter particles, was managed by the Geant4 code. For given momentum of a generated K_L, $\beta = v/c$ was calculated and the flight length L were decided randomly assuming the following exponential distribution:

$$\exp\left(-\frac{L}{c\gamma\tau}\right), \tag{5.6}$$

where v is the speed of the K_L, c is the speed of light, $\gamma = \frac{1}{\sqrt{1-\beta^2}}$, and τ is the lifetime of a static K_L. The lifetime was given as $c\tau = 15.34$ m from Ref. [16]. If there existed some materials such as the vacuum window, air, and detectors along the way of the K_L, interactions with them were also considered.

In case that the K_L decayed, daughter particles were generated and behavior of each particle was simulated. In the generation of the daughter particles, $V - A$ interaction was assumed and the decay form factors were taken from Ref. [16].

For simplicity, simulations for each K_L decay mode were separately performed and analyzed. Finally, their results were added considering branching fraction of each mode.

5.3.2 Interaction inside detectors

Interaction of particles with detector materials were also handled by the Geant4 code.

A particle incident to a detector can make various interactions with the detector material: energy loss, scattering, generation of secondary particles, decay and absorption. Such interactions were simulated considering cross section of each process, and momentum of the original particles was changed or new particles were generated as a result of the interaction. These processes were repeated for all generated particles until they lost all their kinetic energy or went out of the defined volume. Each process was called a step and energy deposit, time, and three-dimensional position in active materials were recorded for each step. Below, these information is denoted as $(e_i, t_i, x_i, y_i, z_i)$, where i represents the step number.

Among possible interactions inside materials, reliable prediction for hadronic interactions is difficult and there was large model dependence. QGSP_BERT [50] was adopted as a hadron package unless anything was specified.

5.4 Detector response

The obtained energy deposit and timing information by the Geant4 simulation was ideal one and it needed to be modified considering responses of each detector. The responses contained position dependence of output, timing shift due to light propagation, timing resolution, and photon statistics effect. In order to simulate timing shift due to pulse overlapping, waveform was generated based on simulated information and waveform of accidental hits taken by the TMon trigger (Sec. 3.3.5) was overlaid. In this section, the general methods to modify simulated energy and timing are described, and explanation of detector responses and accidental overlay follows. For detectors placed inside the beam, namely BHCV and BHPV, which are read with 500-MHz ADC, different schemes were adopted and they are separately described.

5.4.1 Light propagation and position dependence

In all the KOTO detectors except BHPV, scintillation light which comes from energy deposit by an incident particle is detected after traveling from the interaction point to the photosensors. Finite timing difference exists between the time of interaction and detection due to this propagation process. This effect was considered for each simulation step by adding proper delay to the time of the interaction depending on its position and the readout direction. In this process, "effective speed of light" in each detector, which is explained in Fig. 5.3 and had been measured, was used. Implemented values are summarized in Table 5.1. Energy information obtained in the simulation also should be modified based on the interaction positions to reflect effects of attenuation and/or light collection efficiency. Statistical fluctuation of detected number of photons was also considered.

In summary, recorded information in the simulation for the step i, $(e_i, t_i, x_i, y_i, z_i)$, was converted into a pair of energy and time which to be observed in the detector, $(e_i^{'}, t_i^{'})$, where description for the first five variables are given in Sec. 5.3.2. In the following sections, this conversion process in each detector, including its response and the method of accidental overlay, is described.

5.4.2 Implemented response for each detector

This section describes detail of methods to convert a simulation output, $(e_i, t_i, x_i, y_i, z_i)$, into $(e_i^{'}, t_i^{'})$ for each detector. In detectors which did not appear in this section, namely NCC and the downstream collar counters, no detector responses were considered and the raw output itself was used as $(e_i^{'}, t_i^{'})$.

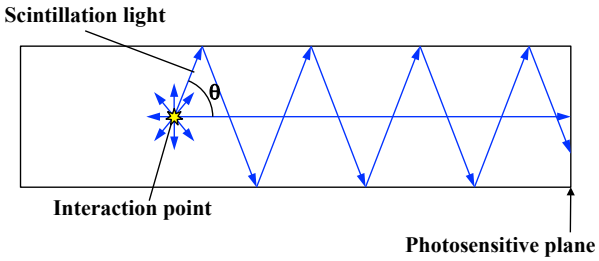

Figure 5.3: Illustration of light propagation inside a detector. Scintillation light or secondary light emitted by the wavelength shifter travels a longer way than the distance between the interaction point and the photosensitive plane. This makes speed of light look slower than c/n, where n is the refractive index of the detector materials. The average propagation speed over emission angle θ corresponds to the effective speed of light.

Table 5.1: List of effective speed of light for each detector.

Detector	Notation	Value [mm/ns]	Remarks
CsI (small crystal)	$v_{\mathrm{CsI}}^{\mathrm{small}}$	91.0	
CsI (large crystal)	$v_{\mathrm{CsI}}^{\mathrm{large}}$	95.9	
CC03	v_{CC03}	88.3	
MB	v_{MB}	168.1	Also applied to BCV
FB	v_{FB}	181	
CV	v_{CV}	177	Also applied to OEV and LCV
BHCV	v_{BHCV}	154.9	

CsI

Modification of simulated timing t_i into $t_i^{'}$ is summarized as in the following equation:

$$t_i^{'} = t_i + \Delta t_i + \mathrm{Gaussian}(\sigma_t(E)) \tag{5.7}$$

where the function Gaussian(x) gives a random number following a Gaussian with its mean and width(σ) of zero and x, respectively. The second term of Eq. (5.7), Δt_i, represents the time delay due to light propagation for the step i and was given as

$$\Delta t_i = |z_{\mathrm{downstream}}^{\mathrm{CsI}} - z_i| / v_{\mathrm{CsI}}, \tag{5.8}$$

where $z_{\mathrm{downstream}}^{\mathrm{CsI}}$ is the z position of the downstream edge of the calorimeter and v_{CsI} represents $v_{\mathrm{CsI}}^{\mathrm{small}}$ or $v_{\mathrm{CsI}}^{\mathrm{large}}$ in Table 5.1 according to the type of the crystal. The effective speed of light inside the CsI, v_{CsI} was derived of cosmic ray data. Timing resolution was considered in the third term of Eq. (5.7), where smearing by the Gaussian with the following standard deviation was added,

$$\sigma_t(E) = \frac{a}{E} \oplus \frac{b}{\sqrt{E}}, \tag{5.9}$$

where σ_t is given in the ns unit, E is a sum of corrected energy, to be described below, in the MeV unit, $a = 5.00$, and $b = 3.63318$.

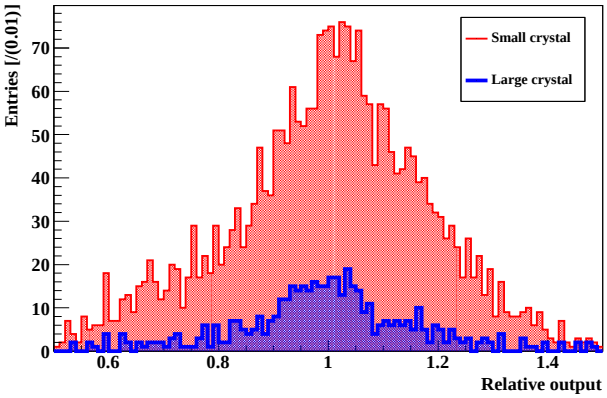

Figure 5.4: Distribution of mean relative outputs to the standard crystal.

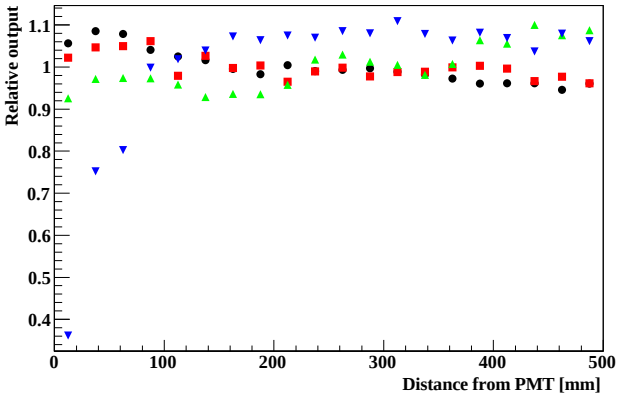

Figure 5.5: Examples of position dependence. For each crystal, relative outputs to the mean of each crystal were shown.

As for responses related to energy, position dependence and effect of photon statistics were considered. Difference of signals for the same energy deposit at different positions was considered with the measurement data using ^{137}Cs radioactive source. Outputs corresponding to the photoelectric absorption peak of 662 keV γ from the source were measured as relative values to a certain standard crystal at twenty positions with 25 mm intervals for all the crystals. Distribution of position-averaged relative outputs for all the crystals is shown in Fig. 5.4 and examples of measured position dependence are shown in Fig. 5.5. Crystal by crystal outputs have $\sim$20% variation and some crystals have a larger position dependence. Such position dependence was reflected as the following procedures. First, the expected number of a photoelectron yield was calculated with the relative output data and the absolute photoelectron (p.e.) yield in the standard crystal, denoted as N_{CsI}. Using Y_k as a relative output at the k-th measurement point for a given crystal, which corresponds to the position of energy deposition, this was obtained as

$$e_i Y_k N_{\mathrm{CsI}}, \tag{5.10}$$

where $N_{\mathrm{CsI}} = 9$ p.e./MeV. This value was separately measured with cosmic ray data [90] and tuned to fit the experimental condition in the physics run[*1]. The obtained number was fluctuated assuming the Poisson distribution to consider photon statistics effect and again converted into energy, where the position-averaged relative output $\tilde{Y}$ was used. Finally, a calibration factor, C, which was given crystal by crystal as described in App. C, was multiplied. In summary, modified energy for the step i, $e_i^{'}$ was expressed as follows:

$$e_i^{'} = C \times \mathrm{Poisson}(e_i Y_k N_{\mathrm{CsI}})/(\tilde{Y} N_{\mathrm{CsI}}), \tag{5.11}$$

where the function Poisson(x) gives a random integer number which follows the Poisson distribution with its mean of x.

[*1] Although the original N_{CsI} value was given as 12.7 p.e./MeV according to Ref. [90], it was decreased because decreased of light outputs were observed in the real experimental condition with the vacuum environment. This was due to contamination of silicon cookies and detailed description will be found in Ref. [64].

MB and BCV

Since signals of each module were read by the upstream and downstream PMTs in the MB and BCV detector, two sets of energy and timing information were obtained from a simulation output of a single module as

$$(e_i, t_i, x_i, y_i, z_i) \longrightarrow (e_i^{'\mathrm{u}}, t_i^{'\mathrm{u}}), (e_i^{'\mathrm{d}}, t_i^{'\mathrm{d}}). \tag{5.12}$$

Here, the superscripts "u" and "d" represent the upstream and downstream readouts, respectively. Timing for each readout for a hit in the step i was calculated with the effective speed of light v_{MB} and distance between the position of energy deposit and each edge of the detector. The same effective speed was used also for BCV. v_{MB} was determined with cosmic ray data [64]. Using $z^{\mathrm{MB}}_{\mathrm{upstream}}$ and $z^{\mathrm{MB}}_{\mathrm{downstream}}$ as the z position of the upstream and downstream edges, respectively, corrected timing for each side was written as follows:

$$t_i^{'\mathrm{u}} = t_i + |z_i - z^{\mathrm{MB}}_{\mathrm{upstream}}|/v_{\mathrm{MB}}, \tag{5.13}$$

$$t_i^{'\mathrm{d}} = t_i + |z^{\mathrm{MB}}_{\mathrm{downstream}} - z_i|/v_{\mathrm{MB}}. \tag{5.14}$$

Energy was equally shared by the two readouts and weighted depending on z position with Eq. (4.17). The corrected energy for each readout then was

$$e_i^{'\mathrm{u}} = \frac{e_i}{2} \exp\left(\frac{-\Delta z_i}{\Lambda + \alpha \Delta z_i}\right), \tag{5.15}$$

$$e_i^{'\mathrm{d}} = \frac{e_i}{2} \exp\left(\frac{\Delta z_i}{\Lambda - \alpha \Delta z_i}\right), \tag{5.16}$$

where $\Delta z_i = z_i - (z^{\mathrm{MB}}_{\mathrm{upstream}} + z^{\mathrm{MB}}_{\mathrm{downstream}})/2$. Equations (5.13)-(5.16) were pplied also for BCV with the same parameters Λ and α.

CV

Signals of each CV module were read from two sides, referred to as short-fiber side and long-fiber side, and two sets of corrected energy and timing were extracted. Below the superscript "s" ("l") represents the variable for short-fiber (long-fiber) side.

Timing response is schematically drawn in Fig. 5.6. In the real data, light detection timing in the two sides was adjusted to be the same by the timing calibration when an energy deposit was given at the position x_0. x_0 was defined as the position of $y = 0$ ($x = 0$) for vertical (horizontal) modules in the global coordinate. Sign of Δx in Fig. 5.6 was defined to be positive (negative) when the interaction point is located in the short-fiber (long-fiber) side with respect to the standard position x_0. In case that an interaction point was located in the normal region, where fibers were laid in grooves and glued with scintillator, the timing correction for the short-fiber (long-fiber) side, denoted as $\Delta t_i^{\mathrm{s}}(\Delta t_i^{\mathrm{l}})$, was

$$\Delta t_i^{\mathrm{s}} = -\Delta x/v_{\mathrm{CV}} \tag{5.17}$$

$$(\Delta t_i^{\mathrm{l}} = \Delta x/v_{\mathrm{CV}}), \tag{5.18}$$

where v_{CV} is the effective speed of light inside the fibers. Here, light emission timing in the wavelength shifting fiber was assumed to be the same as interaction timing. On the other hand, in case that an interaction point was in the fiber-lifted region, scintillation light was not absorbed immediately but travelled to the normal fiber-glued region. Therefore, common delay corresponding to

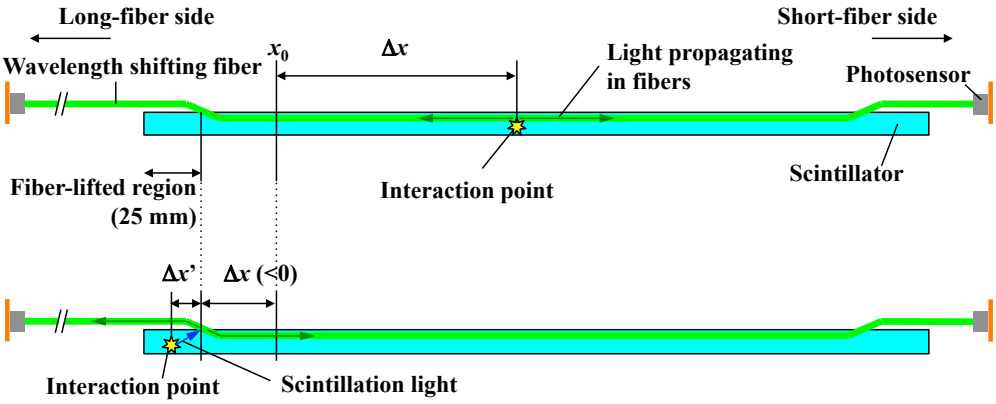

Figure 5.6: Schematic view of light propagation in the CV detector. Timing of the short-fiber and long-fiber sides were adjusted to be the same when the interaction point was at the position labeled as x_0. The upper figure is for the case that the interaction point is in the normal region and the bottom that the interaction occurred in the fiber-lifted region.

the propagation time in scintillator was added for the both side. Using $\Delta x'$ and Δx shown in the bottom of Fig. 5.6, the timing correction is obtained as

$$\Delta t_i^{\rm s} = \Delta x^{'}/v'_{\rm CV} - \Delta x/v_{\rm CV}, \tag{5.19}$$
$$\Delta t_i^{\rm l} = \Delta x^{'}/v'_{\rm CV} + \Delta x/v_{\rm CV}, \tag{5.20}$$

where the effective speed of light in the scintillator $v'_{\rm CV}$ was assumed to be the same with $v_{\rm CV}$. Timing resolution was then considered by adding Gaussian smearing. The corrected timing for the short(long)-fiber side, $t_i^{'\rm s}(t_i^{'\rm l})$ was eventually written as follows:

$$t_i^{'\rm s,l} = t_i + \Delta t_i^{\rm s,l} + {\rm Gaussian}(\sigma_t), \tag{5.21}$$

where the timing resolution σ_t was given as 1.8224 ns independently of the deposit energy.

Energy correction was made by considering the position dependence of the photoelectron yield and statistical fluctuation with Poisson distribution. The absolute light yield was measured for every 50 mm region of all modules with a tracking system consisting of series of drift chambers in June, 2012 [82, 84], before the construction of the whole KOTO detector system. Its results were presented in Fig. 5.7 and these values were used after applying correction due to difference of over-voltage of the MPPCs between this measurement and the physics run[*2]. Numbers of photoelectrons which were obtained assuming Poisson distribution with the measured light yield were again converted into energy with calibration constants and gain for a single photoelectron for the corresponding module, denoted as $Q_{\rm 1p.e.}^{\rm s,l}$ and $c^{\rm s,l}$, respectively. Using $N_{\rm CV}^{\rm s,l}$ as the absolute photoelectron yield per unit energy deposit at the corresponding position and module, modification of energy for the simulation step i, e_i, including all above responses, is as follows:

$$e_i^{'\rm s} = {\rm Poisson}(e_i \times N_{\rm CV}^{\rm s}) \times c^{\rm s} Q_{\rm 1p.e.}^{\rm s}, \tag{5.22}$$

[*2] Operation voltage of the photosensors or the MPPCs was set differently because it was adjusted so that the same one photoelectron gain would be obtained in this measurement while in the physics run, it was tuned to have the same pulse height among modules for online veto.

and the same for the long-fiber side, $e_i^{\prime l}$. Here, $c^{\mathrm{s,l}}$ and $Q_{\mathrm{1p.e.}}^{\mathrm{s,l}}$ are given in units of MeV/(ADC counts) and (ADC counts)/(p.e.) and $N_{\mathrm{CV}}^{\mathrm{s,l}}$ included the correction of different MPPC over-voltage.

FB, LCV, CC03 and OEV

Signals from these detectors were read from a single side: upstream for the FB detector and downstream for the OEV and LCV detector. Considering a direction of readout for each detector, timing correction was made as follows:

$$t_i^{'} = t_i + |z_i - z_{\mathrm{upstream}}^{\mathrm{FB}}|/v_{\mathrm{FB}} \quad \text{for FB}, \tag{5.23}$$

$$t_i^{'} = t_i + |z_{\mathrm{downstream}}^{\mathrm{LCV}} - z_i|/v_{\mathrm{CV}} + \mathrm{Gaussian}(\sigma_t(e_i)) \quad \text{for LCV}, \tag{5.24}$$

$$t_i^{'} = t_i + |z_{\mathrm{downstream}}^{\mathrm{CC03}} - z_i|/v_{\mathrm{CC03}} \quad \text{for CC03}, \tag{5.25}$$

$$t_i^{'} = t_i + |z_{\mathrm{downstream}}^{\mathrm{OEV}} - z_i|/v_{\mathrm{CV}} \quad \text{for OEV}, \tag{5.26}$$

where $z_{\mathrm{upstream}}^{\mathrm{FB}}$ is the z position of the FB upstream edge, $z_{\mathrm{downstream}}^{\mathrm{LCV}}$, $z_{\mathrm{downstream}}^{\mathrm{CC03}}$, and $z_{\mathrm{downstream}}^{\mathrm{OEV}}$ the z position of the LCV, CC03 and OEV downstream edge, respectively. In case of LCV, smearing by a Gaussian was added considering its timing resolution[*3],

$$\sigma_t(e) = \frac{a}{\sqrt{e}} \oplus b, \tag{5.27}$$

where σ_t and the energy are in the ns and MeV units, respectively, $a = 1.7656$, and $b = 1.1984$. In case $e < 0.1$ MeV, $\sigma(0.1)$ was used. The same effective speed of light with CV was used for OEV and LCV as the same wavelength shifting fibers were used in these detectors[*4].

In the FB detector, light attenuation was considered with an simple exponential function and the corrected energy was given as

$$e_i^{'} = e_i \exp\left(-\frac{z_i - z_{\mathrm{calib}}^{\mathrm{FB}}}{\lambda_{\mathrm{FB}}}\right), \tag{5.28}$$

where $z_{\mathrm{calib}}^{\mathrm{FB}}$ was z position outputs at which were used to obtain the calibration constants of this detector and λ_{FB} an attenuation length given as $\lambda_{\mathrm{FB}} = 2700$ mm.

LCV energy response was similar to that of CsI; a relative output to that at $z = z_{\mathrm{calib}}^{\mathrm{LCV}}$, which had been measured before installing the detector with beta rays from ^{90}Sr radioactive source and are shown in Fig. 5.8, was multiplied and smearing due to photon statistics was applied. The absolute photoelectron yield per unit energy deposit, denoted as N_{LCV}, was estimated for each module with cosmic ray data taken in-situ and summarized in Table. 5.2. Finally, the corrected energy deposit would be

$$e_i^{'} = \mathrm{Poisson}(e_i \times Y(z_i) \times N_{\mathrm{LCV}})/N_{\mathrm{LCV}}, \tag{5.29}$$

where the function $Y(z)$ gives the relative output at a position z, which was calculated by interpolating two points around given z in Fig. 5.8, and $\mathrm{Poisson}(x)$ gives a random integer number following the Poisson distribution as in Eq. (5.11). Detail of the measurement of the position dependence and evaluation of the absolute photoelectron yield will appear in App. C as well as methods of in-situ calibration.

[*3] Parameters used in this smearing was obtained with the constant fraction method.

[*4] Y11 by Kuraray [79]. Density of wavelength shifter is slightly different in the fibers of OEV.

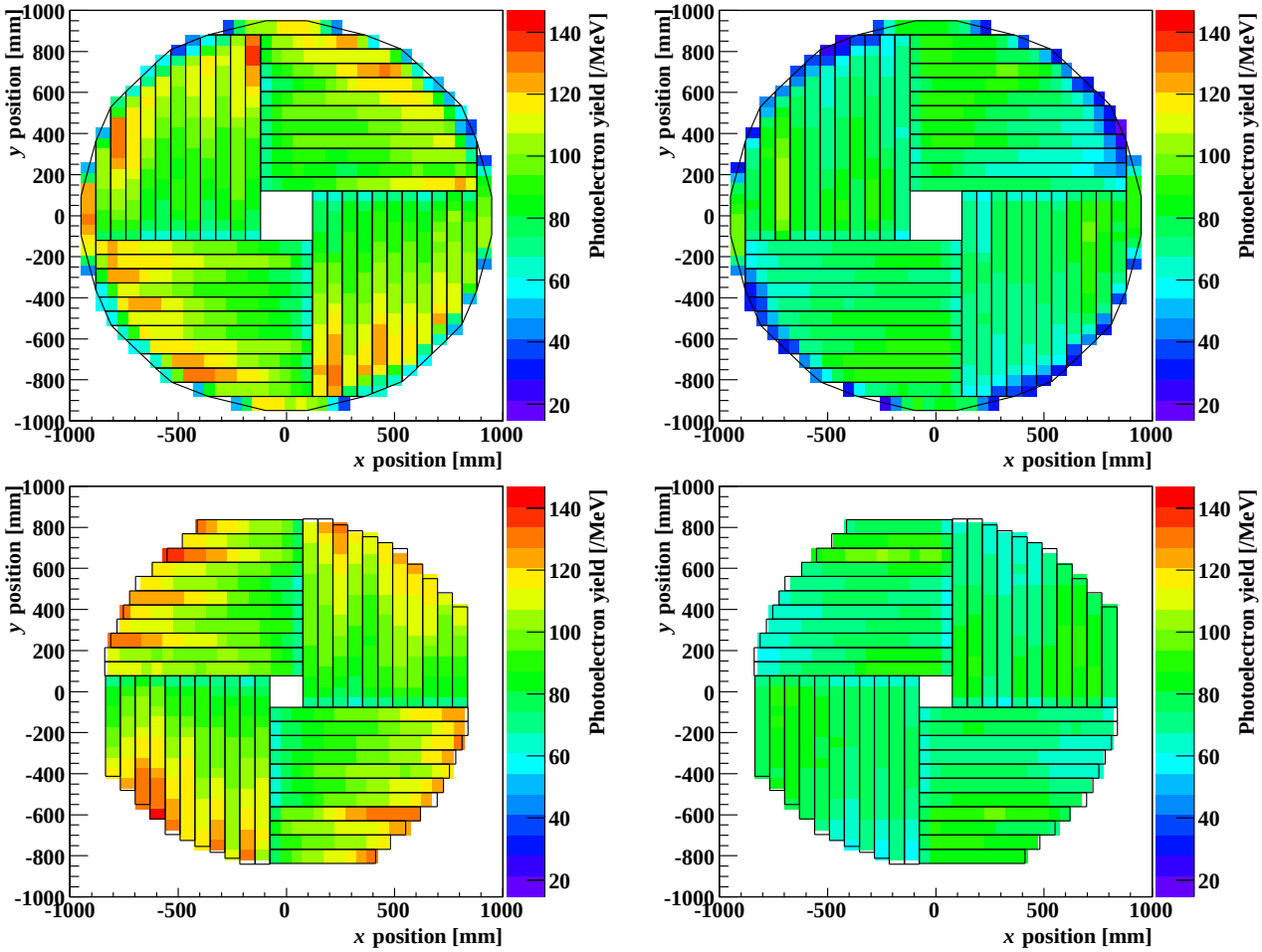

Figure 5.7: Position dependence of the absolute photoelectron yield in the CV detector. The top left (right) figure shows measured photoelectron yield obtained in the short(long)-fiber side in the front plane. Similarly, the bottom left (right) figure is for the short(long)-fiber side of the rear plane. In every figure, the detector is viewed from the downstream direction.

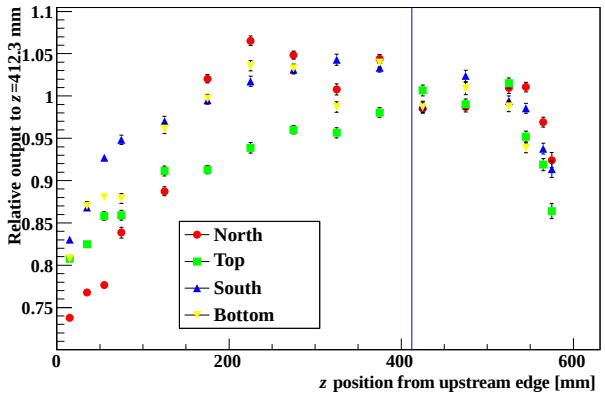

Figure 5.8: Position dependence of outputs for each channel of the LCV detector.

Table 5.2: Photoelectron yield N_{LCV} for unit energy deposit in each module of the LCV detector.

Module	Photoelectron yield [p.e./MeV]
North	34.38
Top	30.08
South	37.69
Bottom	31.03

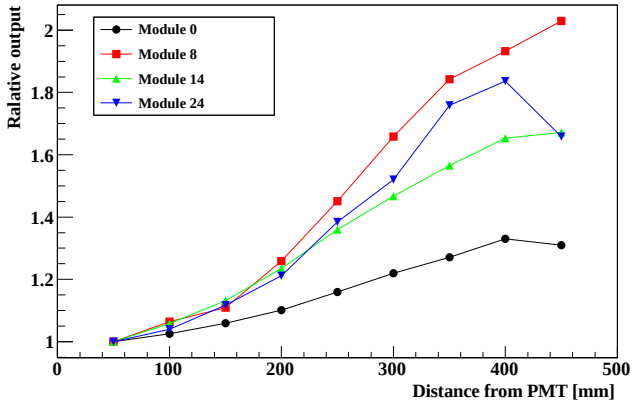

Figure 5.9: Examples of position dependence in the CC03 detector.

As for the CC03 detector, attenuation effect was considered based on measurements and examples of correction value are shown in Fig. 5.9. Corrected energy would be thus

$$e_i^{'} = Y(z_i)e_i, \tag{5.30}$$

where $Y(z)$ is the correction value for the interaction position z.

No correction was made for energy deposit in the OEV detector.

5.4.3 Waveform generation

In order to reproduce timing shifts due to pileups, simulation outputs were once converted into waveform with 64 samples so that the same analysis procedures with data were applied.

First, each pair of corrected energy and timing for the step i, $(e_i^{'}, t_i^{'})$, was converted into a set of 64 values for the step, $\{a_n^i\} = (a_0^i, a_1^i, \cdots, a_j^i, \cdots, a_{63}^i)$. This waveform was obtained by taking 64 values of a function $f(t)$ as below with intervals of 8 ns around its peak:

$$f(t) = \exp\left(-\frac{(t-\mu)^2}{(\sigma_0 + a(t-\mu))^2}\right), \tag{5.31}$$

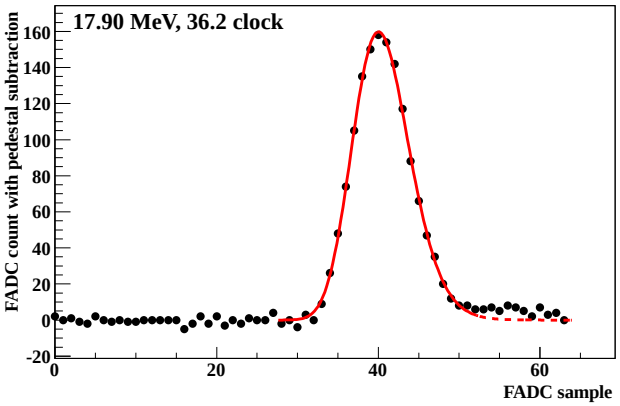

Figure 5.10: An example of waveform fitting with Eq. (5.31). Black points are a waveform sample with pedestal subtraction. This was taken from cosmic ray data of a channel in the CsI calorimeter. The solid red line is a result of fitting and the dashed one is its extension for the tail region with parameters obtained by the fitting.

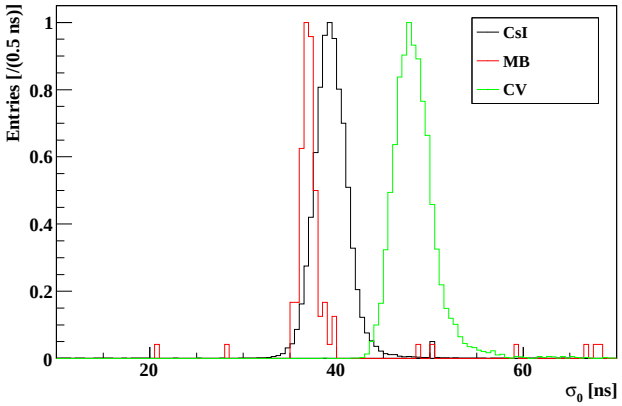

Figure 5.11: Distributions of parameters σ_0. Examples of three detectors, the CsI calorimeter, MB, and CV are presented. Each distribution was normalized so that the peak height was 1.

$$\mu = \mu_0 + t_i^{'} - \delta t + t_{\text{offset}}, \tag{5.32}$$

where t is given in the unit of ns, μ is the peak timing, δt is the timing calibration constant, and t_{offset} is to adjust timing between data and MC. μ_0, σ_0 and a are parameters and given detector by detector by fitting waveform of the real data with Eq. (5.31). These parameters represent time difference between the half maximum in the early side and the peak of this function, the width of the Gaussian, and a tail of a waveform, respectively. Examples of fitting and distributions of the resultant parameters over events are shown in Fig. 5.10. Obtained parameters for all detectors and detailed process are written in App. D. The function of Eq. (5.31) with given $t_i^{'}$ was then normalized so that a sum of corresponding 64 values was equal to $e_i^{'}$. That is, $\{a_n^i\}$ was given as follows:

$$a_j^i = e_i^{'} \frac{f(8j)}{\sum_{k=0}^{63} f(8k)}, (j = 0, 1, \cdots, 63) \tag{5.33}$$

where the function $f(t)$ is given in Eq. (5.31).

The waveforms for all steps are finally summed to get the waveform of the event $\{A_n\} = (A_0, A_1, \cdots, A_{63})$:

$$A_j = \sum_i a_j^i, (j = 0, 1, \cdots, 63). \tag{5.34}$$

5.4.4 Accidental overlay

In the real case, signals from detectors are affected by some noises and accidental activities. In particular, accidental hits can have critical influence in calculation of timing, which led to mis-detection of hits through wrong timing information as described in Sec. 4.2.1.

In order to consider such timing mis-calculation, waveform of accidental hit samples taken with the TMon trigger as described in Sec. 3.3.5 were overlaid on the generated waveform for all channels

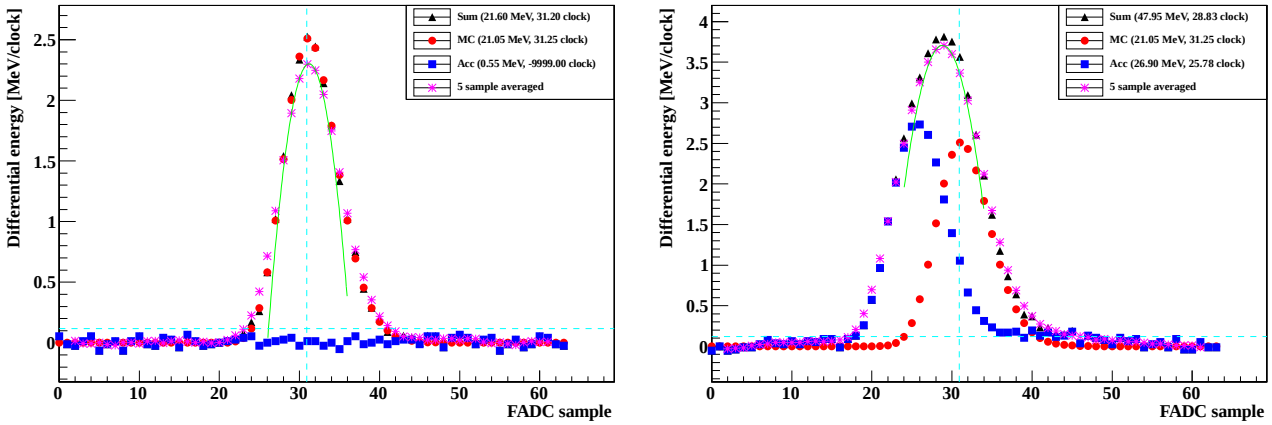

Figure 5.12: Examples of accidental overlay in the MC simulation of $K_L \to 3\pi^0$ for a channel of the FB detector. Red circles, blue squares, and black triangles show waveform for a simulation output, a TMon event and sum of these two, respectively. Purple asterisks show smoothed waveform with five-sample moving average, which is used to calculate parabola-fit timing and fitted parabola function is drawing with a green line. Horizontal and vertical dashed cyan lines indicate the threshold and nominal timing for this detector, respectively. The left and right figures obtained from the common simulation output but with different events added in accidental overlay.

of all detectors. For a MC event, one TMon event was randomly selected among approximately 40 million events, which had been taken simultaneously with the physics data. Corresponding 64 sample data of the TMon events were added to the generated waveform sample by sample after subtracting pedestal and multiplying by a calibration constant for the channel as mentioned in Sec. 4.2.1.

Since the real data was used for overlay, channel by channel noise and accidental hits were included in the simulation with above process properly. Correlation among channels were also correctly handled. These were critical in considering background, where simultaneous accidental hits in multiple channels could cause correlated inefficiency. Detail of this background is described in Sec. 7.4.6.

For waveform after accidental overlay, energy and timing were calculated with the same procedures described in Sec. 4.2.1.

5.4.5 Beam hole detectors

In order to accommodate with high hit rates, multi hits in a single event were handled in the beam hole detectors, namely BHCV and BHPV. Simulated energy and timing information were modified considering detector responses without generating waveform. Accidental activity was then considered by adding extra hits taken from the TMon data. Since the BHPV detector dealt with Čerenkov light, treatment of simulation information was different from other detectors. Below, implementation of responses of these detectors are separately presented.

BHCV

In the BHCV detector, information of energy deposit, $(e_i, t_i, x_i, y_i, z_i)$, was first transformed into $(e_i^{'}, t_i^{'})$ including its detector response, as was done in detectors above. From series of this modified information for a channel, a single energy and timing value were extracted. Timing delay due to light propagation and attenuation effect was considered as

$$t_i^{'} = t_i + \frac{|x_i - x_{\mathrm{edge}}|}{v_{\mathrm{BHCV}}}, \tag{5.35}$$

$$e_i^{'} = e_i \times A \exp\left(\frac{|x_i - x_{\mathrm{edge}}|}{\lambda_{\mathrm{BHCV}}}\right), \tag{5.36}$$

where x_{edge} is x position of the scintillator's end to which side a PMT was attached, λ_{BHCV} is the attenuation length of this detector, and A is a correction factor of position dependence in calibration. λ_{BHCV} and A were evaluated to be 56.95 mm and 0.891. From a set of corrected energy and time $(e_i^{'}, t_i^{'})$, the earliest timing and sum of energy whose timing was within 10 ns from the earliest timing were used as timing and energy for the channel, respectively.

BHPV

Since BHPV used Čerenkov light for detection of incident particles, information of energy deposit was not used in the simulation of the BHPV detector. When a charged particle with its speed larger than Čerenkov threshold, given as c/n, passed in the aerogel, Čerenkov light was generated and traced through the aerogel and light collection mirrors to PMTs, where c and n are the speed of light and the refractive index of aerogel, respectively. The number of generated optical photons was given by the refractive index of aerogel and the speed of the charged particle as the following equation:

$$\frac{\mathrm{d}N}{\mathrm{d}x\mathrm{d}\lambda} = 2\pi\alpha z^2 \sin^2\theta \frac{1}{\lambda^2}, \tag{5.37}$$

where λ, z, and α are wavelength of the Čerenkov light, charge of the running particle and the fine structure constant, respectively. θ is given as $\cos\theta = 1/(n\beta)$, where β is the speed of the charged particle in the unit of c. For detection of each generated photon, absorption and scattering in the aerogel tiles, reflection by the mirrors and quantum efficiency of PMTs were considered. Its detail will be described in App. E. Timing of each photon detected by the PMT was given as the generation timing of the photon with delay due to propagation to the PMT. The earliest value was adapted as timing of the channel. The total number of above photons for a PMT was used as the observed number of photoelectrons in the channel.

Accidental overlay for BHCV and BHPV

First, series of energy and timing information in a randomly-selected TMon event was assigned as hits of the channel. When there was a hit in the simulation, its energy and timing was added to the list. Here, if timing of an accidental hit in the TMon data was within 10 ns from the hit timing from simulation, these two hits were merged and regarded as a single hit, where timing of the earlier hit and the sum of energies of the two hits were used.

5.4.6 Online trigger effect

In data taking, some selections were applied for triggering events at the online level. Since it was not easy to reproduce these selections by the online trigger in the MC simulation, resultant trigger

bias was evaluated with data and considered in the simulation. Related to the calorimeter, two kinds of trigger selections were used in the data taking as described in Sec. 2.2.8 and Sec. 3.3; the total energy (Et) cut and the Center Of Energy (COE) cut.

Bias of this online trigger was evaluated with data taken with lower online Et threshold and shown in the left of Fig. 5.13. By setting the 650 MeV threshold for total energy of reconstructed photons in the offline analysis, the bias was found to be small enough.

The online COE cut was applied only for the physics trigger data, and its bias was evaluated with data taken with the normalization trigger data, where only the online COE cut was removed. The bias of this trigger was basically removed by requiring the tighter condition for the a corresponding offline variable, the "offline-COE" R_{COE}, which was defined as

$$R_{\mathrm{COE}} = \frac{\sqrt{(e_1 x_1 + e_2 x_2)^2 + (e_1 y_1 + e_2 y_2)^2}}{e_1 + e_2}. \tag{5.38}$$

The result of the evaluation was shown in the right of Fig. 5.13. Even for R_{COE} larger than the nominal threshold of 165 mm as given in Table 3.1, trigger efficiency was still lower than 100% although it was closer to 100% for a larger R_{COE} value. This was because the online COE trigger decision used energy calculated as an integral of all the 64 samples and was affected by accidental activities, which made the COE value smaller. To take this trigger bias into account, the threshold for R_{COE} was set as 200 mm and simulation events were weight according to the value of R_{COE} as the follows:

$$\frac{1}{1 + \exp(-(R_{\mathrm{COE}} + a)/b)}, \tag{5.39}$$

where $a = 52.7654$ mm and $b = 174.999$ mm.

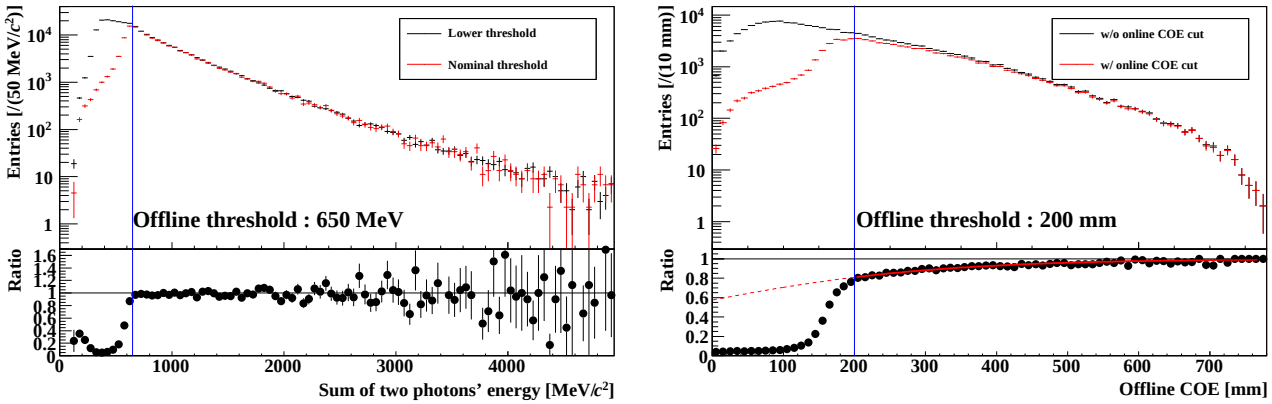

Figure 5.13: Evaluation of online trigger biases as a function of a corresponding offline value. The left figure was for the online Et cut, where total energy of reconstructed photons in two-photon events taken with the normalization trigger was compared between runs with the lower (black) and the nominal (red) online Et threshold in the top panel and their ratio for each energy were shown in the bottom panel. The right figure was for the online COE cut, where distributions of offline COE values were compared between the all events (black) and those which would be accepted by the online COE cut (red) were compared in the top panel. Two photon events with the minimum bias trigger were analyzed. Again, the graph in the bottom panel showed their ratio for each offline COE value. The red curve shows the fit function of Eq. (5.39), which would be used for efficiency correction, where the solid line was the effective region of this function and the dashed region was simply its extension. For the both figures, the threshold values of each offline variable was indicated with a blue line.

Chapter 6

Performance Evaluation of the Beam Hole Photon Veto Detector

Preceding to the analysis of $K_L \to \pi^0\nu\overline{\nu}$ search, performance evaluation of the Beam Hole Photon Veto (BHPV) detector by using beam data is described in this chapter.

6.1 Overview

As already mentioned, a high sensitivity search of $K_L \to \pi^0\nu\overline{\nu}$ with an intense neutral beam requires both high detection efficiency for K_L decay particles and tolerance against the high beam rate. The in-beam photon detector, or BHPV, is a typical detector where such conditions are the most severely considered. With ordinary photon detectors with a calorimeter type, it is difficult to handle the intense neutral beam, or enormous amount of neutrons and low-energy photons accompanying K_Ls, in terms of high counting rates for stable operation and large signal losses due to overveto by fake signals coming from beam particles. Hence a new idea for this detector to overcome these difficulties is necessary in order to achieve higher sensitivity for the $K_L \to \pi^0\nu\overline{\nu}$ decay. In the KOTO experiment, as described in Sec. 2.2.6, lead-aerogel sandwich detector was adopted, which enabled this detector to have high blindness to neutrons with high efficiency to high energy photons arising from K_L decays. Since this kind of detector is the first trial to use aerogel for photon detection and based on completely a novel concept, evaluation of its performance on photon detection had great importance.

In this chapter, operation of this detector in the actual neutral beam during the period of the KOTO physics data taking in May, 2013 is reported. It begins with basic property such as gains and photoelectron yields of aerogel in Sec. 6.2. The methods of calibration to obtain these values and their stability are reported. Performance of the detector in the neutral beam environment is then examined in Sec. 6.3, followed by evaluation of photon detection efficiency using data taken during the physics run period in Sec. 6.4 Future improvements are finally discussed in Sec. 6.5.

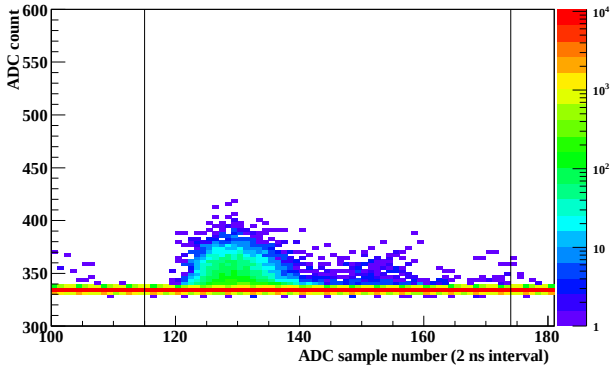

Figure 6.1: Examples of one photoelectron waveform. Waveform of many LED events was overlaid and shown as a two-dimensional histogram. The two vertical lines indicate integration range for this channel.

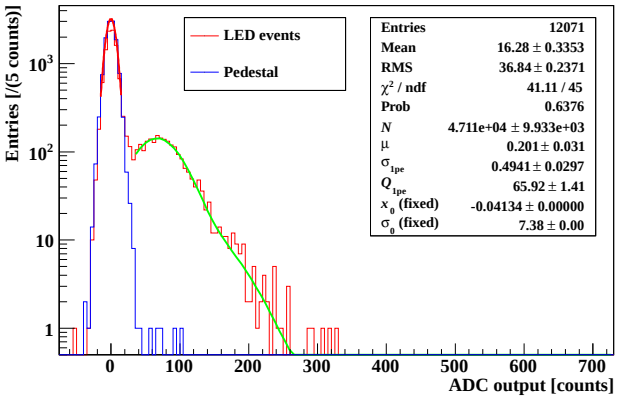

Figure 6.2: Example of fitting for a single photoelectron peak with Eq. (6.1).

6.2 Calibration and stability

6.2.1 Photoelectron calibration and its stability

As the number of photoelectron was used in veto decision, gain of a single photoelectron needed to be measured to calibration outputs of the detector. Such measurement was done for all channels with Light Emitting Diodes (LEDs), which were installed for each PMT as shown in Fig. 2.24. Here, light intensity of the LEDs was adjusted so that the PMT observed $O(0.1)$ photoelectron in average. The data was taken with the same waveform digitizers as were used in the physics data taking, and an example of waveform output in LED trigger events is shown in Fig. 6.1. Pedestal of each event was obtained as described in Sec. 4.2.2 and an "ADC output" was defined as a partial integral of obtained waveform after subtracting pedestal. The width of integration range was fixed to 60 samples or 120 ns and its timing inside 256 samples of an event window was adjusted channel by channel so that pulses from LEDs was completely contained. Finally, the distribution of the partial integral was fitted with the convolution function of Gaussian and Poisson distribution:

$$f(x) = N \sum_{n=1}^{10} \frac{\mu^n e^{-\mu}}{n!} \frac{1}{\sqrt{2\pi\sigma_n^2}} \exp\left(-\frac{(x - nQ_{\mathrm{1pe}} - x_0)^2}{2\sigma_n^2}\right), \tag{6.1}$$

where N, x, μ, σ_n, Q_{1pe} are a normalization factor, ADC output, a mean light yield of LED, width of a n-photoelectron peak and gain of a single photoelectron, respectively. By using σ_0 and σ_{1pe}, which were width of peaks for the pedestal and single photoelectron, respectively, σ_n was defined as $\sigma_n = \sqrt{n\sigma_{\mathrm{1pe}}^2 + \sigma_0^2}$. x_0 was a pedestal value obtained by fitting the partial integral defined above for clock trigger events, which were taken without flashing LEDs. σ_0 was also taken as a result of the fitting and these were used as fixed parameters in fitting the LED data with (6.1). An example of fitting is shown in Fig. 6.2.

Stability of single photoelectron gain during the physics run period was also studied. Measurement of one photoelectron gain was performed run by run, where each run corresponded to one hour data taking. Data was acquired in parallel with beam data taking as well as cosmic ray data

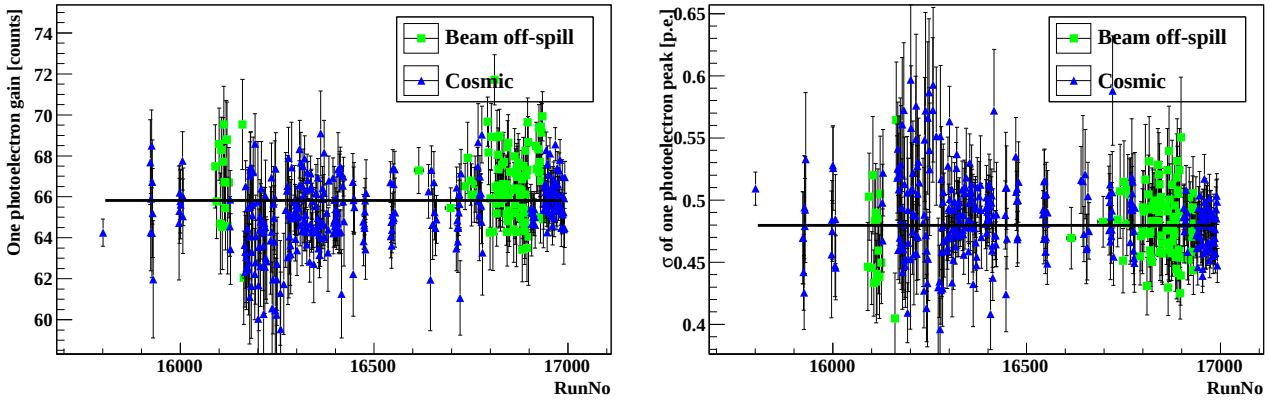

Figure 6.3: Examples of single photoelectron gain history (left) and σ of its peak (right). Results for the channel 1, south side of the most upstream module are shown. A cluster of green markers in the left (right) side corresponds to data in April (May) beam time. The range of horizontal axes correspond to approximately one month. Blue points are data taken in parallel with cosmic data acquisition and green points are based on data during the beam operation. The black lines indicate fitting with a constant function.

taking when the accelerator was not in beam operation. Figure 6.3 shows an example of history of measured single photoelectron gain ($Q_{1\mathrm{pe}}$ in Eq. (6.1)) and resolution of its peak ($\sigma_{1\mathrm{pe}}$ in Eq. (6.1)), respectively. Here, only runs with enough number of events and proper light intensity of LEDs were analyzed for each channel[*1]. In data during the physics runs, events only in the off-spill period, whose detailed definition is described in Sec. 6.3.1, were selected to avoid contribution from beam particles. Stability during the beam on-spill timing is discussed also in Sec. 6.3.1. In this channel of Fig. 6.3, data for the whole run period of one month including the physics data taking period was available. The standard deviation of one photoelectron gain was 2.7% through the monitor period and the gain was found to be quite stable during the data taking. The final calibration constant was decided by fitting this history of one photoelectron gain with a constant function. Stability for others channels was also examined. Figure 6.4 shows the standard deviation over mean value for channels with enough data is available. Although LED light intensity was not adjusted properly for all the 24 channels and there were several channels without enough data to evaluate stability[*2], gain during the run period was found to be stable within 5% in all the monitored channels.

6.2.2 Photoelectron yield of aerogel

The photoelectron yield against relativistic charged particles was measured to tune the photoelectron yield in the MC simulation and monitor the stability of aerogel. Data in the beam muon runs as described in Sec. 3.4.1 was used. Charged particle events were tagged by requiring hits in both the BHCV and BHTS detector, each of which was located in the upstream and downstream of

[*1] At least 5 000 LED trigger events were required and the mean observed photoelectron yield μ' was needed to satisfy $0.05 < \mu' < 2.0$ p.e. The μ' value was calculated from a ratio of pedestal events to the total number of LED events with an assumption of Poisson statistics.

[*2] This was due to lack of LED drivers and only 12 LEDs were available in this beam time. Hence only either of two LEDs installed in each module was used and it was difficult to adjust light intensity properly for both channels. Originally, longer beam time was scheduled and monitoring channels were planned to be switched.

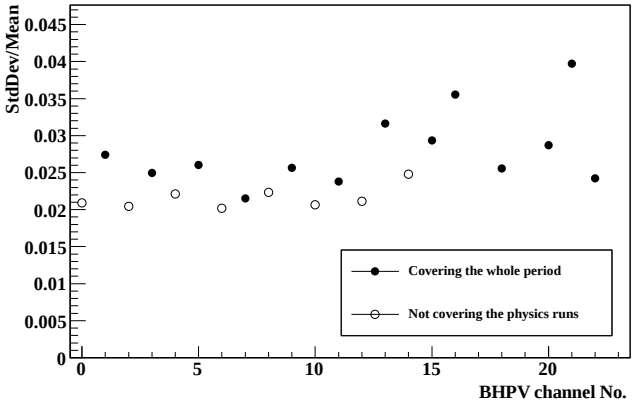

Figure 6.4: Result of single photoelectron gain stability for each channel. Data for three channels are absent, and those indicated with open circles do not cover the May beam time period.

BHPV, respectively as shown in Fig. 6.5. In addition to the above selection, hits in all the other BHPV modules than that to be calibrated were required. This was to select only relativistic charged particles, whose velocity was higher than that of Čerenkov threshold, and reduce velocity-dependence of photoelectron yields. Here, the hit of a module was identified by observation of photoelectron yield larger than 2.5 p.e. as a sum of the two channels of the module. Note that the analysis in this section and Sec. 6.2.3 was based on photoelectron yield from an integral of all the 256 samples and constant fraction timing with the maximum point among all the 256 samples.

An example of photoelectron distribution for a module is shown in Fig. 6.6. The photoelectron yield in each event was defined as a sum of those from the two channels in the module. The calibration factor in the MC simulation was tuned so that the most probable photoelectron yield agreed to that of the data in each module[*3]. The result is shown in Fig. 6.7. The photoelectron yields in all modules ranged from 6.6 to 8.6 and this could be also confirmed with the following analytical calculation. The number of photons emitted in Čerenkov radiation is written as

$$\frac{\mathrm{d}N}{\mathrm{d}x\mathrm{d}E} = \frac{\alpha}{\hbar c} z^2 \sin^2\theta, \tag{6.2}$$

where energy of emitted photon is taken as a variable in Eq. (5.37). Considering efficiency of photon detection, observed number of photoelectrons, denoted as N_{obs} is expressed as follows:

$$N_{\mathrm{obs}} = \frac{\alpha}{\hbar c} z^2 \sin^2\theta \int_0^T \int \epsilon(x,E)\mathrm{d}x\mathrm{d}E, \tag{6.3}$$

where T is thickness of aerogel and $T = 5.9$ cm and $\alpha/(\hbar c) = 370\ \mathrm{eV}^{-1}\mathrm{cm}^{-1}$. Dispersion of aerogel was neglected in Eq. (6.3) and $\sin^2\theta$ does not depend on photon energy. For $n = 1.03$, $\sin^2\theta = 0.057$. $\epsilon(x,E)$ is photon detection efficiency including photon scattering in aerogel, reflectance by mirrors, and quantum efficiency (Q.E.) of PMT. This was decomposed as

$$\epsilon(x,E) = \epsilon_{\mathrm{ref}}\epsilon_{\mathrm{scat}}(x,E)\epsilon_{\mathrm{Q.E.}}(E), \tag{6.4}$$

[*3]This tuning was performed using data of beam time in March, 2013.

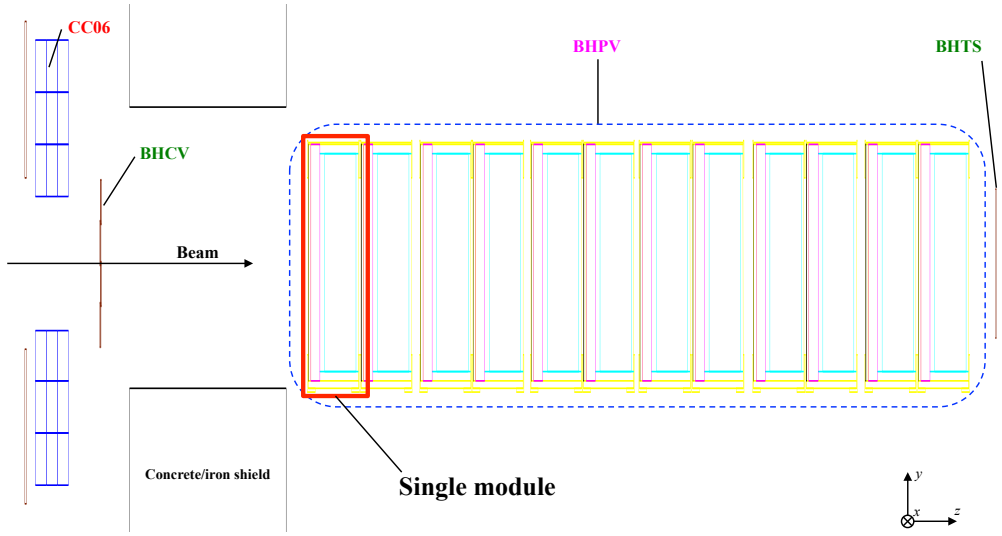

Figure 6.5: Layout of the downstream detectors.

where each factor represented losses in reflection by mirror, scattering in aerogel, and Q.E. of PMTs. Survival probability by scattering in aerogel was given as $\exp\left(-\frac{T-x}{\Lambda}\right)$ for photons generated at position x, where Λ was scattering length and given ϵ_{ref} is given as 0.65[*4]. Using catalog values for the PMT Q.E., energy and position integral of ϵ is obtained as 0.515 eV·cm. Finally, Eq. (6.3) gives 10.9 photoelectrons for $n = 1.03$ as an expected number of observed photoelectron yield against relativistic charged particles. Considering calibration factors, this number well agreed to the observed photoelectron yield.

Stability of the photoelectron yield during the run period was also examined. The result is shown in the left of Fig. 6.8. Any significant decrease or increase of photoelectron yield was not observed. More quantitatively, stability for each module was evaluated by calculating standard deviation over mean. This value are shown in the right of Fig. 6.8 and is found to be smaller than 5% for all modules. From these observations, the conclusion was obtained that aerogel used for this detector worked properly in the physics data taking period without any serious damage even under a hard radiation environment.

6.2.3 Timing calibration

The timing offsets difference among channels, which derived from various matters such as difference in PMT transit time and cable length, needed to be correct in order to get better timing resolution. Such correction values, referred to as timing calibration constants, were measured by the beam muon runs. The event selection was slightly different from that for aerogel light yield measurement in the previous section. Coincidence of hits in two BHCV module in the same vertical position was required. in order to ensure that a tagged charged particle passed around the center in the horizontal direction, For the selected events, distribution of timing difference between two channels for all the possible pair is obtained and it is fitted with a Gaussian. The fit mean value and its

[*4] Assuming twice reflections at the flat mirror (85%) and the Winston cone (85%) as well as transmittance of a polyvinylidene chloride sheet located just downstream of aerogel tiles (90%).

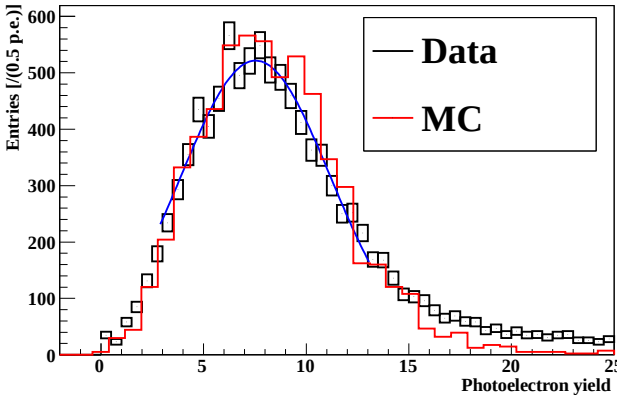

Figure 6.6: Example of photoelectron distribution in a muon run. The blue line is a fit result with a Gaussian for data.

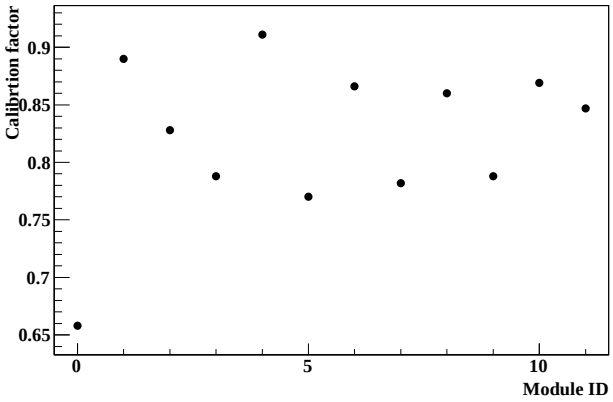

Figure 6.7: Calibration factors for all modules obtained as a result of a muon run.

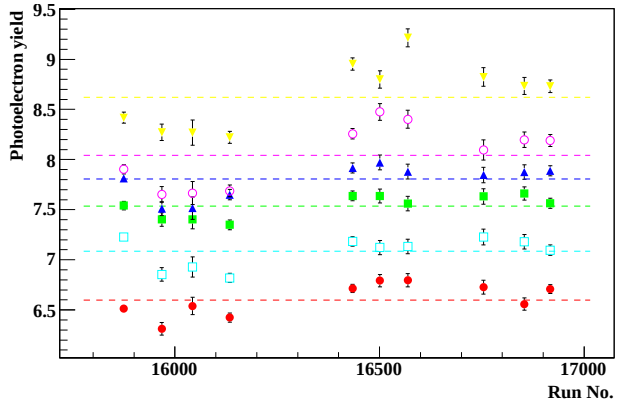

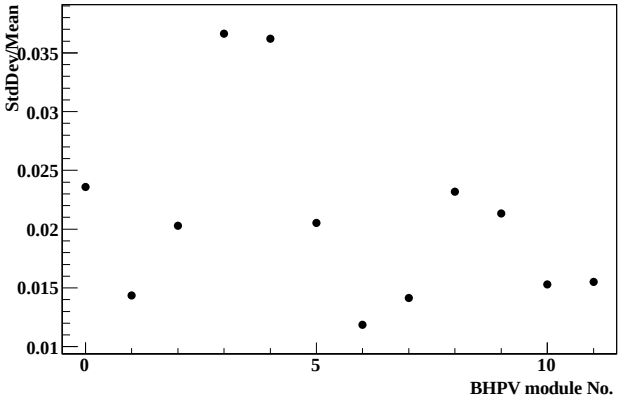

Figure 6.8: Stability of aerogel light yield measured in muon runs. The right figure shows history of observed photoelectron yield in upstream six modules. Dashed lines are fit results with constant functions. The left one shows its standard deviation over mean value for all modules.

error for the channel pair of i and j were denoted as t_{ij} and Δt_{ij}, respectively. Then, the timing calibration constant for each channel, denoted as t_i, was calculated so as to minimize the following χ^2:

$$\chi^2 = \sum_{i>j} \frac{(t_{ij} - t_i + t_j - \mathrm{TOF}_{ij})^2}{(\Delta t_{ij}^2 \oplus \delta\mathrm{TOF}_{ij} \oplus \delta\mathrm{BHCV})^2}. \tag{6.5}$$

TOF_{ij} is the Time Of Flight between two modules corresponding to the channel i and j, which was calculated by assuming velocity of charged particles to be $\beta = 0.985 \pm 0.015$. Detail of the flight length is described in Sec. 4.4.3. Error of TOF_{ij}, written as $\delta\mathrm{TOF}_{ij}$, was calculated as a quadratic sum of alignment error of 1 mm and that of β. δBHCV is time of light propagation for 9 mm region of two overlapping region. An example of result of minimization is shown in Fig. 6.9. Here, minimization was perfumed by Minuit package in ROOT. The minimized χ^2 value in the example was 19.52 for the number of degree of freedom 23 and a typical error for each parameter is around 25 ps. This χ^2 value means good convergence of the minimization process and indicates

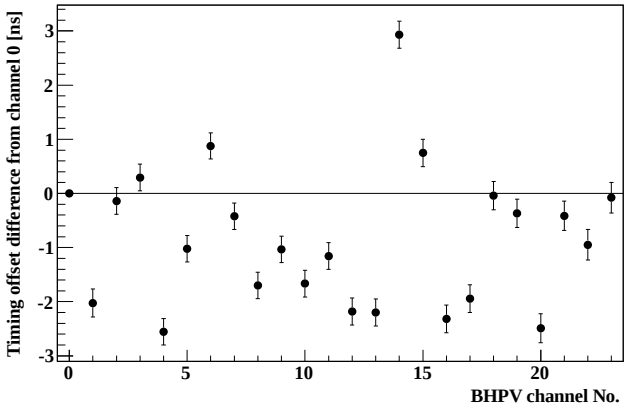

Figure 6.9: An example of timing calibration result. Error bars are enlarged by a factor of 10. Channel 0 was taken as the standard, and the value for this channels is exactly 0 by definition.

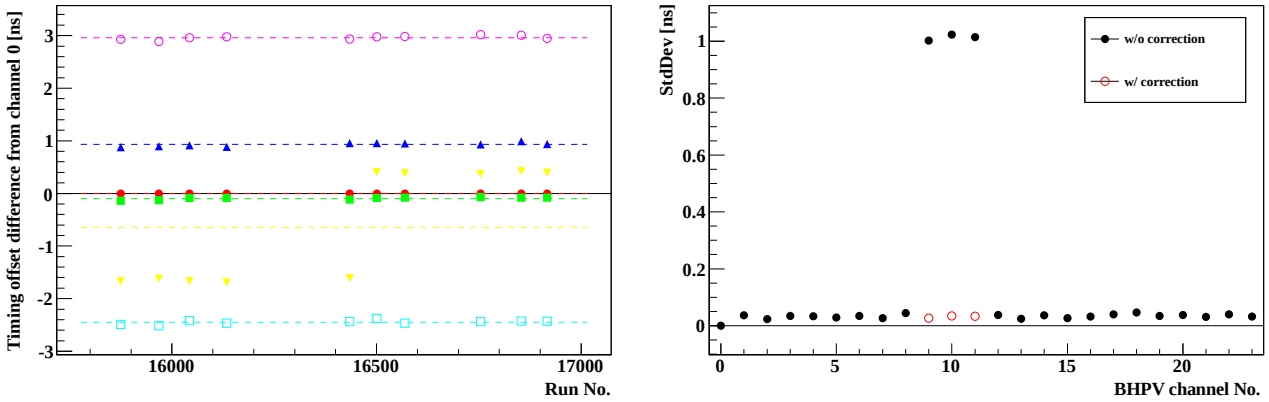

Figure 6.10: Results of timing calibration for all channels. The left figure shows history of selected six channels. Each color correspond to history of one channel and yellow color is one of the three channels with discontinuous shift. The right one shows standard deviation value for all channels.

the calibration constants were calculated properly with this method. In addition, the error value was much better than timing resolution of this detector, ∼500 ps and the detail will be discussed later, and shows enough precision of this calibration method.

This timing calibration was performed in every muon run and stability of the calibration constants was examined. Example of history for several selected channels is shown in the left of Fig. 6.10. In three channels among twenty-four, discontinuous shifts were observed as shown in the yellow points in the left of Fig. 6.10. This shift was considered to derive from ADC operation since width of this shift was consistent with exactly 2 ns or one sampling interval and this shift occurred after updates of firmware in the corresponding ADCs. Although the real cause was not specified, correction of exact 2 ns or one sampling interval gave constant timing offset value, and the standard deviation value of all the muon runs got smaller than 35 ps. Stability for other channels were evaluated with the standard deviation value of history and result for all the channels are shown in the right of Fig. 6.10. With the correction, timing offset values were found to be stable within 40 ps.

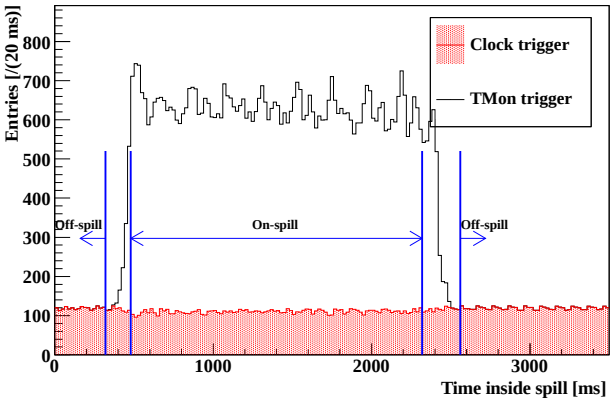

Figure 6.11: Distribution of event timing inside a spill.

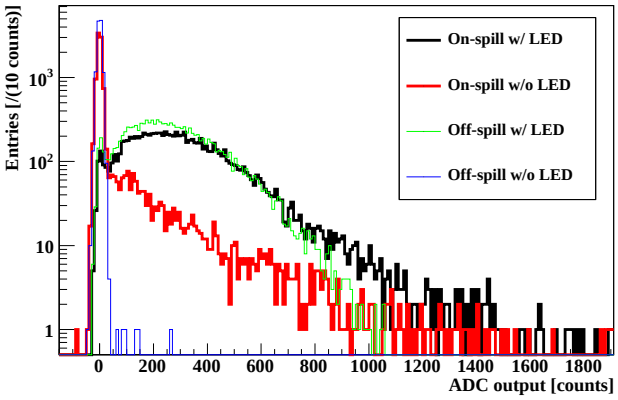

Figure 6.12: Example of ADC outputs in on/off-spill with and without flashing LED.

6.3 Operation under the intense neutral beam

In this section, performance was evaluated with data taken during the operation in the real neutral beam.

6.3.1 Output stability

During the beam operation, counting rates were very high and these could cause instability of operation of the PMTs. To examine such effect, PMT outputs with LED flashing were compared during on-spill and off-spill timing and their difference was studied. The on-spill and off-spill timing was distinguished by timing inside each spill cycle as shown in Fig. 6.11. As contribution of accidental hits was not negligible in the on-spill LED data, its effect was subtracted by using clock trigger data without flashing LEDs. Defining $\tilde{Q}^{\rm on}_{\rm LED}$ and $\tilde{Q}^{\rm on}_{\rm clock}$ to be ADC outputs, which was calculated as described in Sec. 6.2.1, in LED and clock trigger data during on-spill periods, respectively, and $\tilde{Q}^{\rm off}_{\rm LED}$ and $\tilde{Q}^{\rm off}_{\rm clock}$ to be corresponding values during off-spill timing, following quantity was defined:

$$\frac{\tilde{Q}^{\rm on}_{\rm LED} - \tilde{Q}^{\rm on}_{\rm clock}}{\tilde{Q}^{\rm off}_{\rm LED} - \tilde{Q}^{\rm off}_{\rm clock}}. \tag{6.6}$$

This ratio indicates deviation of PMT outputs during the on-spill timing. Here, $\tilde{Q}^{\rm on}_{\rm LED}$, $\tilde{Q}^{\rm on}_{\rm clock}$, $\tilde{Q}^{\rm off}_{\rm LED}$, and $\tilde{Q}^{\rm off}_{\rm clock}$ were obtained as a mean value of each distribution.

This ratio was calculated for every run and every channel. An example of a certain channel is shown in the left of Fig. 6.13. Most points distributs around 1.00 and gain deviation during high rate period of beam on-spill timing is small. As a measure of stability, the mean value of these ratios were evaluated for other channels. The result is shown in the right of Fig. 6.13. Here, only data with photoelectron yields large enough for the stability evaluation was used. The photoelectron yield, calculated as $\tilde{Q}^{\rm on}_{\rm LED}/Q_{\rm 1pe}$, was required to be larger than 0.5. An average value of photoelectron yield for each channel is also shown in the right of Fig. 6.13. As a result, PMT gain deviation in on-spill timing was as small as around 1% for monitored channels and the detector was operating properly even under the high rate environment.

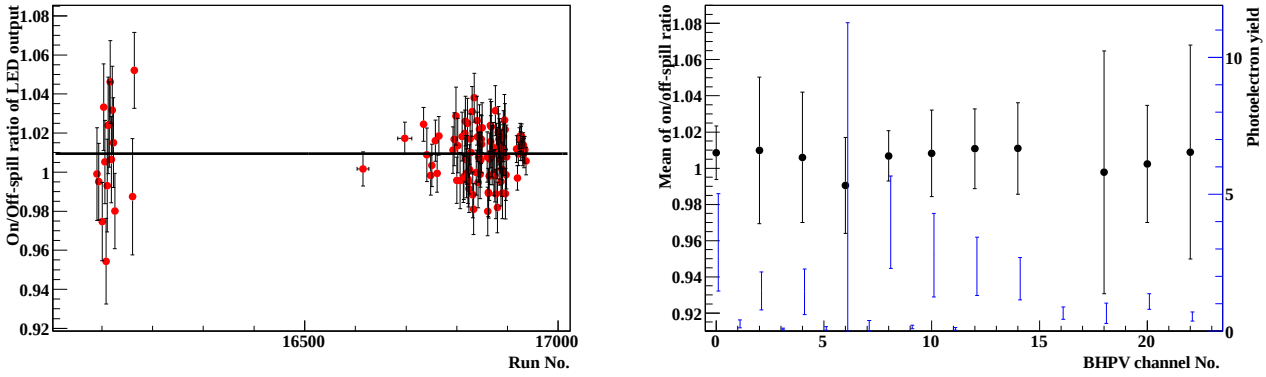

Figure 6.13: History of on-spill and off-spill output ratios. The left figure shows an example of the history for channel 0, north side of the most upstream module. The cluster of points in the left (right) side corresponds to data in April (May) beam time. The black line is a fit result with a constant function. The right one is a mean value of the ratios for each channel. An error bar indicates its standard deviation. Photoelectron yields during the monitor period are also presented with blue lines, where their center and half length indicate mean and standard deviation, respectively.

6.3.2 Single counting rate

To understand the operation of the detector during the physics data taking, its single counting rate was evaluated and compared with results from MC simulations. In the measured data, events taken with the TMon trigger and the clock trigger as described in Sec. 3.3.5 were used for the counting rate evaluation. Since the TMon trigger was issued with a rate proportional to an instantaneous rate of the beam, counting rates measured with this trigger were close to those in the physics trigger events. One the other hand, the clock trigger was insensitive to the beam time structure and hence data taken with this trigger was used to compare the measured rate with simulation expectation. For both trigger types, On-spill events were selected as shown in Fig. 6.11, and the number of pulses in specific 50 ns range was counted for each channel. Threshold for photoelectron yield was set as 2.5 p.e. Finally, the total number of pulses over events was normalized with the number of all events analyzed to obtain a counting rate for the channel. The number of coincidence with three or more modules was also counted with the same way.

In the simulation, results of the beam line simulation [60] were used as inputs for the KOTO detector simulation. In the beam line simulation, interaction of primary protons in the target and transportation of the secondary particles through the collimators were simulated. Particles which reached the exit of the second collimator, mainly γ, neutrons and K_L, were collected and used as incident particles of the following detector simulation. Since the simulated flux of K_L was known to be inconsistent with measurements, K_L incident events were weighted with a factor of 1.76 in the simulation to fit the measurement result [63, 64]. Although the real target was made of gold, the platinum target was used in the beam line simulation as described in Sec. 2.2.4.

Data/MC comparison of single counting rates for all the channels as well as the coincidence rate is shown in the top of Fig. 6.14 and a ratio of the observed rate with the clock trigger to the MC expectation for each channel is in the bottom of Fig. 6.14. The data was taken with dedicated runs where trigger decision was made only by clock or TMon signals in order to avoid effect of dead time

Table 6.1: Fluxes of particles with the 9-cm-thick absorber with the beam line simulation. The scale factor for K_L to fit the simulated yield to the measured value with the 9-cm-thick absorber was assumed to be the same with that in case of the 7-cm-thick absorber.

Particles	Flux for 2.0×10^{14} P.O.T.	Ratio to 7 cm absorber
γ (> 1 MeV)	8.31×10^8	0.38
γ (> 50 MeV)	7.55×10^6	0.55
neutron (> 1 MeV)	1.10×10^9	0.79
neutron (> 1 GeV)	1.33×10^8	0.83
K_L	3.69×10^7	0.88

due to [*5]. The beam intensity was 24 kW and the photon absorber with the nominal thickness of 7 cm was inserted. The simulation result showed beam photons dominantly contributed to the counting rate and the largest difference between the measured and expected rates was 60%, where the clock trigger data was used for the rates by the measurement. This difference was reasonable considering the beam line simulation involved hadronic interactions in the target with protons and there would be large uncertainty in fluxes and spectra. Distribution of the number of coincidence modules is shown in Fig. 6.15. Even the distribution ranged over several magnitudes of orders, the MC agreed to the data within a factor of 2.

There existed a factor of 2.4 difference between measured rates with two types of triggers. Since the TMon trigger was made with a rate proportional to as instantaneous beam intensity, this difference meant non-uniformity of the spill time structure. The ratio was found to be consistent with an inverse of duty factor provided by the hadron beam group and such time structure was well measured by this detector.

Counting rates with a different beam condition were compared. Figure 6.17 shows results of counting rate ratio with the thicker photon absorber of 9-cm length and the default one. Quantitatively, beam photons were expected to be reduced drastically compared to hadrons, namely neutrons and K_Ls thanks to relatively short radiation length compared to hadron interaction length of the absorber material, lead. This is shown in Fig. 6.16 and Table 6.1. The number of low energy photons, which mainly contributed the BHPV single counting rates, was reduced to less than half while neutron and K_L components decreased only by $10 - 20\%$ independently on their kinetic energy or momentum. Counting rates measured with the two kinds of the photon absorbers under the same beam intensity of 15 kW were compared channel by channel. As expected, the single rate was decreased to 35% in the upstream modules as shown in Fig. 6.17 and this was almost consistent with the simulation expectation shown in Table 6.1. This fact showed the counting rate of this detector when placed in the neutral beam was dominated by the photon component, not neutron and indicated that the detector was well blinded to neutrons as expected for the upstream module. Although rate ratios for downstream modules of the data were larger than simulation expectations, they were still smaller than 0.8, or expected flux ratio of neutrons and neutrons did not contribute dominantly for these modules.

Finally, absolute measured rates were evaluated with respect to influence to the experiment.

[*5] These triggers were mixed in regular runs for physics data and data taken with such a condition was also available for this analysis. However, counting rates measured using these trigger suffered bias due to the dead time of the Level 2 trigger system as described in Sec. 3.3.1. Since this dead time occurred more frequently with higher instantaneous rate, events with lower rate were triggered more often and observed counting rates were evaluated to be smaller.

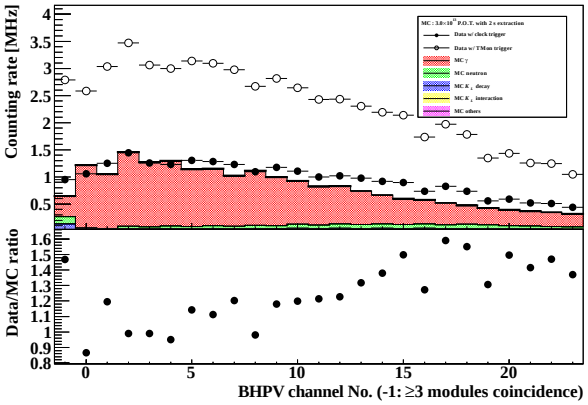

Figure 6.14: Results of counting rate measurement. Ratios of measured rate with the clock trigger to the simulation result for each channel are shown in the bottom part. The most left bin indicates the coincidence rate. Among other bins, smaller channel numbers correspond to upstream modules, and channels with neighboring even and odd numbers belong to the same module.

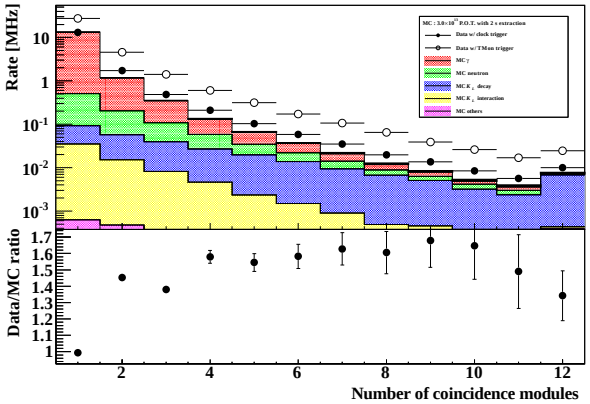

Figure 6.15: Distribution of the number of coincidence modules in simulation and measurement data. Ratios of measured rate with the clock trigger to the simulation result are shown in the bottom part.

High counting rates can cause instability of PMT operation and large signal loss due to overveto. In order to evaluate the former issue, average ADC counts in the random trigger events were converted to average output current as follows

$$\epsilon \frac{V_{\max}}{2^n Z} \sum \left(\frac{\sum_{i=0}^{255} a_i}{256} \right) / N, \tag{6.7}$$

where $V_{\max}$ and n are voltage and the number of bits for the full range of the ADCs, respectively, Z was the input impedance, a_i $(i = 0, 1, \cdots, 255)$ was an ADC count after subtracting pedestal, N was the total number of events, and ϵ was a small correction factor to take an attenuation effect by cables into account. Each variable was given as $V_{\max} = 2$ V, $n = 12$, $Z = 50$ Ω and $\epsilon = 1.21$. A calculated current value with Eq. (6.7) for each channel is shown in Fig. 6.18. As the PMT base current was 1.4 mA for all channels, ratios of this value to the output anode current for all the channels were larger than a factor of 35 and satisfied the requirement of the minimum value of 20, which was needed for proper operation [104].

The signal loss was evaluated with the rate of coincidence. Using coincidence rate of 2.8 MHz, which was measured with the TMon trigger and shown in Fig. 6.14. Assuming length of veto window to be 15 ns, which would be used in $K_L \to \pi^0\nu\overline{\nu}$ analysis in the next chapter, signal loss was estimated to be

$$1 - \exp(-(2.8 \text{ MHz} \times 15 \text{ ns})) = 4.1\%. \tag{6.8}$$

Although more realistic estimation, where correlation with other detectors should be considered, was needed, the loss was found to be small enough in $K_L \to \pi^0\nu\overline{\nu}$ search.

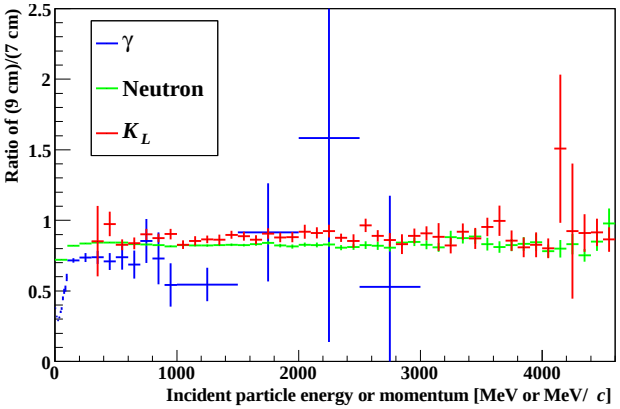

Figure 6.16: Ratios of beam particle fluxes with the 9-cm-thick absorber to those with the 7-cm-thick one for various energy or momentum region. Only contribution from K_L was measured in units of MeV/c and others were measured with the MeV unit.

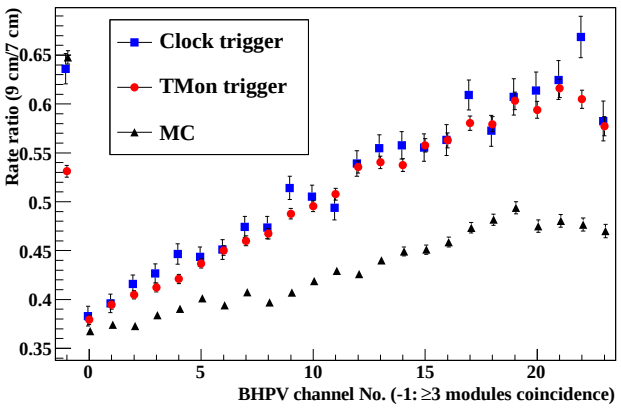

Figure 6.17: Comparison of counting rates with different the γ absorbers.

6.4 Evaluation of response to high energy photons

Finally, response of this detector against incidence of high energy photons was evaluated. For this purpose, the $K_L \to 3\pi^0$ decay with one missing photon, part of which hits the BHPV detector, was tagged by requiring five clusters on the calorimeter. Below, procedures to reconstruct such events are described and the photon detection by this detector is demonstrated. The remaining sections are dedicated to more quantitative discussions, where reproducibility of the MC simulation and detection efficiency were evaluated together with their systematic uncertainty.

6.4.1 Reconstruction of $K_L \to 3\pi^0$ with five clusters on the calorimeter

Reconstruction of K_L mass

For the selection of events mentioned above, K_L mass was reconstructed from the five clusters on the calorimeter assuming each of these cluster came from five among six photons in $K_L \to 3\pi^0 \to 6\gamma$ decays. Though basic methods of reconstruction were similar to that in case of reconstructing K_L from six clusters as described in Sec. 4.3.4, there were several points to be considered due to the difference in the number of π^0s available to determine the K_L z vertex. Thus, detailed procedures for calculation of K_L z vertex position were as follows:

1. select four among the five clusters to make two pairs of clusters
2. reconstruct two π^0s for each pair of two clusters assuming x and y vertex to be zero to obtain its z vertex position
3. calculate z vertex position of the parent K_L as a weighted average of the above vertex positions
4. apply the processes 1.-3. for all the 15 possible combinations of clusters[*6]

[*6] Strictly speaking, as two solutions of π^0 vertices could exist for each photon pair, $2 \times 2 \times 15 = 60$ patterns can exist at maximum.

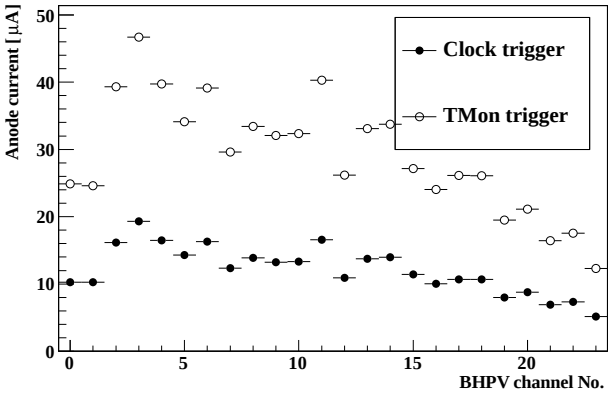

Figure 6.18: Average output current calculated from ADC data.

5. select the "best" combination among all combinations in the process 4.

6. make corrections for energies and positions of five clusters based on the K_L z position obtained in the process 5.

7. apply all the above processes with the updated five clusters in the process 6. again

Here, the two π^0s which were reconstructed from four out of the five clusters were assumed to share their vertices. The selection of the "best" combination in the process 5. was based on the z-vertex χ^2 as was defined in Sec. 4.3.4.

As the next step, 3-momentum of the missing γ was reconstructed based on the z vertex position of the parent K_L obtained above. Below, the number of 1-5 was assigned for each of the five photons on the calorimeter like γ_1, γ_2, $\cdots$, γ_5 and the number 6 was assigned for the missing γ, which did not hit the calorimeter. γ_5 was for the cluster which was not used in the reconstruction of the two π^0s. Additional assumptions were introduced for this reconstruction process. First, transverse momentum of the parent K_L was assumed to be zero in order to get x and y components of γ_6 from the following equations:

$$P_x \sim 0 \quad = \quad \sum_{i=1}^{6} p_{i,x} \tag{6.9}$$

$$P_y \sim 0 \quad = \quad \sum_{i=1}^{6} p_{i,y}, \tag{6.10}$$

where P_x and P_y are x and y momentum of the parent K_L, respectively, and $p_{x,i}$, $p_{y,i}$ were those for the photon with the number of i. Since $p_{i,x}$ and $p_{i,y}$ for i =1-5 were obtained with the K_L z vertex, $p_{6,x}$ and $p_{6,y}$ were determined. The remaining unknown parameter, z momentum of the missing γ, $p_{6,z}$, was calculated through an assumption that an invariant mass of γ_5 and γ_6 gave the π^0 mass

M_{π^0}. Then, following equation was obtained:

$$\begin{aligned} M_{\pi^0}^2 &= E_3^2 - \sum_{j=x,y,z} P_{3,j}^2 \\ &= (e_5 + e_6)^2 - \sum_{j=x,y,z} (p_{5,j} + p_{6,j})^2 \\ &= (e_5 + \sqrt{p_{6,x}^2 + p_{6,y}^2 + p_{6,z}^2})^2 - \sum_{i=x,y,z} (p_{5,j} + p_{6,j})^2, \end{aligned} \tag{6.11}$$

here, E_3 and $P_{3,j}$ represent energy and momentum x, y or z component of the third π^0, respectively, and e_i is energy of the i-th photon. Equation (6.11) eventually gives a quadratic equation of $p_{6,z}$ when the π^0 mass is assumed and easily solved. Finally, the invariant mass of the K_L was calculated. However, two solutions appear from Eq. (6.11), where one with larger (smaller) $p_{6,z}$ is referred to as "forward" ("backward") solution and the corresponding reconstructed K_L mass was denoted as $M_{K_L}^{\rm forward}$ ($M_{K_L}^{\rm backward}$). In principle, this ambiguity is solved by selecting the solution which gives the proper K_L mass although poor mass resolution makes their separation difficult. The detail is discussed in the following.

Event selection

Several cuts on energy and hit position of reconstructed photons were applied to ensure quality of the reconstruction in advance. They are summarized in Table 6.2. According to MC simulations, forward solution was always correct in events with γ_6 in the geometrical acceptance of BHPV, referred to as "BHPV events." Hence further selection was applied based on reconstructed K_L masses $M_{K_L}^{\rm forward}$ and $M_{K_L}^{\rm backward}$ calculated above, to identify K_L events and to to reduce backward solution events. Events with $M_{K_L}^{\rm forward}$ around the the nominal K_L mass (~500 MeV/c^2) were positively selected while ones with $M_{K_L}^{\rm backward}$ around the K_L mass were removed. Concrete cut range was optimized so as to maximize the following Figure Of Merit (FoM) in the MC simulation:

$$\frac{N_{\rm BHPV}}{N_{\rm total}} \sqrt{N_{\rm BHPV}}. \tag{6.12}$$

Here, $N_{\rm total}$ and $N_{\rm BHPV}$ are the number of events after cuts on reconstructed K_L mass and BHPV events among them. This FoM represented a product of an inverse of statistical precision and a ratio of events with BHPV events to those which passed all event selection. Figure 6.19 shows distribution of $N_{\rm BHPV}/N_{\rm total}$ and $N_{\rm BHPV}$ for various cut ranges of $M_{K_L}^{\rm forward}$ and $M_{K_L}^{\rm backward}$. As seen in the figure, tighter cuts which reduced the number of BHPV events were required in order to obtain larger ratio of these events. As an optimum point with the maximum FoM defined in Eq. (6.12), cut range was determined as follows: 480 $<M_{K_L}^{\rm forward}<$570 MeV/c^2, $M_{K_L}^{\rm backward}<$480 MeV/c^2 and 525 MeV/c^2 $<M_{K_L}^{\rm backward}$.

Distribution of reconstructed K_L mass

Figure 6.20 shows the $M_{K_L}^{\rm forward}$ distribution after the above selection except for the cut on $M_{K_L}^{\rm forward}$ itself. The MC result was normalized so that the number of event after all the selection cuts including $M_{K_L}^{\rm forward}$ cut was the same with that of data. Excellent reproducibility of the MC was confirmed though the peak position was slightly shifted from the nominal K_L mass. This shift was derived from incorrect photon combination in a large number of events. As a reference, reconstructed K_L

Table 6.2: List of event selection cuts for five γ analysis.

total 5 γ energy	>650 MeV
γ energy	>50 MeV
γ hit position	>120 mm in square, <850 mm in radius
distance from the dead channels	>53 mm
rec. K_L mass with forward solution	480 $< M_{K_L}^{\text{forward}} <$570 MeV/$c^2$
rec. K_L mass with backward solution	$M_{K_L}^{\text{backward}} <$480 MeV/$c^2$, 525 MeV/$c^2$ $< M_{K_L}^{\text{backward}}$

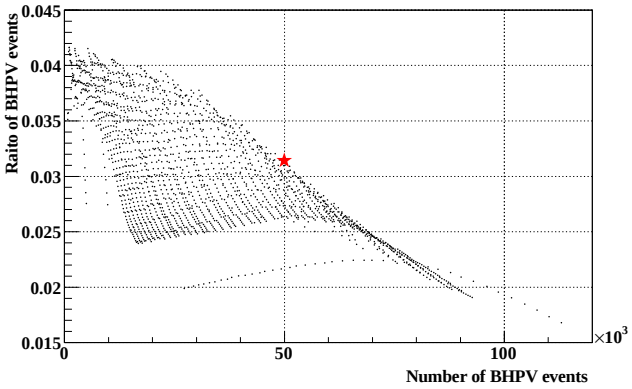

Figure 6.19: Distribution of the number and portion of BHPV events for various cut condition of $M_{K_L}^{\text{forward}}$ and $M_{K_L}^{\text{backward}}$. Each dot corresponds to one cut set of $M_{K_L}^{\text{forward}}$ and $M_{K_L}^{\text{backward}}$. The red star indicates the point with maximum FoM.

mass distribution in six-cluster events is presented in Fig. 6.21. The same event selection as in Table 6.2 except for the K_L mass cuts and the same normalization with the five cluster sample were applied. Although a slight deviation of the K_L mass peak position was seen between the data and the simulation, the numbers of events around the peak region were consistent within the statistical uncertainty of 0.5%.

Hit timing in BHPV

The reconstruction procedure of BHPV hit timing using calorimeter timing is already described in Sec. 4.4.3. The distribution is shown in Fig. 6.22 as well as that obtained in the six-cluster sample. Here, a hit was identified as coincidence with three or more hit modules. In case of the six-cluster events, all photons from the $K_L \to 3\pi^0$ decay hit the calorimeter and no activities associated with the calorimeter hit but only accidental hits were expected. On the other hand, in case of five-cluster events, a missing photon can hit the BHPV detector and a hit at the calorimeter timing is expected in addition to the accidental hits. Such distribution was actually observed as seen in Fig. 6.22: a clear peak existed in the distribution obtained from the five-cluster sample while no such structure was seen in the six-cluster sample. The periodic structure seen in the both distribution stems from

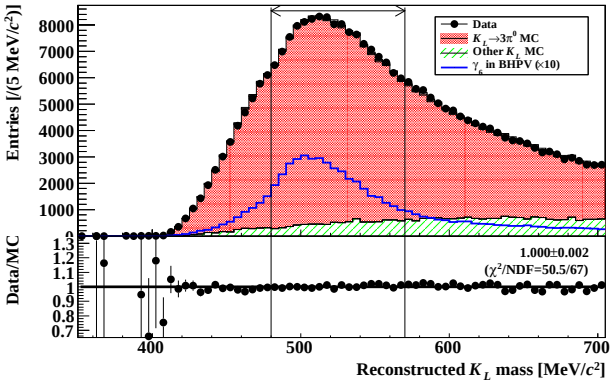

Figure 6.20: Distribution of $M_{K_L}^{\text{forward}}$.

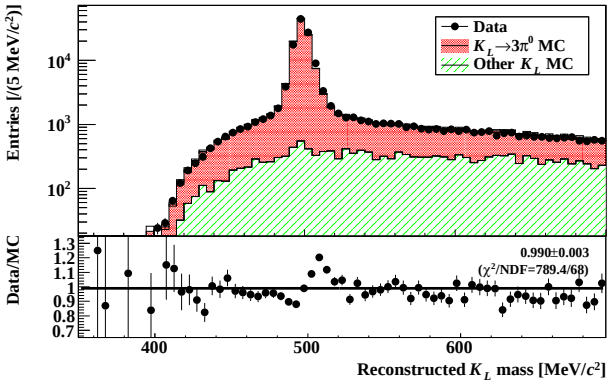

Figure 6.21: Distribution of reconstructed K_L mass from six cluster events.

the "transverse RF" signals applied in the accelerator for improvement of a duty factor of the beam. This RF signal, with frequency of ∼47 MHz, forms bunch structure in the primary proton beam [103] and gives the periodic structure in the hit timing distribution of BHPV.

To subtract the accidental activities, distribution of one-bunch earlier events were used. The comparison and result of subtraction is presented in the top and bottom of Fig. 6.23, respectively. Both distributions showed the excellent agreement in the tail region and a clear peak remains, which correspond the signal coming from photons in $K_L \to 3\pi^0$ decay. Timing resolution, which was evaluated with the Gaussian σ was found to be as good as 0.59 ns.

From the above discussions, capability of photon detection by the BHPV detector is successfully demonstrated. The following sections are dedicated for more quantitative performance for high energy photons.

Understanding of time structure of accidental hits and validation of its subtraction

In the discussion of the previous paragraph, components derived from accidental hits were subtracted using events in the earlier bunch[*7]. The validity of using these events was examined using data samples of the $K_L \to 3\pi^0$ decay. At the first step, timing structure due to the transverse RF was examined. Assuming the primary protons to form a ideal bunch structure, or periodic delta functions with frequency of 47 MHz, hit timing in BHPV would be different between photons which directly came from the target and those from K_L decays due to difference of Time Of Flight between photons and K_Ls. This time difference was named ΔTOF and defined as

$$\Delta\text{TOF} = (L_{\text{beamline}} + Z_{\text{vtx}})/c \times (1/\beta - 1), \tag{6.13}$$

where $L_{\text{beamline}} = 21507$ mm was distance between the target and the upstream edge of FB, and c and β were the speed of light and a ratio of one for a K_L to c. Since the main contribution in BHPV hits derived of beam photons from the target as discussed in Sec. 6.3.2, broad peaks mentioned as accidental hits in Figs. 6.22 and 6.23 were expected to come from such beam photons and they corresponded to bunch timing as the speed of photons was always constant. Hit timing in BHPV

[*7] The "bunch" used in this paragraph was what was made by the transverse RF mentioned in the previous paragraph and was different from what appeared in acceleration of the primary protons in Sec. 2.2.1.

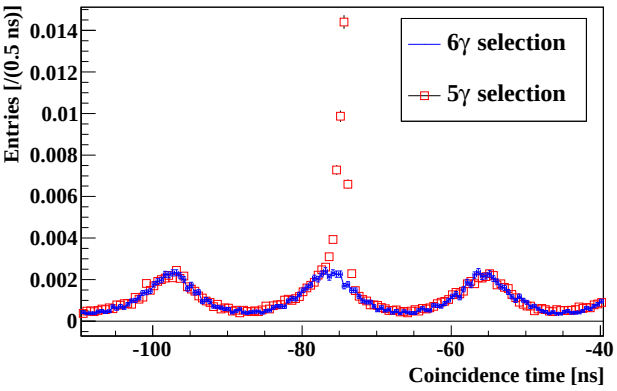

Figure 6.22: BHPV hit timing distribution in five- and six-cluster events.

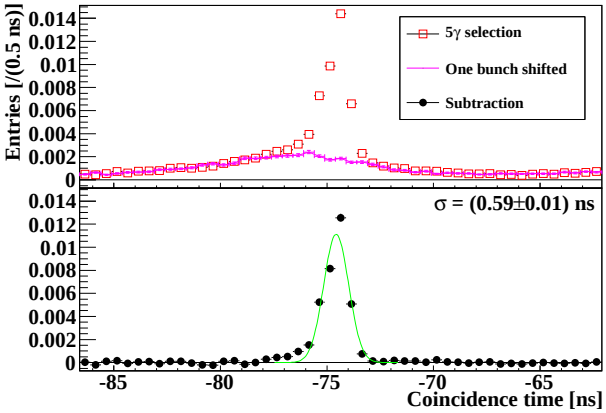

Figure 6.23: (top) Comparison of BHPV hit timing distribution with that from a different bunch in the five-cluster sample. (bottom) Their subtraction. The green line is the fit result with a Gaussian.

was defined with respect to that determined by the calorimeter, hence timing difference should exist between hits from beam photons and K_L decay photons. This is confirmed in Fig. 6.22 or the top of Fig. 6.23: there was seen a finite difference between the peak timing for the broad one and the sharp one, each of which derived from the beam photons and ones from the target, respectively. The interval of ∼2 ns was also consistent with an expectation from simulations. More quantitative confirmation was possible, where $K_L \to 3\pi^0$ decays were reconstructed and ΔTOF was calculated using reconstructed K_L energy E_{K_L} and z vertex position $Z_{\rm vtx}$ as

$$\Delta{\rm TOF}_{\rm rec} = (L_{\rm beamline} + Z_{\rm vtx})/c \times \left(\sqrt{\frac{E_{K_L}^2}{E_{K_L}^2 - M_{K_L}^2}} - 1 \right). \tag{6.14}$$

As another advantage of this event sample, all the photons from the parent K_L hit the calorimeter and no activities associated with the K_L decay existed, which enabled pure observation of beam particles. The left of Fig. 6.24 shows timing distribution of BHPV ≥ modules coincidence in all $K_L \to 3\pi^0$ events[*8] with and without event-by-event ΔTOF correction, where the correction meant to add $\Delta{\rm TOF}_{\rm rec}$ to BHPV coincidence timing. Width of the peaks with this correction got shaper. Events were categorized by $\Delta{\rm TOF}_{\rm rec}$ values with 0.5 ns step and peak timing was examined as a function of $\Delta{\rm TOF}_{\rm rec}$. Correlation of observed peak timing and expected timing from $\Delta{\rm TOF}_{\rm rec}$ values is shown in the right of Fig. 6.24. Obtained peak timing if found to change linearly to $\Delta{\rm TOF}_{\rm rec}$ and the slope of the fit line is closed to 1. These analysis demonstrated that ΔTOF was properly reconstructed in the $K_L \to 3\pi^0$ events and beam timing structure arising from ΔTOF of beam particles was well understood. They also proved that the intrinsic timing width of bunches due to the transverse RF was given as that of the peak in the right of Fig. 6.24 divided by $\sqrt{2}$ and would be $\sigma = 1.8$ ns, considering that both triggered K_Ls and observed beam particles should suffer timing fluctuation.

[*8] In this analysis, trigger types were not distinguished.

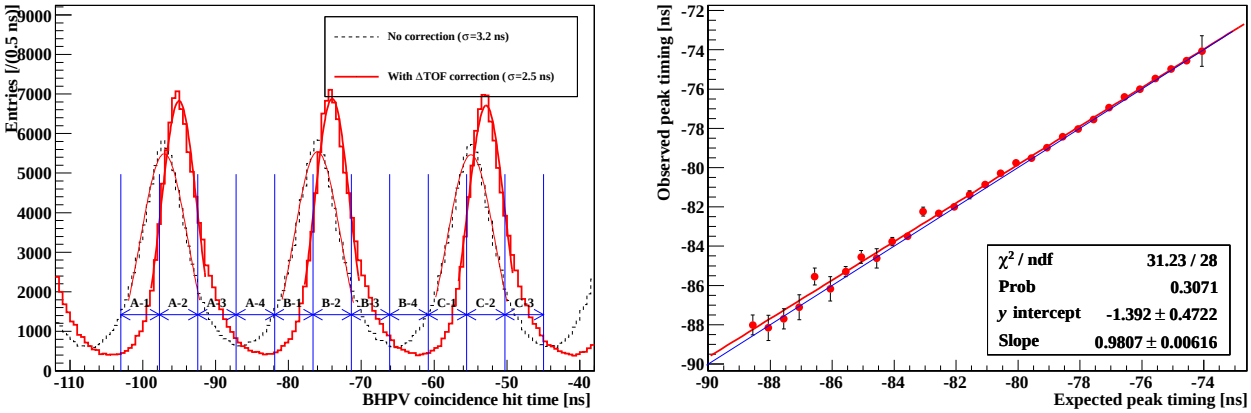

Figure 6.24: Timing distribution of BHPV modules coincidence in $K_L \to 3\pi^0$ events (left) and correlation of expected and observed peak timing for each of given $\Delta\text{TOF}_{\text{rec}}$ regions (right). The dashed (solid) histogram in the left panel is for distribution before (after) correction with $\Delta\text{TOF}_{\text{rec}}$ and the red lines are Gaussian fitting for each peak. Width of fitted peaks for the central one in each histogram is given as their σ values in the legend. Blue lines and arrows with labels for the solid histogram are for the following analysis in Figs. 6.25 and 6.26, where "A," "B" and "C" are labels for each bunch and "1" - "4" for timing inside each bunch. In the right figure, the expected timing is given so that timing of the most left point is the same value with the observed timing. The blue line indicates a line with slope equal to 1.

As the second step, energy spectra for various timing were compared in BHPV as well as BHCV. Again, $K_L \to 3\pi^0$ samples were used and distribution of the number of coincidence modules in BHPV or energy in BHCV corresponding to each timing region shown in the right of Fig. 6.24 was compared. Figure 6.25 is comparison of distribution inside a bunch cycle, label as "B" in the right of Fig. 6.24. Observed spectra showed significant difference for each region. Distribution for BHCV showed an interesting characteristic, where larger energy components contributed more in the valley and earlier tail region, labeled as "B-4" and "B-1" in the right of Fig. 6.24, corresponding to large ΔTOF or slow particles. This could be interpreted as increase of contribution from slow neutrons compared to photons. In Fig. 6.26, such distributions for different bunch cycles were compared. The fit result for all the ratio graphs in Fig. 6.26 were consistent with 1 within 3% and the detector response was found to be identical for the same timing inside each bunch with this precision. These results showed accidental hits were stable bunch by bunch and the method of subtracting accidental components using a one-cycle earlier bunch was well validated.

6.4.2 Response to high energy photons

From the selected data, response to high energy photons was evaluated by using the result of MC simulations. Events within ± 7.5 ns from the peak in Fig. 6.22 or Fig. 6.23 were selected and various distributions were compared between the data and MC. In order to remove contribution from accidental hits, the same distribution of events for one-bunch-cycle earlier timing was subtracted in the analysis of measurement data as was done in Fig. 6.23. For the MC distribution, timing struc-

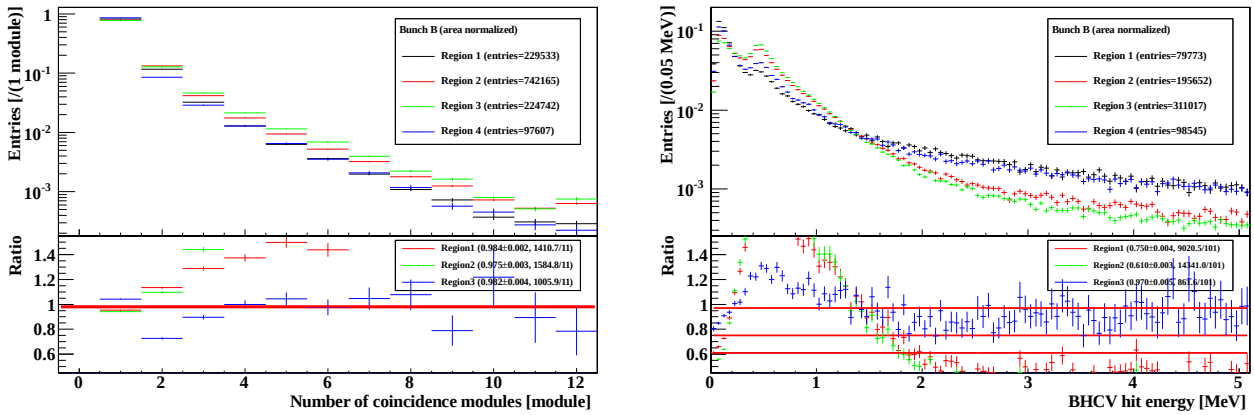

Figure 6.25: Comparison of distribution of coincidence modules in BHPV (left) and energy in BHCV (right) for different timing region in a bunch cycle. In both of the left and right panel, all the histograms in the top parts are normalized so that the total integral would be 1 Ratios of each histogram to that for Region 1 are shown in the bottom part, each of which was fitted by a constant function and the fit result is in the legend.

ture of accidental hits due to the transverse RF was not considered and corresponding distribution with accidental effect does not reproduce that of data, although accidental overlay is necessary to consider "fusion effect" in confidence identification, where hits by a true photon and accidental hit are identified as a single coincidence hit. However, by applying the same procedure with data, contribution from true photons hits was extracted. An example for distribution of total photoelectron yields is shown in Fig. 6.27. Even though there was discrepancy between those of the data and MC before accidental subtraction as in the left panel, those after subtraction agree well as in the right of the figure. Other distributions after accidental subtraction are presented in Fig. 6.28 and Fig. 6.29. Again, the MC well agrees to the data. Reproducibility of accidental overlay in the MC is considered as a source of systematic uncertainty and described in Sec. 6.4.3.

To make quantitative discussion concerned to photon detection efficiency, the number of events with a large photoelectron yield were compared between the data and MC. As seen in Fig. 6.27, most of events with a total photoelectron yield larger than 200 come from hits by photons with energy greater than 1 GeV, where the fraction of such events was 90.3% from the MC simulation. Agreement of the numbers of such events between the data and MC is hence a good indication of understanding and reproducibility of the response to high energy photon in the simulation. Now, η value is defined as $\eta = N_{\mathrm{data}}^{>200\mathrm{pe}}/N_{\mathrm{MC}}^{>200\mathrm{pe}}$, where $N_{\mathrm{data}}^{>200\mathrm{pe}}$ and $N_{\mathrm{MC}}^{>200\mathrm{pe}}$ were the number of events with photoelectron yield larger than 200 in data and MC, respectively. If this value is close to 1, it indicates the detector worked as expected in the MC simulation. By integrating histograms in Fig. 6.27 for photoelectron yield larger than 200, it was found that

$$\eta = 1.025 \pm 0.050 \pm 0.068, \tag{6.15}$$

where the first and second error were statistical and systematic one. Methods of estimation for the systematic errors are explained in the next section. The obtained η value was consistent to 1 within the errors and this fact indicates the detector owned expected detection efficiency to high energy

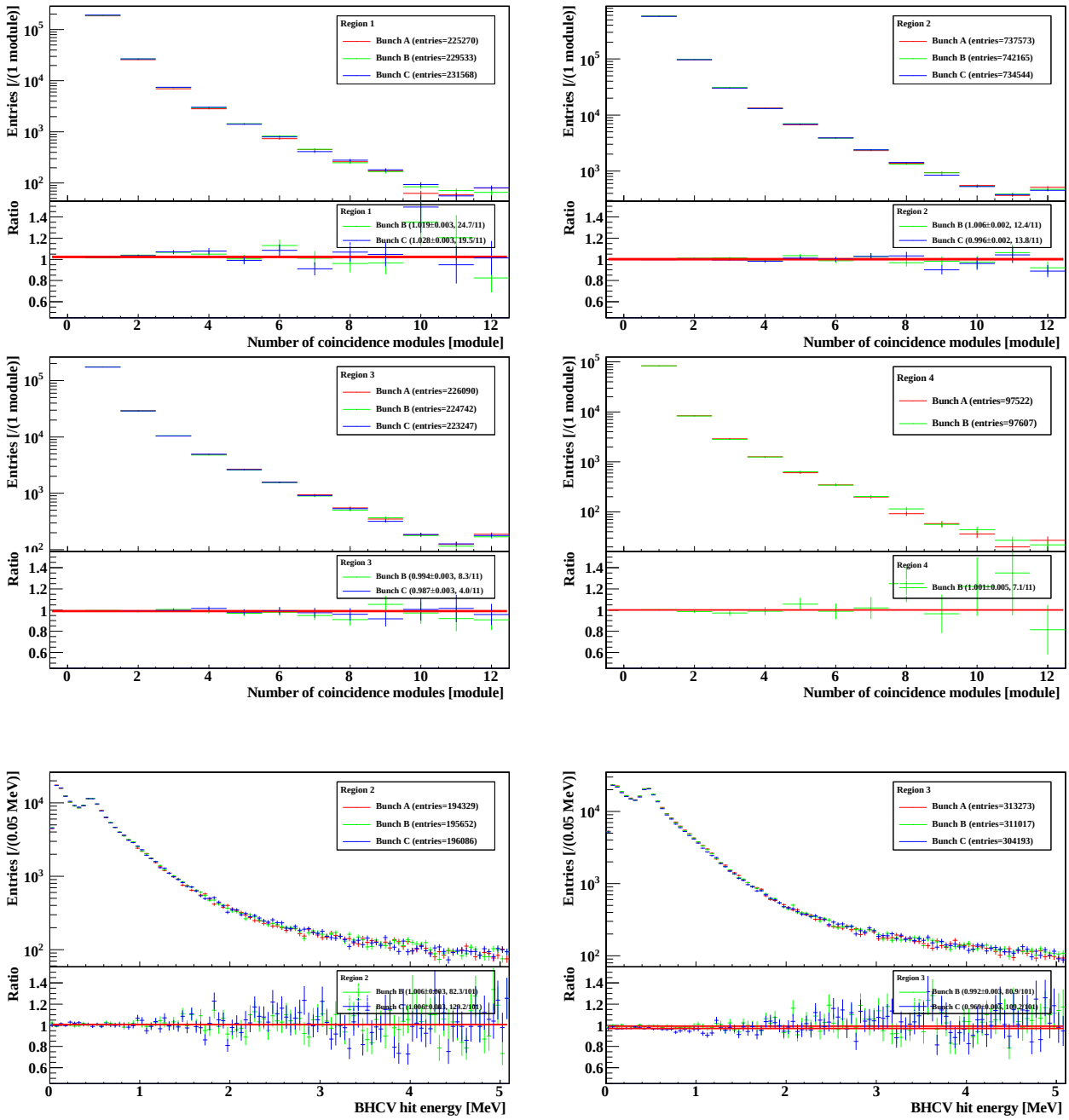

Figure 6.26: Comparison of distribution of coincidence modules in BHPV and energy in BHCV for the same timing for different bunches. The top four panels are for BHPV and the bottom two are for BHCV. In BHPV, distribution for each of four region is compared and that for BHCV, Region 2 and 3 was compared. Here, histograms are not normalized by their entries. In the bottom part in each panel, ratios to the histogram for Bunch A are shown.

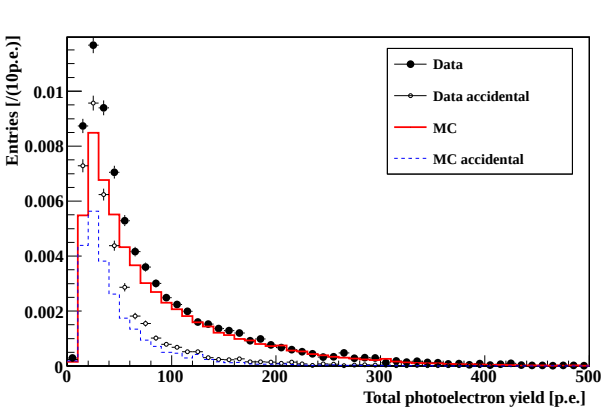

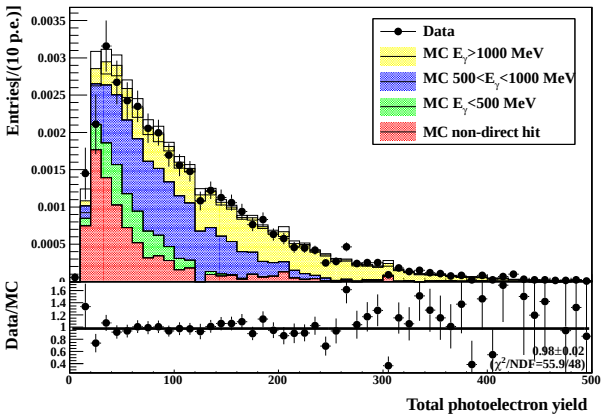

Figure 6.27: (left) Distribution of total photoelectron yield before accidental subtraction. (right) Their subtraction.

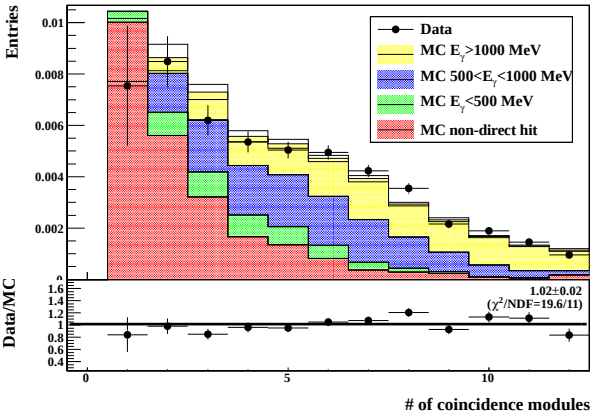

Figure 6.28: Distribution of the number of module for the coincidence.

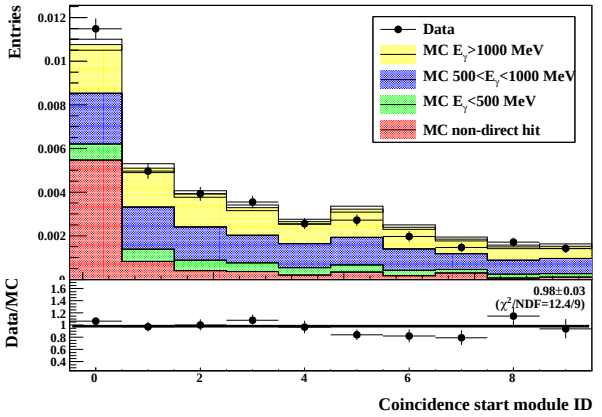

Figure 6.29: Distribution of ID of the most upstream module in the coincidence.

photons.

The concrete value of the efficiency was now estimated below. It was defined as

$$\epsilon_{\rm data}^{>1{\rm GeV}} = N_{\rm data}^{>1{\rm GeV}} / N_{\rm true,incident}^{>1{\rm GeV}} \tag{6.16}$$

was estimated from the η value obtained above, where $N_{\rm data}^{>1{\rm GeV}}$ ($N_{\rm true,incident}^{>1{\rm GeV}}$) was the number of events with γ_6 detected by (incident in) the BHPV detector, when their energy was larger than 1 GeV. Now, we assumed

$$\frac{N_{\rm data}^{>200{\rm p.e.}}}{N_{\rm data}^{>1{\rm GeV}}} \simeq \frac{N_{\rm MC}^{>200{\rm p.e.}}}{N_{\rm MC}^{>1{\rm GeV}}}, \tag{6.17}$$

and evaluated $N_{\rm true,incident}^{>1{\rm GeV}}$ with the simulation ($N_{\rm MC,incident}^{>1{\rm GeV}}$). Eq. (6.16) would be then changed as follows:

$$\begin{aligned} \epsilon_{\rm data}^{>1{\rm GeV}} &\simeq (N_{\rm MC}^{>1{\rm GeV}} / N_{\rm MC}^{>200{\rm p.e.}} \times N_{\rm data}^{>200{\rm p.e.}}) / N_{\rm MC,incident}^{>1{\rm GeV}} \\ &= \epsilon_{\rm MC}^{>1{\rm GeV}} \times \eta \end{aligned} \tag{6.18}$$

Table 6.3: List of systematic uncertainties.

Error source	Percentage error
K_L momentum spectrum	$^{+1.7}_{-1.35}$%
Beam position	0.145%
Calorimeter energy resolution	0.489%
Calorimeter position resolution	4.975%
Detector alignment	1.503%
MC reproducibility on BHPV	
Total photoelectron yield	3.693%
Number of coincidence modules	0.895%
Coincidence timing	0.063%
Total	$^{+6.68}_{-6.60}$%

Efficiency in the MC simulation, written as $\epsilon_{\rm MC}^{>1{\rm GeV}}$, was calculated as 0.938 ± 0.002(stat.). Here, the inefficiency of around 6% mainly came from photon punch-through probability, which was given by the total thickness of lead converter, and would be reduced by adding modules to get enough converter thickness. From Eq. (6.18), efficiency for high energy photons was obtained as $\epsilon_{\rm data}^{>1{\rm GeV}} = 0.962 \pm 0.046({\rm stat.}) \pm 0.064({\rm syst.})$.

6.4.3 Systematic errors

Since extraction of the η value or efficiency $\epsilon_{\rm data}^{>1{\rm GeV}}$ defined above relied on outputs from the MC simulation, its validity needed to be evaluated ant the uncertainty should be taken into consideration. The obtained yield of events with large photoelectrons would be proportional to a product of photon detection efficiency and geometric acceptance of γ_6 in BHPV, each of which was denoted as $\epsilon^{>1{\rm GeV}}$ and $\rho^{>1{\rm GeV}}$. The geometric acceptance $\rho^{>1{\rm GeV}}$ was defined as a ratio of the number of events where γ_6 with energy of >1 GeV was going in the BHPV direction to the total number of events with event selection. This value was estimated through the MC simulation and its uncertainty was directly translated that of η or $\epsilon_{\rm data}^{>1{\rm GeV}}$. Contributions from various sources which possibly affected the $\rho^{>1{\rm GeV}}$ value were estimated by shifting each condition within its uncertainty in simulations. Relative deviation of $\rho^{>1{\rm GeV}}$ was considered as a systematic error for the source. Calculation of the η value also used simulation outputs and the validity should be taken into account. This was achieved by comparing cut efficiency in BHPV variables between data and MC. Results of all systematic uncertainties are summarized in Table 6.3 and the detail of estimation methods for each error source is described below.

K_L momentum spectrum

The $\rho^{>1{\rm GeV}}$ value has strong dependency on incident K_L momentum as in Fig. 6.30 and changes of the momentum distribution can have influence to $\rho^{>1{\rm GeV}}$. Deviation of the $\rho^{>1{\rm GeV}}$ value due to this effect is estimated and considered as a systematic error.

As is already mention in Sec. 5.2.1, the momentum distribution of incident K_L was parametrized

with four parameters and written as follows:

$$f(p,\vec{a}) = \exp(-\frac{(p-\mu)^2}{2(\sigma_0(1-(A+Sp)(p-\mu))^2}), \tag{6.19}$$

where p denotes incident K_L momentum in units of MeV/c and $\vec{a}^T = (\mu, \sigma_0, A, S)$ is a parameter vector. A set of the original parameters given in Eqs. (5.2)-(5.5) is written as $\vec{a_0}$. These parameters were slightly shifted within their uncertainty and deviation of $\rho^{>1\mathrm{GeV}}$ value from that with the original parameter was examined. In this process, a new value of $\rho^{>1\mathrm{GeV}}$ was calculated by "reweighting method" instead of repeating simulations with the new momentum distribution. For a new set of parameters $\vec{a}$, a ratio of a K_L yield to that with the original one was given as $f(p,\vec{a})/f(p,\vec{a_0})$ for each momentum. Defining $g(p,\vec{a_0})$ as momentum distribution for events after the selection in Table 6.2 and $h(p,\vec{a_0})$ as that for events with γ_6 in geometric acceptance of BHPV, the new acceptance value, denoted as $\rho^{>1\mathrm{GeV}}(\vec{a})$, is given as

$$\rho^{>1\mathrm{GeV}}(\vec{a}) = \frac{\int h(p,\vec{a_0}) f(p,\vec{a})/f(p,\vec{a_0})\mathrm{d}p}{\int g(p,\vec{a_0}) f(p,\vec{a})/f(p,\vec{a_0})\mathrm{d}p}, \tag{6.20}$$

where the original acceptance value $\rho^{>1\mathrm{GeV}} = \rho^{>1\mathrm{GeV}}(\vec{a_0})$ is given as

$$\rho^{>1\mathrm{GeV}} = \frac{\int h(p,\vec{a_0})\mathrm{d}p}{\int g(p,\vec{a_0})\mathrm{d}p}, \tag{6.21}$$

from its definition. The distributions of $g(p,\vec{a_0})$ and $h(p,\vec{a_0})$ correspond to blue and red histograms in the top of Fig. 6.30, respectively.

In creating the new momentum spectrum, the four parameters were smeared by assuming a Gaussian considering their correlations. The error and covariance values were given in the following variance-covariance matrix V:

$$V = \begin{pmatrix} 0.000810964 & -0.000430554 & -0.000634841 & -0.000616456 & 0.0000534209 \\ -0.000430554 & 0.0014402 & 0.000629142 & 0.00133248 & -0.000170238 \\ -0.000634841 & 0.000629142 & 0.00103403 & 0.00126643 & -0.000127379 \\ -0.000616456 & 0.00133248 & 0.00126643 & 0.00216038 & -0.000264671 \\ 0.0000534209 & -0.000170238 & -0.000127379 & -0.000264671 & 0.000035702 \end{pmatrix} \tag{6.22}$$

These derived from analysis of measurement data taken with spectrometers as well as the calorimeter, which was used to determine the original parameters [100].

The above process is repeated 10^7 times and distribution of relative deviation of $\rho^{>1\mathrm{GeV}}$ to its original value, $(\rho^{>1\mathrm{GeV}}(\vec{a})/\rho^{>1\mathrm{GeV}} - 1)$, is shown in Fig. 6.31. The final systematic uncertainty value was determined as $1\sigma = 68.27\%$ region in this distribution and was $^{+1.35\%}_{-1.7\%}$. As an error for η or $\epsilon^{>1\mathrm{GeV}}_{\mathrm{data}}$, these intervals were inverted since these values were calculated as ratio of the number of events in data to that in MC simulations, and $\rho^{>1\mathrm{GeV}}$ is proportional to the denominator.

Beam position

K_L in a different position inside the beam could have different acceptance of γ_6 as is illustrated in Fig. 6.32. If there existed overall shift of the beam compared to the expected position, this could affect the $\rho^{>1\mathrm{GeV}}$ value. This uncertainty was estimated through reweighing method, but in a different way from one in the estimation due to K_L momentum spectrum. Two kinds of position

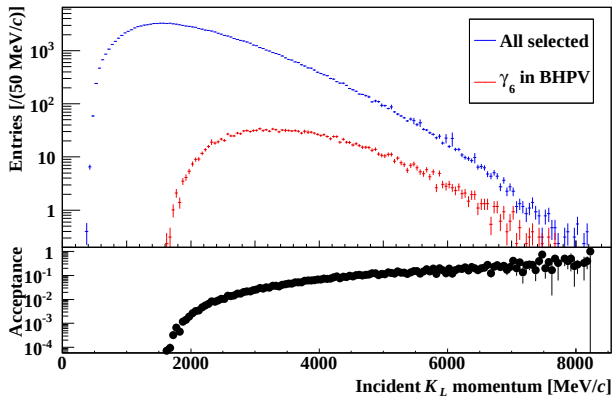

Figure 6.30: (Top) Distribution of incident K_L momentum for events after event selection and those where γ_6 is in geometric acceptance of BHPV. (Bottom) Momentum dependence of γ_6 geometric acceptance.

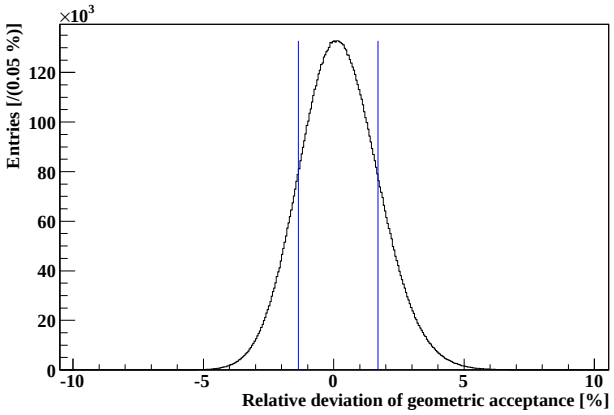

Figure 6.31: Relative deviation of $\rho^{>1\mathrm{GeV}}$ due to uncertainty of K_L momentum distribution. The blue lines indicate 1σ region.

acceptance as a function of an incident K_L position were defined for each of the x and y directions. The first one, named acceptance A, is an event number ratio of those after the event selection in Table 6.2 to all the simulated events and the other one, name acceptance B, is for events with γ_6 in the geometric acceptance of BHPV. Figure 6.33 shows these acceptance functions for the x and y directions. Each functions was fitted with a Gaussian as in Fig. 6.33. Fit function for the acceptance A (B) is denoted as $f(x)$ ($g(x)$). Using the distribution of incident K_L position at the collimator exit, $F(x)$ and the number of K_L yield there, yields with the nominal beam position for each category, written as N_A and N_B, are calculated as follows:

$$N_A = \int F(x)f(x)\mathrm{d}x, \tag{6.23}$$

$$N_B = \int F(x)g(x)\mathrm{d}x, \tag{6.24}$$

and geometric acceptance is given as $N_\mathrm{B}/N_\mathrm{A}$. Calculation of expected geometric acceptance with a beam shift δx, denoted as $\rho'(\delta x)$, was then performed using fit functions $f(x)$ and $g(x)$. The reason to use the fit functions is to make an acceptance value for an outside of the original beam profile available, which is required to estimate acceptance with a beam shift. An expected acceptance value of $\rho'(\delta x)$ is then given as

$$\rho'(\delta x) = \frac{\int F(x-\delta x)g(x)\mathrm{d}x}{\int F(x-\delta x)f(x)\mathrm{d}x}. \tag{6.25}$$

And the absolute value of its fractional difference, given as

$$\rho'(\delta x)/\rho'_0 - 1, \tag{6.26}$$

is finally regarded as a systematic error coming from uncertainty of the beam position. Here $\rho'_0 = N_\mathrm{B}/N_\mathrm{A}$. The value δx is uncertainty of the beam position and was taken as $\delta x = \pm 1$ mm. Although precision of the beam center position measured with $K_L \to 3\pi^0$ events was smaller than

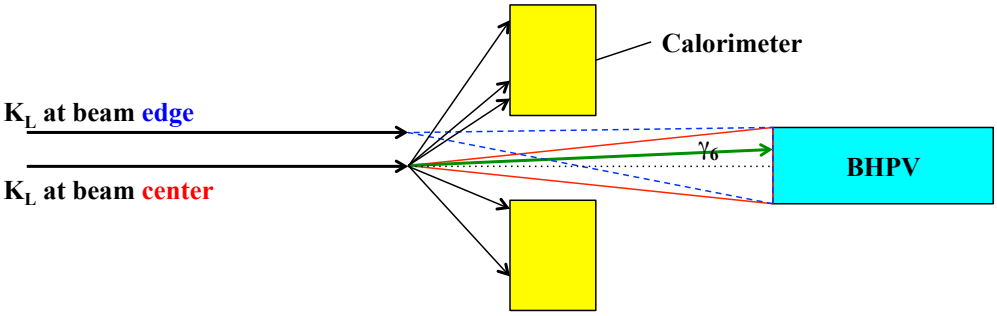

Figure 6.32: Difference of γ_6 acceptance according to a K_L position inside the beam.

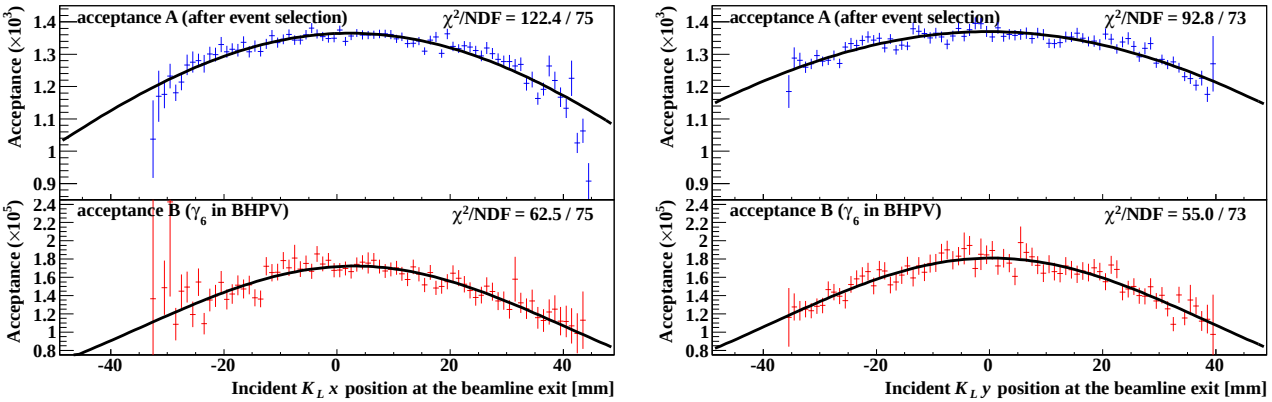

Figure 6.33: Acceptance function used in estimation of signal yield with beam shift. The left (right) figure shows that for x (y) profile. In each panel, the top (bottom) shows that for acceptance A (B) described in the main context.

this value, conservatively the large δx value was chosen since the resultant systematic error was found to be small as shown below. The same procedure was applied for both x and y profiles. The results are summarized in Fig. 6.34. Calculated ρ' value is shown in the left of Fig. 6.34 as well as $\rho^{>1\mathrm{GeV}}$ value obtained from the full simulation, a point shown with an error bar. The right figure shows fractional difference from the ρ'_0 value for x and y direction. As a total error, a quadratic sum of larger fractional difference for $+1$ mm or -1 mm beam shift in each of x and y direction was adapted. The resultant value is $0.145 = (0.130 \oplus 0.063)\%$, where the former (latter) contribution comes from beam shift in x (y) direction. The systematic error from uncertainty of the beam position is found to be quite small.

Energy and position resolution of the calorimeter

Uncertainty in the calorimeter performance could have influences on the $\rho^{>1\mathrm{GeV}}$ value through change of reconstruction and event selection efficiencies. To estimate uncertainty due to this effect, additional energy and position smearing were applied in the MC samples and changes of $\rho^{>1\mathrm{GeV}}$ were examined. Their resolutions for a cluster with energy e were assumed to be expressed as the

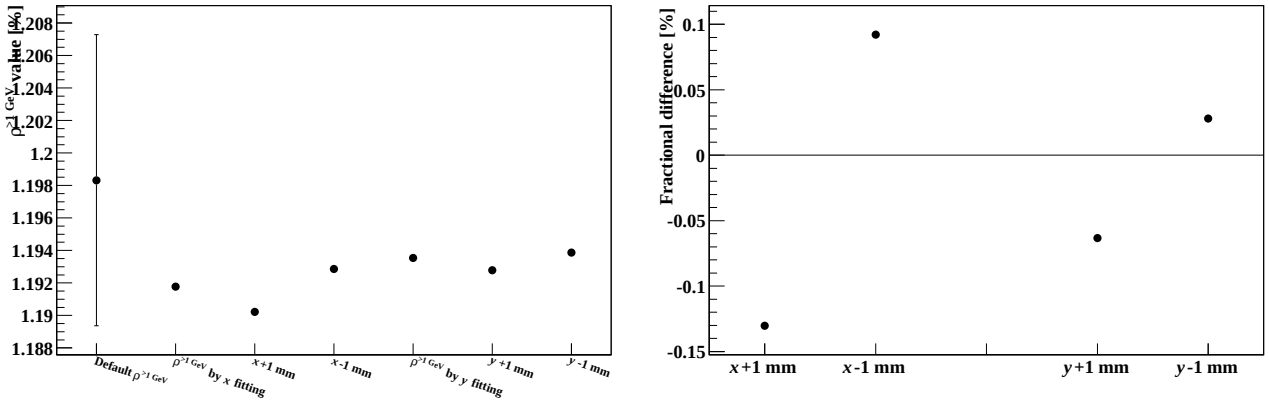

Figure 6.34: Result of systematic error estimation due to beam shift. The left panel shows the obtained result of ρ values as well as the nominal geometric acceptance. The right panel shows the fractional difference of acceptance with beam shifts.

following functions [64]:

$$\frac{\sigma_{\mathrm{E}}(e)}{e} = \frac{0.01935}{\sqrt{e/\mathrm{GeV}}} \oplus \frac{3.956 \times 10^{-8}}{e/\mathrm{GeV}} \oplus 0.005954, \tag{6.27}$$

$$\sigma_{\mathrm{x}}(e)/\mathrm{mm} = \frac{3.663}{\sqrt{e/\mathrm{GeV}}} \oplus \frac{2.331 \times 10^{-6}}{e/\mathrm{GeV}} \oplus 2.148, \tag{6.28}$$

which were obtained by comparing true and reconstructed information in $K_L \to 3\pi^0$ simulation. Energy and position of each cluster, written as e and x, respectively, were modified so that these resolutions got worse by a factor of α as

$$e \longrightarrow e + \mathrm{Gaussian}(\sigma_{\mathrm{E}}(e)\sqrt{\alpha^2 - 1}), \tag{6.29}$$

$$x \longrightarrow x + \mathrm{Gaussian}(\sigma_{\mathrm{x}}(e)\sqrt{\alpha^2 - 1}), \tag{6.30}$$

where "Gaussian(σ)" means to give a random number following a Gaussian distribution with its mean zero and given σ. In case of position resolution, smearing with Eq. (6.30) is applied for both of the x and y directions. There exists a small difference in width of reconstructed K_L mass distribution in the six-cluster analysis between data and simulation with the cut set used in five-gamma analysis here. The factor α was then determined so that the width of the reconstructed K_L mass peak in simulations with the smearing agreed to that of the data. It was given as $\alpha = 1.003$ for energy resolution smearing and $\alpha = 1.25$ for position resolution smearing and shown in Fig. 6.35. Reconstruction after these modification was performed and resultant geometric acceptance was calculated. Finally, fractional difference from $\rho^{>1\mathrm{GeV}}$ before smearing was calculated as Eq. (6.26) for each case with energy resolution and position resolution smearing. As a result, systematic errors from energy and position resolution were estimated to be 0.489% and 4.975%, respectively. The change of acceptance by the energy resolution mainly comes from deterioration of probability to choose correct photon pairing and that by the position resolution from change of selection efficiency on cuts for photon hit position.

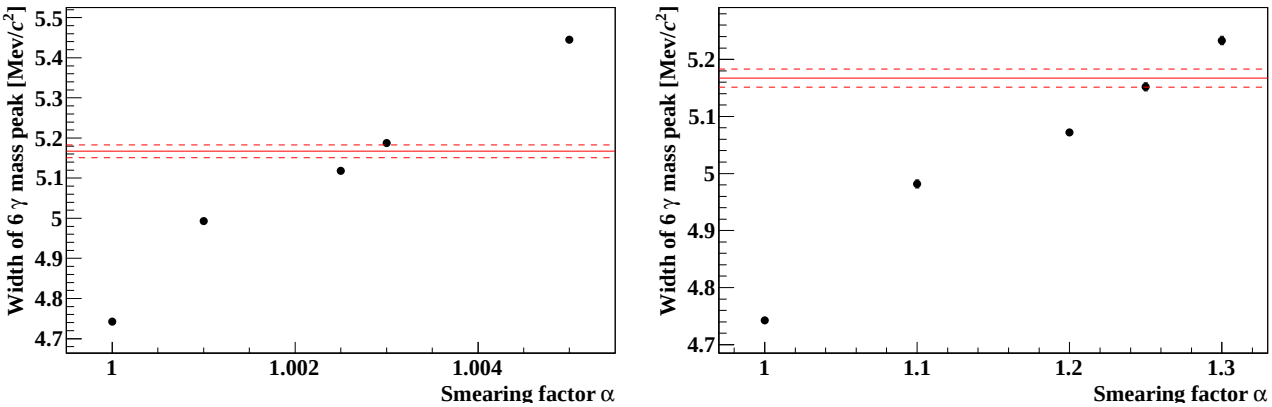

Figure 6.35: Determination of the smearing factor α for energy resolution (left) and position resolution (right). The red bands indicates width of the K_L mass peak in data.

Alignment of detectors and materials around the BHPV detector

An effective yield of γ_6 for BHPV would be changed by an aperture of detectors or materials located in the upstream of BHPV. Uncertainty of alignment of these components then could affect the yield and should be considered as a source of systematic errors. This effect was estimated by virtually changing apertures of the CC06 detector and the concrete shield in MC simulations as shown in Fig. 6.36. First, γ_6 xy positions at the upstream surface of CC06 cesium iodide crystals was calculated for each from true track information and its distribution was prepared. The nominal yield on CC06, denoted as N_0^{CC06} was then calculated by counting the number of events satisfying $\max(|x|, |y|) < 85$ mm, which correspond the actual beam hole size of CC06. For estimation in case that the detector was mis-aligned, integration range was varied as in Fig. 6.36, considering possible cases, and fractional difference of obtained yield, N, to N_0^{CC06}, defined as N/N_0^{CC06}, was calculated for each configuration. The maximum absolute value for these configurations were considered to be an error of CC06 mis-alignment. The same procedure was taken for the concrete shield. In this case, only events with γ_6 whose xy position at CC06 was $\max(|x|, |y|) < 85$ mm were selected and integration range was set as ± 125 mm. The amounts of shifts, 5 mm or 2.5 mm, were conservatively taken to be large since the resultant uncertainty was not dominant when compared with other ones. The results are shown in Fig. 6.37. A quadratic sum of the errors from CC06 and the concrete shield is adapted as a total error due to alignment and given as $1.503 = (1.452 \oplus 0.391)\%$, where the former and the latter value indicated contributions from CC06 and the shield, respectively.

BHPV responses in MC

As several selection cuts for variables related to the BHPV were applied, reproducibility of responses of this detector needed to be confirmed. These effects were evaluated by comparing cut efficiency between the data and MC. Here, the cut efficiency ϵ was defined as

$$\epsilon = \frac{\text{integral of the histogram for the region to be selected}}{\text{integral of the histogram for all the region}} \tag{6.31}$$

As error values, absolute values of their fractional difference presented below were used:

$$\frac{\epsilon^{\mathrm{data}}}{\epsilon^{\mathrm{MC}}} - 1. \tag{6.32}$$

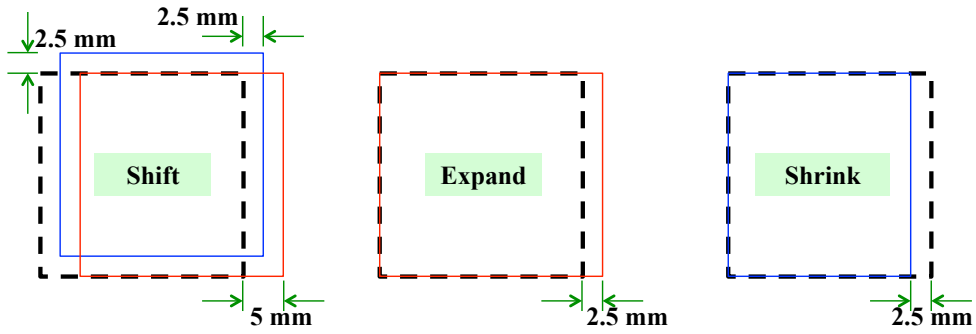

Figure 6.36: Estimation due to uncertainty of detector and material alignment around BHPV.

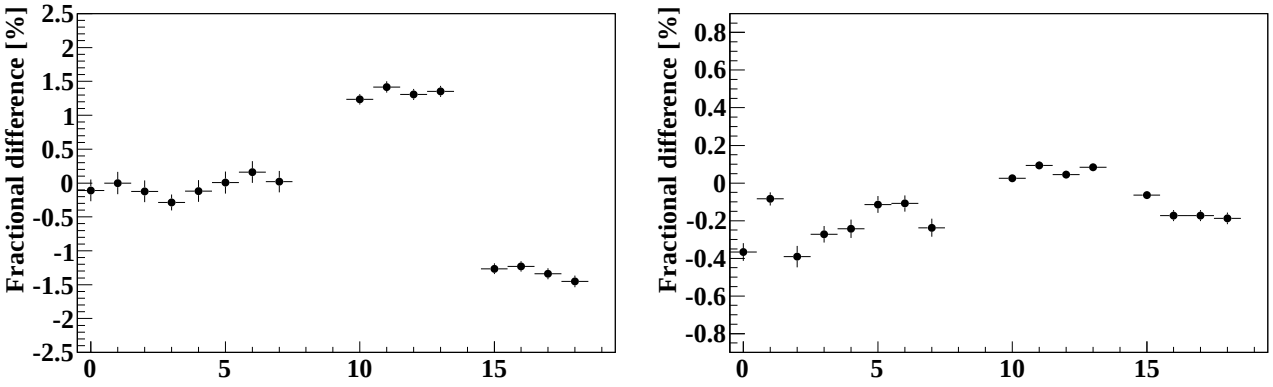

Figure 6.37: Result of systematic error estimation for alignment of CC06 (left) and the concrete shield (right). The horizontal axis in each panel indicates integration ranges shown in Fig. 6.36: 0-7 corresponds to "shift," 10-13 "expand," and 15-18 "shrink" in Fig. 6.36, respectively.

The cut efficiency on the total photoelectron yield was obtained $(14.31 \pm 0.73)\%$ and $(13.79 \pm 0.33)\%$ for data and MC, respectively, and the error due to this cut was determined as 3.693%. For the cut on the number of coincidence modules, distribution after applying the total photoelectron cut was used, which is shown in Fig. 6.38. The efficiency was calculated as $(101.33 \pm 6.35)\%$ and $(100.14 \pm 2.89)\%$ for data and MC, respectively[*9], and the resultant error value was found to be 0.895%.

A different method of error estimation was used for the event selection on timing. Instead of veto timing distribution itself, distribution for standard deviation of each hit timing in a coincidence hit was used in order to evaluate effect of difference in hit timing between the data and the MC. Random numbers which followed Gaussians were generated, where its mean was fixed to zero and its σ value was taken randomly from distribution of the hit timing standard deviation. The measured and simulated distribution is shown in the left of Fig. 6.39. This process was repeated 10^6 times and ratio of events within ± 7.5 ns was calculated for both data and MC. Finally, fractional difference of these ratios, as given in Eq. (6.32), was calculated and considered as a systematic error. The result

[*9] Because the efficiency calculation is based on histograms after subtracting accidental activities, an efficiency value can exceed 100% within statistical uncertainty.

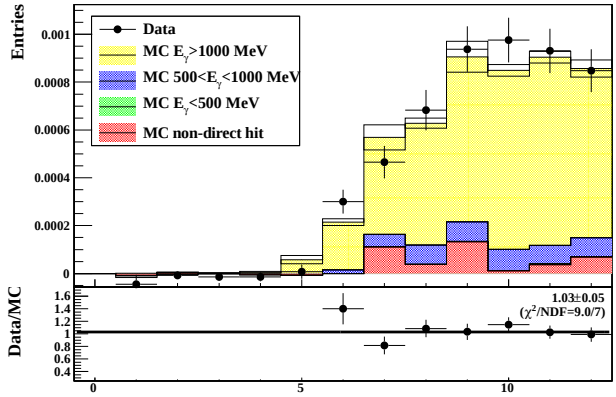

Figure 6.38: Distribution of the number of coincidence modules for events with a total photoelectron yield larger than 200.

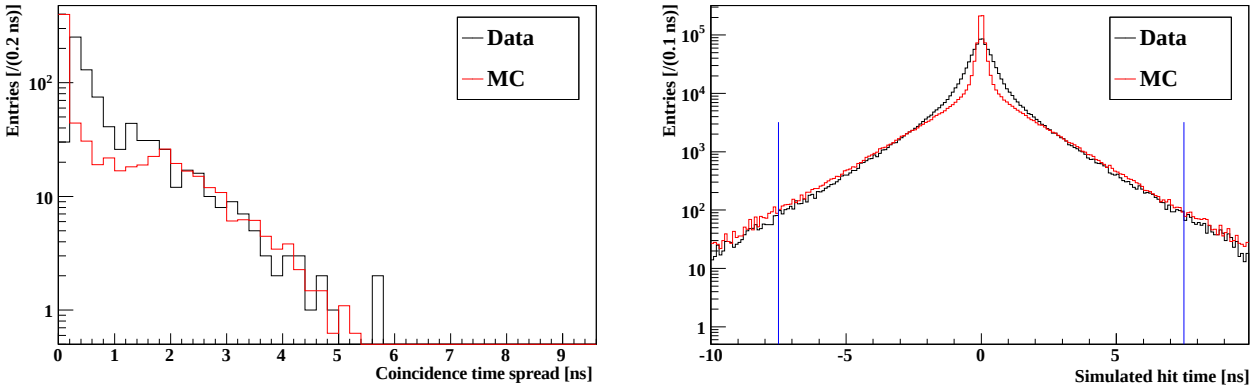

Figure 6.39: Systematic error estimation arising from the timing cut. The left panel is distribution of timing standard deviation for hit channels in coincidence. The right one shows a result of the simulation with distributions in the left panel. Ratios of events between the two blue lines to the total number of entries are used for estimation of the systematic error.

of generated random numbers is shown in Fig. 6.39 and the obtained error value is found to be as small as 0.063%, which is small compared with other errors.

6.4.4 Conclusion

Detection efficiency of photons coming from K_L decay was examined with data taken during the physics run in 2013. The number of events with large photoelectron yield was compared between data and MC in order to examine detector responses of this detector to high energy photons. The data/MC ratio is found to be $1.025 \pm 0.050(\text{stat.}) \pm 0.068(\text{syst.})$, which means the obtained efficiency was consistent with MC expectation within an uncertainty of 8.2% as a quadratic sum of the statistical and systematic errors. This result shows the detector successfully worked as a high energy photon detector in the neutral beam, with underlying larger fluxes of beam photons and neutrons.

6.5 Discussion for future beam time

6.5.1 Reduction of inefficiency

Inefficiency due to short radiation length

Expected efficiency for high energy photon of 93.8%, which was found to be consistent with measurement data, was not enough for a search of the $K_L \to \pi^0\nu\overline{\nu}$ decay with higher sensitivity. From simulation studies, efficiency for high energy photons was required to be smaller 5×10^{-3} in order to make $K_L \to 2\pi^0$ background small enough. This would be achieved by adding modules to increase radiation length, since the inefficiency of 6% mainly came from insufficient conversion probability due to the short radiation length. If we increased the total radiation length up to $9X_0$, or 50 mm in lead thickness, the "punch through" probability, where an incident photon passed through the detector without any interaction, would be reduced to 0.1%. This configuration, which would be realized with nine additional modules with a 3.0-mm-thick lead sheet, for example, safely satisfies the requirement for $K_L \to 2\pi^0$ background. Quantitative discussion on the number of background events appears in the next chapter.

Inefficiency at the edge of the detector

Although the transverse size of the BHPV detector is enough to cover all photons incident in this detector, the long longitudinal size of this detector would allow their divergence and photon conversion points would be outside of the effective area at the downstream. This situation would deteriorate detection efficiency, which would be more conspicuous when the number of modules increased. Figure 6.5.1 shows incident energy dependence of simulated photon inefficiency with divergence of incident photons considered. Photons obtained in the $K_L \to 2\pi^0$ simulation were shot to the BHPV detector with two kinds of configuration: one with twelve modules used in the physics run and with additional four modules equipped with a 3.0-mm-thick lead sheet. Detail of this simulation will be described in Sec. 7.4.4. Events were categorized into two types of "center" and "edge," where xy positions after extrapolating an incident photon track to the downstream of the detector was within $\pm$125 mm in the former type and outside this region in the latter type. A event number ratio of the edge type to the center one was estimated to be 1.9 ± 0.2 (2.8 ± 0.4) in case of the twelve (sixteen) modules, where the error value represents statistical uncertainty of the MC simulation. Relative inefficiency of edge type events to center type ones for high energy photons is found to be larger with additional modules and this can limit reduction of background events. To overcome this situation, an additional detector to cover the edge region, named the guard counter [105], was introduced at the downstream of BHPV for the next run as well as additional four modules. The outline of the new detector is shown in Fig. 6.41. It was consisted of a lead sheet and an acrylic plate, and designed to detect incident photons with acrylic Čerenkov light. Simulation studies were performed to estimate effect of this detector on background reduction. Here, $K_L \to 2\pi^0$ decay was simulated and events including photons hitting BHPV was collected. For each event, photon interaction with BPHV was separately simulated and background events were counted as those where the hit condition was satisfied. Veto reduction by other detectors was evaluated following methods used in what we call the fast simulation, detail of which is described in Sec. 7.4.4. The numbers of background events before and after introducing the guard counter were calculated. As a result, $K_L \to 2\pi^0$ background related to BHPV was found to be reduced by 60% thanks to this detector.

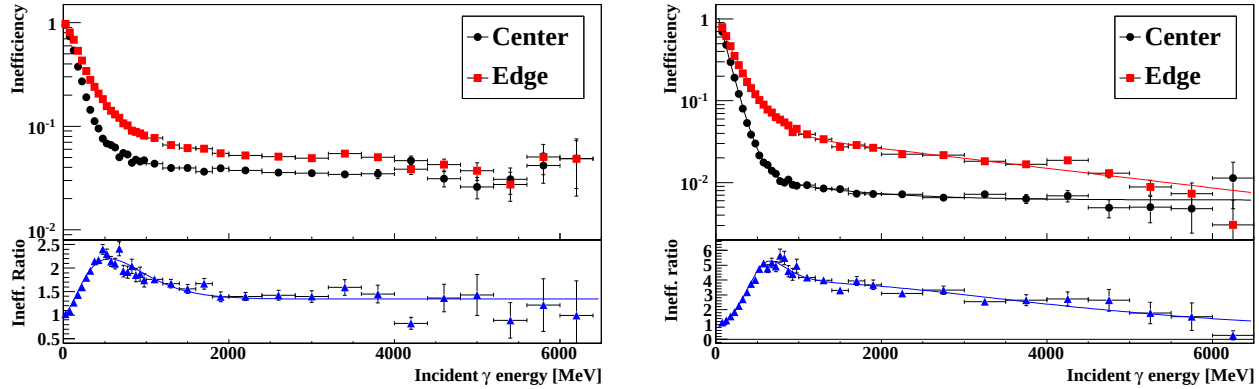

Figure 6.40: Inefficiency as a function of incident photon energy. The left figure is for the configuration used in the physics run in May, 2013 with twelve modules. The right one is in case that four modules are added.

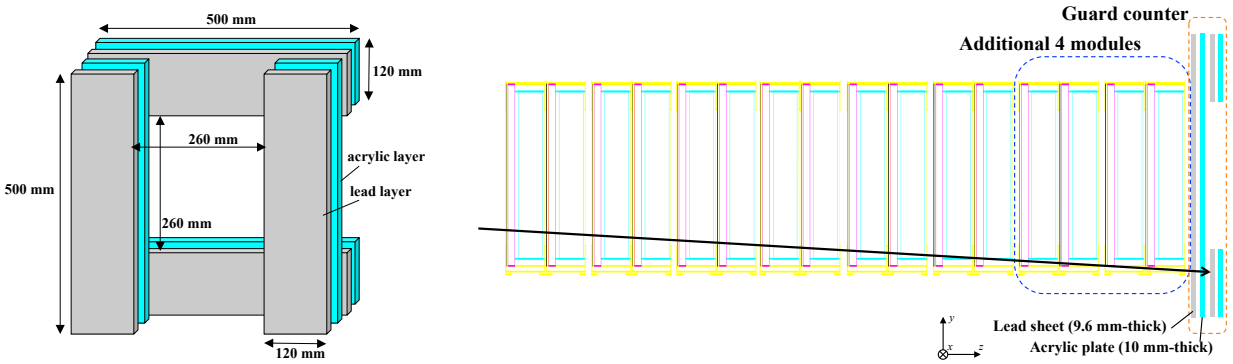

Figure 6.41: Outline of the Guard Counter (left) and configuration of downstream detectors in the next physics run (right). The black arrow in the right figure indicates an example of a photon track to be handled by the Guard Counter.

6.5.2 Counting rate

Although stable operation was confirmed in the physics run in 2013, the design beam power of 291 kW was not achieved and operation with more intense beam should be considered.

One measure of operation stability in the high rate environment wss, as already discussed in Sec. 6.3.2, a ratio of base current over output current for each PMT and at least a factor of 20 should be maintained for stable operation in order to prevent possible gain fluctuation under high-rate environment. The minimum value among all channels was 35 and increase of beam power up to 40 kW would be tolerable under assumption of the same target and duty factor. Needless to say, other effects such as space-charge effect which deteriorate PMT performance should be carefully considered. For more intense beam, optimization of lead and aerogel thickness will be necessary. For example, using thinner aerogel gives smaller light yield and will be helpful in reducing counting rate. Possible deterioration of efficiency in particular for low energy photons with energy <1 GeV would be compensated by making lead thickness smaller. An example of performance on single counting

Table 6.4: Lead-aerogel sampling in the optimized design.

Module number	Lead thickness [mm]	Aerogel thickness [mm]
1	1.5	15
2-5	0	15
6-9	1.5	29
10-22	3.0	58
23-24	0	58

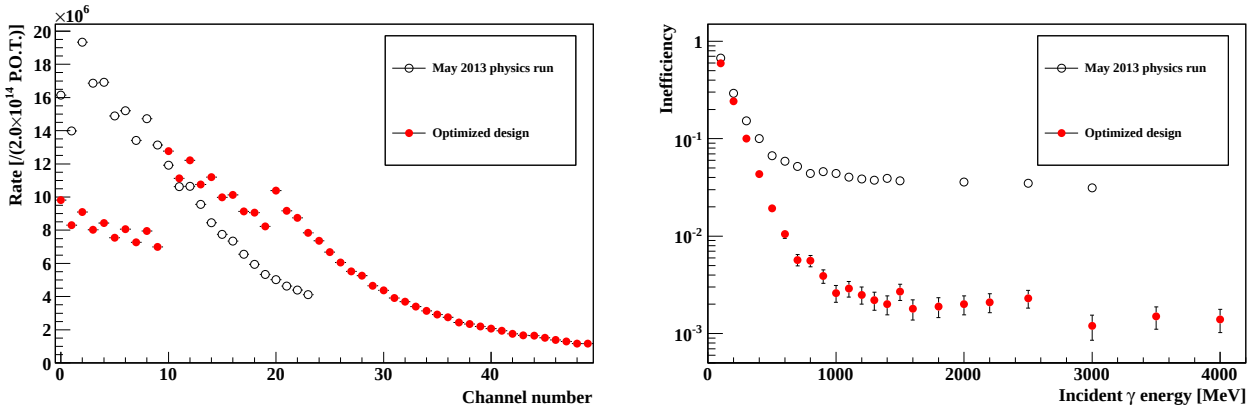

Figure 6.42: Expected performance with optimized design. (Left) Single counting rate for each module. (Right) Inefficiency as a function of incident photon energy. In inefficiency evaluation, photons with a fixed energy was injected perpendicularly to the detector in 25 cm square.

rate and photon detection efficiency is shown in Fig. 6.42, where optimized lead and aerogel sampling was summarized in Table 6.4. Counting rates were found to be reduce to 2/3, while inefficiency for photons with energy larger than 1 GeV was kept smaller than requirement value of 0.5%.

There is also a room of improvement in a duty factor of the accelerator. The counting rates measured with the TMon trigger were higher by a factor of 2.4 than that with the clock trigger in the physics run of May, 2013, each of which corresponded to the effective and ideal counting rates in the physics analysis, respectively. This was considered to come from noise of power supplies used in the MR accelerator and at maximum a factor of 2.4 improvement would be expected by planned replacement of these power supplies.

Although the design beam power of 291 kW is more than 10 times higher than that in the physics run in May, 2013, the nickel target is planned to be used with this beam power, which is expected to yield smaller particle yields. As a result of the beam line simulation, a flux of beam photons with >10 MeV was 1/4 of that with the platinum target[*10]. Hence increase of counting rate with the design beam power is expected to be a factor of 3. Taking further tolerance, optimization of lead-aerogel sampling and possible improvement of a duty factor discussed above into account, this detector is considered to accommodate intense neutral beam with the design beam power.

[*10] As mentioned in Sec. 2.2.3, simulated fluxes with the platinum and the gold target were consistent within 20%.

Chapter 7

Analysis for the $K_L \to \pi^0\nu\overline{\nu}$ Search

In this chapter, procedures and results of the analysis for $K_L \to \pi^0\nu\overline{\nu}$ search are presented.

7.1 Overview

The overall analysis flow is shown in Fig. 7.1. In the search for the $K_L \to \pi^0\nu\overline{\nu}$ decay, simple cut-based analysis was adopted. For a given data set, various selection cuts based on information from the calorimeter and veto detectors, are applied and survived events are regarded as $K_L \to \pi^0\nu\overline{\nu}$ signal events. These selection cuts are optimized according to results of background estimation so as to maximize signal acceptance as far as the expected number of background events is small enough. In this process, the "blind analysis" method is used, where events inside the signal region are kept hidden until all the analysis conditions are fixed. Here, the signal region is shown in Fig. 2.2; where both conditions of 3000 $<Z_{\rm vtx}<$4700 mm and 150 $<P_{\rm T}<$250 MeV/c are satisfied in the $Z_{\rm vtx}$-$P_{\rm T}$ plane. Here, $Z_{\rm vtx}$ and $P_{\rm T}$ are z-vertex position and transverse momentum of reconstructed π^0. Since the definition of the signal region itself also needs to be optimized, the region to be hidden, referred to as the "blind region" below, is slightly extended from the above region: 2900 $<Z_{\rm vtx}<$5100 mm and 120 $<P_{\rm T}<$260 MeV/c. After the optimization, the number of events inside the signal region with all cuts is counted and it is finally scaled to a branching fraction value or its upper limit using the "normalization factor" and signal acceptance. For this purpose, what are called the "normalization modes," namely the $K_L \to 3\pi^0$, $K_L \to 2\pi^0$ and $K_L \to 2\gamma$ decays, where the final state contains only photons and an incident K_L can be fully reconstructed, are analyzed in advance. The normalization factor is the number of K_Ls available in the physics data, and obtained by comparing the number of reconstructed events in each decay between the data and the MC simulation. This is also used to scale simulation outputs to the numbers corresponding to the physics data. In this analysis, cut conditions with the $K_L \to \pi^0\nu\overline{\nu}$ analysis were used. Signal acceptance is calculated as a ratio of the number of observed events to that of incident K_Ls in the signal MC sample. This acceptance value is validated by confirming reproducibility of various distributions in analysis of the normalization modes. This comparison is also important to make the background estimation using MC simulations reliable.

In the following sections, such procedures and results of the analysis are described. The selection cuts for $K_L \to \pi^0\nu\overline{\nu}$ events are summaried in Sec. 7.2. Before going to the $K_L \to \pi^0\nu\overline{\nu}$ analysis, the normalization modes are analyzed in Sec. 7.3, where the normalization factor is calculated and simulation reproducibility is evaluated. Based on the analysis result of the normalization mode,

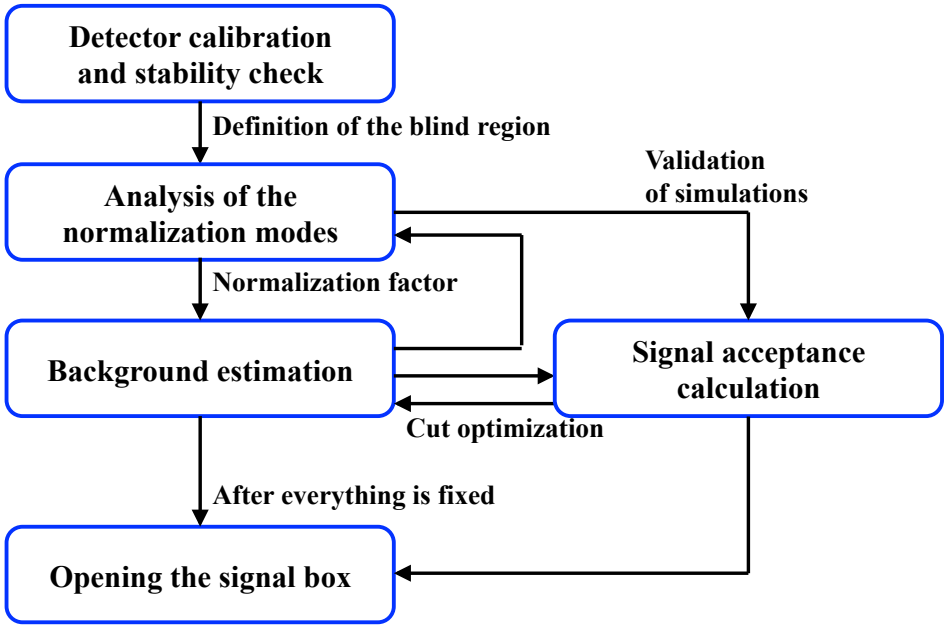

Figure 7.1: Overview of analysis flow for the $K_L \to \pi^0\nu\overline{\nu}$ search.

background contribution in the $K_L \to \pi^0\nu\overline{\nu}$ analysis is evaluated in Sec. 7.4. Here, mechanism, method of estimation, results and cut optimization are described for each background source. Finally, the result after unblinding is presented in Sec. 7.5, and several discussions on the result and future prospect follow in Sec. 7.6.

7.2 Event selection for the $K_L \to \pi^0\nu\overline{\nu}$ analysis

7.2.1 Number of clusters

For the $K_L \to \pi^0\nu\overline{\nu}$ analysis, events taken with the physics trigger, which is described in Sec. 3.3.1, were used. Photon clusters are then identified from calorimeter hit information with the procedures give in Sec. 4.3.2. Events are then categorized according to the number of photon clusters and a π^0 is reconstructed for those with two or more photon clusters (Sec. 4.3.3) as well as veto information (Sec. 4.4). In π^0 reconstruction, a pair of two photon clusters which has the minimum timing difference among all the possible pairs is chosen. Finally, selection cuts to identify $K_L \to \pi^0\nu\overline{\nu}$ signal events are applied. Detail of the selection cuts is described in the following sections.

7.2.2 CsI cuts

The selection criteria is classified into the following two types: one related with the CsI calorimeter and veto detectors. The former is referred to as "CsI cuts" and the latter "veto cuts."

In the following description, among two photons hitting the calorimeter, corrected energy, xy position on the upstream calorimeter surface and reconstructed vertex timing are denoted as e_i, x_i, y_i, t_i respectively, where $i = 1, 2$ and $e_1 > e_2$.

The CsI cuts are used mainly for the two purposes. One is to ensure data quality so that events are properly reconstructed and compared with MC simulations by removing hits which are not well identified and effect of the online triggers. For this purpose, the following cuts were applied:

Total photon energy
Sum of two photons' energy, $e_1 + e_2$ is required to be greater than 650 MeV. This threshold value was determined so as to eliminate effect of the online trigger as discussed in Sec. 5.4.6, which was based on total energy observed by the whole CsI calorimeter.

Center Of Energy (COE)
An offline-COE R_{COE}, which is defined in Eq. (5.39), is required to be larger than 200 mm. Similar event selection based on the COE position is made in the online trigger as described in Sec. 3.3.1 and this cut is necessary for eliminating the online trigger effect as discussed in Sec.5.4.6.

Energy of each photon
Energy of each photon is required to be larger than 100 MeV and smaller than 2000 MeV in order not to use low energy photons with poor energy and position resolution.

Position of each photon on the calorimeter surface
To ensure that electromagnetic showers are well contained in the calorimeter, reconstructed xy positions on the calorimeter surface of each photon are required to satisfy $\max(|x|, |y|) > 150$ mm and $\sqrt{x^2 + y^2} < 850$ mm.

Distance of two photons
Distance of reconstructed hit positions for two photons in the xy plane, or $\sqrt{(x_2 - x_1)^2 + (y_2 - y_1)^2}$, is required to be larger than 300 mm in order to ensure separation of two clusters.

Other cuts were applied in order to distinguish $K_L \to \pi^0\nu\overline{\nu}$ signals from background and the following cuts were used. Detail of some important ones are described in sections corresponding to each background source.

Cluster distance to the nearest dead channel
For both photon clusters, reconstructed x and y positions are required to be far from positions of both dead channels by 53 mm in order to avoid energy mis-measurement and resultant wrong z-vertex reconstruction. This cut is important in considering the upstream neutron background described in Sec. 7.4.7.

Energy ratio of two photons
Ratio of two photons' energy, written as e_2/e_1, is required to be larger than 0.2. Since energies of two photons do not get extremely asymmetric, this cut is effective to reduce the "odd" type of $K_L \to 2\pi^0$ background events where two photons originates from different π^0s. Explanation of the "odd" type will be given in Sec. 7.4.1.

$e\theta$
A product of energy and angle made by a reconstructed photon track and the beam axis is required to be larger than 2500 mm deg. This cut is used to reduce the "odd" type of $K_L \to 2\pi^0$ background events.

Projection angle

An opening angle of the two photon tracks projected in the xy plane, calculated as

$$\cos^{-1}\frac{\vec{r_1}\cdot\vec{r_2}}{|\vec{r_1}||\vec{r_2}|}, \tag{7.1}$$

is required to be smaller than 150° in order to reject two photon clusters from the $K_L \to 2\gamma$ decay, where $\vec{r_i} = (x_i, y_i)$ $(i = 1, 2)$. This angle is always 180° when two photons come from K_L with zero transverse momentum.

Veto by extra clusters and isolated hit crystals

Additional clusters other than the two main photon clusters are treated as extra clusters and used for veto as described in Sec. 4.3.5. When there exist isolated hit crystals which do not belong to any clusters, they are also used for veto as shown in Sec. 4.3.5.

Vertex time difference

Difference of two photons' reconstructed vertex time, $|t_1 - t_2|$, is required to be within 2 ns to ensure the two clusters to come from a common vertex. When two clusters come from particles other than photons, such as charged particles or neutrons, reconstructed vertex time for each photon cluster does not always the same. This cut is necessary for hadron cluster background which is discussed in Sec. 7.4.8.

π^0 kinematic cut

Allowed regions in $Z_{\rm vtx}$-$(P_{\rm T}/P_z)$ and $Z_{\rm vtx}$-E, where P_z and E denoted as longitudinal momentum and energy of reconstructed π^0 are limited as shown in Fig. 7.2. This cut is effective to reduce neutron background, where halo neutrons hit the CV detector and the $\eta \to \gamma\gamma$ decay occurs[*1].

Shape χ^2 cut

This cut is to evaluate how shape of an observed photon cluster is likely to be created by a single photon incidence. Template shape is made with single-photon simulation with various incident energy, position and angle in advance. Each cluster shape in data is then compared to the templates. Background derived from particles except a signal photon is effectively reduced such as charged pions, neutrons and multi photons hitting nearby each other and forming a single cluster. A χ^2 value was defined to evaluate consistency with single-photon incidence for each cluster and this value is required to be smaller than 4.6 for both clusters. Detailed description on definition of this value is found in Ref. [100] or [106].

Photon quality cut In order to distinguish clusters made by hadronic interaction, events with small-size clusters are rejected. For this purpose, the numbers of crystals in both clusters are required to be equal to or larger than five. In addition, "cluster RMS," defined as

$$\sqrt{\sum_i \frac{\epsilon_i r_i^2}{\sum_j \epsilon_j}}, \tag{7.2}$$

[*1] This type of background was one of the major source of background in the KEK E391a experiment. However, this background is less serious in the KOTO experiment since the η production probability is much smaller due to softer halo-neutron momentum and a lower amount of material of CV.

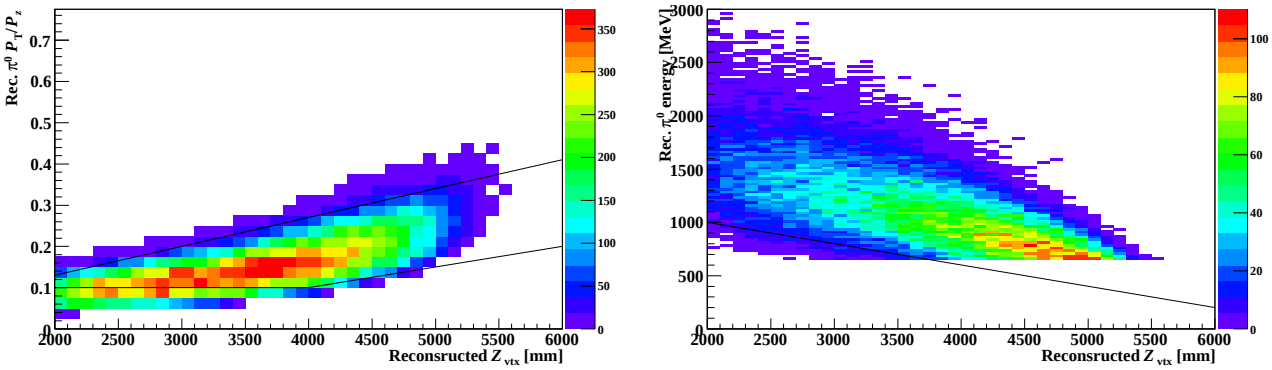

Figure 7.2: Accept region in the π^0 kinematics cut. Distribution of the signal MC is shown.

must be larger than 10 mm, where ϵ_i denotes energy of i-th crystal contained in the cluster and r_i is defined with i-th crystal positions of x_i, y_i and their COE position inside the cluster $x_{\rm COE}$, $y_{\rm COE}$ as

$$r_i^2 = (x_i - x_{\rm COE})^2 + (y_i - y_{\rm COE})^2, \tag{7.3}$$

$$x_{\rm COE} = \sum_i \frac{\epsilon_i x_i}{\sum_j \epsilon_j}, \tag{7.4}$$

$$y_{\rm COE} = \sum_i \frac{\epsilon_i y_i}{\sum_j \epsilon_j}. \tag{7.5}$$

Neural network cuts

Two kinds of neural network cut were developed and used for rejection of neutron background. One of them is called the "kinematical neural net (NN) cut" and introduced to distinguish neutron events by using difference of distributions in reconstructed kinematics, which includes hit position of a cluster with larger energy, projection angle, distance of two clusters, energy ratio, and vertex time difference. The other one is the "shape NN cut," used for further separation of neutron events with cluster shape difference in addition to the shape χ^2 cut. Cluster shape information such as energy spread inside each cluster was used as inputs. Both neural net values were trained with single MC samples and data taken in aluminum target runs. Details will be described in Sec. 7.4.8 and App. H.

7.2.3 Veto cuts

Since signal events are identified by the condition of "π^0 and nothing," events where any other visible particles exist need to be rejected in order to prevent background contamination. This selection is realized with a series of the veto cuts. As described in Sec. 4.4, veto energy and timing for each detector is calculated based on energy and timing information for each module as well as reconstructed vertex time and z position and these values are used for the veto decision. In determining veto energy thresholds, losses of signal acceptance must be taken into account. The $K_L \to \pi^0\nu\bar{\nu}$ decay itself sometimes gives energy deposition in veto detectors due to backsplash of electromagnetic showers. There is also a possibility where accidental hits coincide and events are also rejected in these cases. Since too tight veto, or low energy thresholds, leads to larger acceptance

Table 7.1: List of veto conditions. When veto energy, or the number of coincidence modules in case of BHPV, exceeded the given thresholds in any detectors, the event is rejected. Veto decision by BHPV, which is indicated with an asterisk (*), is made by coincidence of three or more successive modules.

Detector	Energy [MeV]	Timing [ns]
Calorimeter		
Isolated hit crystal	(depends on distance)	±10
Extra clusters	(if exist)	±10
MB	2	±30
BCV	1	±30
FB, NCC	2	±20
OEV	2	±10
CV	0.2	±40
LCV	0.6	±15
CC03-06 (CsI)	3	±15
CC04-06 (scintillator)	1	±15
BHCV	0.3	±7.5
BHPV	*	±7.5

loss, veto condition was decided considering both of background rejection and signal acceptance. The detailed condition is summarized in Table 7.1.

7.2.4 Blinding of the signal region

In process of cut optimization and background estimation, the "signal region" and its surroundings were kept blinded in order to prevent human biases from affecting these processes. The signal region and blind region given as its extension was defined in $Z_{\rm vtx}$-$P_{\rm T}$ plane with the following condition:

- $3000 < Z_{\rm vtx} < 4700$ mm ($2900 < Z_{\rm vtx} < 5100$ mm),
- $150 < P_{\rm T} < 250$ MeV/c ($120 < P_{\rm T} < 260$ MeV/c),

where values in parenthesis represent the blind region. Here, the upstream or downstream limit in $Z_{\rm vtx}$ is set in order to eliminate tail components of background events which are made by neutron interaction with the veto detectors. The lower limit in $P_{\rm T}$ is to discriminate $K_L \to \pi^+\pi^-\pi^0$ background as is discussed in Sec. 7.4.3 and the upper limit comes just from the kinematical limit of π^0 from the $K_L \to \pi^0\nu\overline{\nu}$ decay.

After event reconstruction, events satisfying the above conditions of the blind region were removed from the data set regardless of other cut variables. Analysis was performed with this data set until all the selection cuts and background estimation were fixed and they were finally applied for complete data set where the removed events were combined.

7.3 Analysis of the normalization modes

7.3.1 Overview of the normalization

Prior to the $K_L \to \pi^0\nu\overline{\nu}$ analysis, the normalization modes, which include the $K_L \to 3\pi^0$, $K_L \to 2\pi^0$, and $K_L \to 2\gamma$ decays, were analyzed as mentioned in Sec. 7.1. The main goals of this analysis are determination of the normalization factor and validation of signal acceptance calculation which is obtained with the $K_L \to \pi^0\nu\overline{\nu}$ MC simulation, both of which are necessary to convert the number of events after all the selection cuts into the branching fraction or its upper limit. These are also required for background estimation with MC simulations, where simulation outputs needed to be scaled to the corresponding number of events in the data and their reliability should be guaranteed. Here, as mentioned in Sec. 7.1, the normalization factor is the "effective" number of incident K_Ls at the exit of the beam line, where the "effective" means that efficiency of DAQ described in Sec. 3.3.1 is already included.

Six(four)-cluster events were selected from data taken with the minimum bias and normalization trigger for the analysis of the $K_L \to 3\pi^0$ ($K_L \to 2\pi^0$) decays and the invariant mass of the six (four) photon system was reconstructed as described in Sec. 4.3.4. Various selection cuts on reconstructed kinematic variables and veto information were then applied in order to purify contribution of each decay. The same selection was applied for MC simulation samples in order to calculate acceptance ϵ. Here, acceptance is defined as probability where a single incident K_L at the exist of the beam line is detected after all selection cuts and actually calculated to be a ratio of the number of survived events to that of incident K_Ls in the MC simulation. Detail of the MC simulation samples and the selection cut for this analysis are described in Sec. 7.3.2 and Sec. 7.3.3, respectively. Using the number of events after all the selection cuts for each mode, denoted as $N_{\rm data}$, as well as the branching fraction of the mode, B, the normalization factor $N_{\rm norm}$ was obtained as

$$N_{\rm norm} = \frac{pN_{\rm data}}{\epsilon B} \tag{7.6}$$

for each mode, where p is the prescaling factor and given as 30 (300) for the normalization (minimum bias) trigger data. In case of the $K_L \to 2\gamma$ decay, two-cluster events were analyzed and the following analysis process were the same with the other two modes, but the invariant mass was not reconstructed since it needed to be assumed for reconstruction of this mode. Consistency of results among the three modes is a strong indication that the detector system properly working as expected. Distributions of various measured values were then compared between the data and the MC for each mode after scaling the simulation output with the obtained normalization factor, where simulation reproducibility is examined. These discussions are presented in Sec. 7.3.4 in Sec. 7.3.5. With this normalization factor and signal acceptance, $\epsilon_{\rm sig}$, the branching fraction of the $K_L \to \pi^0\nu\overline{\nu}$ decay, $\mathrm{Br}(K_L \to \pi^0\nu\overline{\nu})$ is given as

$$\mathrm{Br}(K_L \to \pi^0\nu\overline{\nu}) = \frac{N_{\rm sig}}{\epsilon_{\rm sig} N_{\rm norm}}, \tag{7.7}$$

when $N_{\rm sig}$ events are observed with no background. An advantage of the method to extract the normalization factor is cancellation of common systematic uncertainties in acceptance of the signal and the normalization mode such as veto detector responses, event selection cuts, decay probability, the accumulated number of Protons On Target (P.O.T.) and DAQ efficiency. For this purpose, selection cuts used in analysis of the normalization modes were chosen so as to be similar to those used in the $K_L \to \pi^0\nu\overline{\nu}$ analysis. Remaining discrepancy between the simulation and the data

Table 7.2: Simulated K_L decay modes in the normalization analysis. The branching fractions were taken from Ref. [16]. Statistics is the number of simulated K_L, where it was shot at the exit of the second collimator.

Decay mode	Branching fraction	Statistics
$K_L \to 3\pi^0$	19.52%	2×10^9 for $K_L \to 3\pi^0$, 1×10^9 for $K_L \to 2\pi^0$, 1.5×10^8 for $K_L \to 2\gamma$
$K_L \to \pi^+\pi^-\pi^0$	12.54%	5×10^7
$K_L \to 2\pi^0$	8.64×10^{-4}	6×10^8
$K_L \to 2\gamma$	5.47×10^{-4}	5×10^7
$K_L \to \pi e\nu_e$	40.55%	5×10^7
$K_L \to \pi\mu\nu_\mu$	27.04%	5×10^7

which did not cancel out was considered as a systematic uncertainty and estimated at the last of this section (Sec. 7.3.6).

7.3.2 MC simulation samples

The following main four decay modes, $K_L \to \pi e\nu_e$ ($Ke3$), $K_L \to \pi\mu\nu_\mu$ ($K\mu3$), $K_L \to 3\pi^0$, and $K_L \to \pi^+\pi^-\pi^0$ as well as the $K_L \to 2\pi^0$ and the $K_L \to 2\gamma$ decays were simulated separately one another. In analyzing each mode of the $K_L \to 3\pi^0$, $K_L \to 2\pi^0$, and $K_L \to 2\gamma$ decays, the selection cuts were applied for all the simulation samples of the above six modes and they were finally combined considering each branching fraction. Simulation statistics used in the normalization analysis is summarized in Table 7.2.

7.3.3 Event selection for each normalization mode

Selection criteria on kinematic variables measured with the calorimeter is summarized in Table. 7.3. As described in Sec. 7.2.2, the online trigger effect is eliminated by requiring total energy of photons to be larger than 650 MeV, where the total photon energy is defined as a sum of six, four and two photons to be analyzed in $K_L \to 3\pi^0$, $K_L \to 2\pi^0$ and $K_L \to 2\gamma$ analysis, respectively. Similar photon cluster selection cuts are then applied, where selection on photon energy is loosened so as to increase acceptance. As for timing, vertex time was reconstructed for each photon and its difference from the event vertex time, or weighted average described in Sec. 4.3.3 and denoted as $\Delta T_{\rm vtx}$, was used for selection to reject photons coming from accidental activities. In order to ensure that two clusters really come from two photons, each photon is required to be separated from others by 150 mm. In the $K_L \to 3\pi^0$ and the $K_L \to 2\gamma$ mode, there is background contribution where a cluster is formed not by a single photon incidence, but charged particles or multiple photons. Such events are rejected by the shape χ^2 cut.

Invariant mass of six or four photons is reconstructed and this is required to be consistent with the nominal K_L mass of 497.614 MeV/c^2 [16] in the $K_L \to 3\pi^0$ and the $K_L \to 2\pi^0$ mode. The same selection on reconstructed K_L z-vertex with the $K_L \to \pi^0\nu\overline{\nu}$ analysis is applied. Events with wrong photon combination are rejected by checking consistency of z vertices among multiple

π^0s or whether π^0 mass reconstructed with a given event z vertex agrees to the nominal value of 134.9766 [16]. For this purpose, χ^2_z which is defined in Sec. 4.3.4 is required to be smaller than 7. In addition, ΔM_{π^0} and $\Delta Z_{\rm vtx}$ is defined for each π^0, where the former is given as difference of reconstructed π^0 mass using its event z vertex from the nominal π^0 mass and the latter as difference of the most upstream and the downstream z vertex positions. The cut on reconstructed K_L incident xy positions on the calorimeter surface is used in order to remove events with missing energy in analyzing the $K_L \to 2\pi^0$ mode. The K_L incident xy positions, denoted as X and Y, respectively, are calculated from Center Of Energy (COE) positions of the photons used in reconstruction $x_{\rm COE}$ and $y_{\rm COE}$:

$$x_{\rm COE} = \frac{\sum_{i=1}^{N}(x_i e_i)}{\sum_{i=0}^{N} e_i}, \tag{7.8}$$

$$y_{\rm COE} = \frac{\sum_{i=1}^{N}(y_i e_i)}{\sum_{i=0}^{N} e_i}. \tag{7.9}$$

The COE position in each xy direction is then scaled to the z position of the beam line exit as follows assuming the target to be a point source fixed at the position of $x = 0$ and $y = 0$,

$$X = x_{\rm COE}\frac{z_{\rm exit} - z_{\rm CsI}}{z_{\rm target} - z_{\rm CsI}}, \tag{7.10}$$

$$Y = y_{\rm COE}\frac{z_{\rm exit} - z_{\rm CsI}}{z_{\rm target} - z_{\rm CsI}}, \tag{7.11}$$

where $z_{\rm exit}$, $z_{\rm CsI}$ and $z_{\rm target}$ are the z position of the beam line exit, the upstream surface of the calorimeter, and the target. Finally, K_L transverse momentum was reconstructed and this was required to be small since K_L basically has no transverse momentum.

In addition to the above kinematic selection, anti-coincidence by veto detectors, which is described in Sec. 7.2.3, was required as well as veto by isolated hit crystals and extra clusters in the calorimeter. The same conditions with the $K_L \to \pi^0\nu\overline{\nu}$ analysis, as shown in Table 7.1, were used.

7.3.4 Result of analysis of the normalization modes

$K_L \to 3\pi^0$

This mode has the large branching fraction (19.52% [16]) and is almost free from background contamination thanks to the many number of photons on the calorimeter. Hence a clean sample with large statistics is available and detailed comparison between data and MC is possible. Figure 7.3 shows reconstructed mass distribution without and with veto. Even without veto detectors, a sharp mass peak was obtained as in the left of Fig. 7.3. Although slight shift of the peak positions exits, the reconstructed mass distributions of the data and MC agree very well including tail regions.

Abundance of signal yields made it possible to evaluate stability of K_L yields. Figure 7.4 shows the number of reconstructed $K_L \to 3\pi^0$ events after all the cuts in each run, where one run basically corresponded to one-hour data acquisition or $\sim 1.8 \times 10^{16}$ P.O.T. and each data point is normalized with P.O.T. for the run considering the prescaling factor described in Secs. 3.3.2 and 3.3.3. Results for three different conditions are shown: without veto cuts for the minimum bias trigger data, with all the veto cuts for data with the minimum bias and normalization trigger. In the first one, whose result is shown in the left panel of Fig 7.4, only the calorimeter information was used while the other two also used veto detector information and stability of both components is evaluated. Yields

Table 7.3: Selection criteria in the analysis of the normalization modes. Selection on variables defined for each photon or each pair of photons such as energy, hit position, time, distance and shape χ^2 needed to be satisfied for all reconstructed photons or possible pairs of the photons.

Selection	$K_L \to 3\pi^0$	$K_L \to 2\pi^0$	$K_L \to 2\gamma$
Total photon energy	> 650 MeV	> 650 MeV	> 650 MeV
Photon energy	> 50 MeV	> 50 MeV	> 50 MeV
Photon hit position	$\max(\lvert x\rvert, \lvert y\rvert) > 150$ mm $r < 850$ mm	$\max(\lvert x\rvert, \lvert y\rvert) > 150$ mm $r < 850$ mm	$\max(\lvert x\rvert, \lvert y\rvert) > 150$ mm $r < 850$ mm
Two-photon distance	> 150 mm	> 150 mm	> 150 mm
$\Delta T_{\rm vtx}$	< 3 ns	< 3 ns	< 3 ns
Shape χ^2	-	< 7	< 7
Rec. K_L mass	(Nominal)± 15 MeV/c^2	(Nominal)± 15 MeV/c^2	-
Rec. $Z_{\rm vtx}$	$3000 < Z_{\rm vtx} < 4700$ mm	$3000 < Z_{\rm vtx} < 4700$ mm	$3000 < Z_{\rm vtx} < 4700$ mm
χ^2_z	< 20	< 20	-
ΔM_{π^0}	< 10 MeV/c^2	< 7 MeV/c^2	-
$\Delta Z_{\rm vtx}$	< 400 mm	< 400 mm	-
Rec. K_L incident pos.	-	$\max(\lvert X\rvert, \lvert Y\rvert) < 50$ mm	-
Rec. K_L $P_{\rm T}$	< 50 MeV/c	< 50 MeV/c	< 50 MeV/c

in each condition was fitted with a constant function and the χ^2/NDF value in each fit shows that the event rate is found to be stable within statistical uncertainty. The fit results of the two graphs in the right of Fig. 7.4, corresponding to the two different trigger types with and without the online veto, shows nice agreement, which indicates effect of the online veto is properly eliminated by the offline veto cuts as well as the given prescaling factor is correctly understood with the real data.

Various kinematic variables were compared between the data and the MC and they are shown in Fig. 7.5. Reconstructed K_L energy is obtained as a total energy of six clusters and reflects the momentum spectrum of K_Ls in the neutral beam. Transverse momentum of K_L corresponds to divergence of the K_L beam. Distributions of incident K_L xy positions are the beam profiles themselves. z vertex position is mainly related to geometric acceptance since solid angle of the effective area on the calorimeter changes depending on z position. The sharp drops at $z \sim 2000$ mm and $z \sim 5500$ mm in its distribution, as in the bottom left of Fig. 7.5, are due to existence of the NCC detector (Sec. 2.2.6) and the calorimeter itself, respectively.

Except the timing distribution, reasonable agreement between the data and the MC was obtained, which ensures that the model of the K_L beam mentioned in Chapter 5 well describes properties of the real K_L beam. In order to handle disagreement in the timing distribution and slight peak shift in the reconstructed K_L mass distribution, corresponding cut regions are set to be loose enough so as to remove efficiency difference and reduce systematic uncertainties due to these selections. As for other discrepancies seen in the edge region of the xy position distributions and the total photon energy distribution, reasons are still unknown.

$K_L \to 2\pi^0$

Analysis of the $K_L \to 2\pi^0$ mode plays the most important role among the three normalization

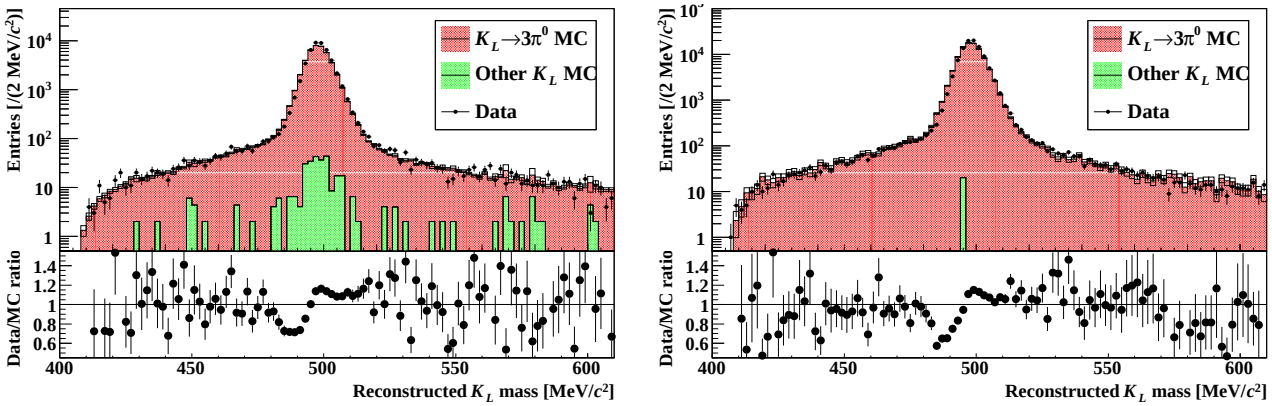

Figure 7.3: Distribution of reconstructed K_L mass in the $K_L \to 3\pi^0$ analysis. In the left figure, data taken with the minimum bias trigger was analyzed without applying veto. The right figure was obtained from data taken with the normalization trigger and veto by all detectors were applied.

mode due to its similarity to the single mode. The $K_L \to 3\pi^0$ decay contribute as background when four photons among six hit the calorimeter and the $K_L \to \pi^+\pi^-\pi^0$ mode can also be background, where two clusters of four derive from two photons from π^0 and the other two from $\pi^\pm$. Since the branching fractions of these modes are larger than that of this mode by two orders of magnitude, $K_L \to 2\pi^0$ component must be extracted from huge background events with both kinematic and veto information as the analysis of the signal mode. Therefore, event reduction by veto and kinematic cuts is able to be evaluated by comparing various distributions between the data and the MC, which is an effective way to validate the MC.

Distributions of reconstructed four-photon invariant mass are shown in Fig. 7.6 for the two different conditions. The left shows a result with data taken with the minimum bias trigger and no veto cuts except for those by the calorimeter were applied. A peak was observed around the nominal K_L mass of $\sim$500 MeV/c^2, but with large contamination from other K_L decay modes, especially $K_L \to 3\pi^0$. Since extra two photons must exist in these $K_L \to 3\pi^0$ events, the veto cuts are expected to reduce these background events significantly. The right histograms of Fig. 7.6 shows the result after applying all the veto cuts as well as the kinematic cuts, where the data taken with the normalization trigger was analyzed for larger statistics. Most of events from the $K_L \to 3\pi^0$ decay were eliminated, particularly in the region below 400 MeV/c^2. The MC simulation well agrees to the data in the whole mass region for both cases and this indicates that the veto reduction is also well reproduced. These results well validate reproducibility of the MC simulation. In particular, remaining events in low mass region of < 400 MeV/c^2 is basically due to inefficiency for extra two photons in the $K_L \to 3\pi^0$ decay, hence orders-of-magnitude event reduction is well confirmed by comparing histograms for these two conditions.

Responses of veto detectors themselves are also evaluated. Figure 7.7 shows veto timing and veto energy distribution for the MB and CV detectors in the $K_L \to 2\pi^0$ samples of the minimum bias trigger data. where all the veto cuts except the calorimeter and the cut on reconstructed K_L mass were removed for larger statistics. In the timing distribution of both MB and CV, sharp peaks

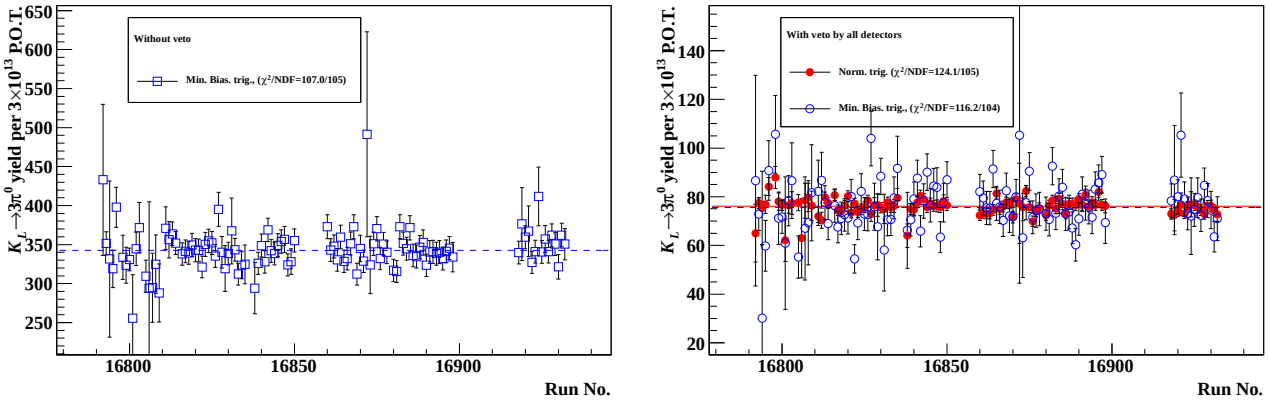

Figure 7.4: Stability of reconstructed $K_L \to 3\pi^0$ events in each run. Data in the left figure was obtained without veto of all the detectors except the calorimeter and that in the right was with all veto cuts applied. Each data set was fitted with a constant function. Blue (red) points and dashed blue (solid red) line indicate that the data was taken with the minimum bias (normalization) trigger.

were observed and extra particles other than four photons or backsplash from the calorimeter were successfully detected. Detector timing in the MC simulation was adjusted so that the peak position agreed to that of the data in each detector. A veto timing range in each detector system was chosen so that the observed peak was completely contained in the veto timing range. Although width of the timing peak in data was not completely reproduced by the simulation, effects by this difference was avoided by setting long veto windows. Veto energy distributions had nice agreement in both detectors and responses of these detectors were well understood.

Timing for other veto systems were also adjusted using observed peaks and veto time ranges were set in the same way with the above detectors. Several examples are shown in Fig. 7.8 for detectors inside the vacuum tank and Fig. 7.9 for those located in the downstream of the whole KOTO detector system. The same trigger and cut conditions with MB and CV in Fig. 7.7 were applied, although several cuts were loosened only for FB and NCC in order to enhance their hit timing peak. In most detectors, width of the peaks in the data was not reproduced by the simulation hence veto timing windows were set to be wide in order to reduce acceptance difference derived from this discrepancy. In FB, the veto timing window was chosen so that the observed peak in Fig. 7.8 located in later timing inside the timing region. Since signals of FB are read only from the upstream side, hit timing is strongly affected by photon incident z position; photon hits in the upstream region gives earlier timing and those in the downstream region are detected in later timing. FB is required to detect photons hitting both the upstream and the downstream of FB in the $K_L \to \pi^0\nu\overline{\nu}$ analysis, whereas only the downstream contribution is observed in this normalization analysis. Therefore, the veto time window was adjusted so that the timing peak in the $K_L \to 2\pi^0$ sample was shifted from its center. In the timing distributions of BHCV and BHPV, the structure of the tail regions, which came from accidental activities, differed between the data and the MC; the wide bump in the data reflected bunch structure arising from the transverse RF as was seen in Fig. 6.22. In the MC simulation, this timing structure was not considered but flat timing distribution with averaged rates

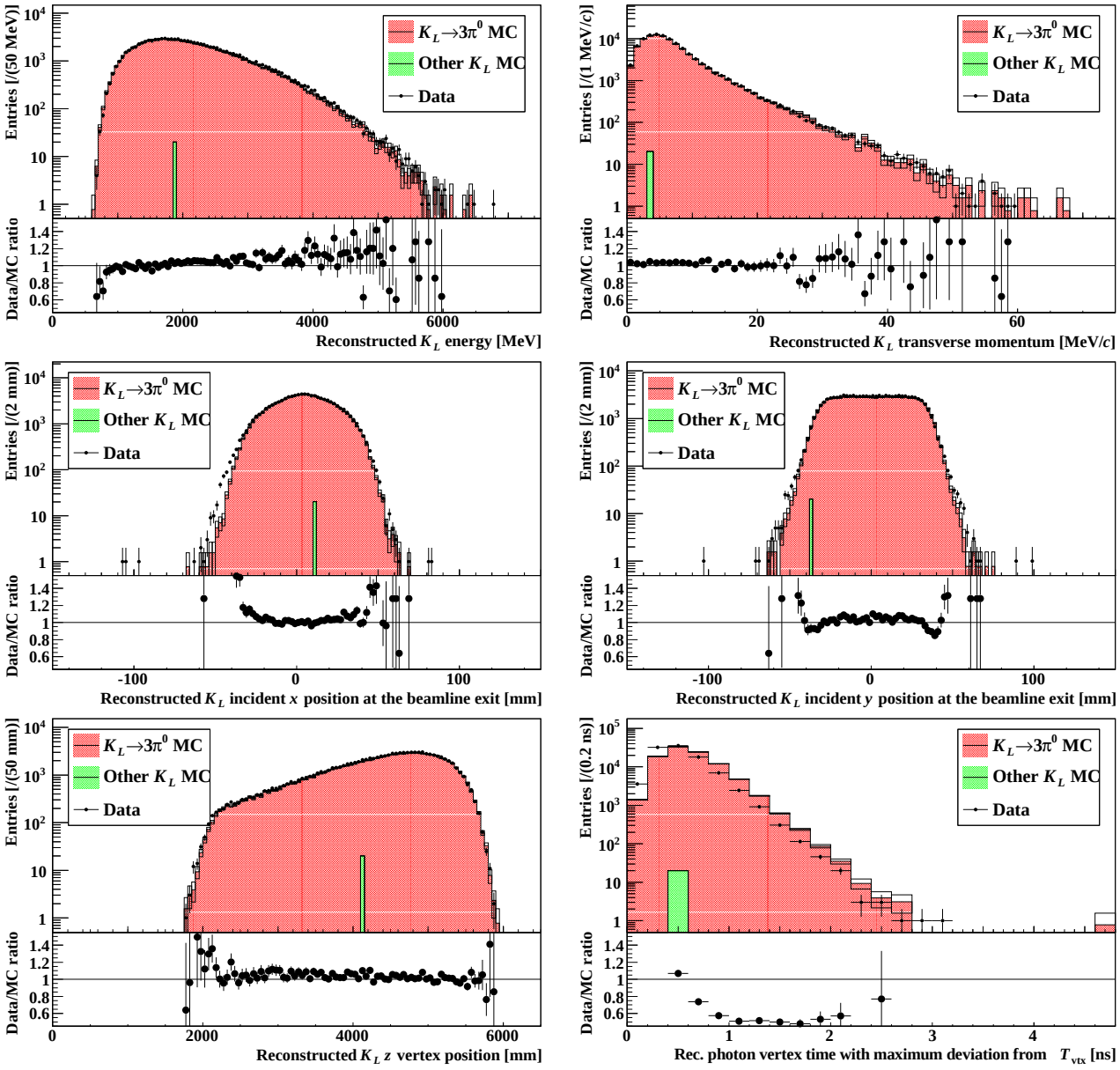

Figure 7.5: Distribution of various kinematic variables reconstructed in the $K_L \to 3\pi^0$ decay analysis. (Top left) Total six photons energies, or reconstructed K_L energy. (Top right) Transverse momentum. (Middle left) x position of incident K_Ls at the exit of the beam line. (Middle right) y position of incident K_Ls at the exit of the beam line. (Bottom left) Decay z vertex position. (Bottom right) Reconstructed vertex time for the photon with the maximum deviation from its event vertex time, or weighted average for six photons.

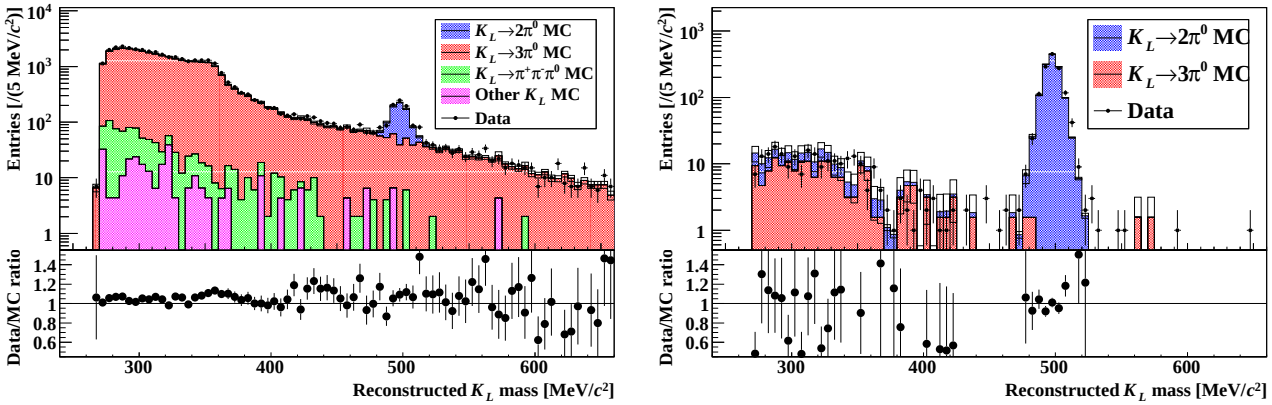

Figure 7.6: Distributions of reconstructed K_L mass in the $K_L \to 2\pi^0$ analysis. Veto cuts other than the calorimeter were not applied in the left figure and all the veto cuts were applied in the right figure.

was implemented as that of accidental hits. Effect of this difference on the signal loss is, however, reduced by setting veto width to be 15 ns, which was close to the periodic cycle of 21-ns interval. Still the data shows slight excesses in energy or the number of hit modules distribution in these detectors and this discrepancy is considered as a source of systematic uncertainty

$K_L \to 2\gamma$

For further confirmation of the analysis, reconstruction of the $K_L \to 2\gamma$ decay was also compared between data and the simulation. Since the K_L mass is assumed to reconstruct this decay, other kinematic variables were examined. Figure 7.10 shows data and MC comparison for various kinematic variables. As in Fig. 7.5, distributions of reconstructed K_L energy, transverse momentum and decay z vertex position agree well between the data and the MC, which validates the model of the K_L beam and the decay simulation again. The broader distribution of reconstructed K_L transverse momentum than in Fig. 7.5 is due to assumption of decay on the beam axis, which was not applied in the $K_L \to 3\pi^0$ analysis. Discrepancy is seen in the timing distribution between the data and the MC as shown in the bottom right of Fig. 7.10, where timing difference of two photons' reconstructed vertex time is presented instead of $\Delta T_{\rm vtx}$ used as a cut value in the $K_L \to 2\gamma$ analysis. Although the timing in the simulation seems to be too much smeared, its distribution in both the data and the MC was found to be well contained in ± 2 ns, which validated use of vertex time difference in the $K_L \to \pi^0\nu\overline{\nu}$ analysis.

7.3.5 Determination of the normalization factor

The numbers of events after all the selections in each analysis for the $K_L \to 3\pi^0$, $K_L \to 2\pi^0$ and $K_L \to 2\gamma$ decay is summarized in Table 7.4 as well as acceptance to an incident K_L at the beam line exit ($z = -1507$ mm). Here, data with the normalization trigger is considered. Taking cancellation of the systematic error as mentioned in Sec. 7.3.1, the normalization factor obtained from the analysis of the $K_L \to 2\pi^0$ mode was adopted as the final value to be used in the $K_L \to \pi^0\nu\overline{\nu}$

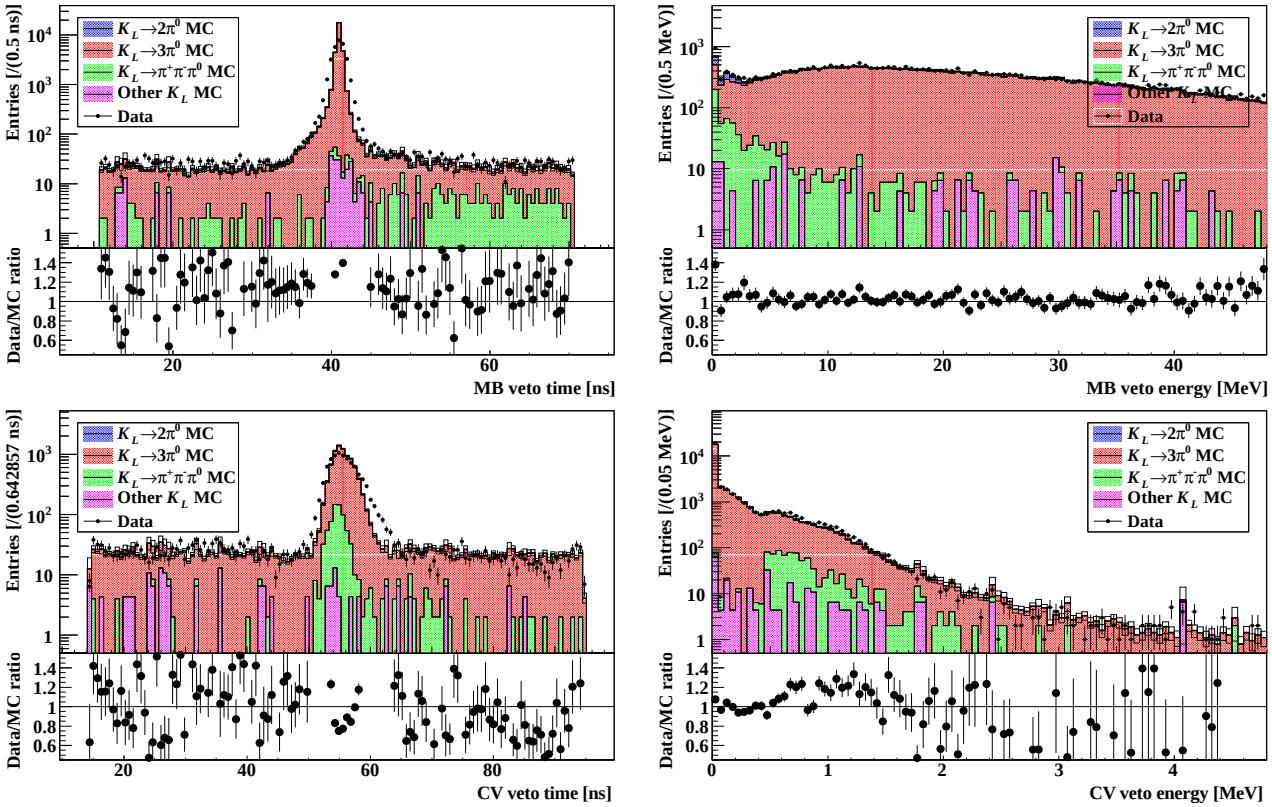

Figure 7.7: Responses of the MB and CV detector in $K_L \to 2\pi^0$ events. In timing distribution, timing only within the veto window is shown.

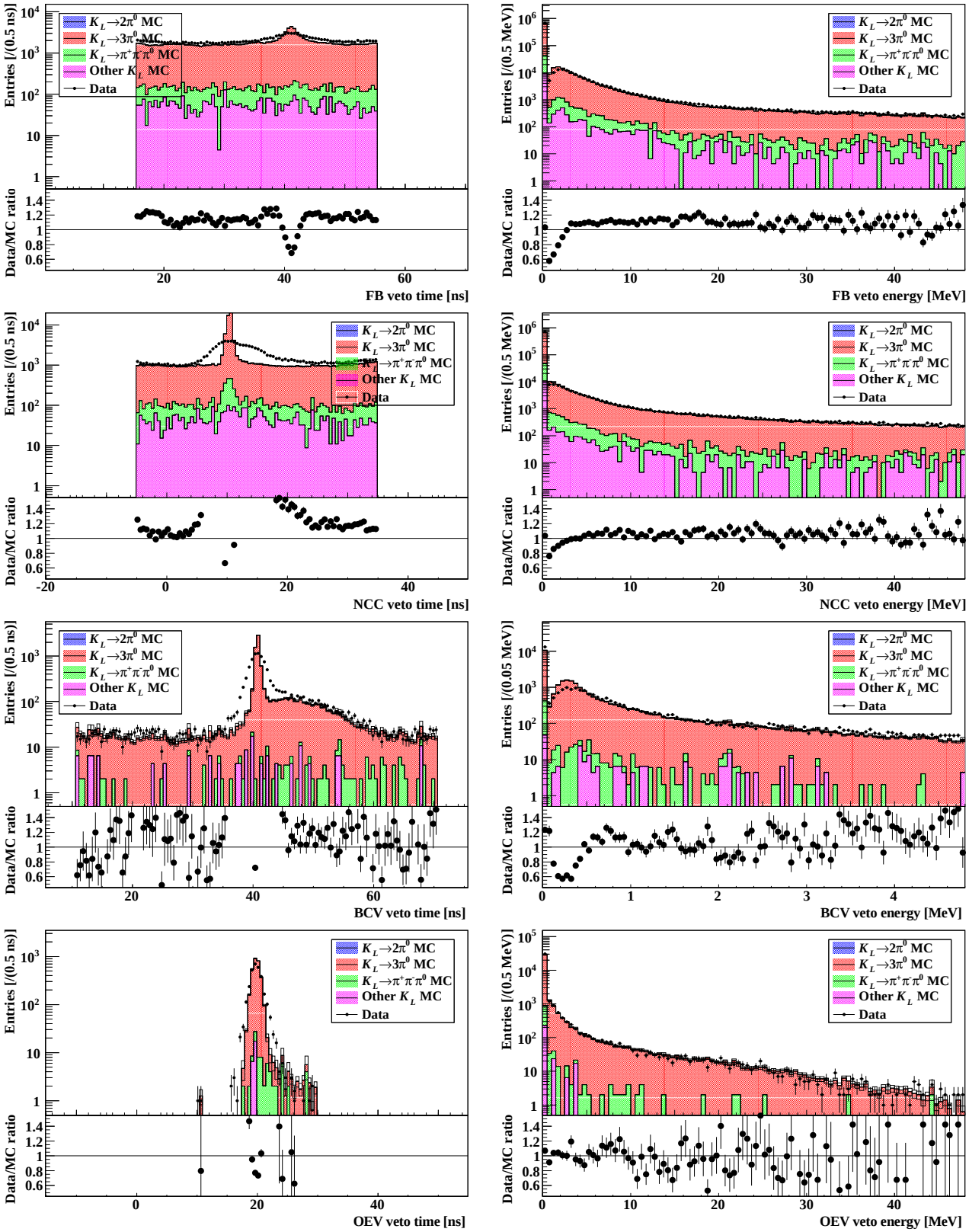

Figure 7.8: Energy and timing responses of FB, NCC, BCV and OEV in $K_L \to 2\pi^0$ events. In timing distribution for FB and NCC, accidental overlay was not applied for simulation samples.

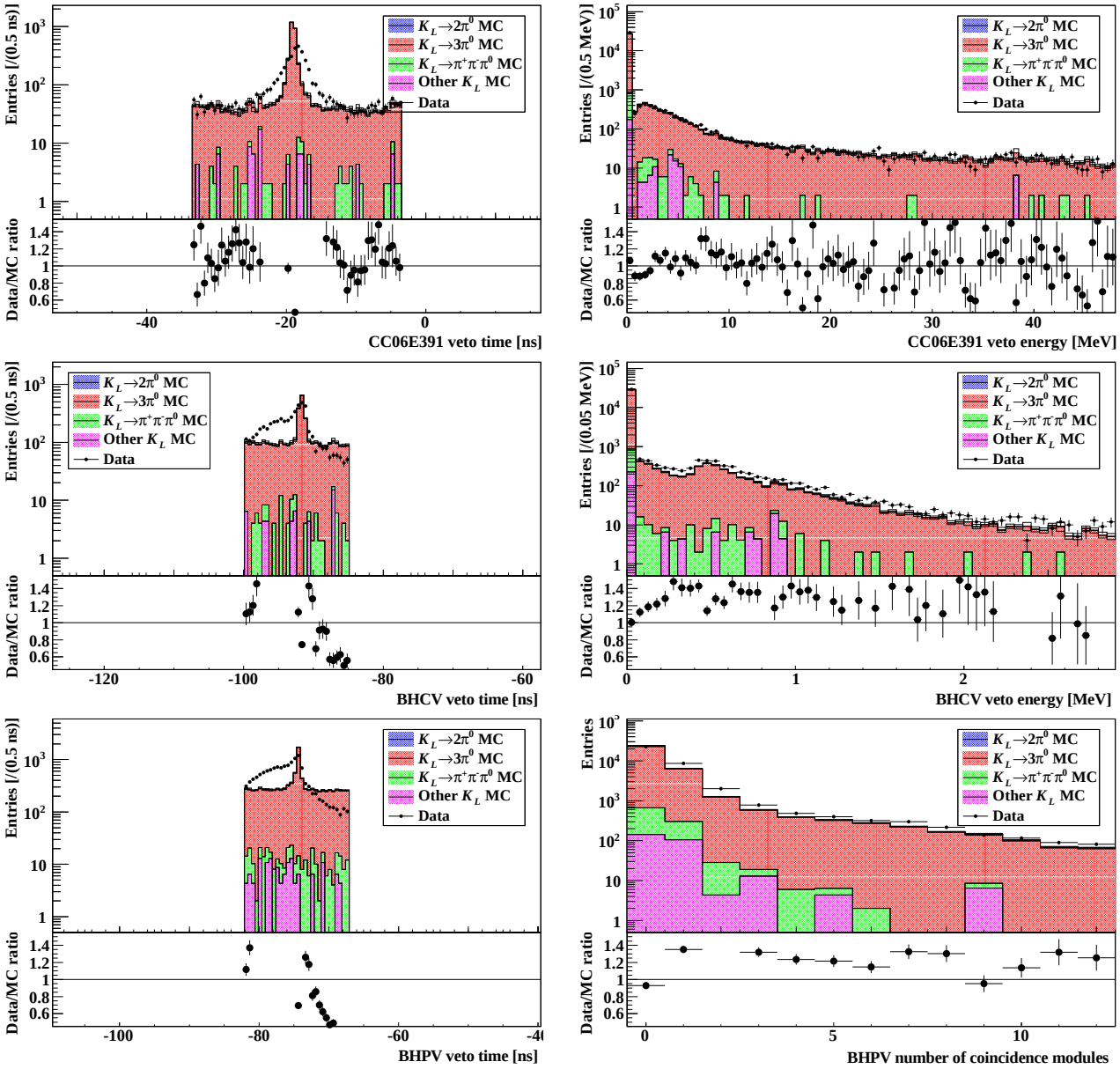

Figure 7.9: Energy and timing responses of downstream veto detectors in $K_L \to 2\pi^0$ events.

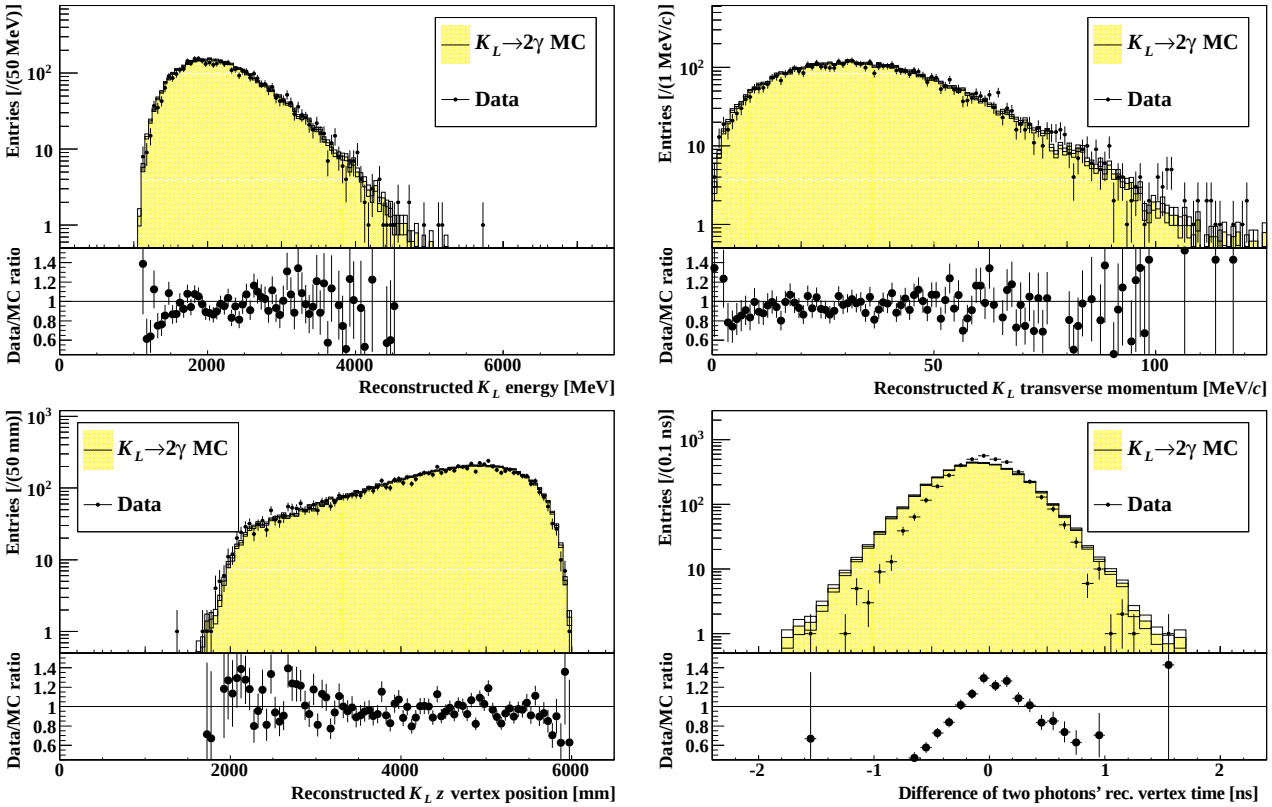

Figure 7.10: Distributions of kinematic variables in analysis of $K_L \to 2\gamma$. (Top left) Reconstructed K_L energy, or sum of two photons' energies. (Top right) Reconstructed transverse momentum. (Bottom left) Reconstructed z vertex position. (Bottom right) Difference of two photons' reconstructed vertex time. Timing with smaller energy was subtracted from that with larger energy.

Table 7.4: The number of events after all the selection cuts in $K_L \to 3\pi^0$, $K_L \to 2\pi^0$ and $K_L \to 2\gamma$ analysis and acceptance in each mode. Normalization factors for each mode are also shown. Branching ratios and the prescale factor are considered in the acceptance values and the normalization factors. Only statistical uncertainty of data and simulation samples was considered in the shown errors of acceptance and normalization factors.

Decay mode	The number of events	(Acceptance)×(Branching fraction)	Normalization factor
$K_L \to 3\pi^0$	100,623	$(1.221 \pm 0.003) \times 10^{-5}$	$(2.472 \pm 0.010) \times 10^{11}$
$K_L \to 2\pi^0$	1,296	$(1.617 \pm 0.005) \times 10^{-7}$	$(2.404 \pm 0.067) \times 10^{11}$
$K_L \to 2\gamma$	3,988	$(5.191 \pm 0.024) \times 10^{-7}$	$(2.305 \pm 0.038) \times 10^{11}$

analysis and determined to be 2.399×10^{11}, where the prescaling factor of 30 is considered.

In order to confirm consistency among the different decay modes the normalization factor which was obtained in each mode was compared and the result is shown in Fig. 7.4, where each value is normalized with 2.399×10^{11}[*2], All the three values are consistent one another within 4%, which indicates that the simulation well describes the real K_L beam and detector response.

By using the total amount of P.O.T., this value is compared with the result of the K_L yield measurement which was carried out in January, 2013, as an engineering run of the physics run. The total P.O.T. was measured to be 1.188×10^{18} as an accumulation of spill-by-spill P.O.T. measurement with SYIM, where dead time due to DAQ is already included. As a result, the K_L flux in the physics run is given as $(4.041 \pm 0.109_{\text{stat.}}) \times 10^7$ per 2×10^{14} P.O.T. According to Ref. [108], the K_L flux is obtained as $(4.183 \pm 0.017_{\text{stat.}} \pm 0.059_{\text{syst.}}) \times 10^7$ per 2×10^{14} P.O.T., which is well consistent with this result within 1.3σ of statistical error.

7.3.6 Systematic uncertainties

In scaling the obtained number of events into the branching fraction or its upper limit, the ratio of acceptance between the $K_L \to 2\pi^0$ and the signal mode plays an essential role as show in the following equations:

$$\begin{aligned} \text{Br}(K_L \to \pi^0\nu\overline{\nu}) &= \frac{N}{\epsilon_{\text{sig}} N_{\text{norm}}}, \\ &= \frac{N}{p N_{K_L\to 2\pi^0}} \frac{\epsilon_{K_L\to 2\pi^0}}{\epsilon_{\text{sig}}} \text{Br}(K_L \to 2\pi^0), \end{aligned} \tag{7.12}$$

where $N_{K_L\to 2\pi^0}$ and $\epsilon_{K_L\to 2\pi^0}$ are the number of observed events in the data and acceptance of the $K_L \to 2\pi^0$ mode in the normalization analysis, respectively, $\text{Br}(K_L \to 2\pi^0)$ is the branching fraction of this mode, and the other variables are given in Sec. 7.3.1. Although the acceptance values are obtained with the MC simulation, there exist some discrepancy between the data and the MC in distributions presented in Sec. 7.3.4, and these disagreement should be considered as a source of

[*2]Since decision of this value was actually based on a separate MC sample where only statistics was different, the data/MC ratio for the $K_L \to 2\pi^0$ mode is slightly shifted from 1, although within statistical fluctuation of 0.3% for the simulation sample used here.

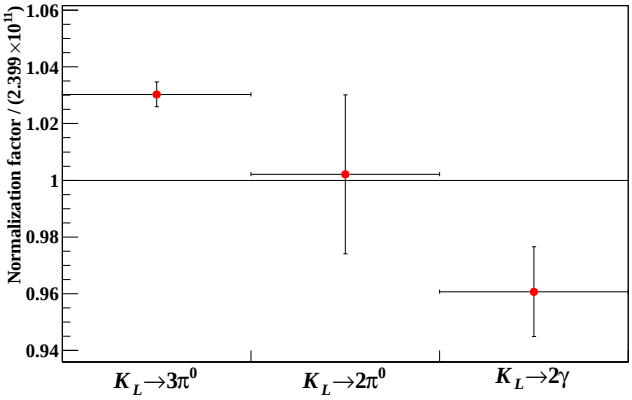

Figure 7.11: The normalization factors obtained in the three decay modes, where acceptance for each mode and the prescale factor is considered and ratios to the nominal value of 2.399×10^{11} are presented. The error bars indicate statistical error only.

systematic uncertainty. On the other hand, as already mentioned in Sec. 7.3.1, some uncertainties are expected to be canceled if they are common both in the signal and the $K_L \to 2\pi^0$ mode. To take this possible cancellation of systematic uncertainties, each acceptance values were assumed to be factorized as follows

$$\epsilon_{K_L\to 2\pi^0} = \epsilon^{K_L\to 2\pi^0}_{\text{geom.}} \times \epsilon^{K_L\to 2\pi^0}_{\gamma} \times \epsilon^{K_L\to 2\pi^0}_{\text{kin.}} \times \epsilon^{K_L\to 2\pi^0}_{\text{veto}}, \tag{7.13}$$

$$\epsilon_{\text{sig}} = \epsilon^{\text{sig}}_{\text{geom.}} \times \epsilon^{\text{sig}}_{\gamma} \times \epsilon^{\text{sig}}_{\text{kin.}} \times \epsilon^{\text{sig}}_{\text{shape}} \times \epsilon^{\text{sig}}_{\text{veto}} \times \epsilon^{\text{sig}}_{\text{onlineCOE}}, \tag{7.14}$$

$$\tag{7.15}$$

where the subscript "geom." is for geometrical acceptance and "γ", "kin.", "shape" and "veto" are for cuts related to photon cluster selection, kinematics of reconstructed π^0 or K_L, cluster shapes and veto. For the signal mode, efficiency of the online COE trigger $\epsilon^{\text{sig}}_{\text{onlineCOE}}$ is considered, which was used only for the physics trigger. Difference of acceptance ratios or acceptance values themselves between the data and MC was evaluated for each factor and finally a square root of their quadratic sum was considered as the total systematic error for the $K_L \to \pi^0\nu\overline{\nu}$ branching fraction.

Geometrical acceptance

Uncertainty of the geometrical acceptance ratio for the $K_L \to \pi^0\nu\overline{\nu}$ decay to the $K_L \to 2\pi^0$ decay, $\epsilon^{K_L\to 2\pi^0}_{\text{geom.}}/\epsilon^{\text{sig}}_{\text{geom.}}$, was evaluated with the fast simulation method as is described in Sec. 6.4.3. Here, the geometrical acceptance was defined as a ratio of the number of events where all the four (two) photons in the $K_L \to 2\pi^0$ ($K_L \to \pi^0\nu\overline{\nu}$) decay hit the calorimeter fiducial region to the total number of K_L whose z vertex is within 3000 - 4700 mm. The fiducial region is defined as $\max(|x|, |y|) > 100$ mm and $\sqrt{x^2+y^2} < 900$ mm, where x and y are photon hit positions at the calorimeter surface. Uncertainties of the K_L momentum distribution and the beam position were considered.

In considering the K_L momentum distribution, true momentum distributions for events in the geometrical acceptance, as shown in Fig. 7.12, were reweighed so as to evaluate change of the $K_L \to 2\pi^0/K_L \to \pi^0\nu\overline{\nu}$ acceptance ratio when the K_L momentum spectrum is changed. As a

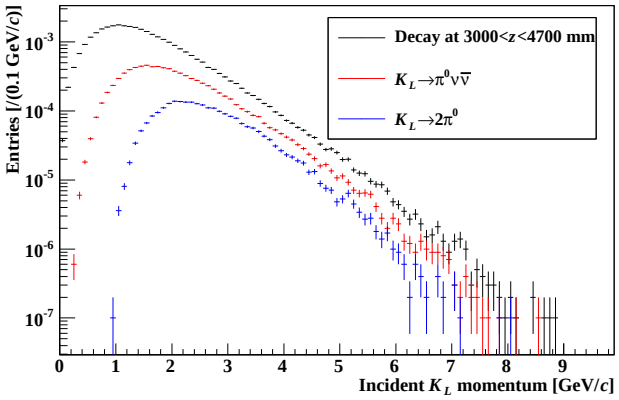

Figure 7.12: Distributions of true incident K_L momentum used in calculation of geometrical acceptance.

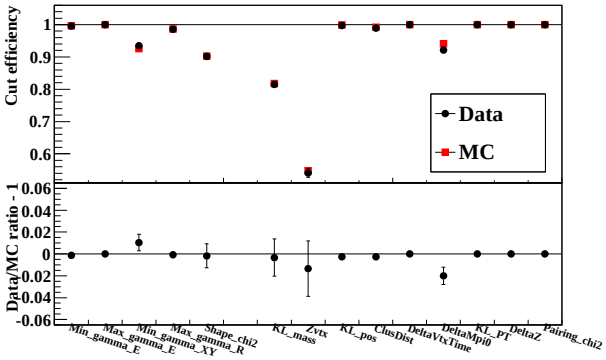

Figure 7.13: Systematic uncertainty evaluation for the photon selection cuts and cuts on reconstructed K_L kinematics. Each label on the horizontal axis corresponds to each selection cut. Its efficiency values in the data and MC are shown in the top part and their difference is in the bottom part. The left and right group of cuts is for the photon selection cut and the kinematic cuts on reconstructed K_L, respectively.

result, this uncertainty was estimated to be $^{+0.93\%}_{-0.85\%}$[*3].

Procedures for uncertainty of the K_L beam position is also almost the same with those in Sec. 6.4.3. Geometrical acceptance ratios when the beam position was shifted in each of the x and y directions by ± 1 mm were evaluated. Uncertainty due to the beam position was given as their relative difference to the nominal value and determined to be 0.055%.

Summing these values in quadrature, the total uncertainty was estimated to be $^{+0.932\%}_{-0.852\%}$.

Photon selection cuts

Although some cancellation is expected between $\epsilon_\gamma^{K_L\to 2\pi^0}$ and $\epsilon_\gamma^{\rm sig}$, uncertainty due to $\epsilon_\gamma^{K_L\to 2\pi^0}$ was considered conservatively. For each cut, "cut efficiency" $\epsilon_{\rm cut}$ was first defined as

$$\epsilon_{\rm cut} = \frac{N_{\rm norm}}{N_{\rm norm}^{\rm cut}}, \tag{7.16}$$

where $N_{\rm norm}$ is the number of events with all the $K_L \to 2\pi^0$ selection cuts and $N_{\rm norm}^{\rm cut}$ is the number of events with all the cuts except for one of interest. This is compared between the data and the MC and their ratio subtracted by 1 was regarded as uncertainty due to the cut. The result for each cut is summarized in Fig. 7.13. A square root of the quadratic sum is calculated as total uncertainty and it was given as $\pm 1.07\%$.

[*3]For more precise estimate, it is desirable to use momentum distribution after applying all the selection cuts in order to consider correlation between geometrical acceptance and selection cut efficiency.

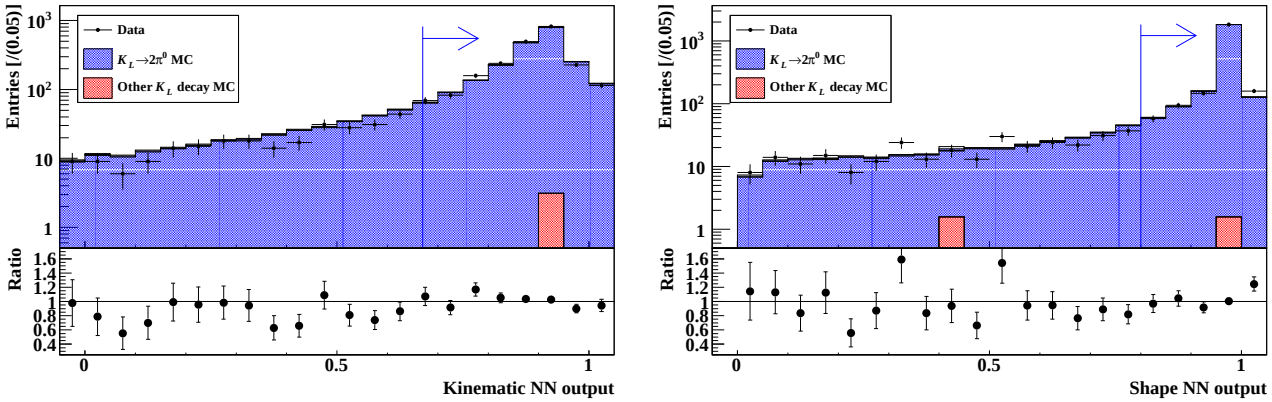

Figure 7.14: Examples of distribution in the π^0 sample obtained in the $K_L \to 2\pi^0$ analysis. The left panel shows distribution of kinematic NN outputs and the right one shows shape NN distribution. The blue line and arrow in each figure indicates the accept region in the $K_L \to \pi^0\nu\overline{\nu}$ anslysis.

Kinematic cuts for reconstructed π^0 and K_L

Since the selection cuts are completely different in these two analyses, both uncertainties of $\epsilon_{\text{kin.}}^{K_L\to 2\pi^0}$ and $\epsilon_{\text{kin.}}^{\text{sig}}$ were taken in the final systematic error. As for the event selection based on kinematics of reconstructed K_L in the $K_L \to 2\pi^0$ analysis, cut efficiency difference between the data and the MC was evaluated as was done for the photon selection cut. The result is summarized in Fig. 7.13. Total uncertainty was estimated to be $\pm 2.46\%$. and their quadratic sum was regarded as uncertainty of $\epsilon_{\text{kin.}}^{K_L\to 2\pi^0}$. In uncertainty evaluation of kinematic cut efficiency used in the $K_L \to \pi^0\nu\overline{\nu}$ analysis, a control sample of reconstructed π^0 was prepared, where each of two π^0s in the $K_L \to 2\pi^0$ decay after all the selection cuts was again reconstructed with an assumption of decay on the beam axis and various kinematic variables were calculated. For each variable, ratios of events which satisfies the same condition with the $K_L \to \pi^0\nu\overline{\nu}$ analysis were compared between the data and the MC. An example of the kinematic NN is shown in the left of Fig. 7.14. Data and MC cut efficiency was calculated as the number of events above the cut threshold, 0.67 for this cut, to the total number of events and their ratio was calculated. Uncertainty due to this cut was then defined as shift of this ratio from 1. The result for all the cuts is summarized in the left part of Fig. 7.15. Total uncertainty was estimated to be $\pm 2.81\%$.

Shape-related cuts

Most of the cluster-shape-related cuts were not used in the $K_L \to 2\pi^0$ analysis, hence uncertainty due to these selections needs to be considered. The same procedures with above were adopted for uncertainty estimation above, where cut variables were calculated for the π^0 sample and an event ratio for each cut condition was compared between the data and the MC. An example of the shape NN output is shown in the right of Fig. 7.14. The result for all the cuts is summarized in the right part of Fig. 7.15, where the shape NN cut, the shape χ^2 cut, the cluster size cut and the cluster RMS cut were considered. Total uncertainty was estimated to be $\pm 2.51\%$.

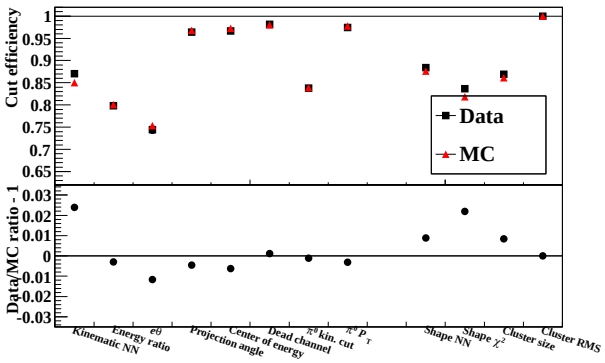

Figure 7.15: Evaluation of systematic uncertainty due to the cuts related to π^0 kinematics and cluster shape.

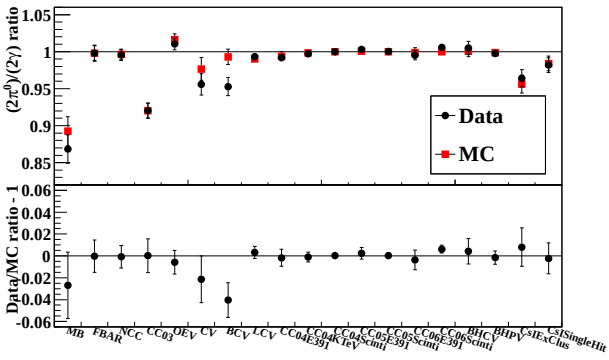

Figure 7.16: Evaluation of systematic uncertainty due to the veto cuts.

Veto cuts

Uncertainty due to the veto cuts was evaluated by comparing ratios of veto cut efficiency between the data and the MC. Here the $K_L \to 2\gamma$ sample was used instead of the $K_L \to \pi^0\nu\overline{\nu}$ decay since these two decays have the same final state of "two photons only." The efficiency ratio is defined for detector by detector as

$$\frac{N_{K_L\to 2\pi^0}}{N^{\rm det}_{K_L\to 2\pi^0}} \Big/ \frac{N_{K_L\to 2\gamma}}{N^{\rm det.}_{K_L\to 2\gamma}}, \tag{7.17}$$

where $N_{K_L\to 2\gamma}$ ($N_{K_L\to 2\pi^0}$) is the number of events after all the selection cuts in the $K_L \to 2\gamma$ ($K_L \to 2\pi^0$) analysis which is given in Table 7.4 and $N^{\rm det}_{K_L\to 2\gamma}$ ($N^{\rm det}_{K_L\to 2\pi^0}$) is the number of events with all the selection cuts except for the veto cut of the corresponding detector system. Results for each veto systems are summarized in Fig. 7.16. There is a discrepancy in the BCV veto cut, which gives the main contribution. The final uncertainty was calculated as the square root of the quadratic sum over all the veto system, where each contribution is assumed to be independent, and obtained as 5.43%.

Efficiency of the online COE trigger

Since the online-COE trigger was not used to collect the $K_L \to 2\pi^0$ sample taken with the normalization trigger, efficiency of this selection is considered only for the signal sample and no cancellation is expected. Effect of this trigger selection was still remaining even after requiring $R_{\rm COE} > 200$ mm, where $R_{\rm COE}$ is an offline-COE value and defined in Sec. 5.4.6. Although this effect was corrected as described in Sec. 5.4.6 for simulation samples, validity of this correction needs to be confirmed. For this purpose, control samples were defined and the following double ratio is considered:

$$\left(\frac{pN^{\rm data}_{\rm norm}}{N^{\rm data}_{\rm phys}}\right) \Big/ \left(\frac{N^{\rm MC}_{\rm norm}}{N^{\rm MC}_{\rm phys}}\right), \tag{7.18}$$

where p is the prescaling factor of the normalization trigger, $N^{\rm data}_{\rm norm}$ ($N^{\rm data}_{\rm phys}$) is the number of events in data taken with the normalization (physics) trigger, and $N^{\rm MC}_{\rm norm}$ and $N^{\rm MC}_{\rm phys}$ are the simulation expectation for each trigger type. The ratio of the numerator (denominator) in Eq. (7.18) represents

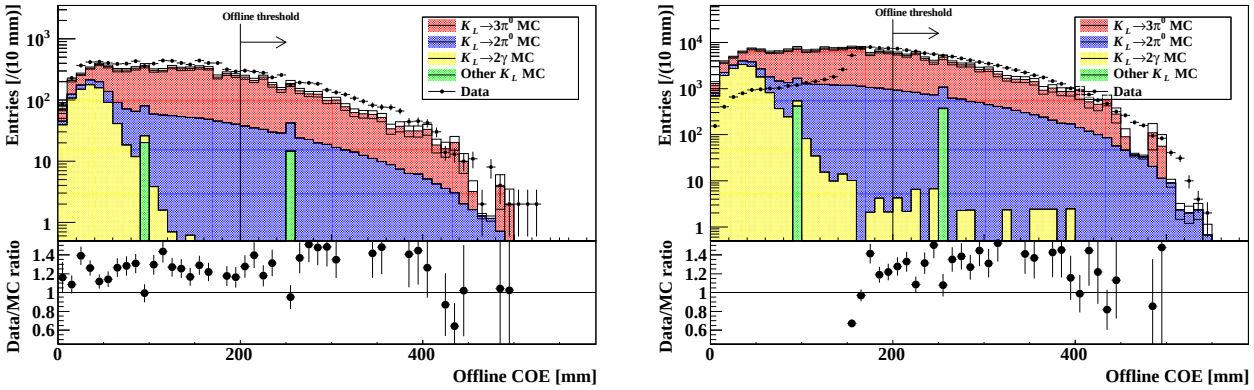

Figure 7.17: Distribution of $R_{\rm COE}$ in the control samples for error evaluation of the online-COE trigger. The left (right) panel is for the sample with the normalization (physics) trigger.

efficiency of the online-COE trigger in data (simulation). The prescaling factor is $p = 30$ and $N_{\rm norm}^{\rm MC}$ was obtained by removing event weights as described in Sec. 5.4.6 in the simulation. The control samples were obtained by removing several kinematic and veto cuts defined in Sec. 7.2[*4] and $P_{\rm T} < 120$ MeV/c and $2500 < Z_{\rm vtx} < 5500$ mm were required. Finally, deviation of this ratio from 1 was regarded as the systematic error. Distribution of $r_{\rm COE}$ for the control sample with the physics and normalization triggers are shown in Fig. 7.17. The double ratio of Eq. (7.18) was calculated using an integral of each histogram over the range of $R_{\rm COE} > 200$ mm. As a result, the uncertainty was estimated to be $\pm 4.47\%$.

Total systematic uncertainty

As the total systematic uncertainty for measurement of the $K_L \to \pi^0\nu\overline{\nu}$ branching fraction, a squared root of the quadratic sum of the above values as well as the error of the $K_L \to 2\pi^0$ branching fraction was considered. These are summarized in Table 7.5. The total relative error of the $K_L \to \pi^0\nu\overline{\nu}$ branching fraction for N-signal-event observation is given as

$$\pm\, 2.7\% \pm (100 \times \sqrt{1/N}\%) \pm 8.5\%, \tag{7.19}$$

where the first two terms are the statistical errors and the last term is the total systematic error.

7.4 Background estimation

This section describes estimation of background, or non-signal contribution which survives the event selection given in the previous section. Figure 7.18 shows $Z_{\rm vtx}$-$P_{\rm T}$ distribution after applying all the selection cuts including both the CsI cuts and veto cuts with the signal region and its surroundings blinded. Background estimation was performed using MC simulations and the side band events in Fig. 7.18 as well as other control samples. The event selection cuts were optimized so as to suppress background contribution to be small enough.

Table 7.6 summarizes result of background estimation. K_L background mainly comes from finite detector inefficiency. Since the mechanism is different according to the decay mode, separate

[*4] The following cuts and veto were removed : the $e\theta$ cut, the projection angle cut, the energy ratio cut, the π^0 kinematics cut, the dead channel distance cut, the FB veto, the BCV veto and the MB veto.

Table 7.5: Summary of the systematic uncertainties in calculation of the $K_L \to \pi^0\nu\overline{\nu}$ branching fraction.

Error source	Relative error [%]
Geometrical acceptance ($\epsilon_{\text{geom.}}^{K_L\to 2\pi^0}/\epsilon_{\text{geom.}}^{\text{sig}}$)	$^{+0.93}_{-0.85}$
Photon selection cuts	± 1.07
K_L kinematic cuts	± 2.46
π^0 kinematic cuts	± 2.81
Shape-related cuts	± 2.51
Veto cuts	± 5.43
Online-COE trigger	± 4.47
$K_L \to 2\pi^0$ branching fraction [16]	± 0.69
Total	± 8.5

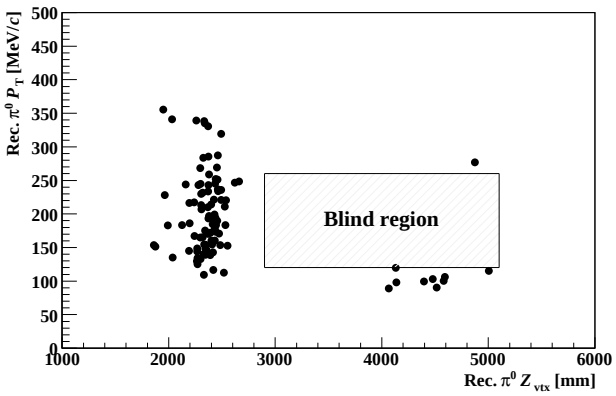

Figure 7.18: Z_{vtx}-P_{T} distribution after applying all the selection cuts with signal region blinded.

estimation methods were developed for each mode. The background due to "masking" is caused by pulse pile-ups in the high-rate environment, where a hit was missed due to wrong timing calculation as described in Sec. 4.2.1. As for neutron background, data taken in the aluminum target run as described in Sec. 3.4.2 was used as a control sample since the simulation poorly reproduced measurement data and was not reliable.

Below, detail of background estimation for each source is described, where K_L and masking-induced background are mainly focused. The same simulation samples shown in Table 7.2 were used unless any specific mentions do not exist.

7.4.1 $K_L \to 2\pi^0$ background

Mechanism

This decay mode was considered to be the most dangerous background source as only two photons were available for veto. Detector inefficiency is critical for this background and those of the MB and BHPV detectors would be expected to contribute to background mainly. Various mechanism

Table 7.6: Summary of background estimation.

Background source	The number of expected events
K_L background	
$K_L \to 2\pi^0$	(0.047 ± 0.033)
$K_L \to 2\gamma$	(0.030 ± 0.018)
$K_L \to \pi^+\pi^-\pi^0$	(0.0016 ± 0.0016)
$K_L \to 3\pi^0$	(0.0050 ± 0.0007)
$Ke3$	(0.0045 ± 0.0045)
Masking by accidental activity	
$K\mu 3$	< 0.016 (90% C.L.)
$K_L \to 3\pi^0$	(0.014 ± 0.014)
$K_L \to \pi^+\pi^-\pi^0$	< 0.007 (90% C.L.)
Neutron background	
Upstream events	(0.056 ± 0.056)
Hadron cluster events	(0.18 ± 0.15)
Total	(0.34 ± 0.16)

as shown below are possible:

- Photon punch-through
  When an amount of materials along path of an incident photon in a detector was not sufficient, it penetrate the detector without any interaction and the photon escaped from detection. This was called "punch-through" and dominating inefficiency in the BHPV detector. Its probability was not negligible in the MB detector. For these detectors, additional modules were planned to be added to reduce this kind of inefficiency.

- Sampling effect
  Since both the MB and BHPV detector owned sandwich structure of alternate active materials and inactive convertor layers, an incident photon was not detected when its shower was completely contained in the convertor layer due to fluctuation of shower development. This type of inefficiency was serious in low energy photons hitting the MB detector.

- Support frames around the edge of the calorimeter
  As shown in Fig. 7.19, several inactive materials were located around the edge of the calorimeter to support the protection cover for the calorimeter and the CV detector. These materials contribute additional inefficiency.

- Photonuclear reactions
  A photon directly interacts with atomic nuclei in detector materials and is absorbed by them. The nuclei are excited and its energy is emitted as hadrons such as neutrons and protons. When neutrons are emitted, they can escape to outside of the detector without any activities. and the photon incidence was not detected in such a case. This reaction dominates inefficiency in high energy region.

- Pileup of accidental activity
  This inefficiency was caused by wrong timing calculation as described in Sec. 4.2.1. This

needed to be taken into account for all the decay modes with extra particles and the detail will be discussed in Sec. 7.4.6.

- Fusion cluster
  Even though three photons of four hit the calorimeter, two of them can fuse into a single cluster when their incident positions are close to each other. The event is then regarded as a two-photon event. In this case, only one photon is available for veto, this type of events can make large contribution to backgrounds.

Background rejection cuts

$K_L \to 2\pi^0$ events are categorized into three types according to topologies: even paring events, odd pairing events, and fusion events. In even (odd) pairing events, two photons on the calorimeter came from the same (different) π^0. In case of an odd pairing event, vertex is not properly reconstructed and inconsistency occurs in its kinematics. Selection with energy ratio of the two photons and $e\theta$ value are examples of use of difference in kinematics. In fusion events, where three photons hit the calorimeter and two of them form one cluster as already explained, discrimination by difference of cluster shape is effective. This was mainly achieved by "shape χ^2 cut," which evaluated how observed cluster agreed to simulated cluster shape with single photon incidence.

Method of estimation

Since the full simulation well describes the data as discussed in Sec. 7.3, background contribution from this decay mode was estimated by fully simulating $K_L \to 2\pi^0$ decays. Here, in the full simulation, interaction of all decay particles in the detectors was fully simulated as described in Chap. 5, and all the possible background sources mentioned above are considered. Simulation results are scaled into the corresponding number of events in the data using the number of K_Ls at the exit of the beam line, 2.399×10^{11}, which is obtained in Sec. 7.3. This K_L number will be used also in the following sections describing background estimation for other sources unless there are any other mentions. Thanks to the small branching ratio (8.64×10^{-4}) in case of the $K_L \to 2\pi^0$ decay, it is possible to simulate the larger number of $K_L \to 2\pi^0$ decays than that is contained in the real data. In order to obtain enough statistics efficiently, simulations were performed in the two steps. First, only decay of $K_L \to 2\pi^0 \to 4\gamma$ was simulated, where daughter photons were stopped at the surface of the detector. As the second step, events satisfying the following conditions were selected in the above simulation,

- True decay z vertex $Z_{\rm vtx}^{\rm true}$ was located within $-1 < Z_{\rm vtx}^{\rm true} < 7$ m[*5],
- Two or more photons hit the calorimeter,
- Total energy of the photons on the calorimeter exceeded 400 MeV.

These assumptions are easily satisfied for $K_L \to 2\pi^0$ background events. Finally, four photons only in the selected events were fully simulated. As a result, statistics larger by a factor of 38.6 than the measurement data was obtained. The same analysis procedures including clustering in the calorimeter, reconstruction of photons and veto information, and event selection were applied to estimate the number of background events.

[*5] Upstream edge of the FB detector was defined as the origin of z axis. The upstream surface of the calorimeter corresponded to 6,148 mm

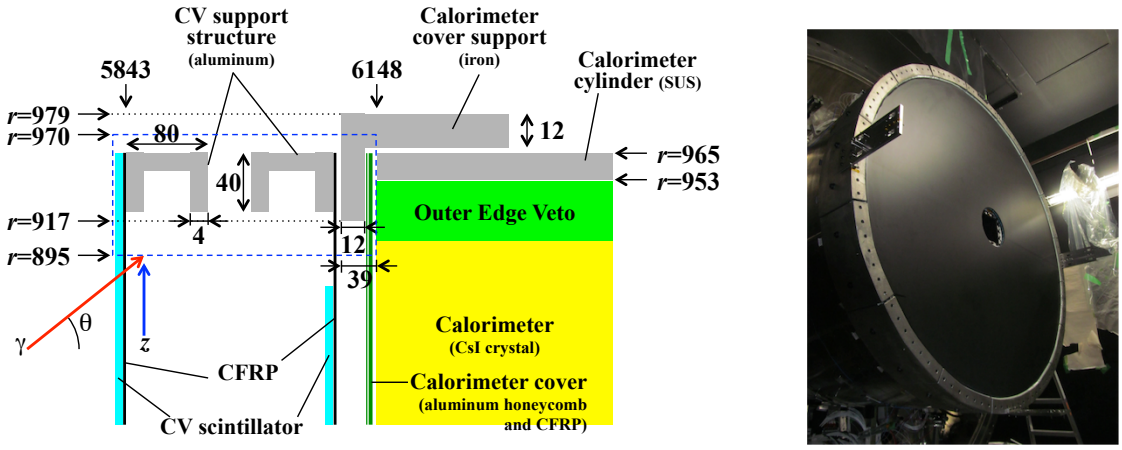

Figure 7.19: (Left) Schematic view of the calorimeter edge region. The dashed blue box indicates position of the calorimeter edge region. (Right) Photograph of the calorimeter with the cover before installation of CV.

Result

Two (four) events were found inside the signal (blind) region as shown in Fig. 7.20 and the background contribution was estimated to be 0.047 ± 0.033. This value is small enough compared to 1. In order to understand the mechanism of inefficiency for further background suppression in future runs, reasons of inefficiencies were examined for all the eight events in Fig. 7.20 and they are summarized in Table 7.7. In both of the remained two events inside the signal region, one photon with low energy of 10-20 MeV is hitting MB and the other with energy of several hundred MeV goes to the edge region of the CsI calorimeter. For other events, BHPV and accidental hits were found to contribute to background. Since various inefficiency could contribute, improvements for all the sources are necessary and detail is discussed later in Sec. 7.6.3.

7.4.2 $K_L \to 2\gamma$ background

Mechanism

Basically, contribution of $K_L \to 2\gamma$ decay to background is negligible because this decay is clearly separated due to unique kinematics of the two-body decay. When an incident K_L has no transverse momentum, directions of decay two photons are back-to-back in xy plane and projection angle of the two photons, as defined in Sec. 7.2.2, is always 180°. However, it is not the case when a K_L has large transverse momentum and/or decays far from the beam axis. Such K_L can be generated by scattering at the upstream vacuum window as shown in Fig. 7.21[*6], which was made of 0.125-mm-thick polyimide and placed to separate vacuum of the beam line and detector[*7]. A large shift

[*6] Like halo neutrons, halo K_L can exist and its $K_L \to 2\gamma$ decay possibly makes contribution to background. The existence and its property were not clear, hence this was not included in background estimation.

[*7] Some powdery materials was observed inside the beam line vacuum region and this vacuum window was set to prevent it from entering into the detector region.

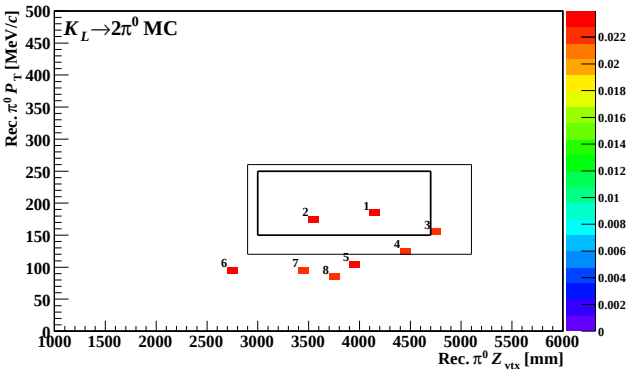

Figure 7.20: Result of $K_L \to 2\pi^0$ background simulation. The number by each event will be referred in Table. 7.7.

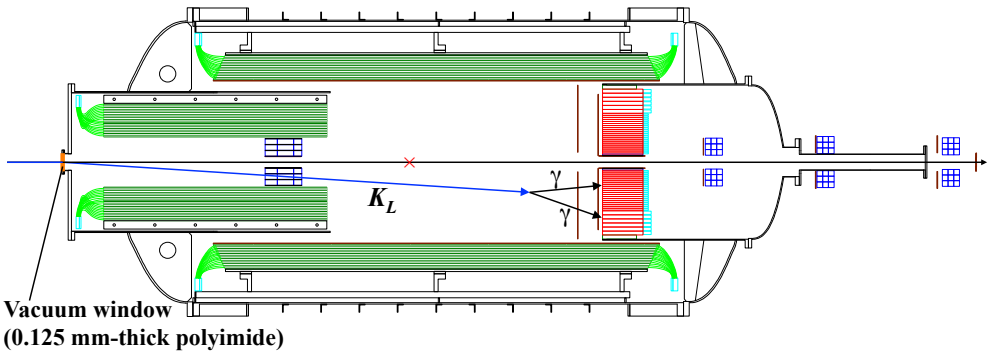

Figure 7.21: Mechanism of $K_L \to 2\gamma$ background.

of the K_L decay vertex from the beam axis enabled the projection angle of decay two photons to be smaller than 180° as in Fig. 7.22 and also resulted in large transverse momentum. Generally, transverse momentum of two-photon system with vertex position $Z_{\rm vtx}$ is written as

$$\sqrt{e_1^2\frac{r_1}{\sqrt{r_1^2+(\Delta Z)^2}}+e_2^2\frac{r_2}{\sqrt{r_2^2+(\Delta Z)^2}}+2e_1e_2\frac{r_1r_2}{\sqrt{(r_1^2+(\Delta Z)^2)(r_2^2+(\Delta Z)^2)}}\cos(\phi_1-\phi_2)}, \quad (7.20)$$

where e_i $(i=1,2)$ is energy of incident photon, r_i and ϕ_i $(i=1,2)$ are shown in Fig. 7.22, and $\Delta Z = Z_{\rm calorimeter} - Z_{\rm vtx}$. With the true xy vertex, $\phi_1 - \phi_2 \sim 180°$, the third term in the square root of Eq. (7.20) is negative and resultant transverse momentum is small. However, an assumption of zero xy vertex leads to zero or positive value of the term due to smaller $\phi_1 - \phi_2$ than 180°, and larger transverse momentum is obtained. In addition, a scattered K_L which decayed at z position close to the calorimeter has large acceptance and wrong mass assumption made reconstructed z vertex more upstream to enter the signal region through smaller opening angle from Eq. (4.2). From the above discussion, the $K_L \to 2\gamma$ decay close to the calorimeter by a scattered K_L can mimic a signal event and should be considered as background.

Table 7.7: Properties for events which passed all the event selection except P_{T} and Z_{vtx} cuts in $K_L \to 2\pi^0$ simulation. Energies and sources of inefficiency for two photons hitting veto detectors were presented. The event number is indicated in Fig. 7.20.

Event No.	Pairing	Energy1 [MeV]	Inefficiency1	Energy2 [MeV]	Inefficiency2
		possible veto1		possible veto2	
1	even	12.6	MB low energy	464.0	calorimeter edge
		-		BCV 0.20 MeV (+26.5 ns)	
2	even	24.1	MB low energy	362.2	calorimeter edge
		MB 0.86 MeV (+2.9 ns)		BCV 0.25 MeV (-0.1 ns)	
3	odd	25.3	MB low energy	3640.9	BHPV punch-through
		MB 1.80 MeV (-9.1 ns)		-	
4	even	67.0	MB accidental	139.8	calorimeter edge
		-		MB 1.21 MeV (+0.8 ns)	
5	even	83.4	MB accidental	103.6	calorimeter edge
		-		OEV 1.24 MeV (+0.3 ns)	
6	even	77.6	FB	93.7	calorimeter edge
		FB 1.85 MeV (+10.2 ns)		OEV 0.93 MeV (-0.4 ns)	
7	odd	32.3	MB low energy	1796.3	BHPV punch-through
		-		-	
8	odd	23.8	MB low energy	2512.9	BHPV edge
		MB 1.89 MeV (+0.7 ns)		-	

Method of estimation

Simulation for this background was performed with two stages as was done in $K_L \to 2\pi^0$ background estimation in order to obtain high statistics effectively. In this case, K_L scattering was simulated as the first stage of the simulation and following $K_L \to 2\gamma$ decay was simulated only for scattered K_L which was obtained in the first stage. In the K_L scattering simulation, particles were stopped behind the vacuum window and only K_L with transverse momentum larger than 20 MeV/c was used for the second simulation. In the following step, $K_L \to 2\gamma$ decay was fully simulated for the selected events and event selection was applied. In total, $K_L \to 2\gamma$ decay larger than that of data by a factor of 91.4 was simulated.

Result

Three events were found inside the signal region as shown in Fig. 7.23 and the number of background due to this decay was estimated to be 0.030 ± 0.018.

7.4.3 $K_L \to \pi^+\pi^-\pi^0$ background

Mechanism

This decay can be a source of background when both of two charged pions are not detected and both of two photons from π^0 hit the calorimeter. Daughter particles tend to go into the forward direction due to the small Q-value of this decay. Hence, detection of these charged pions at the

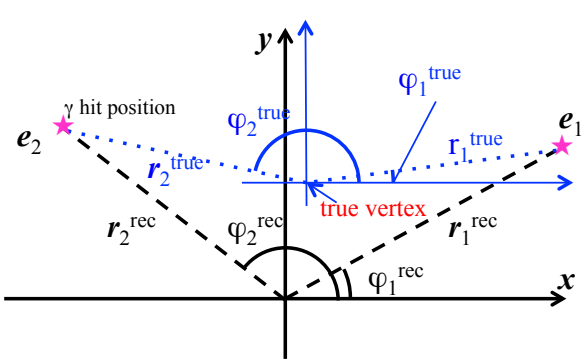

Figure 7.22: xy projection of $K_L \to 2\gamma$ background.

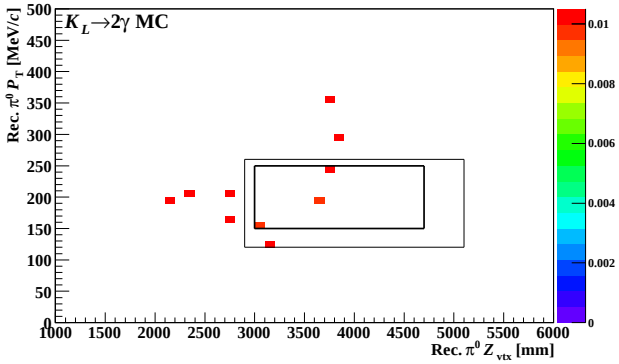

Figure 7.23: Result of $K_L \to 2\gamma$ background simulation.

downstream detectors is critical. In the physics run, vacuum pipe made of 5-mm-thick stainless steel located between CC05 and CC06 made inefficiency of $\pi^\pm$ larger and could give background events as in Fig. 7.24. A full simulation with comparable statistics with data, whose detail is described later, was performed and its result is shown in the left of Fig. 7.25. The number of remaining events in the low-P_T region was (5.2 ± 2.1) with all the selection cuts described in Sec. 7.2. This is consistent with the number of the observed events in the real data, nine events as show in Fig. 7.18. From this simulation, events in the low-P_T region in the data are expected to come from this type of events mainly. Fortunately, π^0 in the $K_L \to \pi^+\pi^-\pi^0$ decay also cannot have large transverse momentum, the maximum of which is 133 MeV/c, this background can be avoided by setting a high P_T threshold. This, however, loses acceptance of signal events and the threshold needs to be carefully optimized. Simulation with enough statistics is necessary for this purpose.

Method of estimation

Only the mechanism described above was considered for $K_L \to \pi^+\pi^-\pi^0$ background since simulation with the whole $K_L \to \pi^+\pi^-\pi^0$ kinematics was not realistic due to the large branching fraction of this decay (12.54% [16]). Since inefficiency of $\pi^\pm$ hitting the beam pipe determine contribution to background, only their interaction was repeatedly simulated by recycling the specific charged pions many times, where the event can be background if both of them are not detected. This "$\pi^\pm$ recycling method" admits of background estimation with large enough statistics. The actual procedures are as follows:

1. $K_L \to \pi^+\pi^-\pi^0$ and subsequent $\pi^0 \to 2\gamma$ decay are simulated where only photon tracks are traced onto a surface of hit detectors.

2. Among the simulated events, those where both of the following conditions are not satisfied are discarded:

   - The true decay z vertex is within the range of $2 < z < 7$ m[*8].

[*8] In case of the $K_L \to \pi^+\pi^-\pi^0$ decay, there are basically only two photon clusters and no ambiguity in photon combination. Hence π^0 is always correctly reconstructed within its resolution and this range can completely cover the $K_L \to \pi^+\pi^-\pi^0$ background.

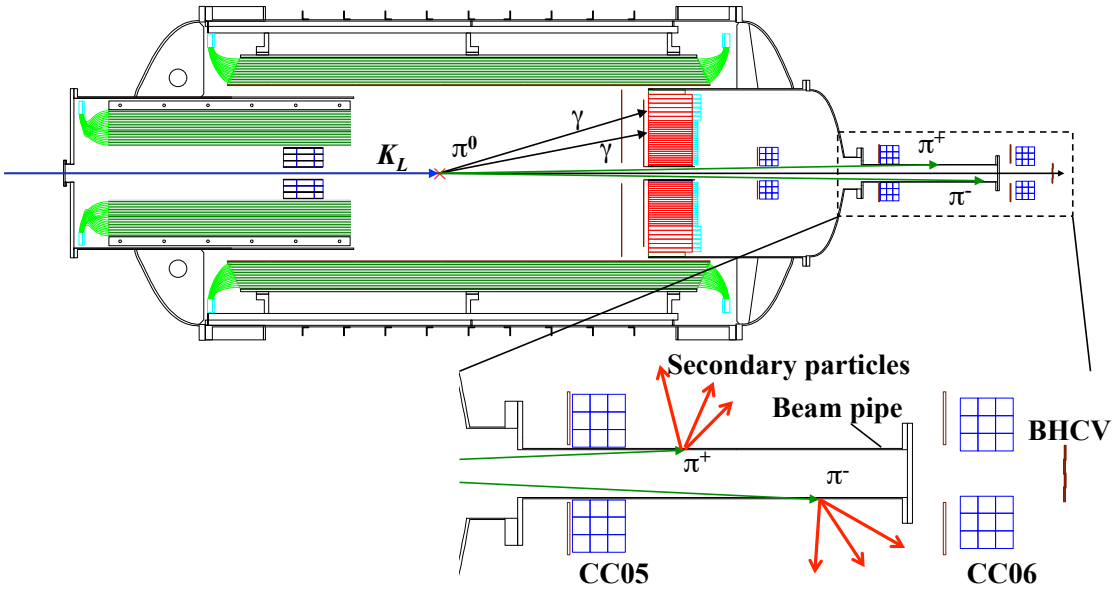

Figure 7.24: An example of $K_L \to \pi^+\pi^-\pi^0$ background.

- Both of the decay two photons hit the calorimeter.

3. Two photons and charged pions are fully simulated for surviving events without overlaying accidental hits.

4. Background candidate events are selected with cut conditions in Sec. 7.2.2 and 7.2.3 except ones on $Z_{\rm vtx}$, $P_{\rm T}$, CC05, CC06 and BHCV veto removed. Here, the "full simulation" result (to be) mentioned in Figs. 7.25 and 7.27 is what was obtained without removing veto cuts by CC05, CC06 and BHCV in this process.

5. Tracks of $\pi^\pm$ in the background candidate events are extrapolated from the decay vertex position to the downstream of CC04.

6. Extrapolated $\pi^\pm$ are fully simulated and analyzed with accidental overlay and reconstructed π^0 information for the event. The same $\pi^\pm$ were reused 500 times for each background candidate event.

In the step 1, almost the same number of the $K_L \to \pi^+\pi^-\pi^0$ decay with the real data (99.7%) was simulated with the branching fraction considered and recycle of $\pi^\pm$ finally gave 498.6 times larger statistics. Distributions of $P_{\rm T}$ and $Z_{\rm vtx}$ with veto by downstream detectors removed for selection of background candidate events in the step 4 are presented in Fig. 7.26. Both distribution shows good agreement between the data and the simulation and this further ensures that the low-$P_{\rm T}$ events in the data originated from the $K_L \to \pi^+\pi^-\pi^0$ decay. In recycling $\pi^\pm$, their tracks were once extrapolated to the behind of CC04 or $z = 7650$ mm in order to evaluate veto efficiency only by detector downstream of CC04, namely CC05, CC06 and BHCV. In this extrapolation, $\mu^\pm$ tracks were used when $\pi^\pm$ decayed before reaching the target z position in the full simulation of the step 3. If the extrapolated xy position was outside the beam hole of CC04 or 87.5 mm square, the track

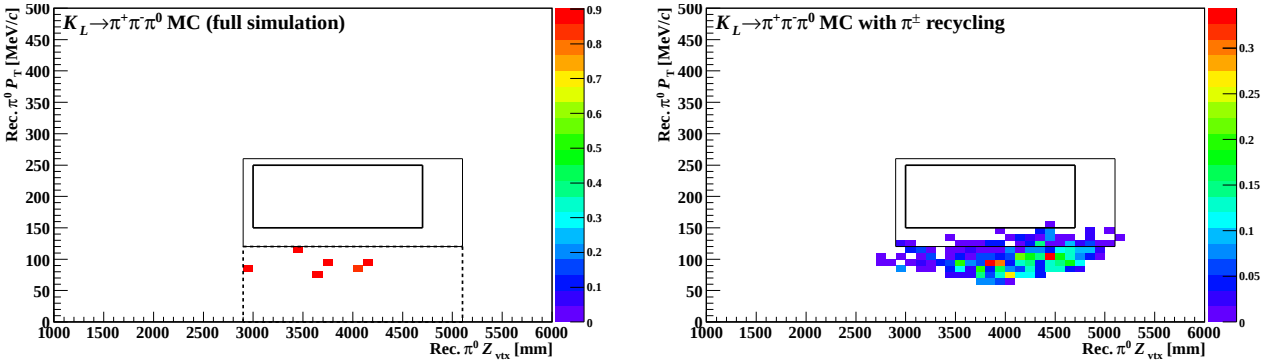

Figure 7.25: Result of $K_L \to \pi^+\pi^-\pi^0$ background simulation. (Left) Result of the full simulation for the $K_L \to \pi^+\pi^-\pi^0$ decay with limited kinematics. The square box surrounded with dashed lines indicates the low-P_T region. (Right) Result with the $\pi^\pm$ recycle method.

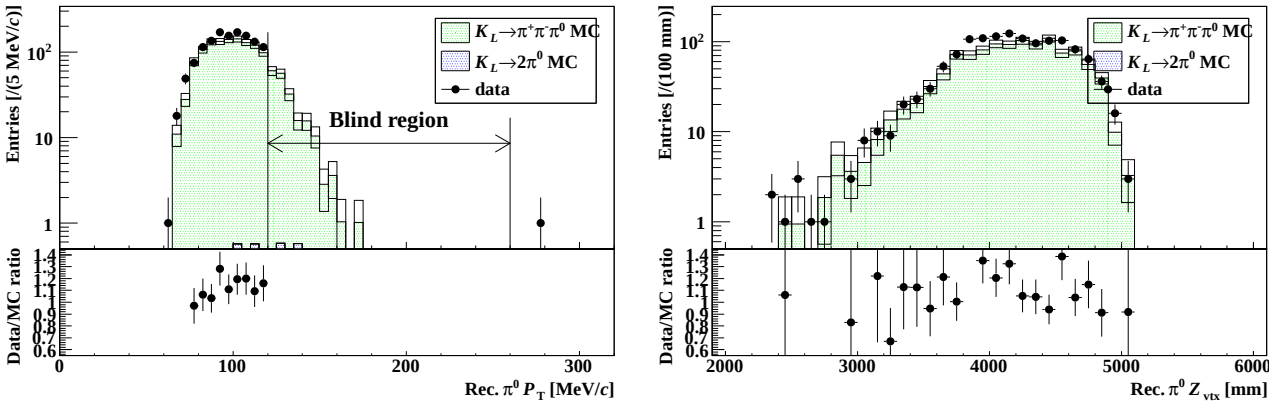

Figure 7.26: Distribution of reconstructed π^0 transverse momentum (left) and decay z vertex (right) in the $K_L \to \pi^+\pi^-\pi^0$ simulation and the data with veto cuts by downstream detectors removed.

was not reused as it should hit the CC04 detector and its detection had been already evaluated in the step 3. In the analysis of simulation output of the last step, veto cuts by all the detectors were considered so as that effect of accidental loss was taken into account.

Result

The right panel of Fig. 7.25 shows $Z_{\rm vtx}$-$P_{\rm T}$ distribution in the analysis of the simulation described above. The expected number of background events are plotted as a function of the $P_{\rm T}$ threshold as well as relative change of signal acceptance in Fig. 7.27. In order to eliminate this background completely, the lower $P_{\rm T}$ threshold was determined to be 150 MeV/c and the resultant number of $K_L \to \pi^+\pi^-\pi^0$ background was estimated to be (0.0016±0.0016) event.

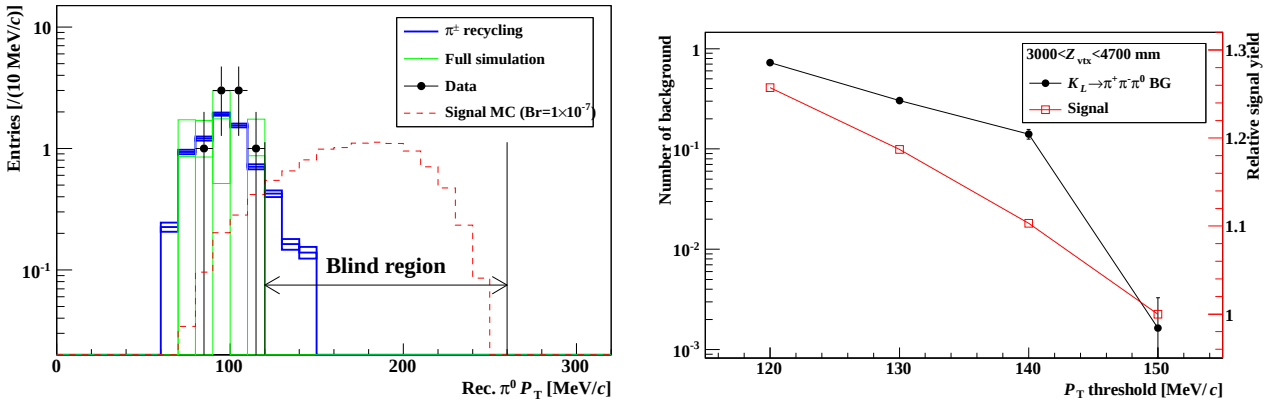

Figure 7.27: Result of $K_L \to \pi^+\pi^-\pi^0$ background estimation. (Left) Distribution of reconstructed π^0 $P_{\rm T}$ for the data and the two kinds of simulations. That for the $K_L \to \pi^0\nu\overline{\nu}$ simulation is also presented. (Right) The expected number of the $K_L \to \pi^+\pi^-\pi^0$ background and signal events as a function of the $P_{\rm T}$ threshold. The background is estimated with the $\pi^\pm$ recycling method.

7.4.4 $K_L \to 3\pi^0$ background

Mechanism

Since the number of photons in the final states of $K_L \to 3\pi^0$ decay is as many as six, this decay is basically easily rejected and background contribution from this decay is expected to be small. However, its large branching ratio and possible contribution from decays in the upstream of the fiducial region can allow this decay to contribute to background with rare topologies. A possible configuration is illustrated in Fig. 7.28. Three photons from the $K_L \to 3\pi^0$ decay inside the FB detector have low energy of < 50 MeV and the other three have high energy of > 100 MeV. If one of the three high-energy photons hit the edge of the calorimeter and is not detected as described in Sec. 7.4.1, the rest of two photons make two clusters. The two-photon pairing is generally the odd type and the z vertex position and $P_{\rm T}$ are wrongly reconstructed, which allows $Z_{\rm vtx}$ and $P_{\rm T}$ to be in the signal box. In addition, the other low-energy three photons are difficult to detect. Eventually no photons can be detected with high efficiency hence this kind of events can easily behave as a signal. In order to estimate $K_L \to 3\pi^0$ background contribution with such a configuration, inefficiency for low energy photons and that in the calorimeter edge region need to be carefully treated.

Method of estimation

The estimation of $K_L \to 3\pi^0$ background is based on what was called "fast simulation." Only K_L decay process was simulated and hit information of each decay particle including particle identification (PID), energy, position and momentum were recorded. π^0 is reconstructed using energy and position of two photons on the calorimeter with their resolution considered. When three or more photons hitting the calorimeter exist, reconstruction is tried for all possible two photon combinations considering a probability that each of two-photon pairs is identified as a single cluster. Event rejection by veto detectors was evaluated as event weight or a probability where the event survived as background using inefficiency functions. The inefficiency functions gives detection inefficiency of

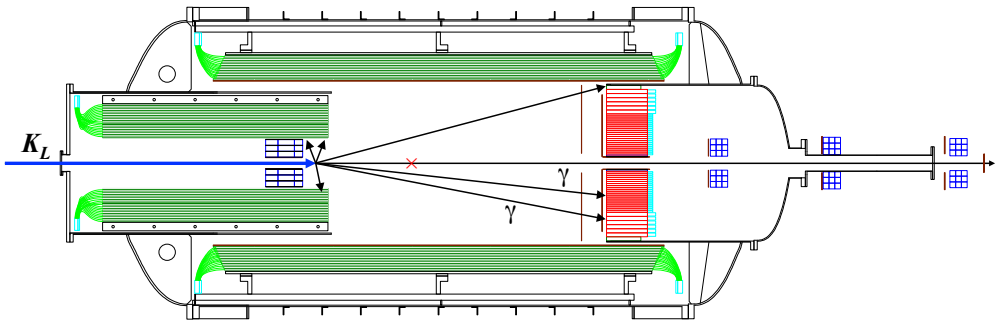

Figure 7.28: An example of $K_L \to 3\pi^0$ background.

a single incident particles according to its PID, energy, position and angle. Defining inefficiency for the i-th particle hitting a veto detector in an event as w_i, the number of background is calculated as

$$N \sum \left(P \prod_i w_i \right), \tag{7.21}$$

where N is the normalization factor and P denotes the probability that the event is reconstructed as a two-cluster event, including fusion effect when three or more photons hit the calorimeter. Values in parenthesis indicates weight for a certain event with a certain fusion pattern. The summation runs over all simulated events and possible patterns in each event. Inefficiency function for each detector was obtained from separate simulations of a single photon with fixed incident energy, position and angle. With this method, the number of background events is estimated with small statistics of simulation. Since the shower developments are not simulated, it also saves lots of computing time. On the other hand, careful treatment of inefficiency functions with realistic geometries is necessary. This was confirmed by comparing results for the $K_L \to 2\pi^0$ mode with this fast simulation method and the full simulation described in Sec. 7.4.1.

Inefficiency functions

Photon detection inefficiency was evaluated with simulations for each detector. Inefficiency of MB is given as a function of incident energy and angle as shown in the left of Fig. 7.29. For a photon hit with a certain energy and incident angle, logarithms of inefficiencies for neighboring simulated energies and angles are interpolated to calculate inefficiency for the photon. In order to make realistic estimation of inefficiency around the edge region of the calorimeter, special treatments were applied for photons hitting this region. Here, the "calorimeter edge region" is defined as shown in Fig. 7.19. Separate inefficiency functions were newly prepared, where photons with various kinds of energies, angles and incident positions were simulated with the realistic geometries of the KOTO detector including the support structures for CV and the cover of the calorimeter. Simulations with 12 fixed energies, five angles and 15 incident positions were performed. In each simulation, a photon was shot from the beam axis with a given angle 10^4 ($<$ 100 MeV) or 5×10^5 ($\geq$100 MeV) times. The number of inefficient events were defined as those with veto energies smaller than thresholds in all of MB, BCV, OEV, CsI and CV, where the same veto timing width and energy as shown in Table 7.1 was used in each detector. Examples of the inefficiency functions are shown in the right of Fig. 7.29. Inefficiency gets drastically worse than that of MB when the photon passes through a long distance

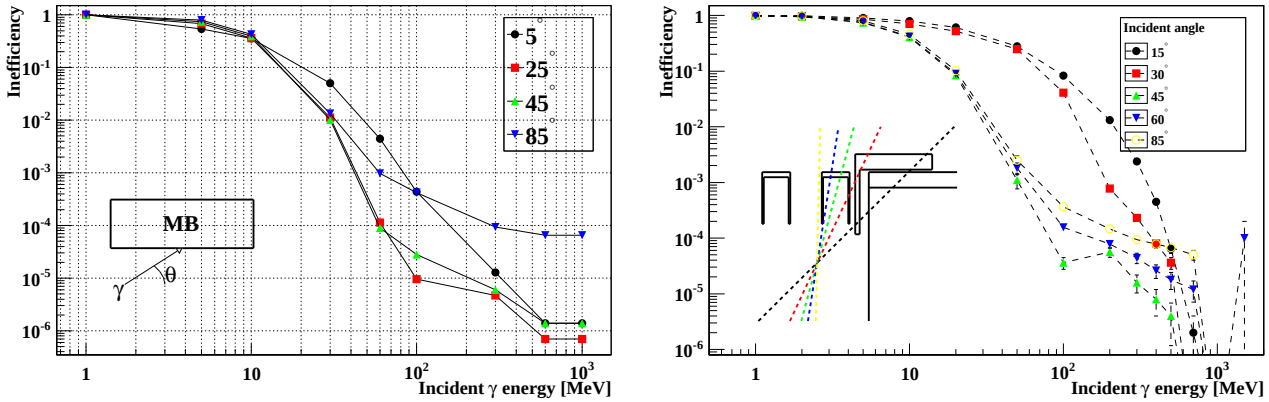

Figure 7.29: Examples of inefficiency function used in the fast simulations. The left one is for MB. The right is an example for the calorimeter edge region in case that the incident z position at the radius of 895 mm is $z = 6000$ mm.

of dead material regions. As for the inefficiency functions of other detectors including FB, NCC, CC03-06 and BHPV, the detail is described in App. F.

Corrections

The number of background events with Eq. (7.21) was corrected considering various effects which were not included in the fast simulation: loss by accidental hits and backsplash from the calorimeter, acceptance difference of the shape χ^2 cut, and other shape related cuts. Accidental and backsplash losses of acceptance were estimated to be 64.2% in total using signal MC samples, where each loss was calculated to be 52.7% and 24.3% by taking an event ratio of samples with and without the accidental overlay, and with the veto cuts included and not[*9], respectively. Selection cuts related on the cluster shapes as well as several cuts were not considered in the fast simulation and effects by these cuts were reflected by multiplying correction factors. Acceptance values by these selection cuts differed according to types of pairings for two photons used for event reconstruction since probabilities of two photons' fusion was calculating using cut efficiency of the shape χ^2 cut. Events were then categorized into the three types, even pairing events, odd pairing events and fusion events, and acceptance correction factor was applied for each event type. Correction factors for each event type are summarized in Table 7.8, which were derived from the $K_L \to 2\pi^0$ full simulation samples as event ratios with and without the shape related cuts for each event type. Here, the "shape related cuts" includes the shape χ^2 cut, the shape NN cut, the photon quality cuts and the kinematic NN cut. Finally, the normalization factor was given as (the number of K_L in data)/(the number of simulated K_L), where the number of K_L in data was 2.399×10^{11} as discussed in Sec. 7.3 and the number of simulated K_L corresponded to 2.0×10^{10} at the end of the collimator for the $K_L \to 3\pi^0$ decay and 1.0×10^{10} for the $K_L \to 2\pi^0$ decay.

[*9]Because both of signal events and $K_L \to 3\pi^0$ background events have two clusters on the calorimeter, backsplash effect was assumed to be the same.

Table 7.8: Acceptance correction used in the fast simulation for each event type.

Event type	Correction factor
Even	0.6841
Odd	0.5243
Fusion	0.6982

Result

Before examining the result of $K_L \to 3\pi^0$ background, the fast simulation result for $K_L \to 2\pi^0$ decay was compared with full simulation result in order to validate this fast simulation method. Figure 7.30 shows results of the fast simulation for the $K_L \to 2\pi^0$ mode. The obtained number of background events was compared with that from the full simulation result described in Sec. 7.4.1 in each region of the $Z_{\rm vtx}$-$P_{\rm T}$ plane. The left of Fig. 7.30 shows which detector system had the largest contribution to the background. MB and the calorimeter edge had the largest contribution, followed by BHPV and FB, which was consistent with the full simulation result as shown in Table 7.7. Although presented values were for events inside the signal region, relative contributions were almost the same with events outside the signal region included. Although the results from the fast simulation gave slightly smaller value, these numbers were found to be consistent within statistical uncertainty.

The result for $K_L \to 3\pi^0$ is shown in Fig. 7.31. The number of background events in the signal region was estimated to be $(5.00 \pm 0.68) \times 10^{-3}$, which indicated that $K_L \to 3\pi^0$ background was small enough. As shown in the right of Fig. 7.31, the remaining events were dominated by contribution from FB, where an incident K_L decayed inside the detector and three of six photons had low energy (< 50 MeV) and the rest of three photons had high energy (> 100 MeV). Two of the high energy three photons formed two clusters to be analyzed and all the low energy three photons hit the inside of the FB detector but not detected efficiently due to their low energy. Such events could survived as background when the last high energy photon hit the calorimeter edge with worse detection efficiency as shown in 7.28. Events where the last photon hit BHPV were also seen. Energy of such photon varied from several hundred MeV to several GeV and the events would not be vetoed when the energy was below 1 GeV due to bad efficiency of BHPV for photons with such energy.

7.4.5 $Ke3$ and $K\mu3$ background

Mechanism

Only two charged particles are emitted in these decay and they can behave as signal events when these two charged particles hit the calorimeter and both of them are identified as photons. Although cluster shape made by charged particles basically differs from that by photons, it is sometimes undistinguishable. In addition, there is uncertainty in simulations of cluster shapes generated by charged particles, particularly when hadronic interactions are involved. Inefficiency of CV against such penetrating charged particles is then critical in rejecting these events effectively. Detection inefficiency arises from groove regions on the scintillator strip and boarder regions between neighboring two modules as shown in Fig. 7.32, where an absolute photoelectron yield is small due to thin active region and contribution from such regions can increase inefficiency with the 200 keV

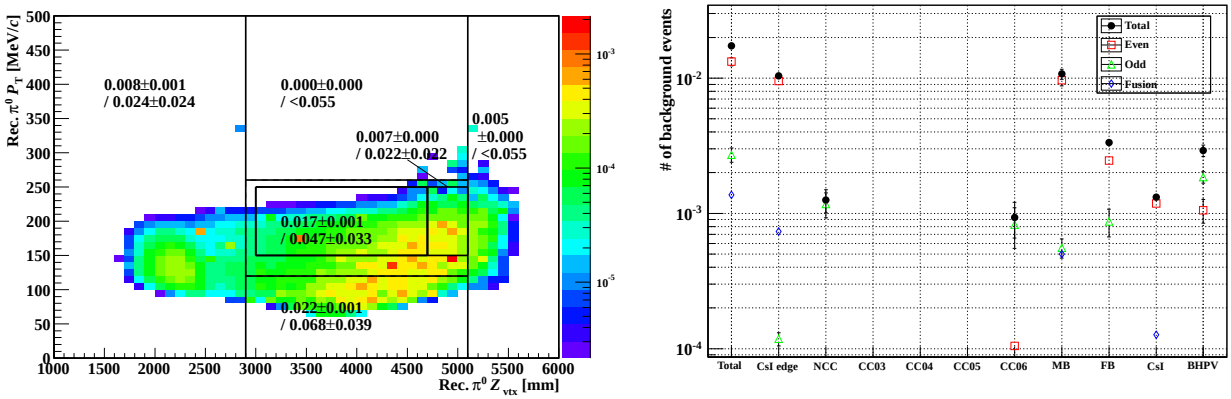

Figure 7.30: Result of $K_L \to 2\pi^0$ background estimation with the fast simulation method. The left figure shows $Z_{\rm vtx}$-$P_{\rm T}$ distribution after applying veto weight of all the detectors. The numbers for each region indicate the number of background events obtained with the fast simulation method and the full simulation described in Sec. 7.4.1, respectively. The right one shows the number of background events related to each detector.

detection threshold[*10]. Below, "groove regions" shall also include boarder regions. Enough number of light yield per energy deposit is helpful to make such inefficiency small and reduce this type of background events. Although it is confirmed that the light yield requirement is successfully satisfied for the design sensitivity of this experiment [82, 84], the evaluation was based on tight threshold of 100 keV, which might not be appropriate for this physics run with much worse sensitivity. Since a tight threshold of CV causes a large signal loss due to a backsplash effect from electromagnetic showers in the calorimeter, it is desirable to set the threshold as loose as possible within a tolerable background level. Evaluation of $Ke3$ background hence needs to be considered for optimization of the CV veto threshold.

Evaluation of CV veto performance

Evaluation of inefficiency against penetrating charged particles in CV is a key to understand this background as already mentioned above. Although photoelectron yields obtained from measurement for the real detector are taken into account as described in Sec. 5.4.2 with corrections for various difference of experimental conditions, it is still worthwhile to validate implemented detector response with the real data. For this reason, in-situ inefficiency was evaluated with data taken in this physics run prior to estimation of background, where CV response in a $Ke3$-enhanced sample was compared between the data and the full simulation.

Events by the minimum bias trigger data, described in Sec. 3.3.3 was used and the same event selection with the previous section (Sec. 7.2) was applied except for CV veto. To enhance $Ke3$ components, several kinematic selections are removed or changed: the π^0 kinematic cuts and selections on neutral net values, cluster sizes, energy ratio, $e\theta$, reconstructed z vertex ($Z_{\rm vtx}$) and transverse

[*10] As another source of inefficiency, cutout holes with a size of 0.6×0.6 mm^2, which is needed to fix modules, can also contribute. This effect, however, is not included in the simulation and not considered as background, since the effect is measured to be small enough [83, 84] and basically threshold-independent.

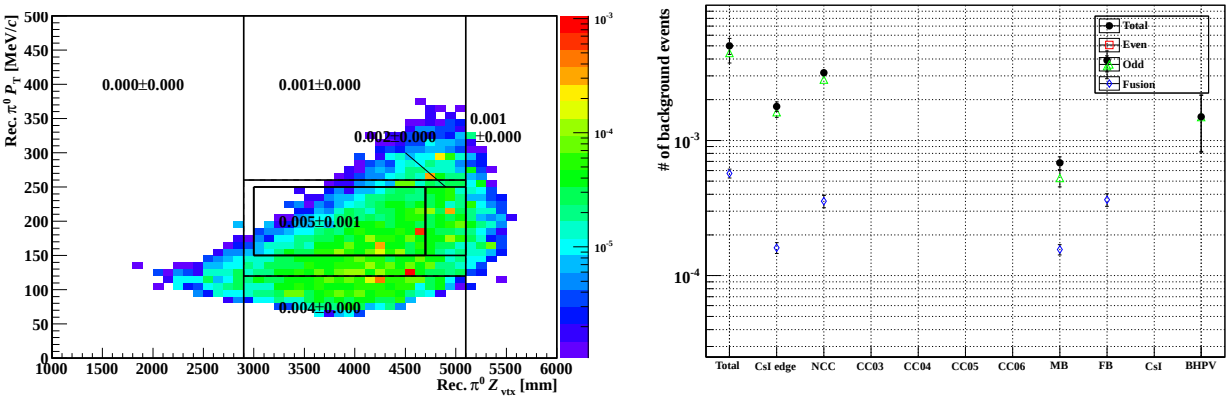

Figure 7.31: Result of $K_L \to 3\pi^0$ background estimation with the fast simulation method.

momentum (P_{T}) are removed. In addition, the shape χ^2 value for the larger energy photon is required to be smaller than 5 and that for the smaller energy photon larger than 5 since $e^{\pm}$ from $Ke3$ decay deposited its all energy through electromagnetic shower and its cluster has the same shape with photon incidence while a charged pion is expected to lost its energy partially and have a different cluster shape from a photon. Finally, hits in the front plane are required for further purification of $Ke3$ decay events. Here the hit in the front plane is defined as the largest energy deposit among all modules in the front plane, whose timing is inside the veto window, exceed the veto energy threshold of 200 keV. Distribution of veto energy of the rear plane, which is defined as the same way with that of the front plane, is shown in Fig. 7.33.

Inefficiency for the data and the MC was calculated by counting the numbers of events below the veto threshold and found to be $(3.45 \pm 1.41) \times 10^{-5}$ and $(2.91 \pm 1.72) \times 10^{-5}$, respectively. Although inefficiency only for the rear plane was evaluated, these values agree well and this validates the CV detector response implemented in the simulation.

Background estimation

Now it was found that the CV inefficiency is well reproduced in the MC simulation, expected background contribution in this analysis was evaluated by using the MC simulation. As is the same with the other K_L main decays such as $K_L \to \pi^+\pi^-\pi^0$, it is not realistic to accumulate large enough statistics with the full simulation method. Therefore, the source of inefficiency was assumed to come only from the detector responses of CV, and its detector responses were repeatedly simulated only for background candidate events as was done in the $K_L \to \pi^+\pi^-\pi^0$ background estimation in Sec. 7.4.3.

First, background candidate events were chosen from the MC sample for the $Ke3$ decay, where all the CsI cuts except for the shape χ^2 and no selection by veto detectors were applied. Removing the shape χ^2 cut by assuming no correlation between this cut and groove contribution is an effective way to obtain higher statistics with limited computing time, with which larger samples by a factor of 14.0 were obtained. Statistics of the background candidate events is critical due to the following reason. As already discussed, groove regions in the scintillator strip module is a main source of inefficiency and the background candidate events should contain a sufficient number of events where

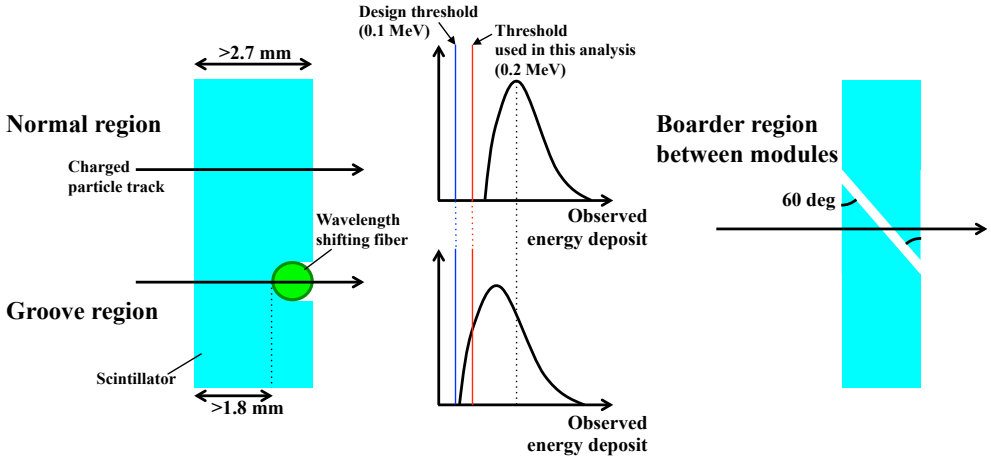

Figure 7.32: Illustration of CV inefficiency due to its groove (left) and boarder (right) regions. The middle distributions show observed energy distribution deposited at the hit module for normal regions and groove regions.

all charged particles pass groove regions and only small energy deposition is obtained. Since the area ratio of groove regions is 10%, the probability with all charged particles in the $Ke3$ and $K\mu3$ decay hitting the groove region is roughly estimated as $(10\%)^4 = 10^{-4}$, where hits are observed basically in four modules: two charged particles for the two layers. The number of background candidate events hence must be much larger than an inverse of this value so that lots of such events with small energy deposition are included. For this purpose, $Ke3$ decays corresponding to 10^9 K_L incidence were simulated and 443,006 events were obtained as background candidate events. Distribution of MC true energy deposition in each module is shown in Fig. 7.34. The smaller peak around 0.3 MeV in the red histogram corresponds to hits in groove regions. In case that all charged particles hit groove regions, the maximum energy deposit, whose distribution is indicated by the black histogram, should be around this region. Approximately 20 events were obtained as this type of events, which were enough to estimate groove contribution. For each background candidate event, only simulation of veto detector responses and accidental overlay was repeated 1,000 times using the same MC energy deposition information so as to obtain enough number of statistics. Here, statistical fluctuation of observed energy in each CV module was mainly simulated. Accidental overlay was also included in order to take background contribution due to accidental activities into account, whose detail is discussed in Sec. 7.4.6. The veto cuts were then applied and the number of background events was counted, which was corrected with efficiency of the shape χ^2 cut. Since there was difference in selecting the background candidate events other than the shape χ^2 cut for technical reasons, this effect is also considered by multiplying a correction factor. The detail of this correction is described in App. G. Thanks to this recycling, the final statistics reaches 203 times of the data.

Result

Figure 7.35 shows the simulation result. As is seen in the left figure, many events survives without CV veto. The right figure shows CV veto energy distribution for events inside the signal, which

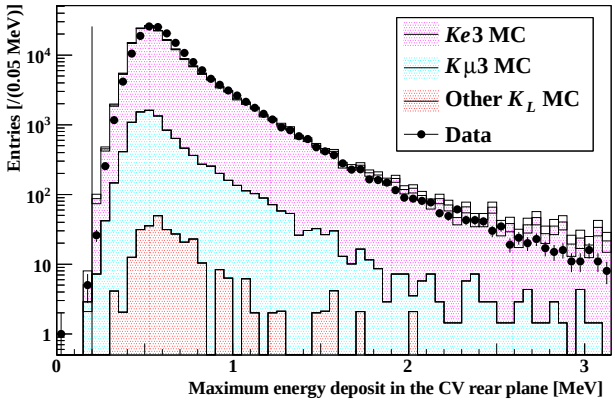

Figure 7.33: Validation of the CV detector response for the $Ke3$ background estimation. Veto energy distribution for the rear plane is shown for the data and the simulation. The vertical line indicates the detection threshold.

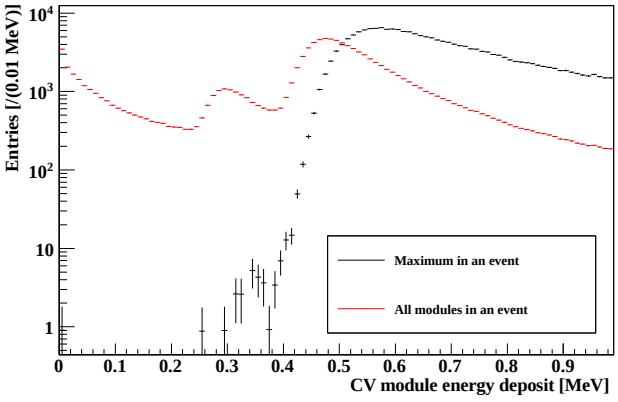

Figure 7.34: Distribution of true energy deposition in the full simulation of the $Ke3$ mode.

was obtained as a result with the above processes. The threshold value of 200 keV is found to be necessary in order to make this type of background small enough and this value was chosen as the energy threshold of this detector. With this threshold, one event survived in the signal box and background contribution was estimated to be 0.0045 ± 0.0045. This event was caused by "masking inefficiency," due to accidental hits, where all of four hits on CV were disabled by four hits from accidental activity in the same modules. Although there was an additional hit which came from one charged particle track of two passing through a module boundary and it did not suffer from masking effect, its energy deposition was too small to be detected Detail of this kind of background is described in the next section (Sec. 7.4.6).

Additional contribution from the $K\mu3$ decay can also exist as a similar type of background. However, this mode has the slightly smaller branching ratio than the $Ke3$ mode and rejection by the shape χ^2 cut is stronger, since both charged particles give clusters with different shapes from ones made from electromagnetic showers while $e^{\pm}$ in the $Ke3$ decay gives a photon-like cluster. Contribution of this decay is hence expected to be much smaller than that from the $Ke3$ decay and was neglected.

7.4.6 Background due to accidental activities

Mechanism

As described in Chap. 4, larger single counting rates in detectors can cause an overlap of pulses and result in wrong timing calculation, which gives a new source of inefficiency in addition to intrinsic one for the detector. Below, this kind of inefficiency due to wrong timing calculation is referred to as "masking" inefficiency and subsequent background as "masking" background. The situation in the physics run was serious from this point : Fig. 7.36 shows counting rates for the MB modules measured with TMon trigger data with simulation expectation. Particularly in outer modules with module ID equal to or larger than 32, observed counting rates were much higher than the simulation expectation. From the right of Fig. 7.36, existence of an unexpected flux, which

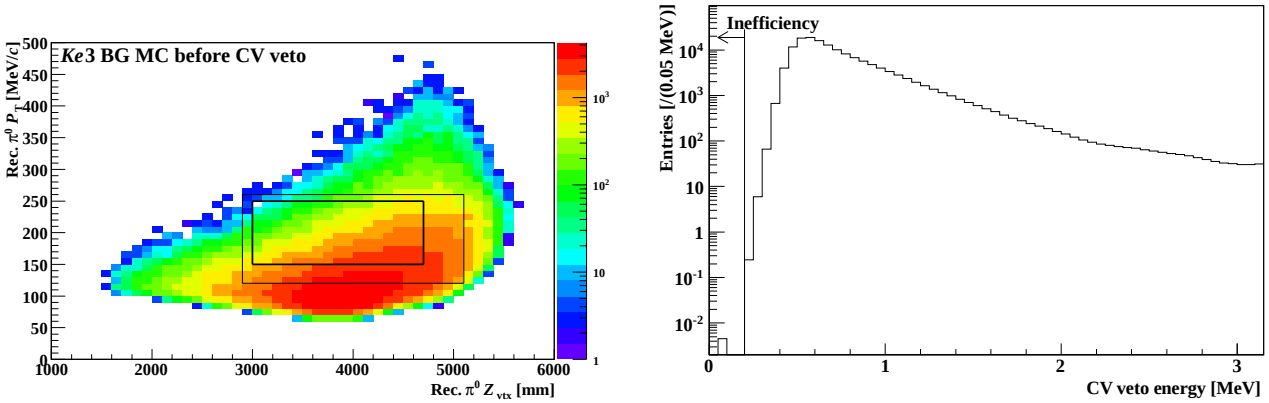

Figure 7.35: Results of the simulation for $Ke3$ background estimation. (Left) Distribution of z vertex and transverse momentum of reconstructed π^0 without CV veto. (Right) Distribution of CV veto energy for events inside the single box in the left figure. Entries in both figures are scaled to the number of events in the data.

is likely to be neutrons from the primary beam line, is indicated. The typical value of 100 kHz corresponds to the 5% probability to have accidental hits in the 500-ns time range of a single event. In the most pessimistic case, additional inefficiency of this order can occur which is much larger than typical requirement of 10^{-4}[*11]. More realistic estimation of inefficiency is shown in Fig. 7.37, where monochromatic energy photon incident on the MB detector was repeatedly simulated and detection efficiency was calculated with and without accidental overlay. With the constant fraction timing as described in Sec. 4.2.1, inefficiency for high energy photons is expected to get larger by a factor of 10 or more due to masking effect, while kept at the same level as those without accidental overlay when timing was defined with the parabola fitting. Increase of inefficiency by accidental activities is then found to be sensitive to methods of timing calculation and careful treatments in timing simulation are necessary in evaluation of background.

Another point to be considered is correlation among modules with accidental hits. In case of the $Ke3$ and $K\mu3$ decays, for example, naively four hits exist in CV and if two $Ke3$ or $K\mu3$ decays happen with close timing each other and daughter charged particles hit the same modules, timing in all hit modules would be wrongly calculated and the event failed to be rejected. This "synchronized masking" effect can give larger background than simple product of masking inefficiency of each hit module hence masking background needs to be considered event by event, not track by track as done in the fast simulation for $K_L \to 3\pi^0$ background.

Method of estimation

Since background due to masking of signal timing can occur all the decay modes so far mentioned except the $K_L \to 2\gamma$ decay, background contribution was estimated for the $K_L \to \pi e\nu_e$, $K_L \to \pi\mu\nu_\mu$, $K_L \to 3\pi^0$, $K_L \to \pi^+\pi^-\pi^0$, and $K_L \to 2\pi^0$ decays. For the $K_L \to 2\pi^0$ decay, masking effect is already taken in consideration in Sec. 4.2.1 and consistency is confirmed by comparing results. The procedure of estimation is almost the same with that for $Ke3$ background in the previous section. For each mode, background candidate events from initial simulation samples, where the

[*11] Since there are basically two photons hitting veto detector, required inefficiency is given as square root of the ratio of sensitivity to the $K_L \to 2\pi^0$ branching fraction, or $\sim ((3.00\times10^{-11})/(8.64\times10^{-4}))^{1/2}$ as a rough calculation.

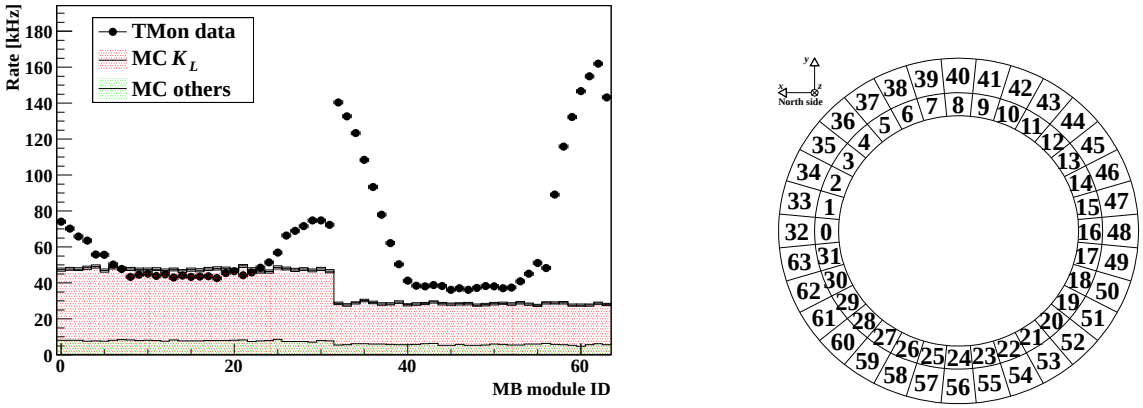

Figure 7.36: (Left) Single counting rate in each MB module. TMon trigger data which was taken parallel with the physics data was used and subsequent DAQ dead time is considered in the MC result. (Right) Illustration of the module number assignment in MB. The detector was seen from the upstream direction.

above five decay modes were fully simulated with K_Ls incident at the exit of the collimator. As already mentioned in Sec. 7.4.5, the selection cut set was slightly different also in this study, which is considered later. Events were reconstructed and background candidate events were selected by applying all the selection cuts on the calorimeter, any information from veto detectors was not used. For each candidate event, detector response simulation was repeated and veto decision was made to count the number of background events with all visible hits in veto detectors masked. In this process, timing of each module used for veto decision was calculated with the parabola fitting method. Statistics used for this background estimation was summarized in Table 7.9. Recycle of the same events many times made it possible to have larger statistics. The number of events inside the signal box was finally scaled to the number of background events in the data with correction of selection cut difference as described in App. G.

Result

Figure 7.38 shows the result of the simulation of the $Ke3$ mode. Masking in CV is a key in this background. The parabola fitting method reduces the probability of wrong timing calculation coming from accidental activities because the genuine pulse is more correctly identified with this method than the constant fraction method as discussed in Sec. 4.2.1. Wider veto window is also helpful for reduction of this type of background since larger timing shift due to accidental hits is allowed. The right of Fig. 7.38 shows the minimum timing difference from the nominal veto timing among hit modules in masking background events, where distribution is compared between the parabola fit method and the constant fraction method. Here, a module hit was defined as energy deposit larger than 200 keV, the same threshold used in other analyses. The tail component in the timing distribution is drastically reduced with the parabola fit method and the number of background events itself gets much smaller. By defining veto timing width as ± 40 ns, masking background from the $Ke3$ decay expected to be reduced small enough and the number was estimated

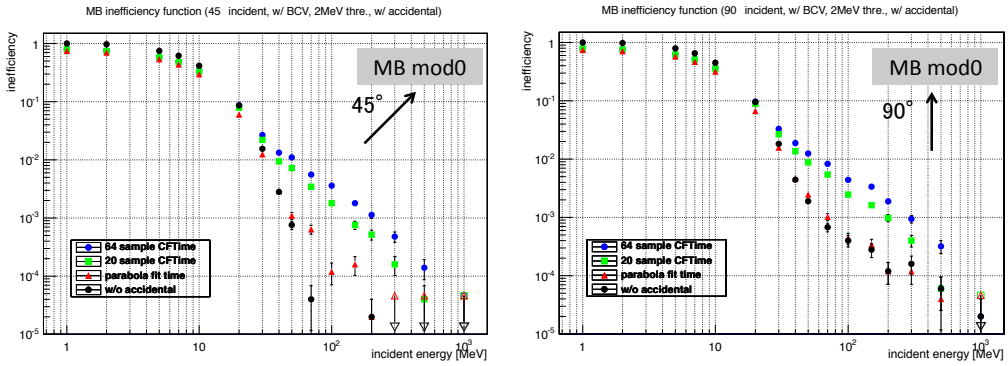

Figure 7.37: Simulated MB inefficiency for monochromatic photons with underlying accidental activities. The left (right) figure is a simulation result where photons were injected with 45° (90°) to the detector.

Table 7.9: Summary of simulation samples used for estimation of background due to accidental activities. "Statistics" here was defined as equivalent number of K_L at the collimator exit, where branching ratio for each mode was considered. The numbers in parenthesis are ratio to the number of K_L in data.

Decay Mode	Initial statistics	Candidate events	Repetition	Final statistics
$K_L \to \pi e \nu_e$	3.9×10^9 (1.6%)	50,662	20,000	7.9×10^{13} (330)
$K_L \to \pi \mu \nu_\mu$	1.8×10^9 (0.8%)	720	20,000	3.7×10^{13} (150)
$K_L \to 3\pi^0$	7.7×10^8 (0.3%)	85,617	20,000	1.5×10^{13} (64)
$K_L \to \pi^+\pi^-\pi^0$	4.0×10^9 (1.7%)	9,448	20,000	8.0×10^{13} (330)
$K_L \to 2\pi^0$	6.9×10^{11} (2.9)	715,126	100	6.9×10^{13} (290)

to be 0.0027 ± 0.0027 event, which is consistent with estimation in Sec. 7.4.5. Since 0.50 event is expected with the constant fraction method and ± 10 ns veto timing window, the parabola fit method and the wide veto window work well for background reduction.

For other modes, $Z_{\rm vtx}$-$P_{\rm T}$ distributions for masking background events are shown in Figs. 7.39. One event remained in the signal box for the $K_L \to 3\pi^0$ mode and no events survived in the $K\mu 3$ and the $K_L \to \pi^+\pi^-\pi^0$ modes. In the $K_L \to 2\pi^0$ mode, masking background contribution was estimated to be (0.055 ± 0.013) for all the region in $Z_{\rm vtx}$-$P_{\rm T}$ distribution, where an event apparently not coming from masking effect was removed. This number is consistent with the full simulation result of 0.045 events, where this value was obtained by summing weights of the two events due to masking inefficiency in Table 7.7. This agreement validates the recycle method used in this background estimation.

As the final background contribution, the results only for the $K\mu 3$, $K_L \to 3\pi^0$ and $K_L \to \pi^+\pi^-\pi^0$ modes were considered since background due to masking inefficiency is already included in the $K_L \to 2\pi^0$ and the $Ke3$ modes as described Sec. 7.4.1 and Sec.7.4.5, respectively.

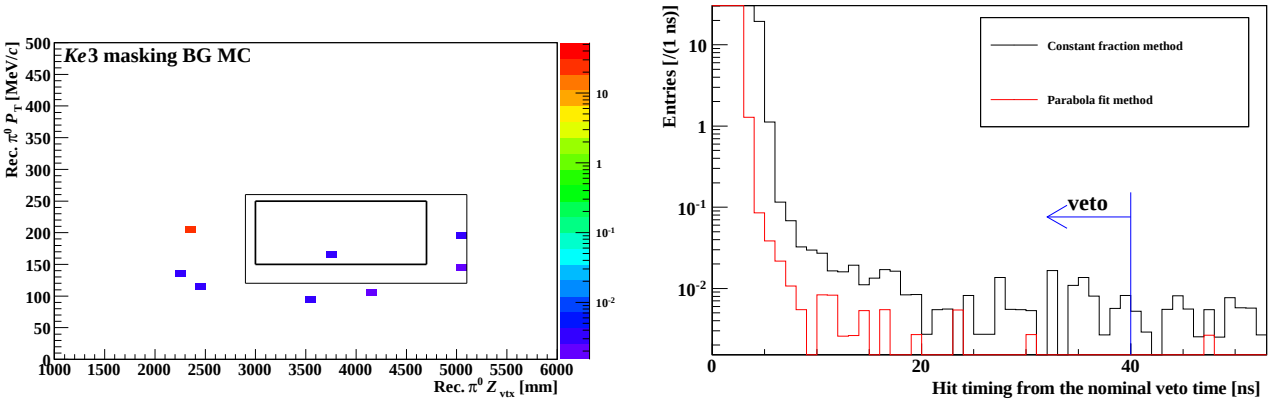

Figure 7.38: Result of masking background for $Ke3$ mode. The left panel shows $Z_{\rm vtx}$-$P_{\rm T}$ distribution after applying all the veto cuts. The right one shows comparison of veto timing between the constant fraction method and the parabola fitting method for events inside the signal region.

7.4.7 Upstream neutron background

Mechanism

Neutrons in the beam halo region would be serious sources of background as discussed in Sec. 2.1.4. One possible mechanism to generate neutron background is π^0 production as a result of their interaction with detector materials. The NCC detector is the main source of halo neutron interaction. In the $Z_{\rm vtx}$-$P_{\rm T}$ distribution of Fig. 7.18, there can be seen a cluster of events whose z vertex is reconstructed in the NCC z position. In these events, reconstructed z vertex positions can shift to the downstream direction and might be in the signal region when energies of two photons from π^0 generated inside NCC are wrongly measured due to shower leakage or photonuclear effect. Since this type of events was the main source of background in the previous KEK-E391a experiment [45], various hardware upgrades have been made for background reduction as follows:

- improvement in the collimator design to reduce halo neutrons,
- shift of the detector position upstream for better separation of the π^0 generation point and the signal region,
- upgrade to the fully-active detector with cesium iodide crystals,
- more radiation length in the calorimeter to reduce wrong energy measurement due to shower leakage,

where the full-active feature allows more rejection with secondary particles generated at the same time with π^0. The ratio of radiation length to hadronic interaction length becomes slightly smaller with cesium iodide crystals than that of the sampling calorimeter with lead and plastic scintillator, which was used as the upstream collar counter in the previous experiment, and this helps more conversion of photons from π^0. Still control of the neutron flux and understanding their interaction is difficult and this expectation needs to be carefully confirmed.

Method and result

Halo neutron MC samples obtained as a result of the beam line simulation was used for estimation

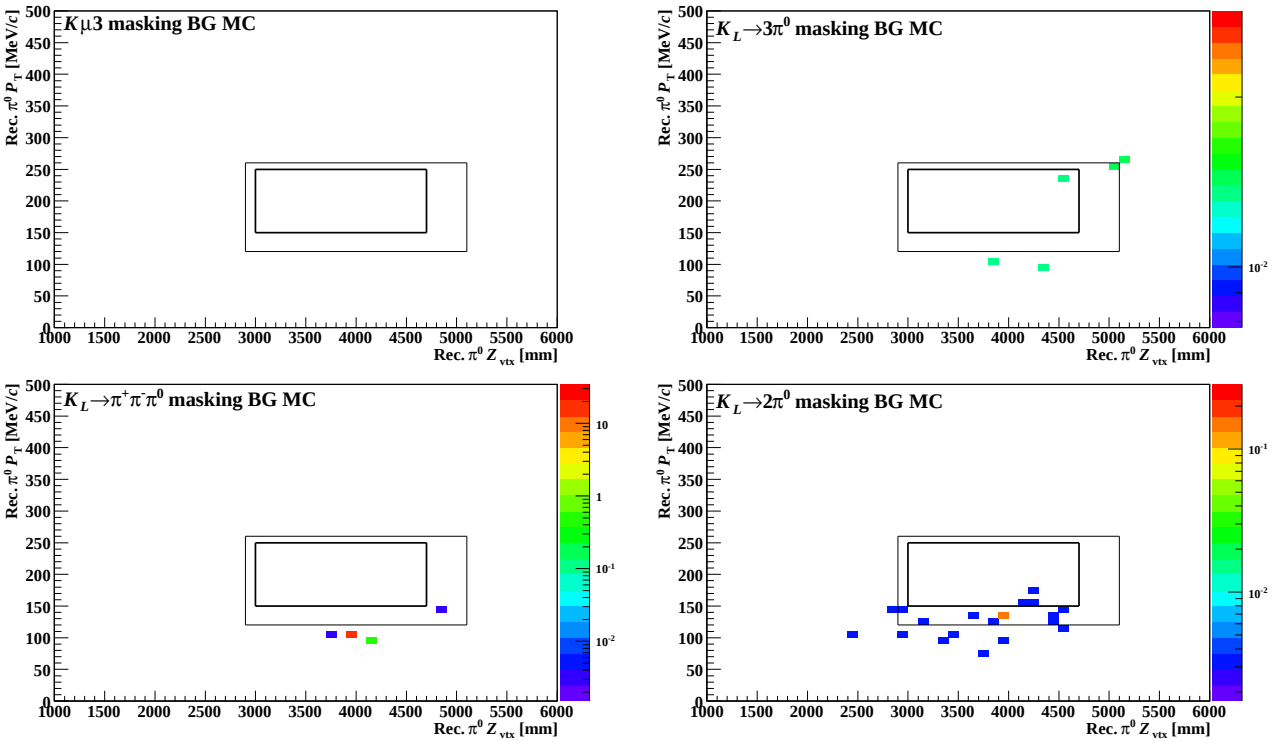

Figure 7.39: Results of the masking background simulations for the other modes. In the $K\mu 3$ mode, no events survived in the whole $Z_{\rm vtx}$-$P_{\rm T}$ plane.

of background contribution. Since it was difficult to understand the halo neutron flux and its energy spectrum and its spatial distribution as well as their interaction completely, the number of survived events around the NCC region, namely $Z_{\rm vtx} < 2900$ mm, was scaled so as to be the same with the measurement data. In addition, the beam position was shifted by 12 mm from the nominal position in the x direction so that more neutrons hit the detector and π^0 production was enhanced.

To confirm validity of the simulation, energy and $P_{\rm T}$ distributions in the NCC z region are compared with data as in Fig. 7.40. In both distribution, the simulation results well reproduced the data. The result of the simulation is shown in Fig. 7.41. One event was found inside the signal region, and the number of background was estimated to be (0.055 ± 0.055). In the survived event, one of the two clusters on the calorimeter derived of a secondary neutron generated in interaction between a halo neutron and the detector.

7.4.8 Hadron cluster background

Mechanism

As the second possible background contribution of neutrons, direct incidence of halo neutrons into the calorimeter needs to be considered. In such case, an incident primary neutron causes hadronic interactions and forms a primary cluster. In the interactions, a secondary neutron can be emitted and it make a secondary cluster after traveling inside the calorimeter. Finally, two clusters are observed without hits in any veto detectors, hence this event can mimic a signal event. A key to reduce events of this type is difference of cluster formation mechanism between neutrons and

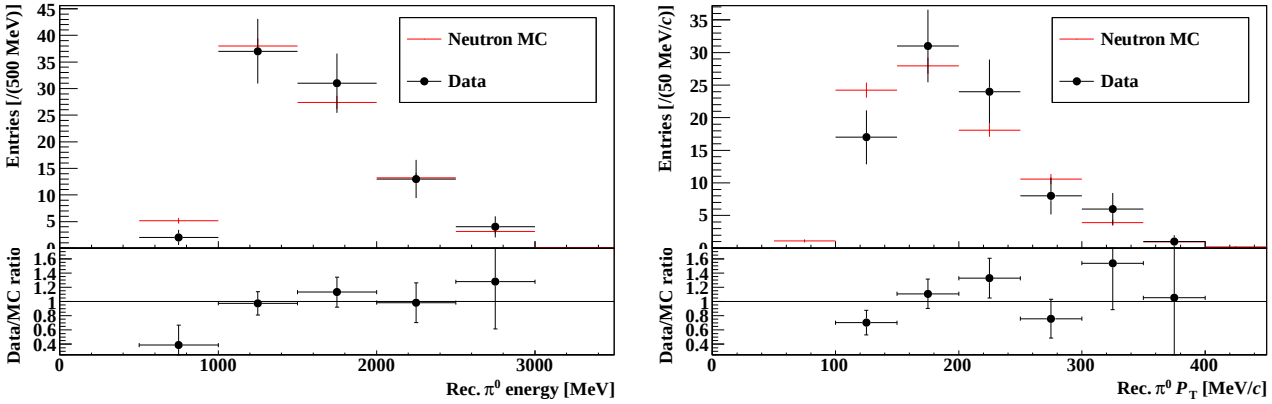

Figure 7.40: Comparison of the data and the neutron simulation for energy (left) and transverse momentum (right) of reconstructed π^0. All the selection cuts except those on P_{T} and Z_{vtx} are applied and $Z_{\mathrm{vtx}} < 2900$ mm is required.

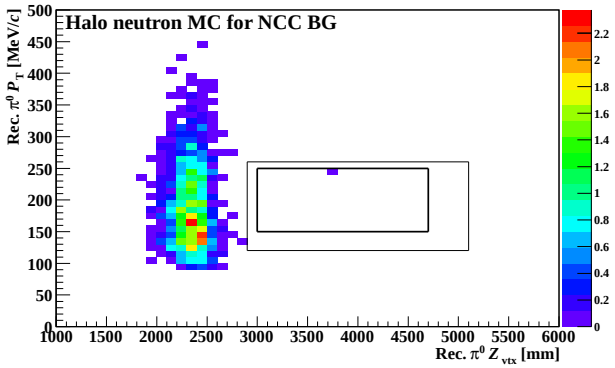

Figure 7.41: Result of an estimation for upstream neutron background.

photons. One example is cluster shape difference, where in background events clusters are basically formed as a result of neutron hadronic interaction, not electromagnetic interaction by photons. Hit timing difference of two clusters is another information which can be used for background discrimination, since there exists timing delay due to traveling of the secondary neutron while two photons from π^0 basically hit the calorimeter simultaneously.

Method and result

Since a reliable simulation of such interaction is difficult due to uncertainties of incident halo neutron information and their interaction with the calorimeter in simulations, data taken in the aluminum target run was used as a control sample of such neutron events. In the aluminum target run, neutrons in the beam core hit the target and are scattered to hit the calorimeter directly. If such a neutron gives a secondary cluster, its response such as Z_{vtx}-P_{T} distribution, for example, is expected to be the same with those caused by halo neutrons. In the real case, there is some discrepancy in distributions, probably reflecting incident energy difference between halo neutrons and scattered neutrons in the beam core. By weighting events in the aluminum target runs so that

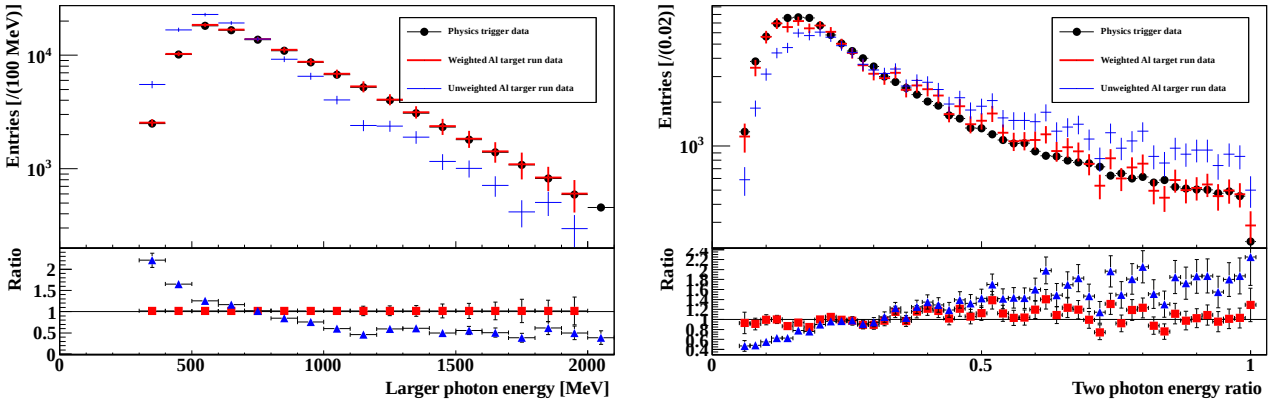

Figure 7.42: Distribution of cut variables in the physics data and the aluminum target run data with and without weighting.

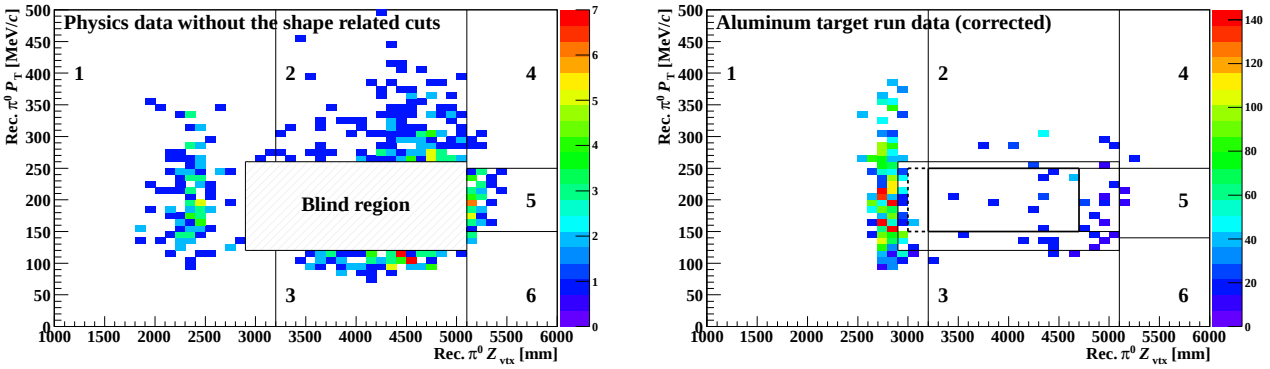

Figure 7.43: Result of an estimation for hadron cluster background. The left figure shows $Z_{\rm vtx}$-$P_{\rm T}$ distribution with the shape-related cut removed in the physics data and the right one $Z_{\rm vtx}$-$P_{\rm T}$ distribution with the shape-related cut removed in the aluminum target run data.

the distribution of larger energy of two clusters agrees between these samples as shown in the left panel of Fig. 7.42, various distribution gets consistent with each other. An example of two-photon energy ratio distribution is shown in the right panel of Fig. 7.42. This validated use of the aluminum target run data as a control sample to estimate this type of background in the physics data. Since statistics of the target run was too poor to be applied by he same selection cuts with the physics data, reduction by the cluster-shape-related cut was separately evaluated from the physics data and this factor was applied to the aluminum target run data to obtain the number of events in the signal box. Here, the cluster-shape-related cut means to apply the shape χ^2 cut and the shape neural net cuts simultaneously. The reduction factor was estimated using side band events and obtained as $(1.07 \pm 0.76) \times 10^{-3}$. This factor was multiplied for the number of events inside the signal region in the corrected aluminum target run data, where all the selection cuts except for the shape-related-cut were applied. The $Z_{\rm vtx}$-$P_{\rm T}$ distribution is shown in Fig. 7.43. Here, the control sample was scaled so that the number of events in the region 5 agrees to that of the physics data with the kinematic NN cut removed. As a result, background contribution from this hadron cluster events was estimated to be (0.18 ± 0.15) event.

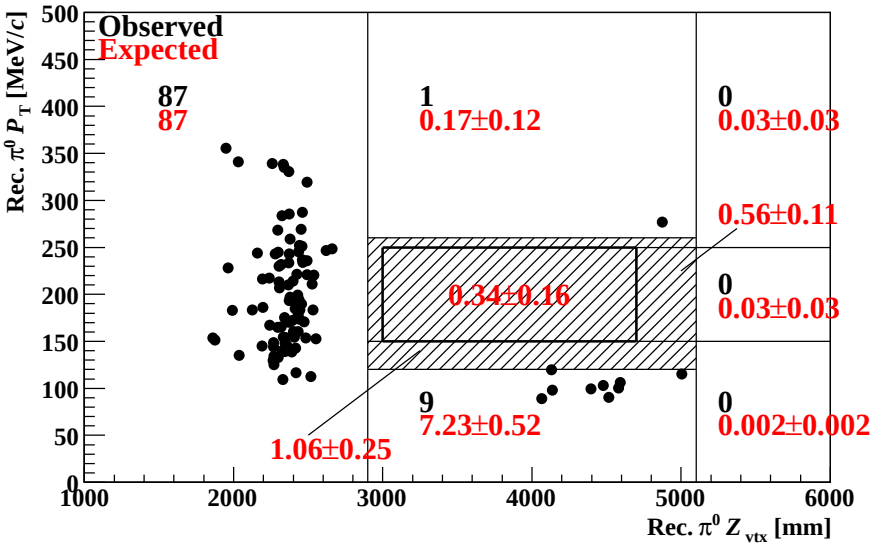

Figure 7.44: Comparison between observed and expected number of events outside the blind region.

7.5 Result of the $K_L \to \pi^0\nu\bar{\nu}$ analysis

7.5.1 Summary of the expected numbers of background

K_L and neutron background was studied and the total contribution inside the signal region was estimated to be (0.36 ± 0.16) event as already presented in Table 7.6.

Figure 7.5.1 shows comparison of the observed numbers of events outside the blind region with the expected numbers of events in each region of the $Z_{\rm vtx}$-$P_{\rm T}$ plane. Although larger statistical uncertainty exists due to small number of observed events in data, they were consistent in every region and reliability of the background estimation as described in Sec. 7.4 was confirmed.

7.5.2 Single event sensitivity

It is convenient to define a value which shows capability to search for the $K_L \to \pi^0\nu\bar{\nu}$ decay in this analysis, particularly in setting an upper limit. Such a value is called Single Event Sensitivity (S.E.S.), which is given as the branching fraction to expect a single event observation. This is calculated from Eq. (7.7) by substituting $N_{\rm sig} = 1$, or

$$\text{S.E.S.} = \frac{1}{N_{\rm norm} \times \epsilon_{\rm sig}}, \tag{7.22}$$

where $N_{\rm norm}$ is the normalization factor or the number of incident K_Ls available in the analysis and $\epsilon_{\rm sig}$ is signal acceptance evaluated with the MC simulation. Using $N_{\rm norm} = 2.399 \times 10^{11}$ as in Sec. 7.3.5, and the acceptance value of 3.25×10^{-4}, the S.E.S. value in this analysis was obtained as

$$\text{S.E.S.} = (1.29 \pm 0.04_{\rm stat.} \pm 0.10_{\rm syst.}) \times 10^{-8}. \tag{7.23}$$

This value is close to that in the final analysis of the previous experiment (KEK-E391a experiment [45]), 1.11×10^{-8}, even with the short beam time of 100 hours.

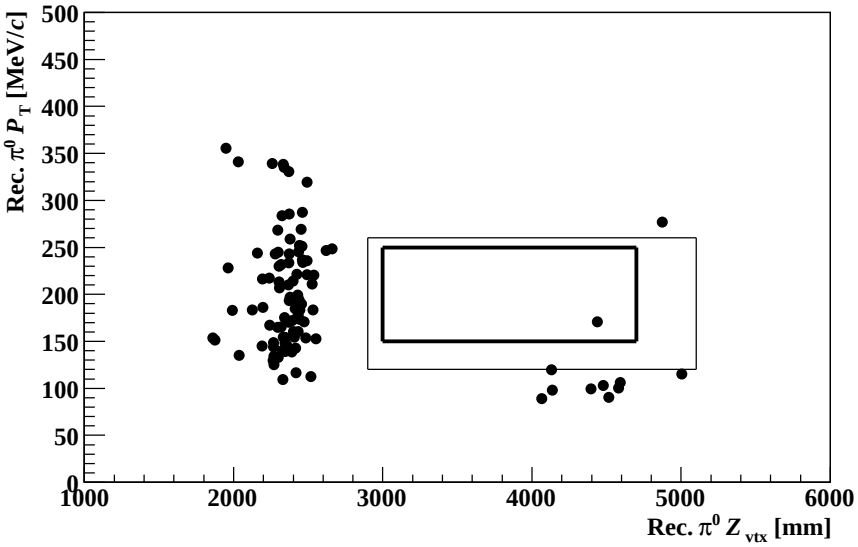

Figure 7.45: Final $Z_{\rm vtx}$-$P_{\rm T}$ plot after opening the blind region.

7.5.3 Unblinding the signal region

The $Z_{\rm vtx}$-$P_{\rm T}$ distribution after applying all selection cuts, including both for CsI and veto detectors, is presented in Fig. 7.45 with unblinding of the hidden region. One event was observed inside the signal region, which was consistent with the expected number of background. An upper limit with 90% C.L. was then set as follows, regarding this event to be a signal event conservatively,

$$\mathrm{Br}(K_L \to \pi^0\nu\bar{\nu}) < 5.1 \times 10^{-8}, \tag{7.24}$$

here, Poisson statistics was assumed for upper limit calculation and the error on S.E.S. was taken into account following the method in Ref. [107].

7.6 Discussion

7.6.1 The observed event

The calorimeter event display for the single observed event is shown in Fig. 7.45 and its kinematic variables are shown in Fig. 7.47 and Table 7.6.1, In Fig. 7.47, their distribution obtained with the $K_L \to \pi^0\nu\bar{\nu}$ simulation sample is also drawn. At a glance, behaviors of the event are like signal events. Waveform for all the veto detectors were also examined and those for some channels are shown in Fig. 7.48. Although hits with small energy deposit were detected in some detectors, namely MB, CV, these are much smaller than the detection threshold. The position of the module with hits in CV is far from both clusters on the calorimeter, which means this small hit is not derived from inefficiency of the detector as described in Sec. 7.4.5. For other detectors, no significant energy deposit were found, which indicates this event was not caused by masking inefficiency due to accidental hits.

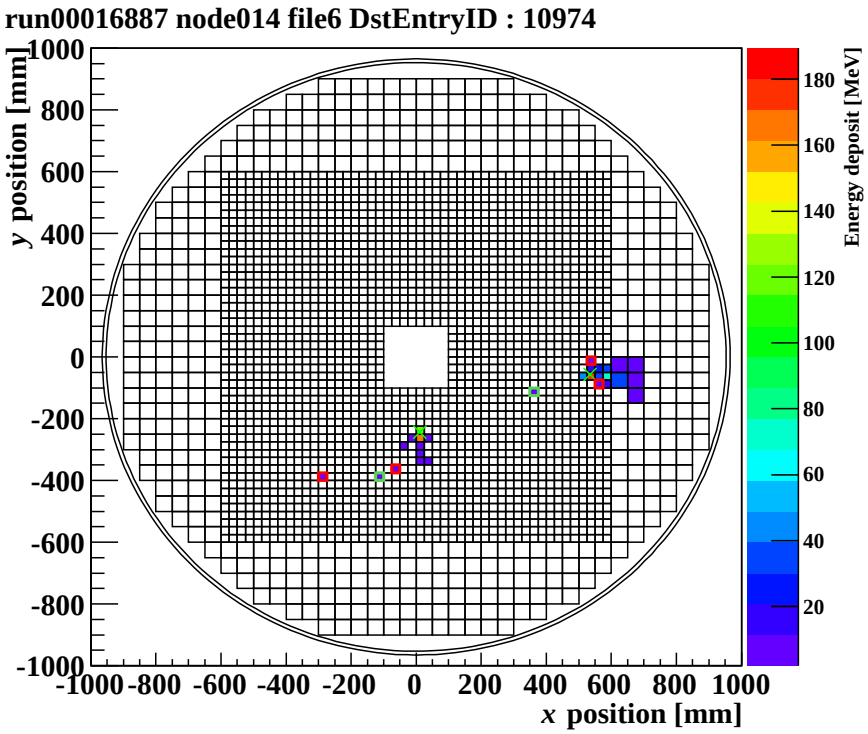

Figure 7.46: Hit pattern in the calorimeter for the observed event. Hits with energy deposit smaller than 2 MeV are ignore. Cross marks indicate reconstructed photon hit positions. Crystals surrounded red (green) boxes are isolated hit crystals which are (are not) regarded as simultaneous hits.

7.6.2 Possible interpretation of the event

Although the observed number of events is consistent with the background expectation, this can be also interpreted as a $K_L \to \pi^0\nu\overline{\nu}$ "signal" event with the branching fraction of 1.29×10^{-8}, for example . Basically, sensitivity in this analysis is one-order of magnitude larger than the Grossman-Nir bound for the $K_L \to \pi^0\nu\overline{\nu}$ decay, 1.4×10^{-9} as given in Eq. (1.41), and it is difficult to think a new physics effect gives such a large branching fraction. However, recently Ref. [109] has pointed out that an existence of a Weakly Interacting Light Boson (WILB) X^0 allows a larger $K_L \to \pi^0\nu\overline{\nu}$ branching fraction than the conventional Grossman-Nir bound through the process $K_L \to \pi^0 X^0$, $X^0 \to$ (invisible) with X^0 mass close to that of π^0. The conventional Grossman-Nir bound was calculated from the result of $K^+ \to \pi^+\nu\overline{\nu}$ in the BNL E949/E787 experiment [32], where there existed "kinematic exclusion region" in π^+ momentum to avoid background from other K^+ decays. One of the excluded momentum was 205 MeV/c, which corresponded to missing mass of π^0, considering the $K^+ \to \pi^+\pi^0$ decay. This is because inefficiency for photons from π^0 decays was so large that background was not reduced to be small enough compared to an expected amount of $K^+ \to \pi^+\nu\overline{\nu}$ events. If a WILB X^0 exists and its mass is around that of π^0, a large branching ratio for the $K^+ \to \pi^+\nu\overline{\nu}$ decay is possible through the process of $K^+ \to \pi^+ X^0$, $X^0 \to \nu\bar{\nu}$ and this could also give a large decay rate of $K_L \to \pi^0\nu\overline{\nu}$ with a similar process. An experimental limit for such a

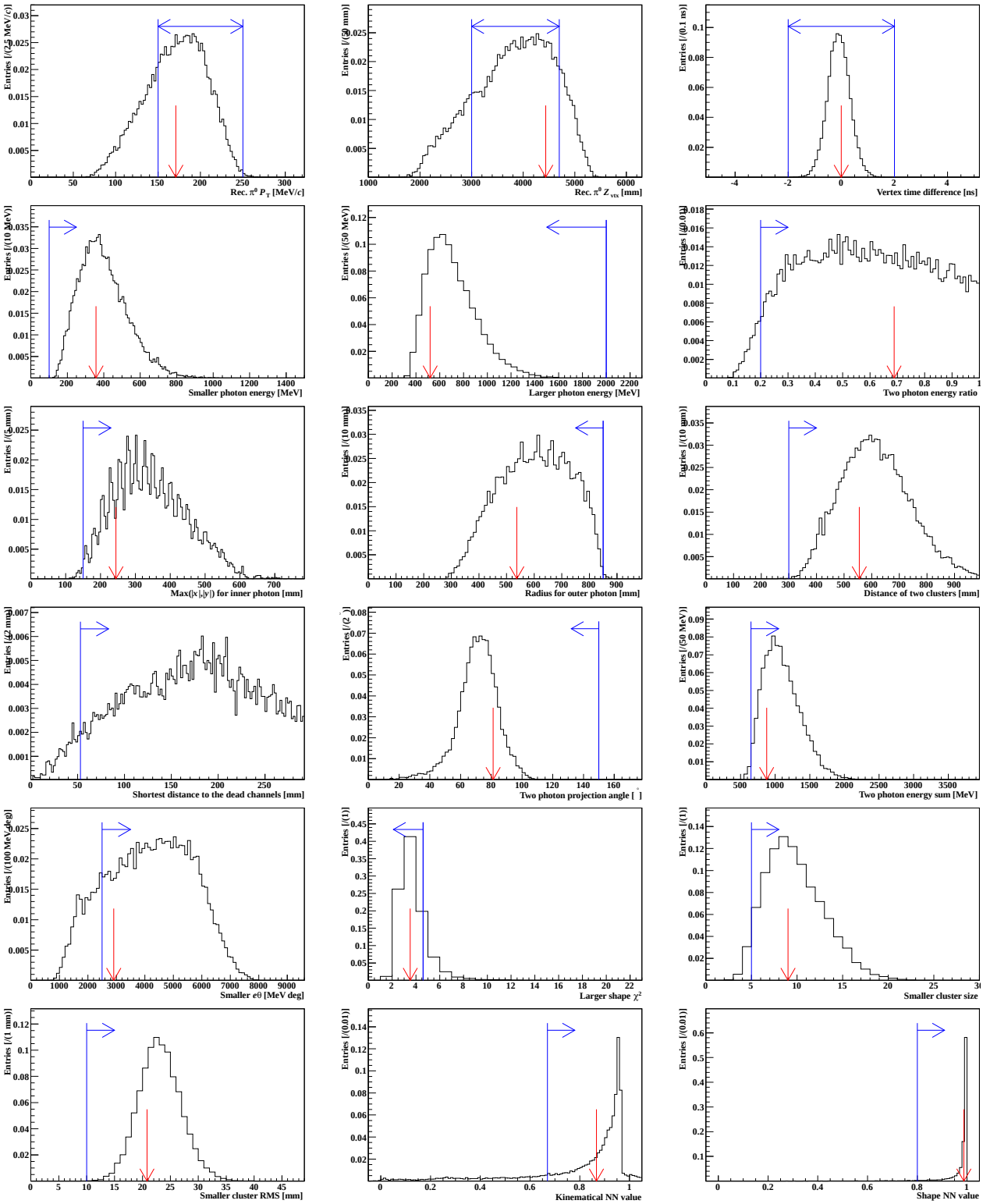

Figure 7.47: Distributions of kinematic variables for the event. Histograms are results from $K_L \to \pi^0\nu\overline{\nu}$ signal MC and blue lines show the accept region. The value for the one event is indicated with a red arrow in each distribution, where the smallest distance from the dead channels of this event was 554.9 mm, outside of the histogram range.

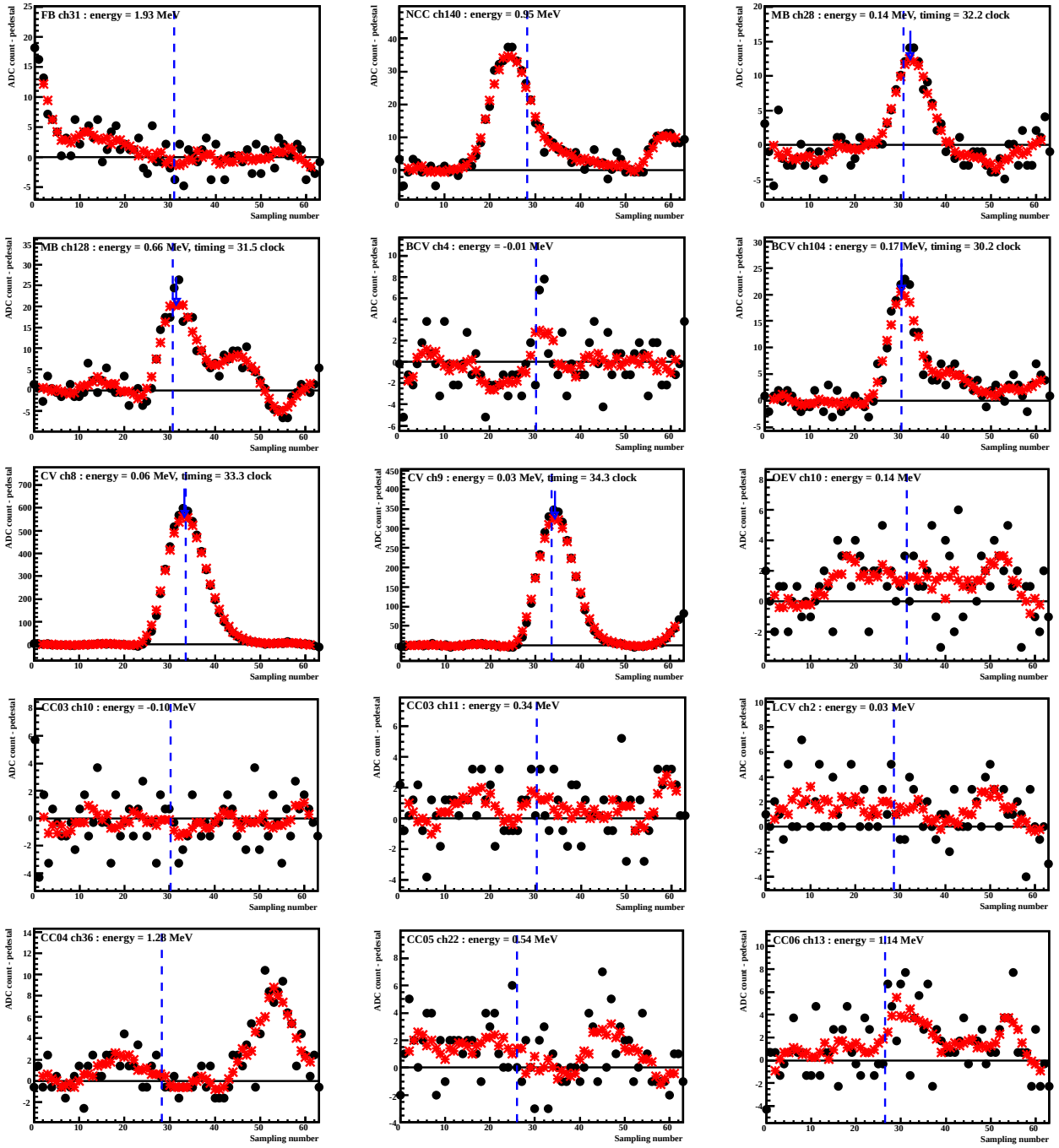

Figure 7.48: Waveform of veto detectors in the observed event. For each detector, a channel with the maximum energy deposit was selected. In detectors with both-side readout, waveform of its partner channel is also presented. Black dots and red stars show waveform of raw data subtracted by pedestal and after smoothing process, respectively. The blue dashed line indicates the nominal timing of hits for the detector and blue arrow indicates detected hit timing with the parabola fitting method.

Table 7.10: Cur variables of the observed event.

	γ_1	γ_2	Selection criteria
Energy [MeV]	519.4	357.4	>100, <2000
x position [mm]	534.3	11.5	$\max(\lvert x\rvert, \lvert y\rvert) > 150$, $\sqrt{(x^2+y^2)} < 850$
y position [mm]	-57.4	-244.3	
Cluster size	13	9	≥5
Cluster RMS [mm]	35.0	20.8	>10
Shape χ^2	3.5	3.5	<4.6
π^0 $Z_{\rm vtx}$ [mm]	4437.6		>3000, <4700
π^0 $P_{\rm T}$ [MeV/c]	170.9		>150, <250
Vertex time difference [ns]	-0.0032		>-2, <2
Kinematical NN value	0.867		>0.67
Shape NN value	0.988		>0.8

process in K^+ decays is obtained as

$$\mathrm{Br}(K^+ \to \pi^+ X^0) < 5.6 \times 10^{-8}\ (90\%\mathrm{C.L.}), \tag{7.25}$$

from the data set of the E949 experiment [113]. This bound is recast as "Grossman-Nir bound for $K_L \to \pi^0 X^0$" by multiplying a factor of 4.3 and it is calculated as 2.4×10^{-7}. Unlike K^+ experiments, background in the KOTO experiment is not sensitive to pion momentum hence sensitivity similar with the $K_L \to \pi^0\nu\overline{\nu}$ decay is expected for this process. Acceptance calculation result for this process is shown in the left of Fig. 7.49, where invariant mass of two neutrino system was calculated from MC true information and this was limited within 135 ± 5 MeV/c^2 in the $K_L \to \pi^0\nu\overline{\nu}$ MC sample. Acceptance values for other X^0 mass regions was also calculated as shown in the left panel. When X^0 mass is light, a decay π^0 has large transverse momentum and larger acceptance is expected. For X^0 with π^0 mass, the acceptance value was larger by a factor of 1.35 than the $K_L \to \pi^0\nu\overline{\nu}$ decay and corresponding S.E.S. is 0.95×10^{-8}. Assuming the observed event to be a signal event, the upper limit is obtained as

$$\mathrm{Br}(K_L \to \pi^0 X^0) < 3.8 \times 10^{-8}\ (90\%\mathrm{C.L.}), \tag{7.26}$$

which is much more stringent than the indirect limit obtained from the E949 experiment.

According to Ref. [109], Z' boson in the gauged $L_\mu - L_\tau$ model [110, 111, 112] was considered as a candidate for X^0, where $s \to d$ transition with Z' occurs through mixing of the standard model quarks with vetctor-like doublet Q and singlet U, D quarks as a diagram shown in Fig. 7.50. Figure 7.51 shows allowed region of Yukawa couplings Y_{Uc} and Y_{Ut}. The left top and right bottom corner region was excluded by Eq. (7.25) and the final result of the E391a experiment [45], each of which is shown with grey color and blue lines, respectively. The red dashed lines show exclusion when the conventional Grossman-Nir bound was applied to the process of $K_L \to \pi^0 X^0$, $X^0 \to$ (invisible). Curved lines indicate corresponding branching fraction of the decay $t \to cZ'$ and the black dashed line shows a reasonable Y_{Uc} region, considering $|Y_{Uc}|$ should be smaller than $|Y_{Ut}|$ in general. Light green bands indicate 2σ allowed regions from slight excess observed in the $B \to K^+\nu\bar{\nu}$ search by the *BABAR* experiment [114], which is consistent with one event observed in this analysis.

Needless to say, the number of observed events was also consistent with the background expectation and the above discussion must be confirmed by further searches with larger statistics and

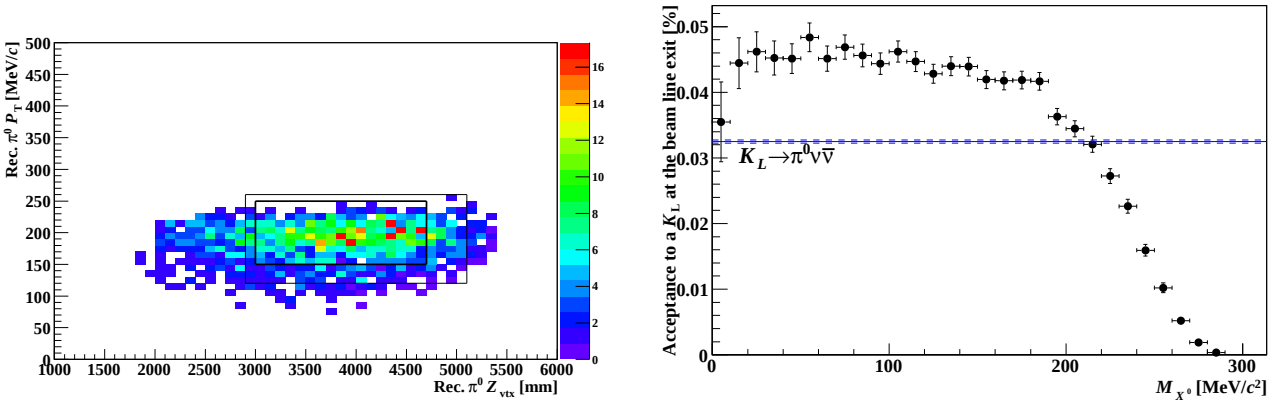

Figure 7.49: Acceptance for the process of $K_L \to \pi^0 X^0$, $X^0 \to$ (invisible) in this analysis obtained from the $K_L \to \pi^0\nu\overline{\nu}$ MC sample. The left panel shows $Z_{\rm vtx}$-$P_{\rm T}$ distribution when X^0 mass is π^0 mass, or 135 ± 5 MeV/c^2. The right one is acceptance dependence as a function of X^0 mass. The blue line shows an acceptance value for the $K_L \to \pi^0\nu\overline{\nu}$ decay and its statistical error of the MC sample is indicated with the dashed lines.

more control samples for better understanding of background events. The strongest emphasis then is put on more reduction of background and control of them. Below, prospects for the next and far future runs are discussed.

7.6.3 Further background suppression

The sensitivity of this $K_L \to \pi^0\nu\overline{\nu}$ search was just the same level of the previous analysis [45] and higher sensitivity must be achieved for the search of physics beyond the standard model. Further background suppression was necessary and this was discussed in the following.

$K_L \to 2\pi^0$ background

Background contribution from the $K_L \to 2\pi^0$ and $K_L \to 3\pi^0$ decay with future conditions was estimated with the fast simulation method, which was used to evaluate the $K_L \to 3\pi^0$ background in Sec. 7.4.4. Inefficiency functions were updated to reflect different detector conditions for further background suppression, while signal acceptance including selection cuts and loss from accidental activities was assumed to be unchanged. Two kinds of future conditions as summarized in Table 7.11 were considered. In the condition A, BHPV was upgraded with additional four modules to have more radiation length ($4X_0 \to 6X_0$) for reduction of the punch through probability. The guard counter, which was mentioned in Sec. 6.5.1, was also introduced and it was assumed to reduce efficiency deterioration in the BHPV edge region completely. These additional detector were already installed for the next physics run in 2015. For other existing detectors, thresholds were tightened as shown in Table 7.11. The acceptance decrease was evaluated using signal MC samples by tightening threshold, and it was found to be 52.0% of the current value. The number of $K_L \to 2\pi^0$ and $K_L \to 3\pi^0$ background was estimated to be $(4.13 \pm 0.42) \times 10^{-3}$ and $(6.0 \pm 1.2) \times 10^{-4}$, respectively, when scaled to the sensitivity obtained in this analysis. This meant that a search with better sensitivity by a factor of 21 than this run would be possible with background contribution from the $K_L \to 2\pi^0$ and $K_L \to 3\pi^0$ decay reduced small enough, or less than 0.1 event. This sensitivity exceeds the

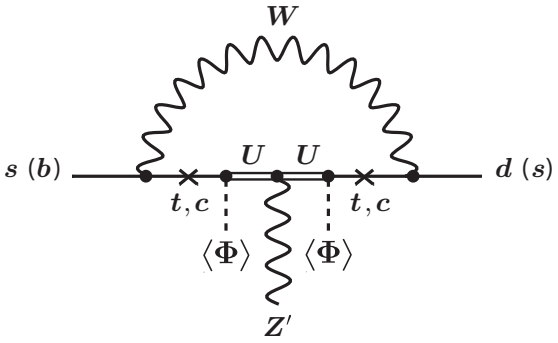

Figure 7.50: Diagram of $K_L \to \pi^0 Z^0$. Quoted from Ref. [109].

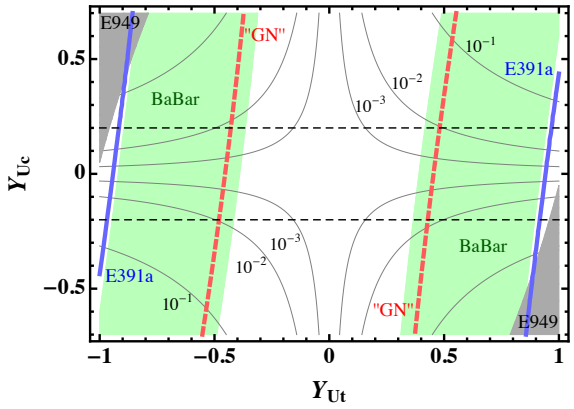

Figure 7.51: Allowed region of Yukawa couplings Y_{Uc} and Y_{Ut} with Z' mass of that of π^0. Quoted from Ref. [109]. Explanation of each component is given in the main context.

current Grossman-Nir bound. As the remaining $K_L \to 2\pi^0$ background mostly originated from MB and the calorimeter edge region, improvements of veto in this systems were necessary to reduce background and perform a search with higher sensitivity. In the condition B, thresholds for MB and BCV were further tightened and additional lead-scintillator sampling layers of $5X_0$ was assumed to be introduced. With this condition, background events were estimated to be (2.7 ± 0.3) and (0.9 ± 0.2) for the $K_L \to 2\pi^0$ and $K_L \to 3\pi^0$ mode, respectively, where the number of events were scaled to S.E.S. of 8.8×10^{-12}. This number allows a search for the signal event with a signal to noise ratio of 0.9 when only these decay modes were considered as background sources and the standard model branching fraction is assumed.

$K_L \to \pi^+\pi^-\pi^0$ background

Improvement of veto efficiency for charged pions in the downstream detector system is necessary for further reduction of this background. Introduction of an additional detector to cover the downstream beampipe significantly improves detection efficiency of such charged pions and $K_L \to \pi^+\pi^-\pi^0$ background is expected to be reduced further. A simulation study with scintillator surrounding the outside of the beam pipe, which was relatively easy since vacuum related works were not involved, showed that the number of $K_L \to \pi^+\pi^-\pi^0$ background with 130 MeV/c P_{T} threshold would become 10% of the current level. Assuming the same reduction factor for 150 MeV/c P_{T} threshold, the number of $K_L \to \pi^+\pi^-\pi^0$ background will be $O(0.1)$ event for S.E.S. larger by a factor of 1,000 of the current level and still small enough. More reduction, with scintillator covering inside surface of the beam pipe, for example, would allow the P_{T} threshold to be lowered and improve signal acceptance and such an effort is worthwhile in order to achieve higher sensitivity in this experiment.

Background due to accidental activities

A finite number of background was expected in $K_L \to 3\pi^0$ and $K_L \to 2\pi^0$ modes and masking background would become non-negligible background in a search with higher sensitivity. even

Table 7.11: Veto condition for future setup. Threshold for detectors with an asterisk(*) was considered only in calculating acceptance. The number of BHPV modules was assumed to be twelve in the acceptance calculation.

Detector	Threshold in this analysis	For condition A	For condition B
MB	2 MeV	1 MeV	0.5 MeV
BCV	1 MeV	0.3 MeV	0.1 MeV
CV	0.2 MeV	0.1 MeV	0.1 MeV
FB, NCC, OEV	2 MeV	1 MeV	1 MeV
*LCV	0.6 MeV	0.3 MeV	0.3 MeV
CC03-06 (CsI)	3 MeV	1 MeV	1 MeV
*CC04-06 (Scintillator)	1 MeV	0.5 MeV	0.5 MeV
*BHCV	0.3 MeV	0.3 MeV	0.3 MeV
BHPV	(12 modules)	(16 modules)	(25 modules)
Relative acceptance	1	0.52	0.37

though the parabola fitting method was used. Waveform analysis with a template fitting method [90] is a powerful tool for identification of multiple pulses in an event [99]. Figure 7.6.3 shows waveform for the remaining event in masking background estimation of the $K_L \to 3\pi^0$ mode, where two kinds of waveform analysis methods were applied and their performance was compared. Larger pulse than genuine one was overlaid as an accidental hit and the event failed to be rejected due to wrong timing with the parabola fit method as indicated with the green arrow in the left figure. A result with the template fitting method is given in the right of Fig. 7.6.3, where timings of two pulses were properly calculated. Figure 7.6.3 shows comparison of two-pulse-separation efficiency between the parabola fitting method and the template fitting method. Two pulses as close as 30 ns to each other are separated with the fitting method while worse efficiency even for more distant two pulses was obtained with the parabola fitting method. Although pulses which are closer in timing than this value is not separated, possible timing shift would be accommodated within a veto window used in this analysis for the physics run and the separation inefficiency in this range is not a problem. Consequently, masking background is expected to be reduced.

Neutron background

Although neutrons were the main sources of background in this physics analysis, understanding of their mechanism is not enough due to the limited data set for control samples. For better understanding of these neutron background and further reduction of them, more control samples with various conditions and larger statistics are necessary as well as efforts to reduce halo neutrons themselves. As was used in Sec. 7.4.8, inserting materials inside the beam core is an effective way to obtain neurons samples. Additional targets with different positions and different amount of material have been installed for the next physics data taking in order to obtain further control samples. For reduction of the halo neutron flux, the upstream vacuum window, as mentioned in $K_L \to 2\gamma$ background (Sec. 7.4.2), has replaced with thinner one in order to reduce scattering of neutrons in the beam core. Proper alignment of the two collimators [61] was necessary to minimize the number of halo neutrons and a new beam profile monitor has also been newly introduced, with which their alignment and monitoring of their in-situ status is achieved during the physics data taking. Efforts

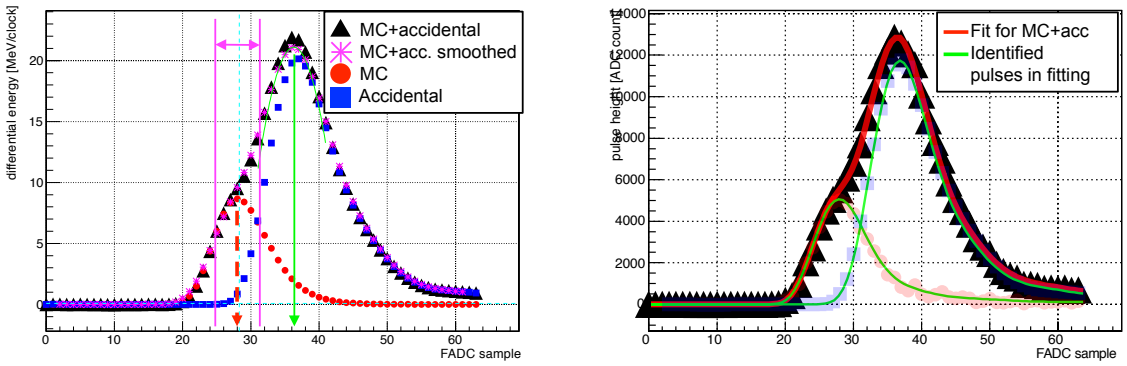

Figure 7.52: Results of the two different waveform analysis for the remaining event in masking background estimation for the $K_L \to 3\pi^0$ mode. The left (right) figure shows an analysis result with the parabola fitting (template fitting) method. The thin green line in the left figure shows a parabola function and the green arrow shows timing determined by this function. The red arrow indicates timing of the genuine hit. Veto window of ± 30 ns range is also shown with purple band in the left figure. Original figures were provided by Y. Sugiyama and some modifications were applied.

in analysis are also of great importance and various studies are in progress such as measurement of the flux with the NCC detector, improvement of further discrimination of hadron clusters with cluster shape information and incident angle reconstruction, and extraction of photon and neutron difference [90]. Measurement of particle Time Of Flight (TOF) using transverse RF signals as mentioned in Sec. 6.4.1 might be effective when momentum of neutrons causing background events is low. If timing information of transverse RF is available, ΔTOF as defined in Sec. 6.4.1 can be measured event by event. Low momentum neutrons give large ΔTOF value as in Eq. (6.13) thanks to the long beam line and resultant long particle flight length. A simulation study indicates halo neutrons with kinetic energy of 1.26 GeV/ are most likely to contribute to background. These neutrons are rejected by requiring a small ΔTOF value. Figure 7.54 shows simulation results of ΔTOF distribution and loss of signal acceptance as a function of threshold neutron kinetic energy. In calculating acceptance loss, a ΔTOF value was required to be smaller than a threshold or larger than 18 ns. Considering a finite width in timing distribution of proton bunches due to transverses RF, some smearing was applied to ΔTOF calculated from true information. Two kinds of smearing, the optimistic and pessimistic cases, were considered for realistic estimation. In the "optimistic" case as shown with red color in Fig. 7.54, each true ΔTOF value was smeared using a Gaussian with the intrinsic timing width of $\sigma = 1.8$ ns as discussed in Sec. 6.4.1. In the "pessimistic" case as shown with blue color, smearing was applied using observed BHPV timing distribution in Fig. 6.24 itself. Periodicity is also considered in acceptance calculation and events with ΔTOF > 18 ns was accepted since a tail component of the next bunch existed. Neutrons with kinetic energy smaller than 1.26 GeV is discriminated with signal loss of 3.9% and 14.8% with the optimistic and pessimistic estimation, respectively. Since this method depends on only neutron TOF and is free from uncertainty of neutron interaction, reliable background reduction is expected if energy spectrum of halo neutrons is clear.

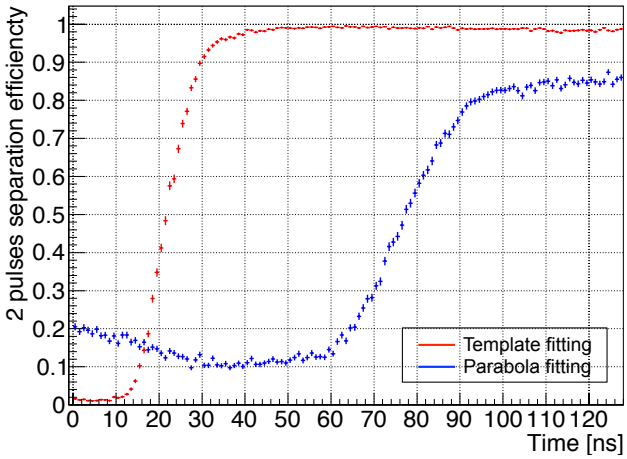

Figure 7.53: Separation efficiency of two pulses with the parabola fitting and the template fitting method as a function of timing difference of the two pulses. Provided by Y. Sugiyama.

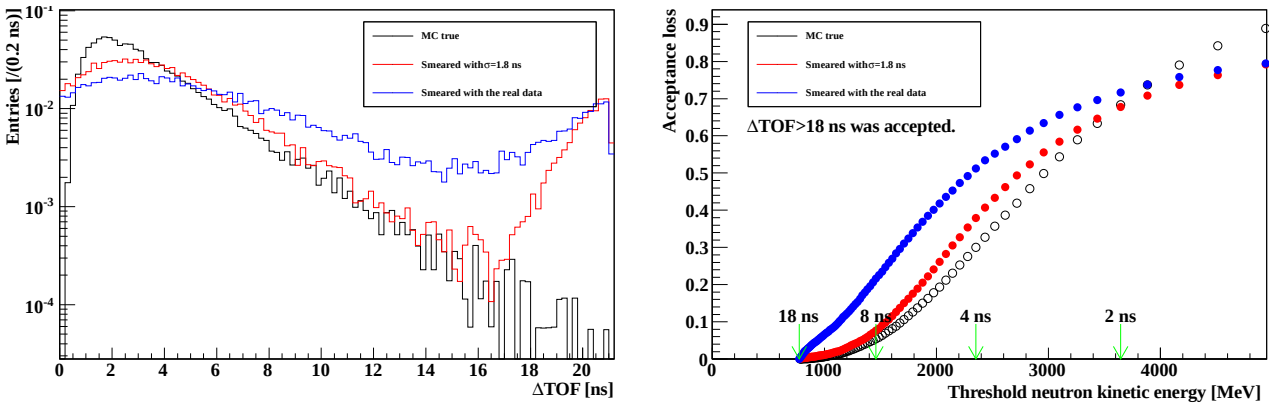

Figure 7.54: Simulated ΔTOF distribution for $K_L \to \pi^0\nu\overline{\nu}$ decay events (left) and acceptance loss as a function of threshold neutron kinetic energy (right). Black ones were obtained from true information and the optimistic (pessimistic) smearing was applied in the red (blue) ones for realistic cases. Green arrows with a timing value in the right panel indicate a corresponding ΔTOF value.

Chapter 8

Conclusion

Through this research, performance evaluation of the novel GeV-energy photon detector named BHPV and a search for the $K_L \to \pi^0\nu\overline{\nu}$ decay were conducted using the first physics data of the KOTO experiment taken in May, 2013.

Tolerance to high rate environment is one of key points to achieve high sensitivity in search of this decay. This requirement is serious particularly for an in-beam photon detector, which needs to detect high energy photons from K_L decays in an underlaying large neutron flux. The new detector, named BHPV, consists of lead photon converter and aerogel Čerenkov radiator, which realized both low sensitivity to neutrons and high efficiency for GeV-energy photons. The waveform analysis method for this detector was established and basic performance such as gain and timing stability was evaluated. Detection efficiency of GeV-energy photons in the real experimental condition was examined with the $K_L \to 3\pi^0$ decay sample, where the beam particle flux reached ∼300 MHz. The ratio of the observed event yield to the MC expectation was found to be $1.025 \pm 0.050(\text{stat.}) \pm 0.068(\text{syst.})$, which means the detector owns expected photon detection capability even in the high rate environment.

As the next step, using information of all the KOTO detectors including BHPV, the first search of the $K_L \to \pi^0\nu\overline{\nu}$ decay in this experiment was performed based on the 100-hour physics data. The high rate environment as mentioned above is again a critical issue in considering background through masking effect by accidental hits. In order to deal with this problem, the parabola fit timing extraction method was newly developed, as a simple but powerful tool for reduction of this type of background. K_L related background including the masking-induced one was also intensively studied. The largest contribution was found to come from the $K_L \to 2\pi^0$ mode among various K_L decays. The total K_L background was estimated to be 0.10 event, which is small enough. The total amount of background was estimated to be 0.36 event, where neutron contribution was also considered. Among the neutron background, their direct interaction with the calorimeter was found to give dominant source of background. As a result, one event was observed in the signal box and a 90% confidence level upper limit for the branching ration of the $K_L \to \pi^0\nu\overline{\nu}$ decay was obtained as 5.1×10^{-8}, which is competitive to the previous search performed in the KEK-E391a experiment. Although this result is consistent with background expectation, there is possibility that the observed event is derived from new physics effect through the process of $K_L \to \pi^0 X^0$, $X^0 \to$ (invisible), where X^0 is what is called a weakly interacting light boson. Further background suppression is necessary in order to confirm this process and achieve higher sensitivity.

Future prospect for background reduction was also discussed. Simulation study showed on-going

detector upgrades in the barrel detector and the beam hole detectors was performed. As a result, a signal to a $K_L \to 2\pi^0$ and $K_L \to 3\pi^0$ background ratio of 0.9 for the standard model branching fraction is found to be achieved with single event sensitivity 8.8×10^{-12}. Also as for neutron background, possibility of their reduction using the beam timing structure due to transverse RF, as well as improvement of shower shape and waveform analysis, was presented.

In summary, in this thesis, in-situ performance of the novel aerogel Čerenkov detector as an beam hole photon detector was verified. The first search of the $K_L \to \pi^0\nu\overline{\nu}$ decay in the KOTO experiment was then performed and sensitivity competitive to the pervious experiment was achieved. These works established a strong basis for the future new physics search in the KOTO experiment.

Appendix A

Module production of the Charged Veto detector

A.1 Thickness measurement

The CV detector is required to own high efficiency for charged particles and sufficient amount of photoelectron yields is necessary. Thickness of scintillator plates directly affects the photoelectron yields This thickness effect on efficiency is serious especially in groove regions as illustrated in Fig. A.1. The most probable energy deposition by minimum ionizing particles (MIPs) gets small in such regions corresponding photoelectron yields are also decreased, and this finally causes large efficiency drops. Although it seems that this situation can be avoided by making grooves shallow so that enough scintillator thickness is obtained, an embedded fiber is then not accommodated inside a groove, which worsens light collection efficiency and reduces photoelectron yield after all. From these discussion, scintillator should be controlled strictly in order not to use thin regions. As a result of simulation and measurement results, the minimum thickness was determined to be 2.7 mm so that required efficiency is achieved for all the regions of the detector.

The scintillator strips of CV are taken from large cast sheets with dimensions of 58.3 $\times$102.4 cm^2 in order to obtain long strips as long as 100 cm at maximum. However, this size makes it hard to keep flatness of the whole regions of a sheet. In case of BC404 scintillator used for this detector, the nominal variation of thickness was 0.35 mm for sheets with this size, which was given as (maximum$-$minimum)/2 in each sheet. Since this variation is too large to be ignored, thickness of the whole regions for each of all the purchased 16 sheets was measured in order to reject thin regions which could give bad performance. A laser displacement sensor, Keyence [115] LB-01, was used. The sensor was calibrated so that its output agreed to measurement in edge regions with micrometer. Distribution of measured thickness for all the regions and all the sheets is shown in Fig. A.2. The average thickness and standard deviation were 3.10 mm and 0.18 mm, respectively, and the sheets were found to be a little thicker than the nominal thickness of 3 mm.

The sheets then were fabricated to obtain strip modules with grooves after this measurement. In this process, thicker regions were assigned for modules in inner regions and regions thinner than 2.75 mm were avoided based on the result of the thickness measurement.

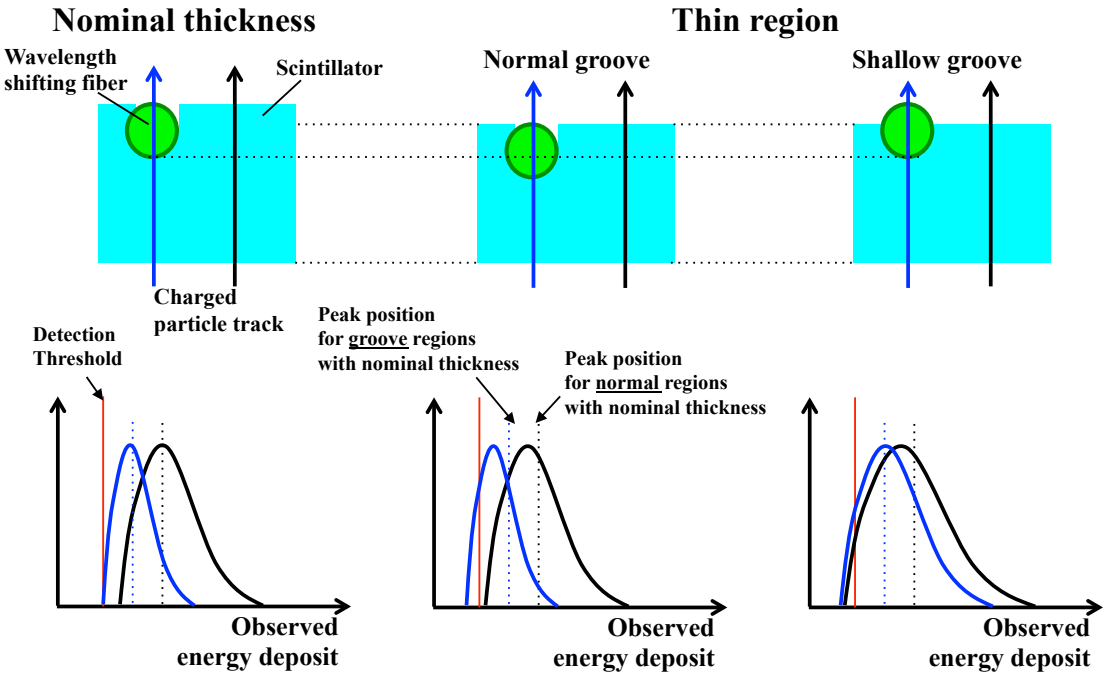

Figure A.1: Scintillator thickness and photoelectron yields.

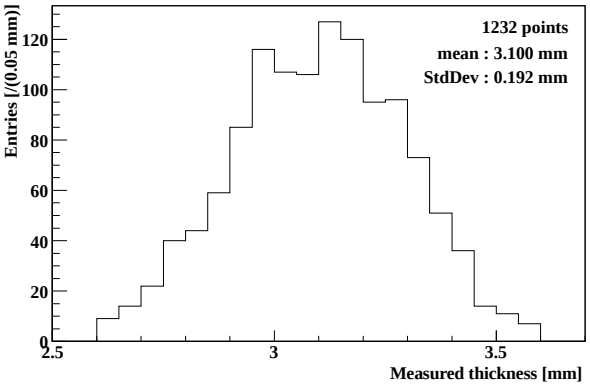

Figure A.2: Distribution of measured scintillator thickness. One entry of the histogram corresponds to one measurement point. For each scintillator plate, thickness for 77 points was measured.

A.2 Glueing of scintillator strips and fibers

Gluing of the fabricated scintillator strips with fibers were achieved with the automatic gluing system consisting of electric sliders and dispensers [82], whose photograph is shown in Fig. 2.20. Fibers were first laid in grooves of a scintillator strip and stretched with tension of 3-6 N for each fiber. Quantity of application per length was set to be 3.6 mg/cm by adjusting speed of the slider. Optical cement of a two-liquid mixing type, Eljen [80] EJ500, was used as glue. The mixing ratio of resin to hardener was optimized as 3.6:1.4 in weight[*1] so that glue is suitable for application by reducing viscosity. Application was split in two times for each fiber in order to avoid overflow of glue from grooves. After slider operation, bubbles below the fibers were inspected by eyes and glue was added by hand in order to eliminate the bubbles. The system could handle four modules at a time, where those with the same type corresponding to each of the four quadrants. Temperature in the production room was controlled to be around 20 °C during glueing periods and around 28-30 °C during cure time, where the former is to maximize working time and the latter is to accelerate curing.

This glueing system was also used for production of the LCV modules. Since signals of the LCV is read only from the downstream side, one end of each fiber was polished and glued with the upstream region of the scintillator plate in advance. Procedures after this are the same with CV.

[*1] The nominal ratio is 4:1 in weight.

Appendix B

Evaluation of Dead Channel Effect

Studies for evaluations of effect by dead channels were described in this section.

B.1 CsI calorimeter

B.1.1 $K_L \to 2\pi^0$ background

Simulations was performed to evaluate effect of a daed channel. This study is based on Ref. [116]. Increase of $K_L \to 2\pi^0$ background was estimated with what we call the fast simulation method, which was also used in Sec. 7.4.4. In order to reflect increase of photon detection inefficiency due to dead channels, a separate simulation was performed in advance, where a single photon incident to "small" crystals stacked in a 20×20 grid was simulated. Additional inefficiency due to a dead channel was evaluated by comparing inefficiencies in case that all the crystals were available and one among them was not available. In case of large crystals, four neighboring crystals were treated as a one crystal. The result of estimation for additional inefficiency was shown in Fig. B.1 as a function of incident photon energy.

The number of $K_L \to 2\pi^0$ background was evaluated as described in Sec. 7.4.4, where one specific channel was assumed to be dead and additional inefficiency was added when an incident photon to be used for veto was located within 80 mm from the given dead channel. Figure B.2 showed the result of the simulation and gave ratio of increase in background events depending on the position of a dead channel. When a channel with a small crystal was dead, increase of $K_L \to 2\pi^0$ background was estimated to be less than 1%. In case of the physics run in May, 2013, two channels were dead and both were for small crystals. Since positions for these crystals were separated enough, additional inefficiency was considered to be the same amount for a single photon and increase of background due to these two dead channels could naively be a simple sum of that for each single channel. Under this assumption, effect on background was still a few percent level.

Note that these studies were not directly used for background estimation in the $K_L \to \pi^0\nu\overline{\nu}$ search described in Chap. 7 since various conditions were different such as energy threshold for each crystal and cut conditions. More realistic treatment was considered by ignoring energy information from the two dead channels in the simulation used for evaluation of signal acceptance and background.

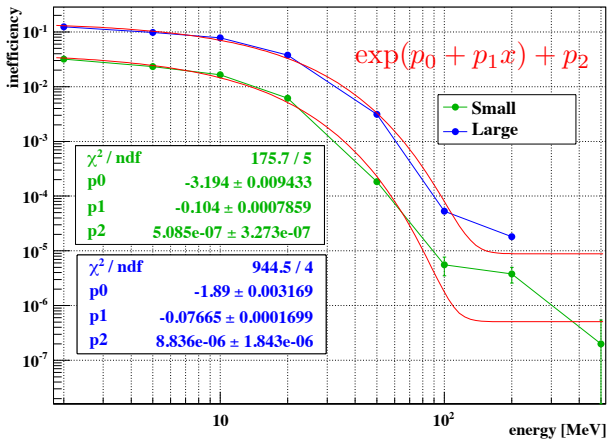

Figure B.1: Additional inefficiency due to a single dead channel. Quoted from Ref. [116].

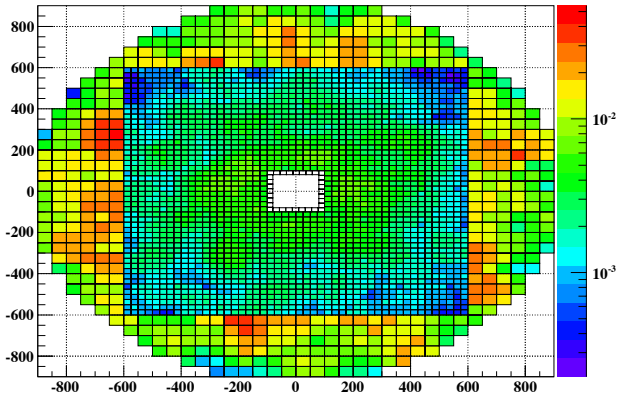

Figure B.2: Ratio of increase of $K_L \to 2\pi^0$ background due to a single dead channel. The color (z-axis) indicates the ratio for each crystal. Quoted from Ref. [116].

B.1.2 Signal acceptance

In the analysis of the $K_L \to \pi^0\nu\overline{\nu}$ search, a selection cut was applied in order to avoid wrong z vertex reconstruction due to the dead channels, where reconstructed photon hit positions were required to be far from the dead channel positions. This cut reduced acceptance by 2.5%. Although wrong reconstruction due to these dead channels can also affect signal acceptance except for the cut, this effect was estimated to be less than 0.1% from simulation with signals for the corresponding channels enabled. Since there are not available accidental hit data for these channels, relative acceptance was evaluated without overlaying accidental activities and with the dead channel cut removed. As a result, increase of acceptance was found to be 0.05%, which is negligible compared to the cut effect.

B.2 CV

Although signals of two modules in the rear plane were read from only one side, this effect on charged particle inefficiency was considered to be small enough thanks to excellent performance of this detector. This was confirmed by performance evaluation was conducted using the real CV detector and a series of drift chambers [82, 83, 84], which was conducted prior to the construction of the KOTO whole detector system in Jun, 2012. In this test, there existed no dead channels and information of all the channels were available. Effect of dead channels were estimated by neglecting hits of the corresponding channels. Here, inefficiency for a single charged particle penetration was evaluated, where tracks of charge particles mainly coming from K_L decays. Hit position on CV was identified one by one with the drift chambers for each track and response in the corresponding CV modules was examined. As a result of this study in Ref. [117], inefficiency of the whole rear plane was found to be $(0.30 \pm 0.07) \times 10^{-4}$ with the two dead channels while it was $(0.16 \times 0.05) \times 10^{-4}$ with all the channels available, both of which were much smaller than the requirement of 10^{-3} given in Ref. [82, 83, 84]. In this analysis, energy threshold was set as 100 keV. Although there were many

difference in condition such as the energy threshold, operation voltage of MPPCs and properties of charged particles, realistic effect by the dead channels were again taken into considered in the MC simulation described in Chap. 5.

Appendix C

Detector Calibration

This chapter describes calibration methods for several major detectors other than BHPV.

C.1 CsI calorimeter

C.1.1 Energy calibration

Energy calibration of the calorimeter was performed in the following three steps:

1. initial calibration using cosmic ray events,
2. relative energy scale tuning using $K_L \to 3\pi^0$ decay events ($K_L \to 3\pi^0$ calibration),
3. correction of the absolute energy scale using data in aluminum target runs.

In the initial calibration, cosmic ray track was reconstructed and a calibration factor for a crystal was calculated so that outputs normalized with pathlength of the reconstructed track inside the crystal corresponded to 5.6 MeV/cm. Slight shift of this nominal energy due to momentum dependence of $\mathrm{d}E/\mathrm{d}x$ and longitudinal non-uniformity of photoelectron yield in a crystal were ignored in this calibration. Gain for each channel was adjusted in this process so as to have the same outputs per energy deposit in all the channels for online-level triggers.

In the second step, $K_L \to 3\pi^0$ decays were reconstructed using the above initial calibration and a correction factor for each crystal was obtained. In this process, vertex xyz positions and energy of selected one among six clusters were fitted to the assumption that the six photon clusters derived from $K_L \to 3\pi^0 \to 6\gamma$ with a method of Lagrange multipliers. Obtained correction factors with this calibration would be affected by systematic shifts particularly in outermost or innermost crystals and those neighboring the dead channels due to shower leakage. To include this effect, the same calibration processes were applied also for simulation samples.

Only relative outputs among channels were tuned in this method and the absolute energy scale was finally adjusted with the last step of the calibration. As already described in Sec. 3.4.2, an aluminum plate was inserted in the beam and π^0 generated in interactions of neutrons were reconstructed. As the reconstructed π^0 mass was proportional to a geometric mean of two photons detected by the calorimeter as in Eq. (2.1), it was possible to correct the overall energy scale which were common to all the crystals using the nominal π^0 mass.

More detail will be find in Ref. [69].

C.1.2 Timing calibration

Relative timing offset for each channel was determined χ^2 method as was used in the BHPV timing calibration in Sec. 6.2.3. Cosmic ray data was used and timing offset for i-th channel t_i was given so as to minimize the following χ^2

$$\chi^2 = \sum_{i,j}^{i>j} \left(\frac{t_{i,j} - t_i + t_j - L_{i,j}/c}{\sigma_{i,j}} \right)^2, \tag{C.1}$$

where $t_{i,j}$ and $\sigma_{i,j}$ were observed hit timing difference between i-th and j-th crystal and its error, respectively, $L_{i,j}$ was distance between i-th and j-th crystals in xy plane, and c was the speed of light. The term $L_{i,j}/c$ represented Time Of Flight (TOF) for a detected cosmic muon, which was assumed to travel into the downward direction with the speed of light.

More detail will be find in Ref. [64].

C.2 CV

C.2.1 Energy calibration

Since signals of the CV detector were also used in an online-level trigger, its outputs were adjusted so that outputs for Minimum Ionizing Particles (MIPs) were the same among all the modules. Here an output of a module was given as a sum of 64-sample waveform integrals from the two readouts in the module. Data for this gain tuning was taken with the minimum bias trigger of 300 MeV threshold. In determining a calibration factor for each channel, the same process was simulated and a MIP peak value for each module was obtained. The calibration factors were the calculated so that the MIP peak in the simulation agreed to that of the data.

C.2.2 Timing calibration

Again χ^2 minimization method was adapted to determine a relative timing offset in each channel. In order to obtain enough numbers of channel combinations, data with the minimum bias trigger and that from muon runs were combined.

C.3 LCV

Cosmic ray data was used for energy and timing calibration of LCV. Using a hit pattern in the calorimeter, a cosmic ray track in the xy-plane was reconstructed. A line was detected with the Hough transformation [118] and a track was determined with a χ^2 fitting method. Hit z direction was calculated with timing information in MB, which was obtained from hit timing difference in PMTs of the upstream and the downstream sides. Using these information, a cosmic ray track was fully reconstructed. The track angle was used for event-by-event path length correction. An energy calibration constant for a module was obtained so that the most probable value of an angle-corrected 64-sample integral corresponded to 0.4663 MeV, which was obtained from simulation with 1 GeV/c μ^+. In order to eliminated position dependence of outputs, only events with reconstructed z position in $320 < z < 400$ mm from the upstream edge of the calorimeter were used for determination of the calibration constants. In addition, events with a large angle were not used to avoid too large

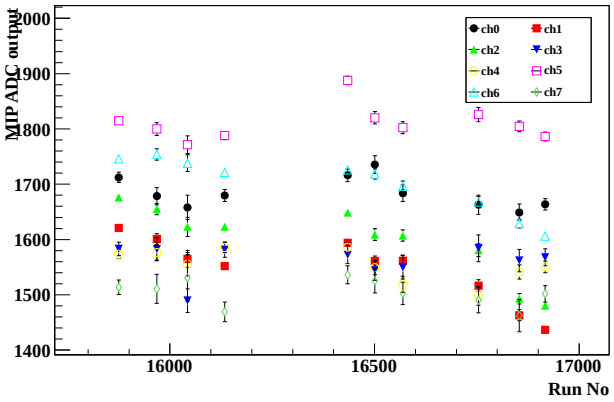

Figure C.1: History of BHCV energy calibration.

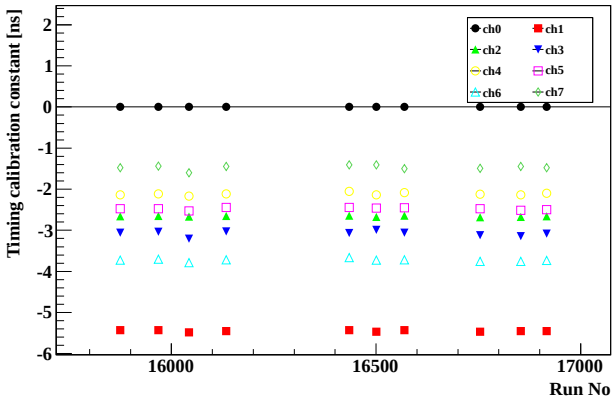

Figure C.2: History of BHCV timing calibration constants.

correction. These values were finally multiplied by small correction factors of $O(1\%)$ in order to consider gain deviation during on-spill periods. This correction factor was obtained from LED data for each channel.

Timing calibration constants were obtained with the χ^2 minimization method. The same cosmic ray data with the energy calibration was used. The track was required to penetrate two LCV modules, where difference of hit z positions on these modules must be within 10 mm and their average needed to satisfy $80 < z < 400$ mm. TOF effect was corrected event by event assuming the reconstructed μ to run with the speed of light. Finally, χ^2 like Eq. (6.5) was defined the calibration constant for each channel was obtained by minimizing this χ^2.

C.4 BHCV

Muon run data was used for energy and timing calibration of BHCV. As described in Sec. 3.4.1, events were triggered with BHCV total energy deposit and a hit in BHTS was required in the following offline analysis. In energy calibration, hits in all the 12 BHPV modules were required and calibration constants were decided so that the most probable ADC output as described in Sec. 4.2.2 agreed to 0.4708 MeV for each module, where an ADC output is defined as integral of ADC counts around an identified peak. As seen in the history of ADC outputs in Fig. C.1, slight decrease was observed particularly in modules for the inner part of the beam. Therefore, energy calibration constants were changed according to the run number. Finally, as was done for LCV in Sec. C.3, correction of gain deviation was applied, where the amount of correction was $\sim 5\%$ and $\sim 1\%$ for modules located in the inner and the outer part of the beam, respectively.

In the timing calibration, only events with hits in both of two adjacent modules were selected in addition to the above conditions. Again, the calibration constant for each channel was calculated by χ^2 minimization. The result is shown in Fig. C.2. Whereas 2-ns discontinuous shifts were observed in three among 24 channels of BHPV, no such changes were seen in this case of BHCV. A standard deviation value for each channel was smaller than 60 ps, which is much smaller than width of BHCV veto timing distribution and stable enough for physics analysis.

Appendix D

Details of the Waveform Analysis and Generation

In this appendix, detailed procedures of waveform analysis are described in Sec. 4.2 as well as parameters used in these processes. Procedures of waveform generation in the MC simulation mentioned in Sec. 5.4.3 are also summarized.

D.1 Procedures of constant fraction timing calculation

A waveform data of 64 samples after pedestal subtraction is denoted as $\{a_i\}$ $(i = 0, 1, \cdots, 63)$. First a peak sample is identified as the maximum point among these 64 samples. Here, the i-th sample is assumed to have the maximum value a_i. A threshold is then defined as $a_i/2$ and the samples with earlier timing than i are search for the j-th sample which satisfied

$$a_j < \frac{a_i}{2} < a_{j+1}. \tag{D.1}$$

When two or more candidates were found, one whose timing was the closest to the peak timing, i, was chosen. Finally, the timing was determined as that at the threshold by interpolating the two points:

$$j + \frac{a_i/2 - a_j}{a_{j+1} - a_j}. \tag{D.2}$$

D.2 Procedures of parabola fit timing calculation

Again, 64-sample waveform data with pedestal subtraction was denoted as $\{a_i\}$ $(i = 0, 1, \cdots, 63)$. This waveform was first modified so as to be smoothed by taking what was called moving averages, where each sample was replaced with an average of itself and its neighboring samples. In this analysis, averages of five samples were used as follows,

$$a'_i = \frac{\sum_{j=0}^{4} a_{i-2+j}}{5} \ (i = 2, 3, \cdots, 61), \tag{D.3}$$

where the series $\{a'_i\}$, $(i = 2, 3, \cdots, 61)$ denoted samples of waveform after smoothing.

Peaks were then identified in the smoothed waveform $\{a'_i\}$ by finding local maximum points with the following conditions:

$$a'_{k-1} < a'_k, a'_k \geq a'_{k+1}, a'_k > a_{\mathrm{thre}}, \tag{D.4}$$

where the k-th sample was what was identified as a peak and a_{thre} was the minimum peak height to recognize pulses and given detector by detector. Actual values would be described in the following section. When two or more peak candidate samples were found, one whose timing k was closest to the nominal timing given detector by detector. This nominal timing would be also described in the following section.

For the selected peak point a'_k, the three points, a'_{k-1},a'_k and a'_{k+1}, were fitting with the following parabola function

$$A(t-B)^2 + C, \tag{D.5}$$

where parameters A, B and C are analytically calculated as follows:

$$A = \frac{a^{'}_{k-1} - 2a^{'}_k + a^{'}_{k+1}}{2}, \tag{D.6}$$

$$B = k - 1 + \frac{3a^{'}_{k-1} - 4a^{'}_k + a^{'}_{k+1}}{4A}, \tag{D.7}$$

$$C = a^{'}_k - A(k-B)^2. \tag{D.8}$$

The parameter B gives the parabola time.

D.3 Pulse height thresholds

In finding a local maximum from a waveform of 64 samples, its peak height was required to exceed a threshold which was given detector by detector in advance. If such peaks were not found, timing of the channel in the event was not defined and it was regarded to have no energy deposit. To eliminate events with significant energy but to be discarded due to this threshold discrimination, the value should be selected to be low enough. On the other hand, too low value causes too much accidental losses and higher value is desirable.

Such optimization was performed using cosmic ray data. For each detector, events with energy in a specific range were selected and the number of "inefficiency" events were counted, whose pulse height is smaller than a given threshold. The lower bound of the energy range is the threshold given in Table 7.1 and the upper bound is around twice of the threshold. This process was repeated for various threshold values and finally the maximum value with the ratio of inefficiency events smaller than 10^{-3} was adopted as the pulse height threshold.

The final values are summarized table. D.1.

D.4 Nominal timing

When two or more local maxima were found, the peak which was the closest to the nominal timing was chosen. The nominal timing was given detector by detector and summarized inTable D.1. These values were determined as the most probable timing of all channels for each detector before timing calibration and event reconstruction.

Table D.1: Threshold pulse height and the nominal timing for each detector.

detector	threshold pulse height [FADC count]	nominal timing [FADC sample]
CsI	10	31.1
FB	10	30.9
NCC	50	28.3
MB	10	30.75
BCV	10	30.25
CV	150	33.5
OEV	50	31.5
CC03	10	30.3
LCV	50	28.6
CC04	10	28.3
CC04 KTeV crystal	10	30.5
CC05	20	26.0
CC06	15	26.4
CC06 scintillator	10	26.4

D.5 Procedures of waveform analysis with 500-MHz ADCs

ADC counts for all the 256 samples were filled into a histogram whose binning was one count per bin. The distribution was then fitted with a Gaussian and the mean value regarded as the pedestal. Here, the number of the largest entries was required to be equal or larger than 10. If this was not satisfied, the histogram was rebinned, or contents in several neighboring bins were merged and again the fitting was tried.

A pulse was identified as a series of samples around a local maximum with its height exceeding the given threshold after pedestal subtraction. i-th sample was defined as the local maximum when the following conditions were satisfied:

$$a_{i-2} < a_{i-1}, a_{i-1} < a_i, a_i \geq a_{i+1}, a_{i+1} > a_{i+2}, \tag{D.9}$$

where the ADC count for i-th sample after subtracting pedestal is denoted as a_i. In addition, following conditions were required:

$$a_i > a_{\mathrm{thre}}, \tag{D.10}$$

$$a_j \leq a_i (j = i-1, i-2, \cdots, i - N_{\mathrm{back}}), \tag{D.11}$$

$$\exists k, a_{i-k} < a_i/2, a_i/2 < a_{i-k+1} (0 < k \leq N_{\mathrm{back}}). \tag{D.12}$$

a_{thre} was given as 10 counts for BHPV and 30 counts for scintillator detectors, namely BHCV and BHTS. N_{back} was given as 5 for BHPV and 6 for scintillator detectors. The second condition was required to prevent ringing after a large pulse from being identified as a pulse. The last requirement is to ensure existence of the constant fraction time.

Table D.2: Parameters used in waveform generation. For detectors with an error in the parameter a, smearing was applied in generating waveform, where a Gaussian with its mean to be the central value and its σ to be the error value was assumed.

Detector	μ_0 [ns]	σ_0 [ns]	a
CsI	30.6098	27.869	0.06202
NCC	32.760	43.864	0.1533±0.02039
MB	29.889	37.416	0.08369
BCV	29.29	36.64	0.06671
CV	36.024	48.30	0.1512±0.01953
OEV	17.02	23.575	0.1787±0.0301
CC03	30.287	39.66	0.1097
LCV	29.71	36.21	0.06172
CC04 crystal	30.9	41.2	0.1449
CC04 scintillator	29.29	35.78	0.068

D.6 Parameters used in waveform generation

In the MC simulations, an asymmetric Gaussian as Eq. (5.31) was assumed for waveform generation and parameters were prepared detector by detector. Cosmic ray data was used to determine these parameters, where waveform was fitted with the function of Eq. (5.31) and the most probable value for each fit parameter, nominal width σ_0 and an asymmetric parameter a, was adapted. These are summarized in Table D.2. In case that an asymmetric parameter sometimes had large deviation, distribution was fitted with a Gaussian and smearing was applied with the Gaussian σ value. For some detectors with similar detector components, common parameters were used, namely, the parameters for MB were used also in FB and those for CC04 were shared by CC05 and CC06.

Appendix E

BHPV Responses Implemented to the Simulation

E.1 Overview of the simulation

Čerenkov photon generation was managed by the Geant4 codes based on inputs of aerogel optical properties such as refractive index and its dispersion as well as physical characteristics such as density and constituting elements. In the simulation, the refractive index was treated as exactly $n = 1.03$ with the dispersion ignored. Density of aerogel was given as 0.11 g/cm^3 and it was assumed to be constituted by silicon, hydrogen and oxygen with ratio of 1:4:4 in the number of atoms, respectively.

Tracing of generated photons was performed. using information of direction and wavelength for each photon. This included transportation of the photons inside aerogel, their reflection by flat mirrors and inner surface of Winston Cone funnels, and detection by the PMT. Treatments of each process are described in the following sections.

As additional minor effect, Čerenkov radiation by air was also simulated. Its refractive index was given as 1.000286 - 1.000271, depending on wavelength of light. The same ray tracing with Čerenkov light from aerogel was applied except the part of transportation inside aerogel.

E.2 Scattering in aerogel

Rayleigh scattering and absorption are important processes in considering losses of Čerenkov photons in aerogel and these effects were implemented in the simulation. Transmittance of light with wavelength λ for aerogel with thickness t was written as follows [102]:

$$\exp\left(-\alpha t\right)\exp\left(-\frac{Ct}{\lambda^4}\right), \tag{E.1}$$

where the first (second) term represents absorption (scattering) effect and characterized with the parameter α (C). As shown in Eq. (E.1), absorption was assumed to be independent of their wavelength and Rayleigh scattering to be inversely proportional to the fourth power of their wavelength. These parameters were obtained from transmittance measurement for aerogel tiles used in this detector and set to be $\alpha = 0.972$ and $C = 0.00692$ μm^4/cm. The setup of the measurement is shown in the left of Fig. E.1 and the result was fitted with Eq. (E.1). In the simulation, absorption

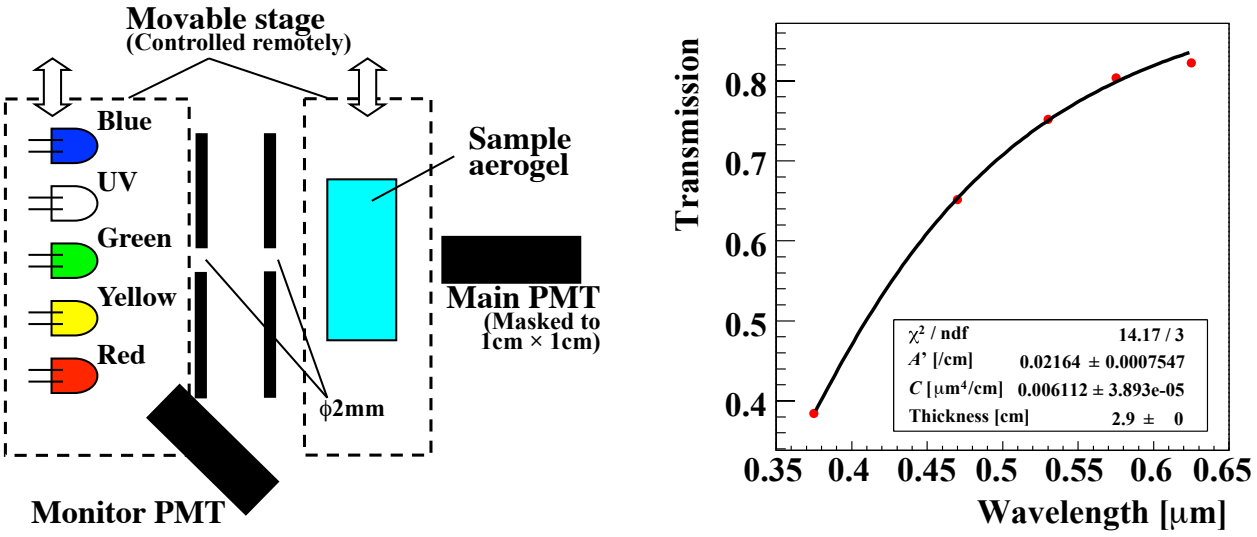

Figure E.1: Measurement of aerogel transparency. The setup of the measurement is shown in the left figure and the right one is an example of results, which is fitted with Eq. (E.1).

length $L_{\rm abs}$ and scattering length $L_{\rm scat}$ was given for each photon as random numbers following distributions

$$\exp\left(-\alpha x\right) \quad \text{for } L_{\rm abs}, \tag{E.2}$$

$$\exp\left(-\frac{Cx}{\lambda^4}\right) \quad \text{for } L_{\rm scat}. \tag{E.3}$$

These values were compared with the path length to the downstream surface of the aerogel tiles, and the process with the shortest one was realized. When the photon is scattered, its direction was changed with a following angular distribution and the same procedure is repeated until it exits aerogel or absorbed.

$$1 + \cos^2\theta, \tag{E.4}$$

where θ is a polar angle with respect to the original photon direction.

Only 90% of photons which reached the aerogel surface proceeded to the following procedures, where transparency of a thin polyvinylidene chloride sheet to support the aerogel tiles was considered.

E.3 Light collection system

The light collection system, which guides Čerenkov light from aerogel to the PMTs, consists of two pieces of flat mirrors and Winston cone funnels [92].

The flat mirrors were placed with an angle of 45° with respect to the beam axis to change direction of photons into the transverse direction. Their reflectivity was assumed to be 90%, independent on wavelength of Čerenkov photons. The junction part of the two mirrors, or the their edge region was regarded as a dead area. Hence photons hitting this region were killed.

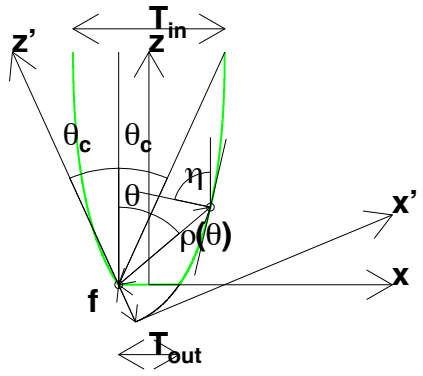

Figure E.2: Illustration of a parabola curve in a Winston cone. This figure was originally made by H. Nanjo. and some modification was applied.

Figure E.3: Photograph of a Winston cone used in BHPV.

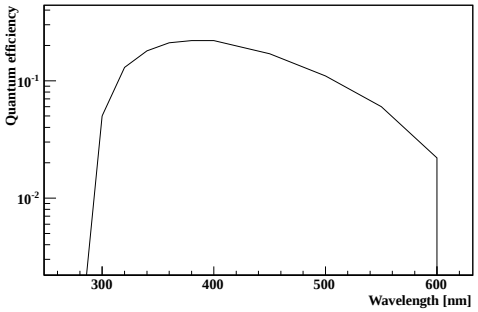

Figure E.4: Quantum efficiency of the PMT (Hamamatsu R1250) as a function of wavelength of an incident photon.

The Winston cone funnels were used as light collection funnels whose input and output diameters were 300 mm and 120 mm, respectively. This allows all photons with incident angle smaller than 23.58° to be collected completely. This angle, denoted as θ_c, is obtained as

$$\sin\theta_c = \frac{T_{\text{out}}}{T_{\text{in}}}, \tag{E.5}$$

where T_{out} and T_{in} are the input and output diameter, respectively. Using this critical angle θ_c, focal length of the parabola, f, is calculated as

$$f = \frac{T_{\text{out}}}{2}(1+\sin\theta_c). \tag{E.6}$$

This f value determines the shape of the parabola curve. The actual shape is shown in Fig. E.2. The green curve in this figure is the outline of the funnel. The original parabola is defined in the $x'z'$ coordinate and it is rotated with respect to the z-axis in the xz coordinated, which was obtained by rotation and shift of the $x'z'$ coordinate.

In the ray tracing process, intersection of a photon track and the funnel surface was calculated and the photon is reflected. The reflectivity was set to be 85%. Although the real funnel consisted of three components as Fig. E.3 shows and their junctions existed, such structures were ignored in the simulation.

E.4 Quantum efficiency of the PMT

When the traced photon reached a surface of the PMT, detection of the photon was judged considering quantum efficiency (Q.E.) of the PMT. A calibration factor, which was introduced to tune the observed photoelectron yield so that it fit measurements, was also considered in this process. A uniform random number was generated and the photon was regarded to be detected when it was below a product of the Q.E. value and the calibration factor. The Q.E. value was given according to

the photon's wavelength and was taken from its catalog [93]. Implemented wavelength dependency is shown in Fig. E.4.

Appendix F

Inefficiency Functions Used in the Fast Simulation

In this appendix, procedures and results to obtain inefficiency functions for each detector, which are used in the fast simulation for the estimation of $K_L \to 3\pi^0$ background.

F.1 FB

Since signal of the FB detector was read from only one side, the output had strong position dependency. The inefficiency function was hence prepared as a function of three variables; incident z position, energy and angle. For each combination of four incident z positions, four incident angles and 11 energies, interaction of photons with FB was simulated and inefficiency of FB was calculated with the same veto condition as the physics analysis. The results are summarized in Fig. F.1. Simulated inefficiency values were then added by the following value in order to avoid 0 inefficiency due to statistical fluctuation in case that incident energy is larger than 10 MeV,

$$4.37 \times E^{-1.83}, \tag{F.1}$$

where E is incident photon energy and measured with a unit of GeV. Effect of NCC structure is seen in case of $z = 1800$ mm, which shows worse inefficiency than that for $z = 2600$ mm with larger signal attenuation. This term corresponds to inefficiency by photo-nuclear effect, which is based on measurement results for a lead-scintillator sandwich detector [119].

In applying this inefficiency function, interpolated values were used, where logarithm of inefficiency was logarithmically interpolated with energy and linearly for the other two.

F.2 NCC

Inefficiency function of NCC was determined based on the simulation results of photons hitting the specific position of NCC with 5°. In calculating inefficiency, both NCC and FB veto were considered. The obtained NCC inefficiency function is shown in Ref. F.2. As was for FB, the simulated inefficiency was used after interpolating with energy. For high energy photons, namely > 100 MeV, a value of the following function f_{CsI} was added

$$f_{\mathrm{CsI}} = \begin{cases} (3.54 \times 10^{-7}) \times E^{-2.23} & \text{for} \quad E < 2 \text{ GeV}, \\ 7.30 \times 10^{-8} & \text{for} \quad E > 2 \text{ GeV}, \end{cases} \tag{F.2}$$

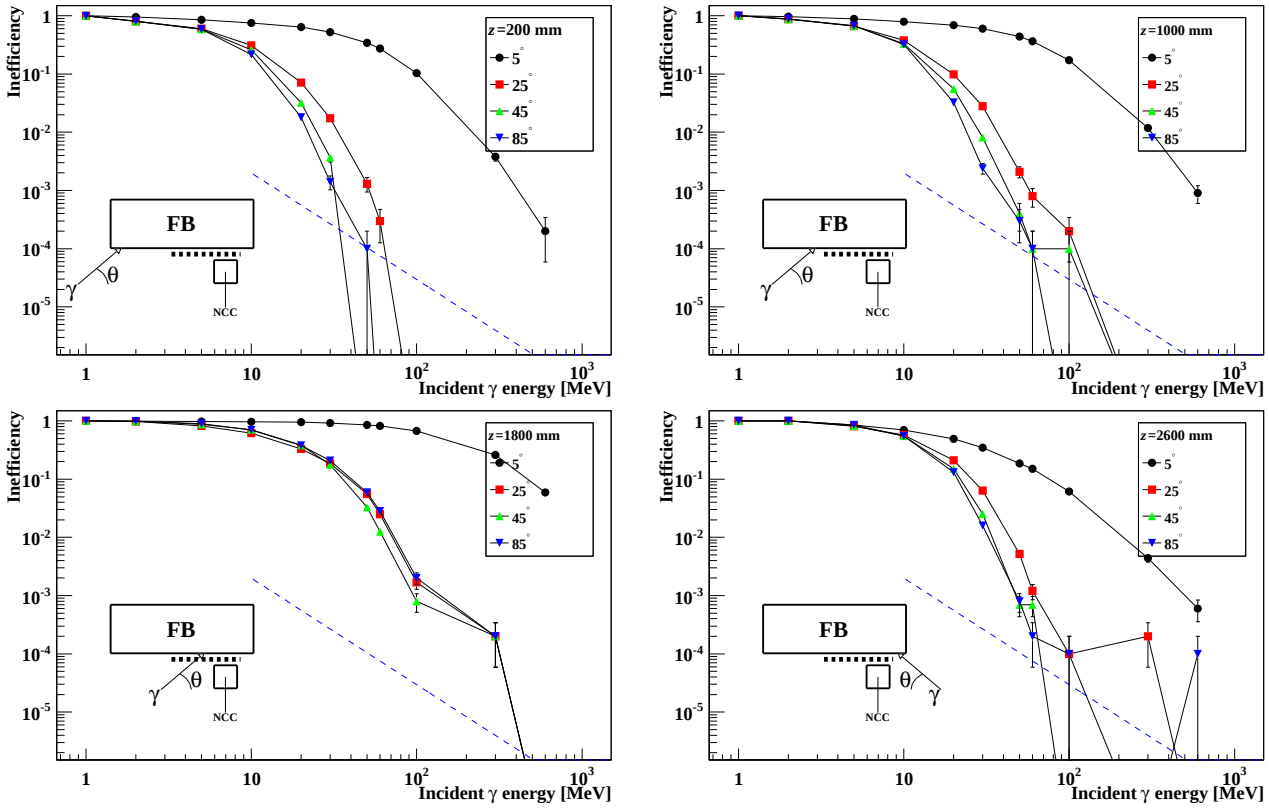

Figure F.1: Inefficiency function of FB. Each panel corresponds to different incident z positions and different colors corresponds to different incident angles, both of which are indicated in each legend. An example of incident photon track is illustrated in the bottom left of each panel, where the bold dashed line indicates the support structure of NCC. The blue line is additional inefficiency, which was introduced in order to avoid 0 inefficiency due to statistical fluctuation in the simulation.

which had been defined in Ref. [56] based on the measurement of photo-nuclear effect in Ref. [119], and E was given in a unit of GeV.

F.3 CC03 and downstream collar counters

The inefficiency functions for CC03-06 consisted of two terms as follows,

$$\max(f_{\rm det}(E), p_{\rm pt}) - p_{\rm pt}(1 - f_{\rm CC06}(E)), \tag{F.3}$$

where $f_{\rm det}$ and $f_{\rm CC06}$ denote the inefficiency functions for the detector with a photon hit and CC06, respectively, and $p_{\rm pt}$ is photon punch-through probability for the hit detector. The function "max()" means to select the larger one among its two arguments. The inefficiency functions $f_{\rm det}$ depended only on incident photon energy E. For CC03, $f_{\rm CsI}(E)$ given in Eq. (F.2) was used. Simulation results were used for inefficiency functions of CC04, CC05 and CC06, where photons with fixed

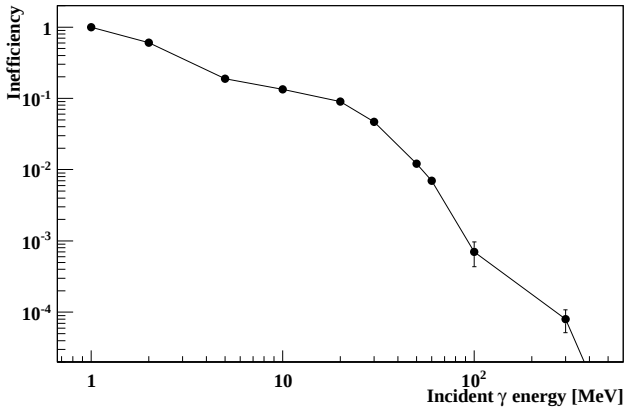

Figure F.2: Inefficiency function of NCC.

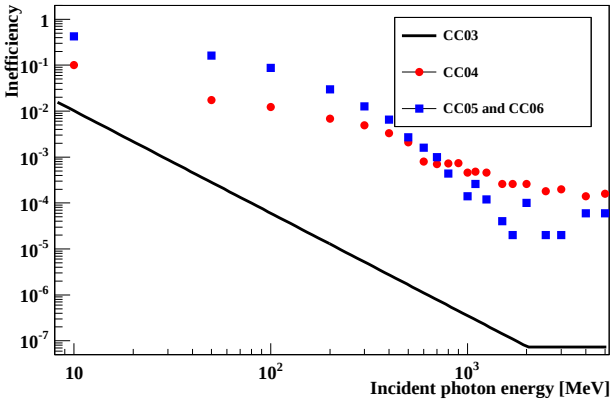

Figure F.3: Inefficiency function for CC03-CC05.

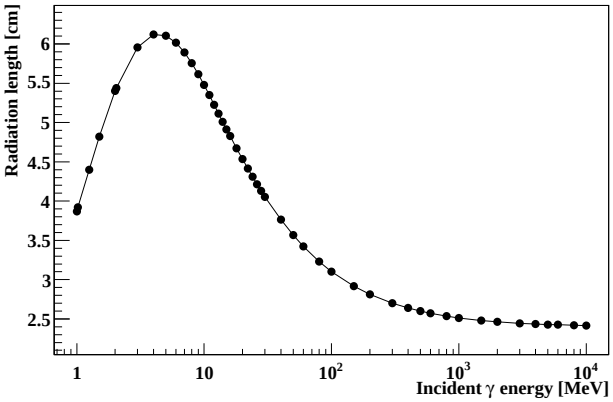

Figure F.4: Interaction length of CsI.

energy were injected into the corresponding detector and inefficiency was calculated with the same veto condition for each detector. The result for CC06 was used also as CC05 inefficiency. These are presented in Fig. F.3.

The punch-through probability p_{pt} is obtained from path length of an incident photon track inside the hit detector and photon cross section with CsI, which was taken from Ref. [120] and is shown in Fig. F.4. This is used to consider photons grazing an edge of these detector; when the path length is short and interaction probability, given as p_{pt} is larger than expected inefficiency f_{det}, p_{pt} is used as an inefficiency value for the detector. This is what the first term of Eq. (F.3). In case that an incident photon graze CC03-05, it can be detected by a downstream detector, which is considered in the second term of Eq. (F.3). Here, the CC06 inefficiency function was used as detection inefficiency of the downstream detector. Such photons need to pass through various materials to reach the next collar counter: PMTs, frontend-electronics boards and cooling pipes for the CC03-CC04 interval; the beam pipe and the vacuum flange for the CC04-CC05 interval, for example. Because material effect due to the beam pipe is considered in the simulation for the CC06 inefficiency function, this was used to consider detection of grazing photons by the downstream

Table F.1: Parameters for BHPV inefficiency functions.

Condition	p_0	p_1	p_2	p_3	p_4
May 2013 run	1.53541	0.00895656	0.0844269	0.00209773	0.0337159
Condition A	1.35771	0.00906818	0.00821133	0.00961246	0.00612500
Condition B	1.53796	0.0093304	0.0483644	0.00338763	0.000943819
Edge effect	2.74351×10^{-5}	0.00384016	0.344792	0.00153235	-

detector. In case of an incident photon hitting CC06, the above issue was not considered hence inefficiency was given by only the first term of Eq. (F.3).

F.4 BHPV

The inefficiency function of BHPV was defined as a function of incident photon energy,

$$f_{\mathrm{BHPV}} = p_0 \exp(-p_1 E) + p_2 \exp(-p_3 E) + p_4, \tag{F.4}$$

where E denotes photon energy in a unit of MeV and parameters p_{0-4} were given for each experimental condition, namely the May 2013 physics run and the two conditions mentioned in Sec. 6.5.1. These were obtained by fitting simulation results with Eq. (F.4). They are summarized in Table F.1 and their graphs for the May 2013 run and the condition A in shown in Fig. 6.5.1. The graph for the condition B is in Ref. [94]. Because the Guard Counter [105] was not installed in the May 2013 run, inefficiency additional factor was multiplied in case that either of an extrapolated photon track x or y position at the downstream of BHPV was outside of ± 125 mm. This is shown in the left panel of Fig. 6.5.1 and given as

$$1 + p_0 E^2 \exp(-p_1 E) + p_2 (1 - \exp(-p_3 E)), \tag{F.5}$$

where E is measured with the MeV unit and parameters are given in Table F.1.

Appendix G

Various corrections in the $Ke3$ and masking background estimation

This appendix describes the detail of the selection cuts and correction related to them in the $Ke3$ and masking background estimation.

G.1 Correction of cut difference

As described in Sec. 7.4.5, there was some difference in the selection cuts for estimation of $Ke3$ and masking background and for $K_L \to \pi^0\nu\overline{\nu}$ events. Namely, the cut on distance from the dead channels, the γ quality cut and the neural network cuts were not applied in the $Ke3$ and masking background studies and the γ quality cut was modified between these two conditions. These differences were considered by multiplying a correction factor to the simulation result as the reduction factor of these cuts. This factor was calculated for each mode as a ratio of the number of events with the two cut sets in the full simulation sample and is summarized in Table. G.1. In this calculation, no selection in $Z_{\rm vtx}$ and $P_{\rm T}$ was not applied. The common value was used in the estimation of background due to CV inefficiency and masking effect for the $Ke3$ mode.

Table G.1: Summary of the correction factors for cut difference in each mode.

Decay Mode	Correction factor
$K_L \to \pi e\nu_e$ ($Ke3$)	0.71
$K_L \to \pi\mu\nu_\mu$ ($K\mu3$)	1.08
$K_L \to 3\pi^0$	0.77
$K_L \to \pi^+\pi^-\pi^0$	0.90
$K_L \to 2\pi^0$	0.93

G.2 Treatment of COE weighting

Since COE weighting as described in Sec. 5.4.6 is able to be calculated with an offline-COE value each background candidate event was weighted according to its offline-COE value and this was commonly applied for all recycled events.

Appendix H

Neural Network Cuts for Neutron Background Estimation

As described in Sec. 7.2.2, two kinds of neutral network cuts, named the kinematical neural network cut and the shape neural network cut, were introduced for further separation of signal from background. Detail of these cuts are described in this appendix.

H.1 Kinematical neural network cut

H.1.1 Training samples

The $K_L \to \pi^0\nu\overline{\nu}$ MC sample and data taken in the aluminum target run were used for the signal and the background samples, respectively. For the signal sample, the veto cuts by the calorimeter information and the following kinematic cuts among those defined in in Sec. 7.2 were applied for the $K_L \to \pi^0\nu\overline{\nu}$ MC sample:

- the cuts on two photon energies and position,
- $3000 < Z_{\rm vtx} < 5000$ mm,
- $130 < P_{\rm T} < 250$ MeV/c,
- the cut on the projection angle,
- the cut on two photons' distance,
- total photon energy is larger than 500 MeV,
- the cut on $e\theta$,
- the cut on two photons' energy ratio,
- the π^0 kinematic cut.

For the background sample, the following conditions were required:

- all the above cuts except π^0 $Z_{\rm vtx}$ and $P_{\rm T}$,

- total photon energy is larger than 650 MeV,
- $R_{\mathrm{COE}} > 180$ mm,
- Z_{vtx} >3200 mm,
- all the veto cuts.

H.1.2 Input variables

The following five variables were used as an input of the neural network:

- distance of photon hit position from the beam axis on the calorimeter surface for larger energy cluster,
- two photon energy ratio,
- two photon distance on the calorimeter surface,
- projection angle,
- two photon hit time difference.

As for the two photon distance, negative sign is given when a photon cluster with larger energy is located outside of that with smaller energy. Distribution of these variables for the signal and the background samples is shown in Fig. H.1. The output of the neural network for these samples are shown in the left of Fig. H.2.

H.2 Shape neural network cut

H.2.1 Training samples

The $K_L \to \pi^0\nu\overline{\nu}$ MC sample and data taken in the aluminum target run were used for the signal and the background samples, respectively. For the signal sample, only the cuts on energies and position of each photon defined in Sec. 7.2.2 were applied for the $K_L \to \pi^0\nu\overline{\nu}$ simulation sample. For the background sample, the following conditions were required:

- total photon energy is larger than 650 MeV,
- $R_{\mathrm{COE}} > 180$ mm,
- Z_{vtx} >3200 mm,
- the photon energy and position cuts,
- all the veto cuts.

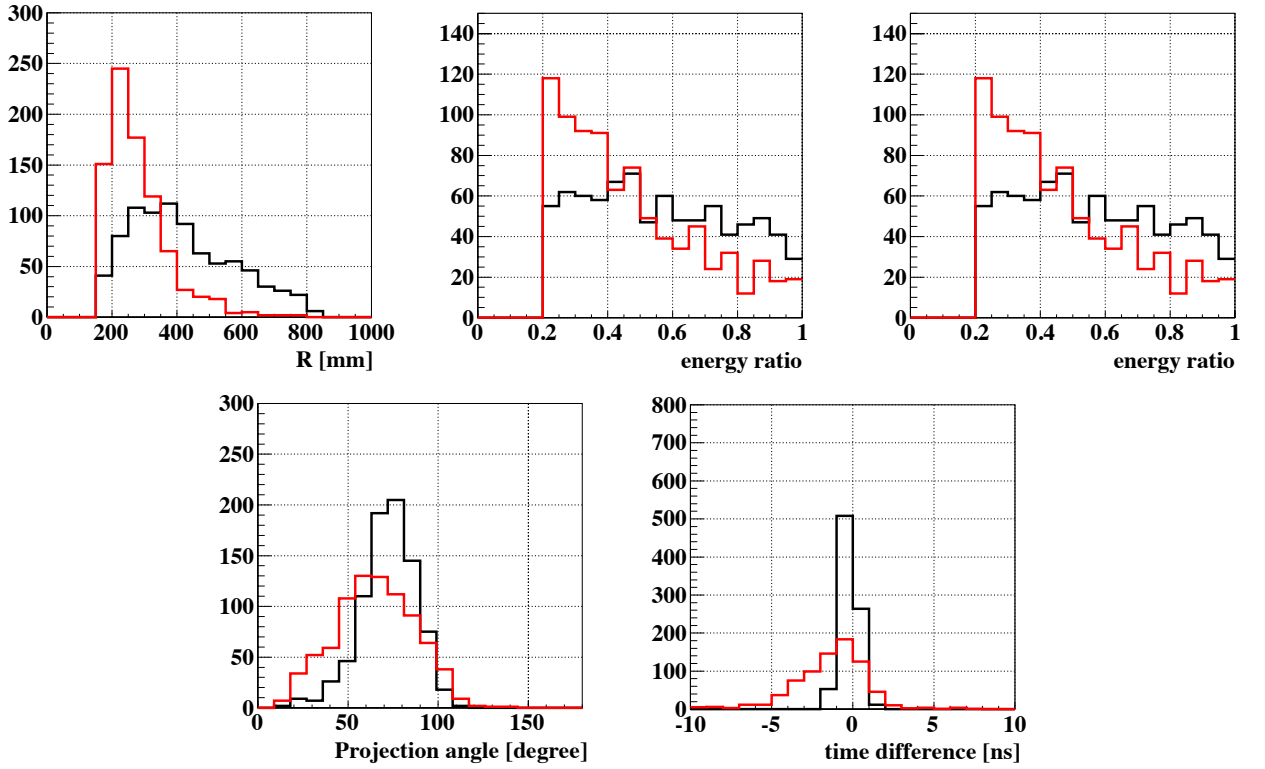

Figure H.1: Distribution of input variables for the kinematic NN value. Black (red) histograms are for the signal (background) sample. Quoted from Ref. [121].

H.2.2 Input variables

The following six kinds of variable for each of two photons, hence twelve in total, were used as an input of the neural network:

- the numbers of crystals,
- cluster RMS values as defined in Eq. (7.2),
- cluster "vertical RMS" values,
- cluster "horizontal RMS" values,
- photon energies,
- photon angles with respect to the beam axis,

where the vertical (horizontal) RMS value is obtained by replacing r_i in Eq. (7.2) with d_{V} (d_{H}) in Fig. H.3. Distribution of these variables for signal and background samples is shown in Fig. H.4. The output of the neural network for these samples are shown in the right of Fig. H.2.

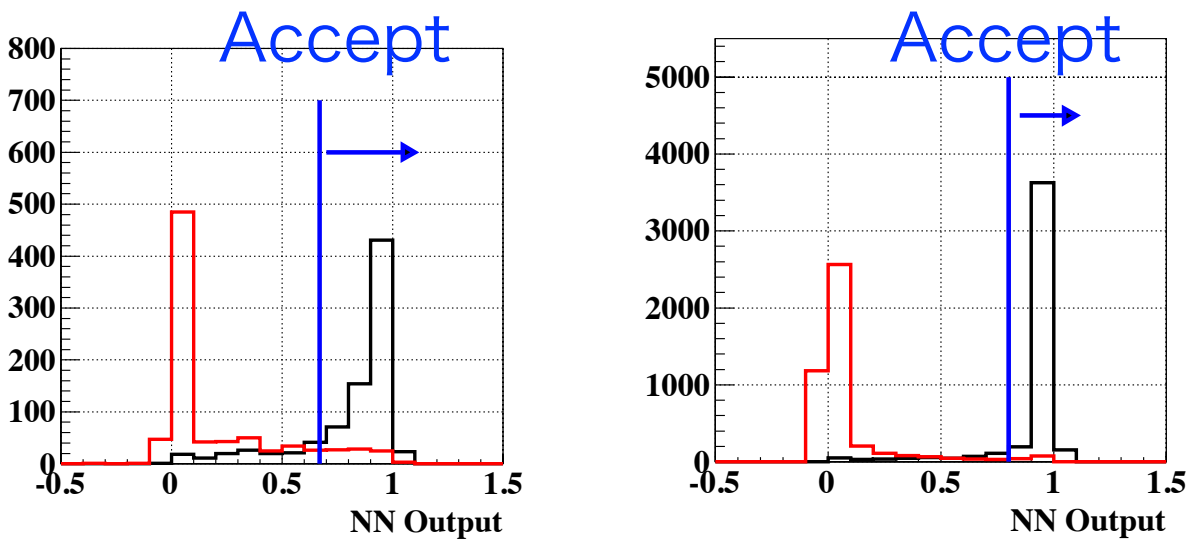

Figure H.2: Distribution of outputs of the two neural networks. The left (right) panel is for the kinematic (shape) NN cut. The blue line in each panel indicates the cut threshold. Quoted from Ref. [121].

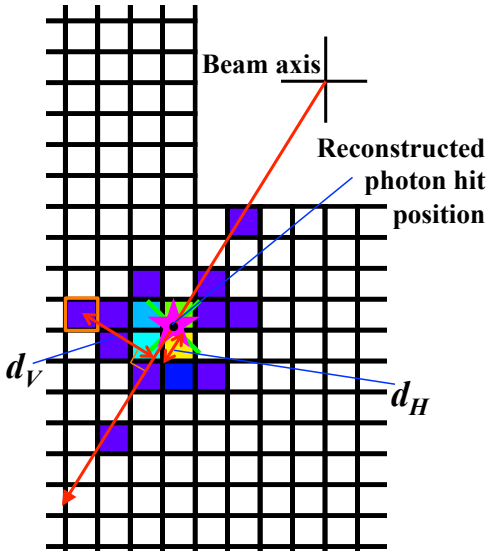

Figure H.3: Definition of distance used in the calculation of the special RMS values. The calorimeter is viewed from the upstream direction. Colors correspond to energy deposition for each crystal. The the orange box indicates the crystal in interest.

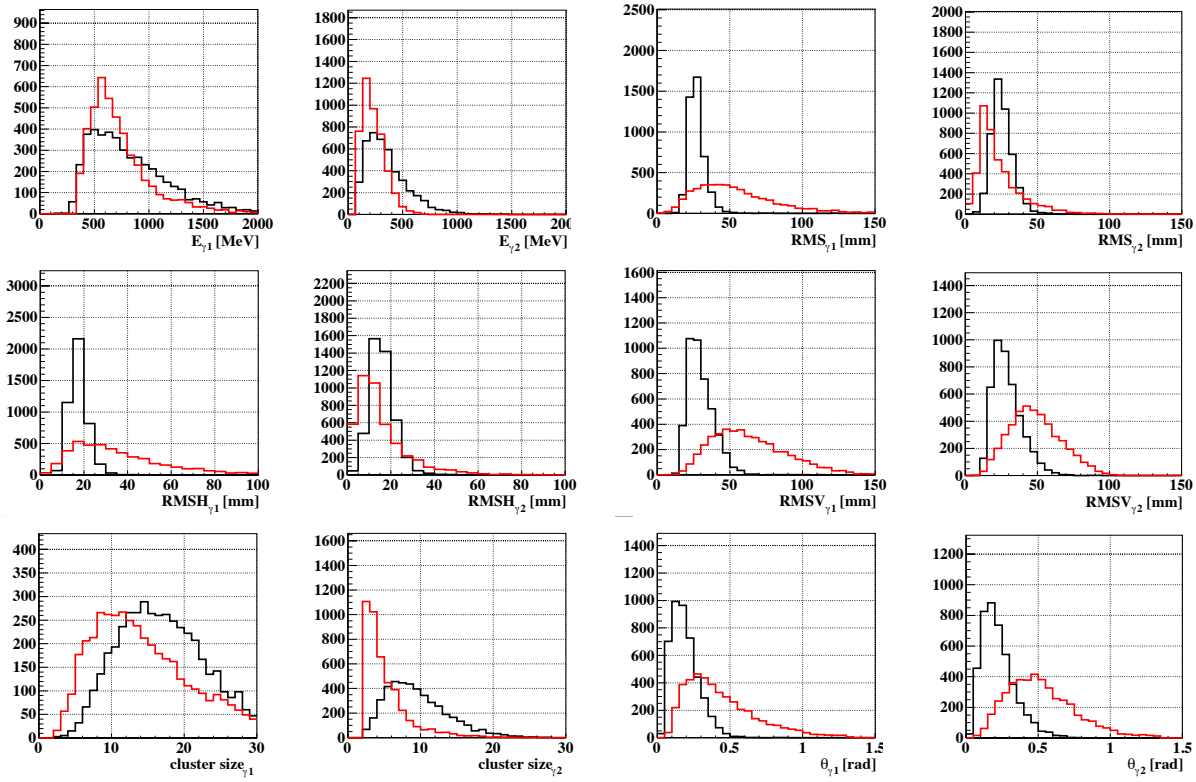

Figure H.4: Distribution of input variables for the shape NN value. Black (red) histograms are for the signal (background) sample. Quoted from Ref. [121].

List of Figures

List of Tables

References

[1] F. Englert and R. Brout, "Broken Symmetry and the Mass of Gauge Vector Mesons," Phys. Rev. Lett. **13**, 321 (1964),
P. W. Higgs, "Broken Symmetries, Massless Particles and Gauge Fields," Phys. Lett. **12**, 132 (1964).

[2] ATLAS Collaboration, "Observation of a new particle in the search for the Standard Model Higgs boson with the ATLAS detector at the LHC," Phys. Lett. **B716**, 1-29 (2012),
CMS Collaboration, "Observation of a new boson at a mass of 125 GeV with the CMS experiment at the LHC," Phys. Lett. **B716**, 30-61 (2012).

[3] G. D. Rochester and C. C. Butler, "Evidence for the existence of new unstable elementary particles," Nature **160**, 855-857 (1947).

[4] T. D. Lee and C. N. Yang, "Question of Parity Conservation in Weak Interactions," Phys. Rev. **104**, 254 (1956).

[5] N. Cabibbo, "Unitary symmetry and leptonic decays," Phys. Rev. Lett. **10**, 531(1963).

[6] S. L. Glashow, J. Iliopoulos and L. Maiant, "Weak Interactions with Lepton-Hadron Symmetry," Phys. Rev. **D2** 1285 (1970).

[7] J. H. Christenson, J. W. Cronin, V. L. Fitch and R. Turlay, "Evidence for the 2π decay of the K_2^0 meson," Phys. Rev. Lett. **13**, 138 (1964).

[8] J. R. Batley, *et al.*, "A precision measurement of direct CP violation in the decay of neutral kaons into two pions," Phys. Lett. **B544**, 97-112 (2002).

[9] E. Abouzaid, *et al.* (KTeV Collaboration), "Precise measurements of direct CP violation, CPT symmetry, and other parameters in the neutral kaon system," Phys. Rev. **D83**, 092001 (2011).

[10] A. D. Sakharov, "Violation of CP invariance, C asymmetry, and baryon asymmetry of the universe," JETP Letters **5**, 24-27 (1967).

[11] A. J. Buras, "CP Violation and Rare Decays of K and B Mesons," lectures given at the 14th Lake Louise Winter Institute, Feb. 14-20, 1999 (arXiv:hep-ph/9905437)

[12] C. S. Wu, *et al.*, "Experimental Test of Parity Conservation in Beta Decay," Phys. Rev. **105**, 1413 (1957).

[13] M. Gell-Mann and A. Pais, "Behavior of Neutral Particles under Charge Conjugation," Phys. Rev. **97**, 1387 (1955).

[14] K. Lande, E. T. Booth, J. Impeduglia, L. M. Lederman and W. Chinowsky, "Observation of Long-Live Neutral V Particles," Phys. Rev. **103**, 1901 (1956).

[15] S. Bennett, D. Nygren, H. Saal, J. Steinberger and J. Sunderland, "Measurement of the charge asymmetry in the decay $K_L^0 \to \pi^\pm + e^\mp + \nu$," Phys. Rev. Lett. **19**, 993 (1967).

[16] K. A. Olive, *et al.* (Particle Data Group), "Review of Particle Physics," Chin. Phys. **C38**, 090001 (2014).

[17] T. T. Wu and C. N. Yang, "Phenomenological analysis of violation of CP invariance in decay of K^0 and $\bar{K^0}$," Phys. Rev. Lett. **13**, 380 (1964).

[18] E. Blucher, B. Winstein, and T. Yamanaka, "Testing the CKM Model with Kaon Experiments," Prog. Theor. Phys. **122**, 81 (2009).

[19] "The Physics in the B Factories," Eur. Phys. J. **C74**, 3026 (2014).

[20] M. Kobayashi and T. Maskawa, "CP-violation in the Renormalizable Theory of Weak Interaction," Prog. Theor. Phys. **49**, 652 (1973).

[21] L. Wolfenstein, "Parametarization of the Kobayashi-Maskawa Matrix," Phys. Rev. Lett. **51**, 1945 (1983).

[22] J. Charles, *et al.* (CKMfitter Group), "CP violation and the CKM matrix: assessing the impact of the asymmetric B factories," Eur. Phys. J. **C41**, 1-131 (2005), http://ckmfitter.in2p3.fr/www/html/ckm_main.html (date last accessed : 4th January, 2016)

[23] L. S. Littenberg, "CP-violating decay $K_L \to \pi^0\nu\overline{\nu}$," Phys. Rev. **D39**, 3322 (1989).

[24] A. J. Buras, S. Uhlig and F. Schwab, "Waiting for precise measurements of $K^+ \to \pi^+\nu\overline{\nu}$ and $K_L \to \pi^0\nu\overline{\nu}$," Rev. Mod. Phys. **80**, 965 (2008).

[25] T. Inami and C. S. Lim, "Effects of Superheavy Quarks and Leptons In Low-Energy Weak Processes $K_L \to \mu\bar{\mu}$, $K^+ \to \pi^+\nu\overline{\nu}$, and $K^0 \leftrightarrow \bar{K}^0$," Prog. Theor. Phys. **65**, 297 (1981), Errata-*ibid.* Prog. Theor. Phys. **65**, 1772 (1981).

[26] F. Mescia and C. Smith, "Improved estimates of rare K decay matrix elements from K_{l3} decays," Phys. Rev. **D76**, 034017 (2007).

[27] A. J. Buras, D. Buttazzo, J. Girrbach-Noe and R. Knegjens, "$K^+ \to \pi^+\nu\overline{\nu}$ and $K_L \to \pi^0\nu\overline{\nu}$ in the Standard Model: status and perspectives," JHEP **1511**, 033 (2015).

[28] K. Shiomi, "Measurement of K_L^0 flux at the J-PARC neutral-kaon beam line for the $K_L \to \pi^0\nu\overline{\nu}$ experiment," Ph.D. thesis, Kyoto University (2012).

[29] M. Trodden, "Electroweak baryogenesis," Rev. Mod. Phys. **71**, 1463 (1999).

[30] Y. Grossman and Y. Nir, "$K_L \to \pi^0\nu\overline{\nu}$ beyond the Standard Model," Phys. Lett. **B398**, 163-168 (1997).

[31] W. J. Marciano and Z. Parsa, "Rare kaon decays with 'missing energy,' " Phys. Rev. **D53**, 1 (1996).

[32] A. V. Artamonov, *et al.* (E949 Collaboration), "New Measurement of the $K^+ \to \pi^+ \nu\overline{\nu}$ Branching Ratio," Phys. Rev. Lett. **101**, 191802 (2008),
A. V. Artamonov, *et al.* (E949 Collaboration), "Study of the decay $K^+ \to \pi^+ \nu\overline{\nu}$ in the momentum region $140 < P_\pi < 199$ MeV/c," Phys. Rev. **D79**, 092004 (2009).

[33] M. Blanke, "New Physics Signatures in Kaon Decays," in proceedings of "2013 KAON International Conference," PoS(KAON13)010 (2013).

[34] M. Blanke, A. J. Buras, B. Duling, S. Recksiegel and C. Tarantino, "FCNC processes in the Littlest Higgs model with T-Parity: an update," Acta Phys. Polon. **B41**, 675 (2010).

[35] M. Blanke, A. J. Buras, B. Duling, K. Gemmler and S. Gori, "Rare K and B Decays in a Warped Extra Dimension with Custodial Protection," JHEP **0903**, 108 (2009).

[36] The CMS and LHCb Collaboration, "Observation of the rare $B_s^0 \to \mu^+\mu^-$ decay from the combined analysis of CMS and LHCb data," Nature **522**, 68-72 (2015).

[37] A. J. Buras, F. De Fazio and J. Girrbach, "The anatomy of Z' and Z with flavour changing neutral currents in the flavour precision era," JHEP **1302**, 116 (2013).

[38] G. Colangelo and G. Isidori, "Supersymmetric contributions to rare kaon decays: beyond the single mass insertion approximation.," JHEP **9809** 009 (1998).

[39] G.E. Graham, *et al.*, "Search for the decay $K_L \to \pi^0 \nu\overline{\nu}$ using $\pi^0 \to e^+e^-\gamma$," Phys. Lett. **B295**, 169-173 (1992).

[40] M. Weaver, *et al.* (E799 Collaboration), "Limit on the Branching Ratio of $K_L \to \pi^0 \nu\overline{\nu}$," Phys. Rev. Lett. **72**, 3758 (1994).

[41] J. Adams, *et al.* (KTeV Collaboration), "Search for the decay $K_L \to \pi^0 \nu\overline{\nu}$," Phys. Lett. **B447**, 240-245 (1999).

[42] A. Alavi-Harati, *et al.* (KTeV Collaboration), "Search for the decay $K_L \to \pi^0 \nu\overline{\nu}$ using $\pi^0 \to e^+e^-\gamma$," Phys. Rev. **D61**, 072006 (2000).

[43] J. K. Ahn, *et al.* (E391a Collaboration), "New limit on the $K_L^0 \to \pi^0 \nu\overline{\nu}$ decay rate," Phys. Rev. **D74**, 051105(R) (2006),
Erratum-*ibid.* Phys. Rev. **D74**, 079901 (2006).

[44] J. K. Ahn, *et al.* (E391a Collaboration), "Search for the Decay $K_L^0 \to \pi^0 \nu\overline{\nu}$," Phys. Rev. Lett. **100**, 201802 (2008).

[45] J. K. Ahn, *et al.* (E391a Collaboration), "Experimental study of the decay $K_L^0 \to \pi^0 \nu\bar{\nu}$," Phys. Rev. **D81**, 072004 (2010).

[46] Y. Yanagida and H. Yoshimoto, "Reusing KTeV CsI crystals for J-PARC KOTO experiment," in proceedings of "2009 KAON International Conference," PoS(KAON09)021 (2010).

[47] S. Nagamiya, "Introduction to J-PARC," Prog. Theor. Exp. Phys. **2012**, 02B001 (2012).

[48] T. Koseki, *et al.*, "Beam commissioning and operation of the J-PARC main ring synchrotron," Prog. Theor. Exp. Phys. **2012**, 02B004 (2012).

[49] S. Agostinelli, *et al.*, "GEANT4–a simulation toolkit," Nucl. Instrum. Methods **A506**, 250-303 (2003),
http://geant4.cern.ch (date last accessed : 4th January, 2016)

[50] S. Banerjee, "Improvements in the Geant4 Hadronic Physics," J. Phys.: Conf. Ser. **331**, 032002 (2011).

[51] M. Ikegami, "Beam commissioning and operation of the J-PARC linac," Prog. Theor. Exp. Phys. **2012**, 02B002 (2012).

[52] H. Hotchi, *et al.*, "Beam commissioning and operation of the Japan Proton Accelerator Research Complex 3-GeV rapid cycling synchrotron," Prog. Theor. Exp. Phys. **2012**, 02B003 (2012).

[53] K. Hasegawa, "Commissioning of Energy Upgraded Linac of J-PARC," Proc. LINAC 2014, TUIOB03, p.417 (2014).

[54] G. I. Budker, *et al.*, "Experiments on charge-exchange injection of protons into a storage ring," Soviet Atomic Energy 19, 6, pp 1479-1481 (1965).

[55] M. Tomizawa, *et al.*, "Performance of Resonant Slow Extraction from J-PARC Main Ring," Proc. IPAC 2012, MOPPD051, p.481 (2012).

[56] J. Comfort, *et al.*, "Proposal for $K_L \to \pi^0\nu\overline{\nu}$ Experiment at J-Parc," J-PARC proposal 14 (2006),
http://koto.kek.jp (date last accessed : 4th January, 2016)

[57] K. Agari *et al.*, "Primary proton beam line at the J-PARC hadron experimental facility," Prog. Theor. Exp. Phys. **2012**, 02B008 (2012).

[58] H. Takahashi, *et al.*, "Construction and beam commissioning of Hadron Experimental Hall at J-PARC," J. Phys.: Conf. Ser. **312**, 052027 (2011).

[59] H. Takahashi, *et al.*, "Indirectly water-cooled production target at J-PARC hadron facility," J. Radioanal. Nucl. Chem. (2015).

[60] T. Shimogawa, "Design of the neutral K_L^0 beamline for the KOTO experiment," Nucl. Instrum. Methods **A623**, 585-587 (2010).

[61] G. Takahashi, *et al.*, "Development of a Neutral Beam Profile Monitor," Jpn. J. App. Phys. **50**, 036701 (2011).

[62] "Technical Design Report of KL Beamline at the J-PARC Hadron Hall," KOTO internal document (2009).

[63] K. Shiomi, *et al.*, "Measurement of K_L^0 flux at the J-PARC neutral-kaon beam line," Nucl. Instrum. Methods **A664**, 264-271 (2012).

[64] T. Masuda, "Development and Experimental Study of the KOTO Detector System using Three K_L Neutral Decay Modes," Ph.D. thesis, Kyoto University (2014).

[65] Hamamatsu Photonics K. K.,
http://www.hamamatsu.com/jp/en/ (date last accessed : 4th January, 2016)

[66] Y. Yanagida, "Development and deterioration assessment of the optical connecting silicone cookie for KOTO CsI calorimeter" (in Japanese), Master thesis, Osaka University (2012).

[67] T. Masuda, *et al.*, "A vacuum tolerant high voltage system with a low noise and low power Cockcroft-Walton photomultiplier base," Nucl. Instrum. Methods **A746**, 11-19 (2014).

[68] J.D. Cockcroft and E.T.S. Walton , "Experiments with High Velocity Positive Ions. (I) Further Developments in the method of obtaining High Velocity Positive Ions.," Proceedings of the Royal Society of London 136, 619 (1932).

[69] J. W. Lee, "Energy Calibration Method for the KOTO CsI Calorimeter," Ph.D. thesis, Osaka University (2014).

[70] T. Matsumura, *et al.*, "Photon-Veto Counters at the Outer Edge of the Endcap Calorimeter for the KOTO Experiment," Nucl. Instrum. Methods **A795**, 19-31 (2015).

[71] M. Itaya, *et al.*, "Development of a new photomultiplier tube with high sensitivity for a wavelength-shifter fiber readout," Nucl. Instrum. Methods **A522**, 477-486 (2004).

[72] Y. Tajima, *et al.*, "Barrel photon detector of the KEK $K^0_L \to \pi^0\nu\overline{\nu}$ experiment," Nucl. Instrum. Methods **A592**, 261-272 (2008).

[73] Y. Yoshimura, *et al.*, "Plastic scintillator produced by the injection-molding technique," Nucl. Instrum. Methods **A406**, 435-441 (1998).

[74] T. Hineno, "Development and performance studies of charged particle detector installed inside of the upstream beam pipe in the KOTO experiment" (in Japanese), Master thesis, Kyoto University (2014).

[75] N. Kawasaki, "A Gamma and Neutron Counter of Undoped CsI Crystals with WLSFiber Readout for the KOTO Experiment," in proceedings of "2013 KAON International Conference," PoS(KAON13)040 (2013).

[76] N. Kawasaki, *et al.*, "Halo neutron measurement for KOTO experiment," JPS Conf. Proc. **8**, 024006 (2015).

[77] N. Kawasaki, *et al.*, "Development of Undoped Cesium Iodide Counter with Wavelength-Shifting-Fiber Readout," to be submitted to Prog. Theor. Exp. Phys. .

[78] Saint-Gobain,
http://www.crystals.saint-gobain.com (date last accessed : 4th January, 2016)

[79] KURARAY Co., LTD., 3-10, Nihonbashi, 2 chome, Chuo-ku, Tokyo, Japan,
http://www.kuraray.co.jp/en/ (date last accessed : 4th January, 2016)

[80] Eljen Technology,1300 W. Broadway Sweetwater, Texas 79556, United States, http://www.eljentechnology.com (date last accessed : 4th January, 2016)

[81] Oike & Co., Ltd., http://www.oike-kogyo.co.jp/english/ (date last accessed : 4th January, 2016)

[82] Y. Maeda, "Charged-particle veto detector for the $K_L \to \pi^0\nu\overline{\nu}$ study in the J-PARC K$^{\rm O}$TO experiment," proceedings of XXXII Physics in Collision, Štrbské Pleso, Slovak Republic, 2012, edited by D. Bruncko, P. Strizenec and J. Urbéan, eConf C120912, pp371-376 (2013).

[83] D. Naito, *et al.*, "Evaluation of the inefficiency of a charged particle detector for the KOTO experiment," JPS Conf. Proc. **8**, 024003 (2015).

[84] D. Naito, *et al.*, "Development of a low-mass and high-efficiency charged particle detector," to be published in Prog. Theor. Exp. Phys.

[85] Y. Odani, "Collar gamma-ray detector for a neutral-kaon rare decay experiment" (in Japanese), Master thesis, Saga University (2012).

[86] T. Ota, "Development of the Charged Veto counters surrounding the beam in the KOTO experiment" (in Japanese), Master thesis, Saga University (2012).

[87] S. Banno, "Development and performance evaluation of gamma-ray detector in downstream of calorimeter for KOTO experiment" (in Japanese), Master thesis, Osaka University (2013).

[88] Y. Takashima, "Development and performance evaluation of downstream gamma-ray detectors for the J-PARC KOTO experiment" (in Japanese), Master thesis, Osaka University (2014).

[89] E. Iwai, *et al.*, "Performance study of a prototype pure CsI calorimeter for the KOTO experiment," Nucl. Instrum. Methods **A786**, 135-141 (2015).

[90] E. Iwai, "CsI calorimeter for the J-PARC KOTO experiment," Ph.D. thesis, Osaka University (2013).

[91] S. Fukui, *et al.*, "KEK-PS Experiment 248 (AIDA) Search for the H particle via the $pp \to K^+K^+X$ reaction," Workshop on Hadron Physics at e^+e^- Collider 38-41 (1994).

[92] R. Winston, "Light collection within the framework of geometric optics," J. Opt. Soc. Amer. **60**, 245 (1970).

[93] http://www.hamamatsu.com/jp/en/R1250.html (date last accessed : 4th Jan, 2016)

[94] Y. Maeda, *et al.*, "An aerogel Cherenkov detector for multi-GeV photon detection with low sensitivity to neutrons," Prog. Theor. Exp. Phys. **2015**, 063H01(2015).

[95] Y. Sugiyama, *et al.*, "The Data Acquisition System for the KOTO experiment," IEEE Trans. Nucl. Sci., 62, 1115-1121 (2015).

[96] M. Bogdan, J.-F. Genat, and Y. W. Wah, "Custom DAQ Module for timing and energy measurements for J-Parc E14," Proc. 17th IEEE NPSS Real Time Conference, 443-445 (2009).

[97] M. Bogdan, J.-F. Genat, and Y. W. Wah, "Custom 12-Bit, 500MHZ ADC/Data Processing Module for the KOTO Experiment at J-Parc," Proc. 17th IEEE NPSS Real Time Conference, 1-2 (2010).

[98] T. Koseki and K. Hasegawa, "Present Status of J-PARC –After the Shutdown due to the Radioactive Material Leak Accident–," Proc. IPAC 2014, THPME061, p.3373 (2014), http://j-parc.jp/HDAccident/HDAccident-e.html (date last accessed : 4th January, 2016)

[99] Y. Sugiyama, *et al.*, "Pulse Identification Method for Overlapped Pulses," JPS Conf. Proc. **8**, 024002 (2015).

[100] K. Sato, "Measurement of the CsI calorimeter performance and K_L momentum spectrum for the J-PARC KOTO experiment," Ph.D. thesis, Osaka University (2015).

[101] S.K. Sahu, *et al.* "Measurement of radiation damage on a silica aerogel Cherenkov radiator," Nucl. Instrum. Methods **A382**, 441-446 (1996).

[102] E. Aschenauer, *et al.*, "Optical characterization of $n = 1.03$ silica aerogel used as radiator in the RICH of HERMES," Nucl. Instrum. Methods **A440**, 338-347 (2000).

[103] A. Schnase, *et al.*, "J-PARC MR Horizontal Exciter Test For Transversal Noise Application," Proceedings of the 8th Annual Meeting of Particle Accelerator Society of Japan, 338 (2011).

[104] "PHOTOMULTIPLIER TUBES Basics and Applications (Edition 3a)," Hamamatsu Photonics K. K. (2007).

[105] S. Shinohara, "Development of Acrylic Cherenkov Counter in the KOTO experiment," in proceedings of "Flavor Physics & CP violation 2015," PoS(FPCP2015)079 (2015).

[106] K. Sato, "Discrimination of background events by shower shape on CsI Calorimeter" (in Japanese), Master thesis, Osaka University (2008).

[107] R. D. Cousins and V. L. Highland, "Incorporating systematic uncertainties into an upper limit," Nucl. Instrum. Methods **A320**, 331-335 (1992).

[108] T. Masuda, *et al.* "Long-Lived Neutral-Kaon Flux Measurement for the KOTO Experiment," to be published in Prog. Theor. Exp. Phys.

[109] K. Fuyuto, W.-S. Hou and M. Kohda, "Loophole in $K \to \pi\nu\bar{\nu}$ Search and New Weak Leptonic Forces," Phys. Rev. Lett. **114**, 171802 (2015).

[110] X.-G He, G. C. Joshi, H. Lew and R. R. Volkas, "New-Z' phenomenology," Phys. Rev. **D43**, 22(R) (1991).

[111] W. Altmannshofer, S. Gori, M. Pospelov, and I. Yavin, "Quark flavor transitions in $L_\mu - L_\tau$ models," Phys. Rev. **D89**, 095033 (2014).

[112] W. Altmannshofer, S. Gori, M. Pospelov, and I. Yavin, "Neutrino Trident Production: A Powerful Probe of New Physics with Neutrino Beams," Phys. Rev. Lett. **113**, 091801 (2014).

[113] A. V. Artamonov, *et al.* (E949 Collaboration), "Upper limit on the branching ratio for the decay $\pi^0 \to \nu\bar{\nu}$," Phys. Rev. **D72**, 091102(R) (2005).

[114] J. P. Lees, *et al.* (*BABAR* Collaboration), "Search for $B \to K^{(*)}\nu\bar{\nu}$ and invisible quarkonium decays," Phys. Rev. **D87**, 112005 (2013).

[115] KEYENCE CORPORATION, 1-3-14, Higashi-Nakajima, Higashi-Yodogawa-ku, Osaka-shi, Osaka, 533-8555, Japan
http://www.keyence.com (date last accessed : 4th January, 2016)

[116] T. Masuda, "Dead channel effect," the slide in the weekly meeting of the Kyoto kaon group at 9th Apr, 2012.

[117] D. Naito, "CV inefficiency result," the slide prepared for the KOTO informal domestic meeting at 9th Nov, 2013.

[118] R.O. Duda and P. E. Hart, "Use of the Hough Transformation To Detect Lines and Curves in Pictures," Comm. of the ACM 15, 1, pp.11-15 (1972).

[119] S. Ajiura, *et al.* "Measurements of the photon detection inefficiency of calorimeters between 185 and 505 MeV," Nucl. Instrum. Methods **A435**, 408-422 (1999).

[120] M. J. Berger, *et al.*, "XCOM: Photon Cross Sections Database,"
http://www.nist.gov/pml/data/xcom (date last accessed : 4th January, 2016)

[121] K. Shiomi, "Summary of the May run analysis," the slide in the KOTO collaboration meeting at 10th Oct, 2014.